Modelling of soft tissues behaviour

J. J. Telega and M. Stańczyk

Institute of Fundamental Technological Research
Polish Academy of Sciences
Świętokrzyska 21, 00-049 Warsaw Poland
`mstan@ippt.gov.pl`

The goal of these notes is to introduce the reader into selected, currently important topics of soft tissues behaviour and modelling. Particular emphasis is put on nonlinear and anisotropic behaviour of various tissues. Approximate linear behaviour of some tissues is also discussed. Averaging methods used in modelling macroscopic behaviour are critically assessed. The study also includes the behaviour and modelling of collagen molecule, collagen fibre and elastin. It is shown that modelling of hyperelastic behaviour of nonlinear soft tissues is essential for elaboration of acceptable macroscopic models. Fluid (blood) – structure (arterial wall) interactions are sketched. Issues pertaining to residual stresses and remodelling are only briefly sketched since the book [570] offers comprehensive papers on those topics. Selected thermal problems are also examined.

1. Introduction

The aim of these lectures is to provide a sort of synthesis on various aspects of soft tissue modelling. In the biomechanical literature such modelling ranges from molecular level, like in muscle contraction, to more standard phenomenological description used in solid mechanics. Having plunged into abundant literature on structure, functioning and modelling of soft tissues one easily perceives that we are faced with extremely challenging problems since biological aspects play an increasing role. In biomechanical modelling, biological aspects, like cell activities, hierarchical architecture, are still not easy to incorporate into constitutive equations. We think that inspiring thoughts by Reed [479], on mathematical biology apply also, with some extensions and modifications, to biomechanical modelling of soft tissues. In biomechanical modelling of interest for us in these notes, the well-established principles of continuum mechanics are in fact exploited, even if not explicitly stated. Yet we are aware that biology of tissues should somewhat be taken into account.

We are convinced that in the years to come biomechanical modelling will profit more deeply from developments offered by biophysics [190], mathematical biology [289, 413] and molecular biology [586]. The situation resembles solid and fluid mechanics, where micro-macro modelling and material science play an ever increasing role, cf. Ponte Castañeda et al. [453].

The aim of these lectures is more modest; we shall focus on mechanical and thermal aspects of soft tissue modelling. An attempt will be made to synthesize various aspects of modelling, to cover a broad spectrum of tissues and provide relevant references. Clinical aspects and phenomena such as muscle contraction are out of scope of this comprehensive paper. The last topic is discussed by Skubiszak (this volume and [528]); for a sort of the state-of-the-art the reader is also advised to consult the book [232], and particularly the paper by Huxley [264], cf. also the relevant papers on modelling cited in Jemioło and Telega [276, 277].

The plan of the paper is as follows. The aim of Section 2 is twofold. First, a concise presentation of tissue classification is given. Next the hierarchical structure, anisotropy and inhomogeneity of selected tissues and organs is described. Section 3 deals with mechanical behaviour of actin, elastin and collagen, including the classification

Selected experimental methods including biaxial and shear tests are presented in Section 4. Elements of nonlinear elasticity and constitutive relationships for isotropic and anisotropic tissues are introduced in Section 5. Section 6 critically assesses the available results on effective (macroscopic) properties of tissues derived from microscopic data. Modelling of active stresses is investigated in Section 7. In Section 8 the pseudoelastic behaviour of soft tissues is investigated. The cases of isotropy, transverse isotropy and orthrotropy are discussed and the appropriate examples are given.

Section 9 is devoted to thermal modelling of tissues. Pertinent heat loads are described, criteria for thermal damage are given and various existing models for vascularized tissue are discussed. The section concludes with a brief discussion of the possibility of hyperbolic conduction phenomena in soft tissues and application of mixture theory to thermally-induced changes in soft tissues.

The paper is summarized in Section 10, where final comments and remarks are presented.

2. Classification of tissues, hierarchical structure, anisotropy, inhomogeneity

Prior to proceeding to soft tissue modelling we shall introduce the classification of tissues and provide examples of their complexity, anisotropy and inhomogeneity.

2.1. Main groups of tissues

A tissue is a collection of cells and extracellular matrices, that perform specialized functions [46, 98]. The extracellular matrix consists of fibres like elastin and collagen, and a ground substance, e.g. proteoglycans. Animal and human tissues are classified into four main groups: connective, epithelial, muscle and nerve. Let us pass to a short description of each of these tissues.

A connective tissue is defined as any tissue, in which the extracellular matrix occupies a greater volume than the cellular component. Connective tissues include cartilage, tendons, ligaments, the matrix of bone, and the adipose (fatty) tissues as well as the skin, blood and lymph. The last two tissues are special connective tissues where the extracellular matrix is the fluid component. Skin provides an example of dense connective tissue. Thin fibrous connective tissue is found to bind vessels and forms a basal membrane to support cells of the tissue of the liver and of the muscle. Connective tissues are composed of various types of cells and extracellular matrix. The fibres of the extracellular matrix consist of high–molecular–weight polymers of the proteins collagen or elastin, see below. The fibres may be either loosely woven or densely packed in either an ordered or disordered arrangement. In dense, irregular connective tissue, the fibers are closely interwoven in a random way, as in skin, whereas in dense regular connective tissue the fibres are arranged in parallel bundles, as in tendons or in flat sheets, as in aponeuroses. Muscle fibers are either attached directly to bone or to an elastic sheet called aponeurosis, which extramuscularly merges into a tendon. The tendon is attached to the skeleton and transmits the force generated by the muscle fibres, cf. Figs. 10 and 11 in Section 2.2.

The relative abundance of the various tissue components varies greatly from one region of the body to another, depending upon the local structural requirements.

Epithelium consists of sheets of cells that line the inner and outer surfaces of the body and have a secretory as well as a protective function. Epithelial tissues include the 'skin' cover of the lungs, stomach, intestines and blood vessels. In contrast to connective tissues, which may contain a great deal of extracellular matrix around each cell, the cells of epithelium are tightly packed with little extracellular substance between them, although they are usually supported on a basal membrane that contains components of the extracellular matrix. One of the main properties of epithelial tissues is a stable apico-basal (outside-inside) polarity, which is expressed not only in morphological, but also in electrophysiological and transport properties. The ionic channels are mostly located with the apical (outside) membrane domain, whilst pumps are in the baso–lateral one (inside), cf. also Layton and Wein-

stein [335]. This is of importance morphomechanically because this property provides a certain amount of turgor pressure in the subepithelial cavities and hence epithelial stretching. The epithelial cells are bound together by junctions to form an integrated net, that gives the cell sheet mechanical strength and makes it impermeable to passive diffusion of small molecules. The junctions are important in mechanically holding the epithelial sheet together to form a protective layer and thus shield the body from injury and infection. One of the most remarkable properties of embryonic epithelial sheets is that the cell rearrangement may occur without compromising the mechanical integrity and chemical barrier function. Extracellular structures also play a strengthening role. There are many kinds of epithelia. The stratified scaly tissue found in the skin and linings of the esophagus and vagina is composed of thin layers of flat scale-like cells that form rapidly above the blood capillaries and are pushed toward the tissue surface, where they die and flake off. Epithelial cells also produce hair, finger–nails, and toe–nails and, in animals, can give rise to feathers and hooves.

Muscle cells consume body fuel (e.g. sugars and fats) to create a force by contracting and thus do mechanical work, see Jemioło and Telega [276], Skubiszak [528] and the lecture in the present volume, also book ed. by Herzog [232]. They are the body's motors or engines. There are three main types of muscle tissues: striated, smooth, and cardiac. Striated muscles attach to bone, usually via tendons. Skeletal muscle forms a lever arm to do work. This group of muscles is also called skeletal or voluntary muscles and consists of large multinucleated cells. Smooth, or involuntary muscle, is found in the internal organs and around larger blood vessels and consists of sheets of cells. Smooth muscles are present in the digestive tract, bladder, arteries, and veins and are activated by the autonomic nervous system. Cardiac muscles are also striated. They perform the pumping action of the heart. Skeletal and cardiac muscles are discussed more completely in Sections 2.2.

Nerve cells, or neurons, are specialized to transfer information from one part of the body to another, cf. Bochenek and Reicher [48]. The brain and spinal cord are tissues composed of neuronal networks. Each neuron consists of a cell body or soma with branching processes called dendrites and one much larger fibre called the axon. The dendrites connect one neuron to another and the axon transmits impulses. A synapse is a specialized neuronal junction where neurons connect with each other or with muscle cells. Electrical and chemical signals are passed from neuron to neuron or from neuron to muscle trough the synapse. In Section 10.10 we briefly discuss the constitutive modelling of brain tissue.

2.2. Structure of selected soft tissues and organs

2.2.1. Heart. The mammalian heart consists of four pumping chambers, the right and left atria and the right and left ventricles, cf. Figs. 1 and 2. The atria collect the blood that returns to the heart: the right atrium (RA) receives oxygen-poor blood from the body via the inferior and superior vena cava, whereas the left atrium (LA) receives oxygen rich blood from the lungs via the pulmonary veins. The atria and ventricles communicate through the atrioventricular valves, the tricuspid in the right heart and the mitral in the left heart. These valves are connected via collagenous fibres called chordinae tendinae, to the papillary muscles that extend from the anterior and posterior aspects of the ventricular cavities. These ventricles pump blood from the heart: the right ventricle (RV) pumps blood through the pulmonary valve and pulmonary arteries to the lungs, and the left ventricle (LV) pumps blood through the aortic valve and aorta to the remainder of the body. In addition to the distinct papillary muscles, the interior surface of the heart is characterized by many trabeculae, or muscular ridges. The cardiac wall is perfused via the coronary arteries, which originate at the left and right coronary ostia located in the sinuses of Valsava immediately distal to the aortic valve leaflets. The three primary vessels are the left anterior descending (LAD) artery, left circumflex artery (CIRC), and right coronary artery (RCA). In general, the left coronaries supply the left atrium and the anterior and lateral portions of LV; the right coronary artery supplies the right atrium and right ventricular free wall. The posterior and inferior portions of the ventricles may receive
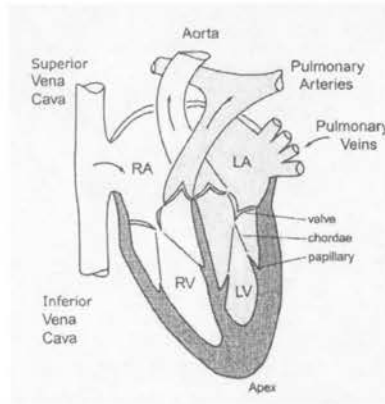

FIGURE 1. Schema of the four chambers of the heart: the right atrium (RA), left atrium (LA), right ventricle (RV), left ventricle (LV). These chambers connect to the vasculature via vena cava, pulmonary veins, pulmonary arteries, and aorta respectively. Flow from the ventricles is maintained unidirectional by one-way valves, see text.

FIGURE 2. Longitudinal cross-section of the heart, after Sideman [520].

POSTERIOR CUSP
MITRAL VALVE
ANTERIOR (AORTIC) CUSP

ANTERIOR (AORTIC) CUSP OF MITRAL VALVE

PULMONARY TRUNK

ASCENDING AORTA

ORIFICES OF CORONARY ARTERIES

AORTIC SINUS (OF VALSALVA)
R. PULMONARY VEIN
L. PULMONARY VEINS
L. AURICLE
R. AURICLE

ASCENDING AORTA
L. ATRIUM
L. CUSP
R. CUSP
AORTIC VALVE

L. CUSP
AORTIC VALVE
POSTERIOR (NONCORONARY) CUSP

SUPRAVENTRICULAR CREST

OUTFLOW TO PULMONARY TRUNK

SUPERIOR VENA CAVA

CONUS ARTERIOSUS

ATRIO-VENTRICULAR PART
MEMBRANOUS SEPTUM
INTER-VENTRICULAR PART

MEDIAL (CONAL) PAPILLARY MUSCLE

R. VENTRICLE

(BROKEN LINE INDICATES LINE OF ATTACHMENT OF SEPTAL LEAFLET OF TRICUSPID VALVE)

R. ANTERIOR PAPILLARY MUSCLE (CUT)

R. ATRIUM

MODERATOR BAND
SEPTO-MARGINAL TRABECULA
SEPTAL BAND

ANTERIOR CUSP (RETRACTED)

L. VENTRICLE

TRI-CUSPID VALVE
MEDIAL (SEPTAL) CUSP
POSTERIOR CUSP

L. ANTERIOR PAPILLARY MUSCLE

R. VENTRICLE

L. POSTERIOR PAPILLARY MUSCLE

R. ANTERIOR PAPILLARY MUSCLE (CUT)

MUSCULAR INTERVENTRICULAR SEPTUM

L. VENTRICLE

R. POSTERIOR PAPILLARY MUSCLE

PLANE OF SECTION

blood from either the left or right coronary systems; this is highly variable from individual to individual and is termed left versus right dominance. The interventricular septum, which separates the left and the right ventricles, is typically supplied by branches off the LAD. The veins in the heart are divided into two systems: a large superficial system, the largest vessels of which parallel the main coronary arteries and drain most of the coronary blood into the right atrium; and a smaller, deeper system (e.g. thebesian veins) drains blood directly into any of the four chambers. The heart wall is perfused primarily during diastole.

The reader is referred to [307, 395] for more details on the coronary circulation.

The wall of the heart consists of three distinct layers, see Fig. 3. An inner wall is called *endocardium*, a middle is called the *myocardium*, and an outer layer is called the *epicardium*. The endocardium lines the inside of each of the cardiac chambers. It is a thin serous membrane (on the order of $100\,\mu$m thick) consisting primarily of 2D (two-dimensional) plexus of collagen and elastin as well as a simple layer of endothelial cells that serves as a direct interface between the blood and the heart wall. The middle layer, or myocardium, is the parenchymal tissue that endows the heart with its ability to pump blood. The myocardium consists primarily of myocytes that are arranged into locally parallel muscle fibres, which in turn are embedded in an extracellular matrix consisting largely of types I and III collagen. The orientation of the muscle fibres changes with position in the wall. The outermost layer, or epicardium,
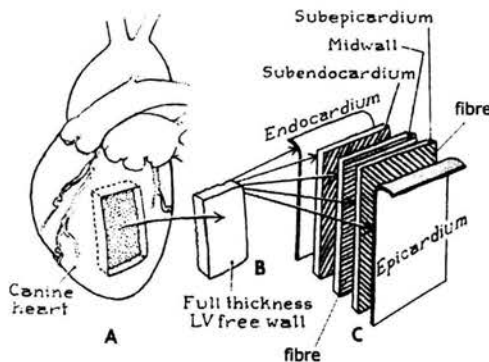

FIGURE 3. Schema of the three primary layers of the ventricular wall: the endocardium (inner layer), myocardium (middle layer) and epicardium (outer layer). Whereas the inner and outer layers are thin collagenous membranes, the middle layer consists of locally parallel fibres that are organized into sheets via an abundant extracellular matrix consisting largely of types I and III collagen, adapted from Humphrey [255].

is also a thin (on the order of $100\,\mu m$) serous layer, consisting largely of a 2D plexus of collagen and some elastic fibres. The heart is surrounded by yet another serous membrane, the *pericardium* (or parietal pericardium). This membrane is thicker than the endocardium and epicardium, but it also consists primarily of a 2D plexus of collagen with some elastic fibres. The pericardium is attached to the diaphragm inferiorly and the hilum superiorly, and it creates a small potential space about the heart that is filled with a 'lubricating' pericardial fluid (about 25 ml in humans). It is thought that the pericardium serves as a type of cradle that limits gross motions of the heart, which is merely suspended in the chest by its connection to the lungs and major blood vessels. These are the major anatomical structures most commonly studied in the field of cardiac mechanics.

The ventricular walls are the most important structures with regard to the pumping action of the heart. From the perspective of mechanics, the ventricles are thick-walled 3D pressure vessels whose thickness and curvature vary regionally and temporally. In the normal heart, the ventricular walls are thickest at the equator and the base of the left ventricle and thinnest at the left ventricular apex and right ventricular free wall. The principal dimensions of the left ventricle vary with species, age, phase of the cardiac cycle, and disease, cf. Table 1.

TABLE 1. Representative dimensions of the LV (minor axis); r – radius, after Humphrey [255].

Species	Comments	Inner r. (mm)	Outer r. (mm)	Thickness to inner radius
Dog (21 kg)	0 mm Hg diastole	16	26	0.62
	2–12 mm Hg	19	28	0.47
	24–40 mm Hg	22	30	0.36
	1–9 mm Hg systole	14	26	0.86
Young rats	0 mm Hg diastole	1.4	3.5	1.50
Mature rats	0 mm Hg diastole	3.2	5.8	0.81
Human	Normal	24	32	0.34
Human	Volume overload	32	42	0.33

2.2.2. Arterial wall. The microstructure of the arterial wall varies with location along the vascular tree, age, species, local adaptations, and disease. Arteries can be categorized according to two general types: *elastic arteries*, which include the aorta, main pulmonary artery, common carotids, common iliacs, and *muscular arteries*, which include the coronaries, cerebrals, femorals

and renals. Elastic arteries tend to be larger-diameter vessels located closer to the heart, whereas muscular arteries are smaller-diameter vessels located closer to the arterioles. Transitional arteries, such as the external carotid, exhibit some characteristics of the elastic and muscular types.

Regardless of the type, all arteries consist of three layers: the tunica *intima*, tunica *media*, and tunica *adventita*, cf. Figs. 4 and 5.
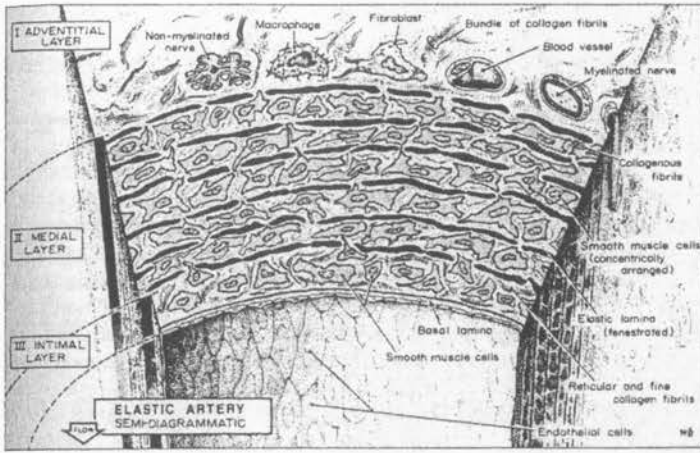

FIGURE 4. Schematic cross sections of a typical elastic artery showing its three primary layers — the intima, media and adventitia — and their primary constituents, after Rhodin [485].
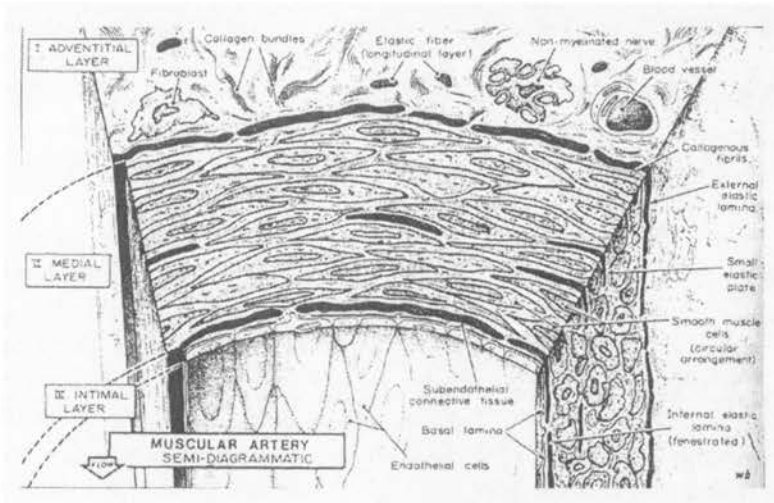
FIGURE 5. Schematic cross sections of a typical muscular artery, after Rhodin [485].

The intima is similar to most elastic and muscular arteries, typically consisting of a monolayer of endothelial cells and an underlying thin ($\sim 80\,$nm) basal lamina. Exceptions include the aorta and coronary arteries in which the intima may contain a subendothelial layer of connective tissue and axially oriented smooth muscle cells. Endothelial cells are usually flat and elongated in the direction of blood flow, often about 0.2 to $0.5\,\mu$m thick, 10 to $15\,\mu$m wide and 25 to $50\,\mu$m long. We observe that exceptions occur near bifurcations wherein the blood flow is complex and the cells are often polygonal in shape. Endothelial cells are interconnected by both tight occluding junctions, which regulate the transport of substances across the endothelium, and in-plane gap junctions, which allow cell-to-cell communication via the transport of ions and metabolites. Endothelial cells may communicate directly with underlying smooth muscle cells via short, blunt processes that extend through the basal lamina into the media. The basal lamina (sometimes referred to as a basement membrane) consists largely of net-like type IV collagen, the adhesion molecules laminin and fibronectin, and some proteoglycans; it provides some structural support to the arterial wall, but acts primarily as an adherent meshwork on which the endothelial cells can grow. Laminin is one of the first extracellular matrix proteins synthesized in the embryo; it has numerous functional domains that bind to type IV collagen, heparan sulfate, and laminin receptor on cells [8].

The internal elastic lamina separates the intima and media, but is often considered to be part of the latter, cf. Figs. 4 and 5. A little thicker in muscular arteries this lamina is essentially a fenestrated 'sheet' of elastin that allows the transport of H_2O, nutrients, and electrolytes across the wall as well as direct transmural cell-to-cell communication. The media contains smooth muscle cells that are embedded in an extracellular plexus of elastin and collagen (primarily types I, II and V) as well as an aqueous ground substance matrix containing proteoglycans. Vascular smooth muscle cells are spindle-shaped (see below for more details on smooth muscles).

In elastic arteries, the medial smooth muscle is organized into 5- to 15-μm-thick concentric 'layers' that are separated by thin ($3\,\mu$m) fenestrated sheets of elastin, cf. Fig. 4. These elastin sheets are similar to the internal elastic lamina, with the fenestra allowing radial transport of metabolites across the wall, direct transmural cell-to-cell communication, and radially oriented connective tissue to tie the wall together threedimensionally. The outermost sheet of elastin is called the external elastic lamina; it separates the media and adventitia but is often considered to belong to the former. There may be as many as 40 to 70 concentric layers of smooth muscle in a thick elastic artery such as the human aorta. According to Clark and Glagov [87, 88] the alternating layers of smooth muscle and elastic laminae in elastic
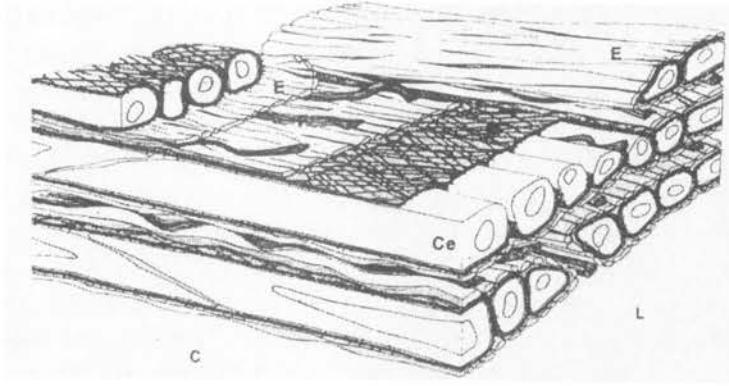
FIGURE 6. Schema of the 'musculo-elastic fascicle' as the basic structural and functional unit of the media in an elastic artery. E – elastin; Ce – smooth muscle cells; F – collagen fiber bundles that exist between the elastin sheets; after Clark and Glagov [88].

arteries (specifically, in abdominal and thoracic aorta) represent a discrete structural and functional unit, called the musculo-elastic fascicle; cf. Fig. 6 (note the collagen fibres between the facing elastic lamina). The thickness of these units is nearly independent of radial location in the wall, but their number increases with increased diameter of the vessel (measured at the mean blood pressure). For instance, a 1.2 mm diameter mouse aorta has 5 musculo-elastic units, whereas a 23 mm diameter pig aorta has 72 units. According to Wolinsky and Glagov (1967), the thickness of aorta increases ~ 0.05 mm for every 1 mm increase in diameter, cf. also Humphrey [255]. These authors also showed that whereas the total wall tension is significantly higher in the larger diameter vessels (e.g. 203 N/m in the pig versus 7.82 N/m in the mouse), the mean tension per lamellar unit is nearly independent of aortic diameter (e.g., about 2 ± 0.4 N/m). Here, tension T was calculated using Laplace's relation for a cylinder, that is $T = P_i r_i$ where P_i is luminal pressure and r_i the current inner radius. We observe that the Laplace law is sometimes still used as a rough estimate of stresses in some soft tissues (e.g. wall stresses of the left ventricle, cf. Moriarty, 1980), see also [255, 307].

The elastic laminae become straight axially at the in vivo length and straight circumferentially at pressures ≥ 60 mm Hg; this pressure-dependent straightening occurs uniformly across the wall, which is likely related to the existence of the residual stresses in the arterial wall, see [570].

In muscular arteries, the smooth muscle appears as a single thick layer that is bounded by a thick internal and less marked external elastic lamina, cf. Fig. 6. Exceptions are the cerebral arteries which do not have an external

lamina and indeed have few elastic fibres in the media. Nonetheless, the smooth muscle in muscular arteries is embedded in a loose connective tissue matrix and arranged as a sequence of concentric layers of cells; the number of layers can reach 25 to 35 in larger vessels. The connective tissue augments the structural integrity of the wall, including its ability to generate force, and acts as a scaffolding on which the cells can adhere to and move on.

The adventitia, or outermost layer of the wall, consists primarily of a dense network of type I collagen fibres with admixed elastin, nerves, fibroblasts, and the vasa vasorum. The adventitial collagen fibres tend to have an axial orientation in most arteries, and they are undulated slightly in the basal state. Although the adventitia comprises only in $\sim 10\%$ and 50% of the arterial wall in elastic and muscular arteries, respectively (see Figs. 4 and 5), it is thought to limit acute overdistension in all vessels. In other words, the collagenous adventitia may serve primarily as a protective sheath, similar to epicardium of the heart. The fibroblasts are responsible for regulating the connective tissue, particularly the type I collagen. The vasa vasorum is an intramural network of arterioles, capillaries, and venules that serve the outer portion of the wall in arteries that are too thick for sufficient transport of O_2, CO_2, nutrients, and metabolites from the intimal surface. It is generally accepted that a vasa vasorum is needed if the number of concentric elastic lamellae exceeds 29 in an elastic artery.

All in all, it is the distributions, orientations and interconnections of the intramural constituents that give rise to the mechanical properties of the arterial wall.

2.2.3. Skeletal muscle.

Fung [175] investigated three kinds of muscles: skeletal, heart and smooth. Skeletal muscle makes up a major part of the animal body. It is the prime mover of animal locomotion. It is controlled by voluntary nerves. It has the feature that if it is stimulated at a sufficiently high frequency, it can generate maximal tension, which remains constant in time. It is then said to be *tetanized*. The activity of the contracting mechanism is then thought to be maximal; for details the reader is referred to the lectures by Skubiszak in this volume, habilitation thesis [528] and to the relevant papers in [232].

Heart muscle is also striated like skeletal muscle, but in its normal function is never tetanized. Heart muscle functions in single twitches and is very different from skeletal muscle.

Smooth muscle, presented in more detail below, are not striated, and are not controlled by voluntary nerves. There are many kinds of smooth muscles, with widely different mechanical properties.

Let us pass to a concise presentation of the structure of skeletal muscle. Its organizational hierarchy is shown in Fig. 7.

It is seen that the units of skeletal muscle are the muscle fibres, each of which is a single cell provided with many nuclei. These fibres are arranged in bundles or *fasciculi* of various sizes within the muscle. Connective tissue fills the spaces between the muscle fibres within a bundle. Each bundle is
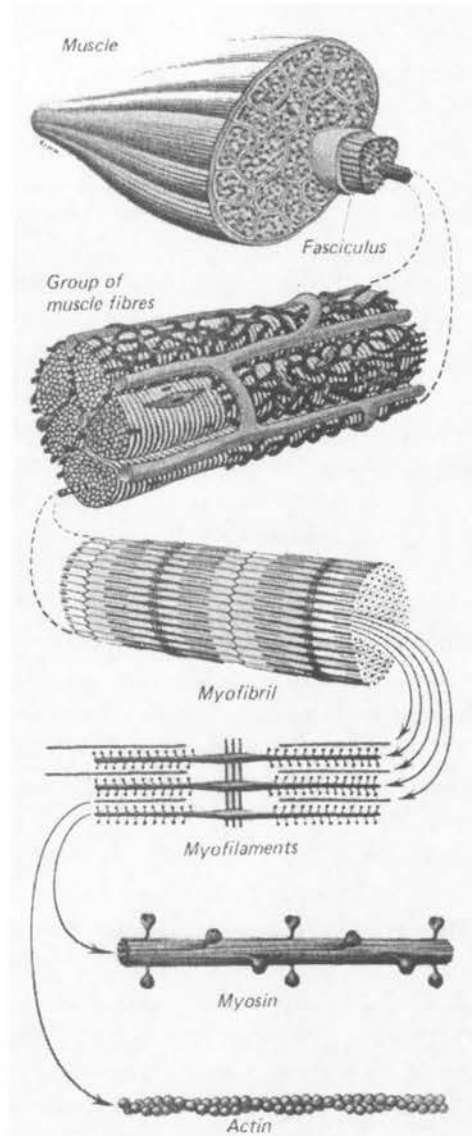

FIGURE 7. The organizational hierarchy of skeletal muscle, after Fung [175]

surrounded by a stronger connective tissue sheath; and the whole muscle is again surrounded by an even stronger sheath.

A skeletal muscle fibre is elongated, having a diameter of 10–60 μm, and a length usually a several millimeters to several centimeters; but sometimes the length can reach 30 cm (in long muscles). The fibres may stretch one end of the muscle to another, but often extend only part of the length of the muscle, ending in tendinous or other connective tissue intersections.

The flattened nuclei of muscle fibres lie immediately beneath the cell membrane. The cytoplasm is divided in longitudinal threads of *myofibrils*, each about 1 μm in diameter. These myofibrils are *striated* when they are stained by dyes and when they are examined optically. For a description of the structure of a myofilament, showing the structure of the spatial arrangement of the actin and myosin the reader is referred to the paper by Skubiszak in this volume and Fig. 9.3:2 in the book by Fung [175].

An important problem, still not fully resolved concerns the modelling of muscle (not necessarily skeletal) at the sarcomere level, cf. the review paper by Huxley [264]. Two approaches can be distinguished; one is descriptive and geometrical like in Skubiszak [528], Redaelli et al. [477] and the relevant papers in [232]. In the second approach one exploits experimental data and elaborates mathematical models of muscle contraction, cf. [644] and the relevant papers cited in [232, 276]. Many papers still appear on the Hill model and its generalization. The model tries to describe the relations like muscle force-velocity and length-tension, cf. [175], Perreault et al. [445], Lin and Nichols [351]. Experimental evidence obtained by Kaya et al. [298] on three medial gastrocnemii from adult, outbred cats (3.0–4.5 kg) shows that muscle fascicle length is not a unique function of muscle force and muscle-tendon length. A suitable relationship between fascicle length and muscle force/length was derived from data of the deactivation phase of isometric contractions covering the approximate physiological range of muscle-tendon lengths. The relationship derived is much more complex than those typically found in Hill-type models of muscle function. Schachar et al. [505] performed a systematic study to quantify the effects of active muscle shortening and stretching on the isometric force-length properties of mammalian skeletal muscle. Shortening and stretching was carried out for magnitudes ranging from 3 to 9 mm, and for speeds ranging from 3 to 27 mm/s in cat soleus ($N = 10$). The purposes of the study performed by Lee et al. [338] were to determine the isometric, steady-state force behaviour following stretch-shortening and shortening-stretch cycles for systematically varying speeds and magnitudes of the first dynamic phase of the stretch-shortening or shortening-stretch cycles, and to determine the effects of repeated stretch-shortening or shortening-stretch cycles on the steady-state, isometric following the dynamic contractions.

Force is transmitted from muscle to bone via several pathways: (i) via the tendons (i.e., myotendinous force transmission), (ii) via intermuscular connective tissue to adjacent muscles (i.e., intermuscular myofacial force transmission), (iii) via structures other than muscles (i.e., extramuscular myofacial force transmission). Maas et al. [362] showed that the fraction of force that is transmitted via these pathways is affected by the position of a muscle relative to adjacent muscles as well as relative to other surrounding tissues. Experiments were performed on male Wistar rats ($N = 6$, body mass= 309.5 ± 21.6 g.). The method of approach relied on manipulating the position of extensor digitorum longus muscle (EDL) relative to intact extramuscular connective tissue of the anterior crural compartment without changing its muscle-tendon complex length. It was also found that the distribution of length of sarcomeres arranged in series within EDL muscle fibres as the distribution of mean sarcomere length of muscle fibres changed as a function of muscle relative position.

Delp et al. [125] provided the first measurement of optimal fascicle length and sarcomere length for three important trunk muscles: rectus abdominis, quadratus lumborum and erector spinae.

The purpose the paper by Bhargava et al. [36] was twofold: first to develop an empirical model for muscle energy consumption, defined as the transformation of chemical energy into the performance of mechanical work and the liberation of heat, that could be used in conjunction with a simple Hill-type model for muscle contraction; and second, to validate the behaviour of the model against available experimental data.

2.2.4. Smooth muscles. As we already know, muscles in which striations cannot be seen are called *smooth muscles*. Smooth muscles of the blood vessels are called *vascular smooth muscles*. These of the intestines are *intestine smooth muscles*. Different organs have different smooth muscles. There are differences among these muscles anatomically, functionally, mechanically, and in their responses to drugs. But there are also common features. All muscles contain actin and myosin and all rely on ATP (adenosine triphospate) for energy.

Changes in the cell membrane induce Na^+ and K^+ ion fluxes and action potentials. The Ca^{++} flux furnishes the excitation-concentration coupling. These properties are similar in all muscles.

Smooth muscle cells are generally much smaller than skeletal and heart muscle. Table 2 gives some typical dimensions obtained by electron microscopy.

Table 2. Size of smooth muscle cells, after Burnstock [64].

Tissue	Animal	Length (μm)	Diameter in nuclear region (μm)
Intestine	Mouse	400	
Taenia coli	Guinea pig	200 (relaxed)	2–4
Nictitating membrane	Cat	350–400	
Vas deferens	Guinea pig	450	
Vascular smooth muscles			
Small arteries	Mouse	60	1.5–2.5
Arterioles	Rabbit	30–40	5

There are a variety of patterns of smooth muscle packing. For details and description of contractile machinery the reader is referred to Burnstock [64] and Fung [175, Chap. 11], cf. also Price [458].

2.2.5. Ligament, tendon aponeurosis. Tendons and ligaments are soft connective tissues composed of closely packed, parallel collagen fibre bundles oriented to provide for the motion and stability of the musculoskeletal system, see [591], [630] and the references therein. Ligaments connect bone to bone, whereas tendons connect bone to muscle. Muscle fibres are either attached directly to bone or to an elastic sheet called *aponeurosis* which extramuscularly merges into a tendon. Structural hierarchy in tendon is represented in Figs. 8 and 9.
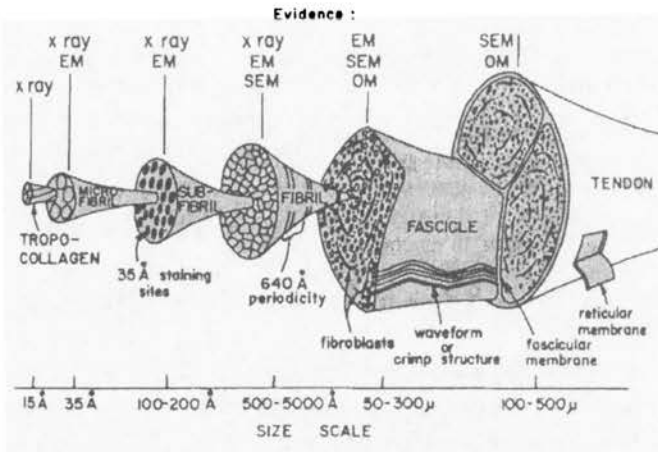

Figure 8. Hierarchical structure of tendon. (S)EM, (scanning) electron microscopy; OM, optical microscopy, after [314]
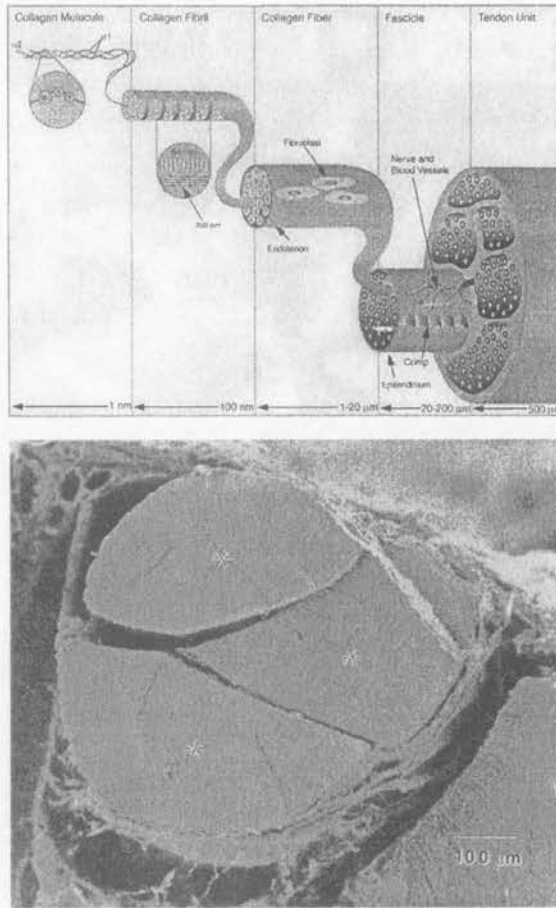
FIGURE 9. Structural hierarchy in tendon. (Top) Diagram illustrating the relationship between collagen molecules, fibrils, fascicles and tendon units. Although the diagram does not show fibril subunits, collagen fibrils appear to be self-assembled from intermediates that may be integrated within the fibril. (Bottom) Scanning electron micrograph of rat tail tendon showing fascicles units (asterisk) that make up the tendon, after Silver et al. [522].

Description of lumbar spine and muscles attached to it include also the *erector spinae aponeurosis* cf. Adams et al. [4, pp.36–38]. This is a broad, flat tendon that covers the lumbar region posteriorly. Its fibers consist exclusively of the candal tendons of the muscle bellies of *longissimus thoracis pars thoracis* and *iliocostalis lumborum pars thoracis*, that lie in the thoracic region. The tendons simply cover underlying muscles, and offer *no attachment* to them. Thus this more insightful description is somewhat different from the traditional one where one claims that the erector spinae aponeurosis is

a large flat tendon arising from the lumbar and sacral spinous processes, the sacrum and ilium, that give rise to the erector spinae muscle that assumes a variety of insertions into the lumbar and thoracic vertebrae, cf. Adams et al. [4, p.37].

The aponeurosis is seen in Figs. 10 and 11.

The myotendinous junction and the bony attachment are complex and vary considerably. Tendons generally have large parallel fibres that insert uniformly into bone. Ligaments have smaller-diameter fibres that can be either parallel, as in the collateral ligaments of the knee, or branching and interwoven, as in the knee cruciate ligaments. Under microscopic examination, ground substance and fibroblasts are observed in the interfibrillar spaces. Ultrastructural methods further demonstrate detailed hierarchies of fibrillar
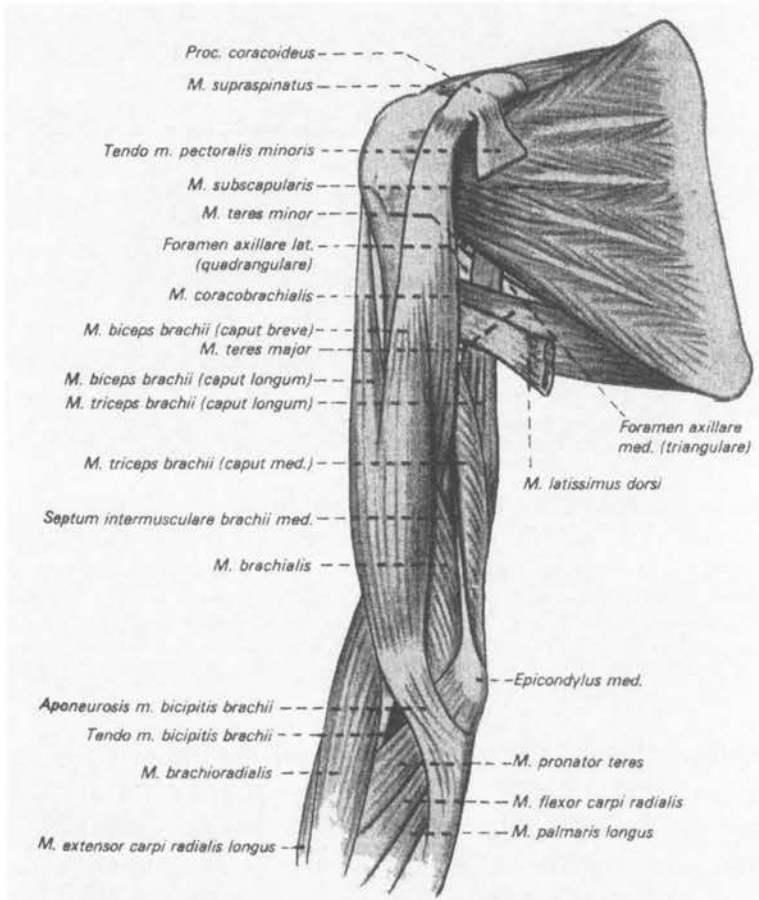

FIGURE 10. Anterior view of right shoulder muscles after removal of the deltoid, after [46]
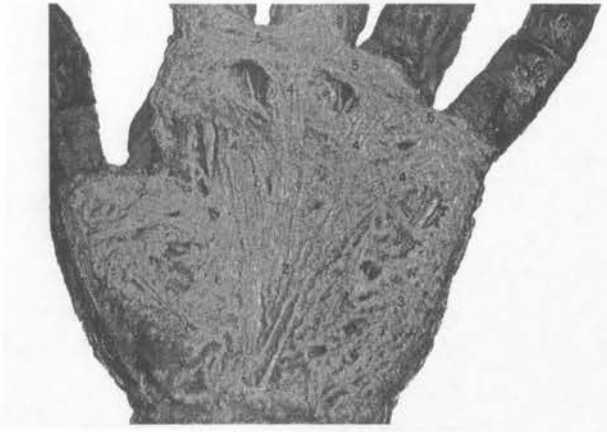
FIGURE 11. Palmar side of left hand. Palmar aponeurosis constitutes a prolongation of the distal edge of retinaculum flexors of wrist. Tendon of long palmaris is attached to the aponeurosis and to distal edge of retinaculum flexors; 1 – *aponeurosis palmaris* covering *thenar*, 2 – middle part of aponeurosis palmaris, 3 – medial part of aponeurosis palmaris, 4 – *fasciculi longitudinales* of aponeurosis palmaris, 5 – *ligamentum natatorium*, 6 – *arteriae digitales* and *nervi digitales palmares proprii*, after [378].

arrangement down to microfibril size in tendons, cf. Figs. 8 and 9. A similar arrangement is thought to exist for ligaments. Although it is agreed that ligaments consist of closely packed collagen fibre bundles that are arranged in a more or less parallel fashion along the longitudinal axis of the ligament, concepts concerning the fibrilla and fibre arrangements of ligamentous tissue differ among investigators, cf. relevant references cited in Woo et al. [630].

There are two types of tendon- and ligament- bone insertions: direct and indirect. In the more direct type of insertion, the tendon or ligament crosses the mineralization front and progresses from fibril through fibrocartilage (usually less than 0.6 mm) to mineralized fibrocartilage (less than 0.4 mm) and finally to bone. In the second, less common type, the tendon or ligament inserts into bone through the periosteum, with short fibres that are obliquely anchored to the bone [630].

Tendons and ligaments consist of interdependent aggregations of collagen, elastin, proteoglycans (PGs), glycolipids, water and cells. Roughly 70% to 80% of the dry weight of normal tendon or ligament is composed of type I collagen, also found in the skin and bone, cf. Section 3 of this paper, where collagen types are presented. This collagen is thought to remain relatively inert metabolically, with a half-life of 300 to 500 days. Certain components of the collagen molecule may turn over faster than others and may thus be of greater functional importance in adaptations to environmental, traumatic

or pathologic processes. Collagen also has the ability to form covalent intramolecular (aldol) and intermolecular (Schiff base) cross-links, which are the keys to its tensile strength characteristics and resistance to chemical or enzymatic breakdown.

The role of PGs in tendon development is discussed by Silver et al. [522]. Probably less known is the issue of *tendon mineralization*. More precisely, the major leg tendons of the domestic turkey, *Meleagris gallopavo*, including the Achilles or gastrocnemius tendon, begin to naturally calcify when the birds reach about 12 weeks, cf the relevant references in Silver et al. [522]. This appears to be an adaptation in response to external forces, but the relationship between skeletal changes and such forces is not understood. The gastrocnemius is relatively thick tendon at the rear of the turkey leg which passes through a cartilaginous sheath at the tarsometarsal joint and inserts into the muscle at the hip of the bird, cf. Silver et al. [522]. After passing through the sheath, the tendon divides into two portions with a decrease in total cross sectional area occurring relative to the original cross section. Mechanically this division results in increased loads borne by the sections after the bifurcation. Initiation of calcification occurs at or near the point of bifurcation and then calcification proceeds along the bifurcated sections.

Morphological observations indicate that initiation of calcification occurs on the surface of collagen fibrils close to or at the centre of the tendon in 15 week old animal. This is associated with changes in the collagen fibril structure. Studies on calcification of turkey tendons suggest that during the early stages, the hydroxyapatite crystals are about 35.0 nm in length (parallel to the collagen molecule) and 4.0–5.0 nm in width, cf. the relevant reference in Silver et al. [522]. In the calcifying turkey tendon the mineral in the hole region is crystalline, but between molecules is amorphous. Electron micrography of the mineral shows that the crystals are plate-shaped and are arranged in parallel arrays across the collagen fibrils and that the collagen fibrils are elongated in cross section.

In areas of the tendon away from the site of mineralization, tendon cells are spindle-shaped and have cellular processes that extend into the extracellular matrix and eventually connect with processes of neighbouring cells. Collagen fibrils range in these areas from 75 to 500 nm in diameter.

2.2.6. Articular cartilage and meniscus. Three broad classes of cartilaginous tissues are present in the body: hyaline cartilage, elastic cartilage and fibrocartilage, cf. Mow and Ratcliffe [410]. These are distinguished by their biochemical composition, molecular microstructure and biomechanical properties and function. Hyaline cartilage is glassy smooth, glistening and

bluish-white in appearance (although older tissues tend to loose this appearance). The most common hyaline cartilage, and consequently the most studied is articular cartilage. This tissue covers the articulating surfaces of long bones and sesamoid bones within synovial joints. Another example of hyaline cartilage is the growth plate, which controls, for example, the growth of bones during skeletal maturation. Other tissues include the larynx, the support structures of the tracheal tube, rib and costal cartilage, and the nasal septum. Examples of elastic cartilage are the epiglottis, the external auditory canal, and the eustachian tube. These tissues are generally yellowish and opaque in appearance and are more flexible than hyaline cartilage. Two fibrocartilages are the anulus fibrosus of the intervertebral disk, which provides flexible junctions between the vertebral body in the spine and the meniscus of the knee.

Hyaline cartilages contain mainly Type II collagen and therefore are distinguishable from fibrocartilages, such as meniscal cartilage. The latter contains mainly Type I collagen and a relatively low content of the proteoglycan aggrecan, cf. Mow and Ratcliffe [410], Poole et al. [454].

Articular cartilage in adults is a comparatively acellular tissue, with cell volume averaging only approximately 2% of total cartilage volume in human adults, [454]. The remainder is occupied by an extensive extracellular matrix that is synthesized by these cells that are chondrocytes. With increasing age, there is a progressive decrease in cell content and in matrix synthesis, the latter reaching its lowest point when the individual is 20 to 30 years. Cell density is at its lowest in the deep zone, cf. the relevant references in Mow and Ratcliffe [410], Poole et al. [454].

The organization of articular cartilage reflects its functional role. At its free surface, which is bathed by synovial fluid the cells and extracellular matrix are arranged differently to the rest of the tissue. More precisely, the chondrocytes are here flattened and aligned parallel to the surface. Only at the articular surface do these specialized chondrocytes synthesize a molecule called superficial zone protein. This now is known to be the same molecule as that called megakaryocyte stimulating factor or lubricin. It also is syntesized by synovial cells. It is thought that lubricin plays an important role in providing almost frictionless articulation provided by the articular cartilage (obviously in healthy joints).

The superficial chondrocytes are surrounded by a very polarized close knit organization of thin collagen fibrils, that generally run parallel to each other and to the articular surface, cf. Fig. 12

The matrix organization is dominated by the fibrillar network. The content of aggrecan is at its lowest here. The superficial zone provides the highest tensile properties found in articular cartilage, endowing it with the ability
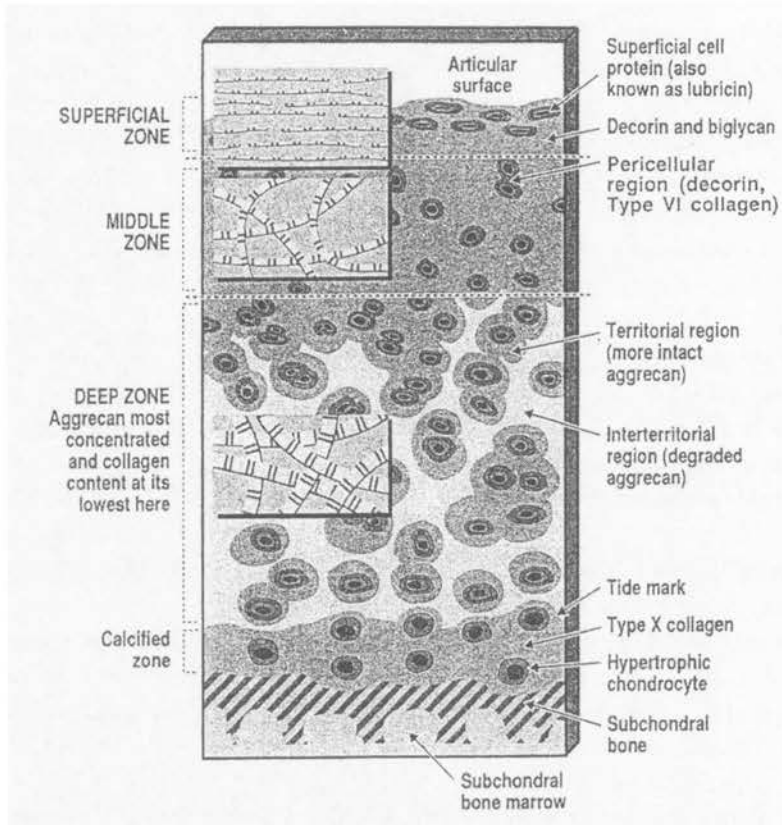
FIGURE 12. Diagrammatic representation of the general structure of human articular cartilage from an adult to show zones, regions and relationships with subchondral bone. The insets show the relative diameters and organizations of collagen microfibril in different zones. Some special features of molecular content or properties are also indicated, after Poole et. al. [454].

to accommodate shear, tensile, and compressive forces encountered during articulation. The fibril-associated small lecine rich decorin and proteoglycans biglycan are most concentrated in the superficial zone, cf. the relevant references in [454].

Below the superficial zone is the midzone where the cell density is lower, cf. Fig. 12. Here the cells are more rounded and extracellular matrix is rich in the proteoglycan aggrecan. The collagen fibrils are of larger diameter and arranged more randomly. Situated between this zone and a layer of calcified cartilage is the deep zone (Fig. 12). Cell density is at its lowest, but aggrecan content and fibril diameter are maximal. The partly calcified layer (Fig. 12) provides a buffer between those of uncalcified cartilage and the subchondral bone. The chondrocytes in this calcified zone usually express the hypertrophic

phenotype. They reach a stage of differentiation that is also achieved in the physis and in fracture repair in endochondral bone formation. These hypertrophic cells are unique in that they synthesize Type X collagen and can calcify the extracellular matrix. This interface provides excellent structural integration with the subchondral bone.

In addition to the described zonation, the matrix surrounding the chondrocytes varies in its organization. All chondrocytes are surrounded by a narrow (approximatelly $2\,\mu$m wide) pericellular region in which few collagen fibrils are detected, cf. Fig. 12. A territorial region surrounds this pericellular region which is present throughout the cartilage. In the deep zone, there is a clearly identifiable third region of structure, distinguishable by the ultrastructure of aggregates of the proteoglycan. This region is called the interterritorial region. It is the part of the matrix most remote from the chondrocytes.

Similarly to other connective tissues with extracellular matrices, the endoskeleton of hyaline cartilages is composed of collagen fibrils that form an extensive network the territorial and interterritorial matrix. This fibrils vary in diameter, from approximately 20 nm in the superficial zone to $70-120$ nm in the deep zone. Type II collagen forms the bulk (approximately 90%) of the fibrils cf. Fig. 13. For more details on collagen network and proteoglycan aggrecan in the articular cartilage the reader is referred to Mow and Ratcliffe
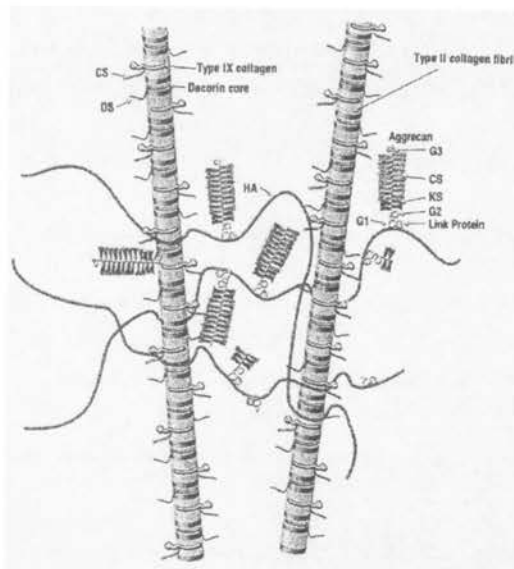

FIGURE 13. Diagrammatic representation of the macrofibrillar collagen network and aggrecan superaggregate with hyaluronic acid; after Poole et al. [454].

[410], Poole et al. [454] and relevant references therein. From the biomechanical point of view it is noteworthy that aggrecan provides the compressive stiffness of cartilage. This is achieved by hydration of the large number of chondroitin sulfate and keratan sulfate chains that occupy the core protein in the keratan sulfate and chondroitin sulfate rich regions between G2 and G3 domains, cf. Poole et al. [454].

Let us pass to the *meniscus*. Its fibrous structure also has a layered appearance, but it differs from that of articular cartilage. The menisci are semilunar in shape and are situated between the femoral condyles and tibial plateau of the knee, cf. Mow and Ratcliffe [410]. The articulating surface of the meniscus is composed of fine fibrils in a random mesh-like woven matrix, though split lines are also present.

Approximately $100 \, \mu m$ from the surface layers are large rope-like collagen fibre bundles that are principally arranged circumferentially around the semilunar meniscus. Smaller radial fibres appear to reinforce the structure of the meniscus by tying the large circumferential fibre bundles together. Such a fibrillar organization predominates throughout the peripheral two-thirds of the tissue, while the inner region appears to contain more randomly arranged smaller collagen fibres and proteoglycans, resembling hyaline cartilage, cf. the relevant references cited in [410].

2.2.7. Intervertebral discs.

The intervertebral discs are designed to separate consecutive vertebrae, thereby producing a potential space between them into which the vertebral bodies can dip and execute bending movements, cf. Adams et al. [4]. Each lumbar intervertebral disc is about 10 mm in height. The essential component of the intervertebral disc is anulus fibrosus. This consists of some 10–20 sheets of collagen, called lamellae, tightly packed together in a circumferential fashion around the periphery disc, cf. Fig. 14.

While packed tightly together, these lamellae are stiff and can sustain considerable compression loads. Being collagenous, the anulus fibrosus is sufficiently pliable that it can deform and thereby enable bending movements between vertebral bodies. However, herein lies the liability of the anulus fibrosus. If it buckles it loses its stiffness, and is less able to sustain compression loads. To prevent this, the anulus fibrosus requires the second component — the *nucleus pulposus*.

The nucleus pulposus is a hydrated gel located in the centre of each disc (Fig. 14). Cooperatively, the NP and AF maintain the stiffness of the disc against compression loading, but both tissues are sufficiently compliant that they allow some degree of movement between vertebral bodies.

VEP

Posterior

AF   AF   AF

NP   NP

VEP   Anterior

coronal section   transverse section
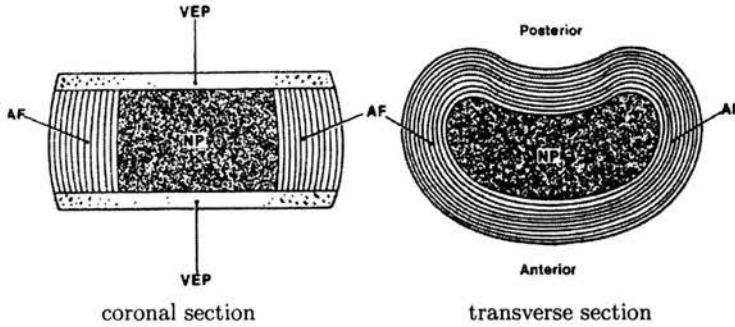
FIGURE 14. The basic structure of a lumbar intervertebral disc. The disc consists of a nucleus pulposus (NP) surrounded by an anulus fibrosus (AF), both sandwiched between two cartilaginous vertebral endplates (VEP), after Adams et al. [4].

The third component of the intervertebral disc are the superior and the inferior endplates, cf. Fig. 14. These are plates of cartilage that cover the superior and inferior aspects of the disc, and bind the disc to their respective vertebral bodies.

The anulus fibrosus consists of Type I and Type II collagen. The concentration of Type I collagen is greater towards the periphery of anulus, while that of Type II collagen is reciprocally greater towards the centre of the disc. This distribution of Type I collagen matches the greater tensile role of the outer anulus fibrosus. Within each lamella of the AF, the collagen fibres are arranged in parallel. They pass obliquely from one vertebral body to the next, at an angle of about $65°$ to the sagittal plane. However, as a rule, the fibres in each successive lamellae are oriented in an opposite sense, with one layer inclined to the right, and so on, cf. Fig. 15.
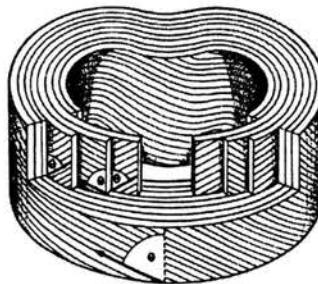

FIGURE 15. The architecture of the anulus fibrosus. Collagen fibres are arranged in 10–20 concentric, circumferential lamellae, but their orientation with respect the vertical (θ) is approximately the same, and measures about $65°$, after Adams et al. [4].

The nucleus pulposus consists largely of proteoglycans. They have the valuable property of being able to imbibe and retain large amounts of water. If the nucleus pulposus loses its proteoglycans, it can no longer hold its water, and the nucleus can no longer brace the anulus fibrosus.

2.2.8. Eye. Figure 16 presents a diagram of the anatomy of the eye whilst Fig. 17—idealized structure of the human cornea, cf. Bryant and McDonnell [61], and Downs et al. [142] and the relevant references therein.
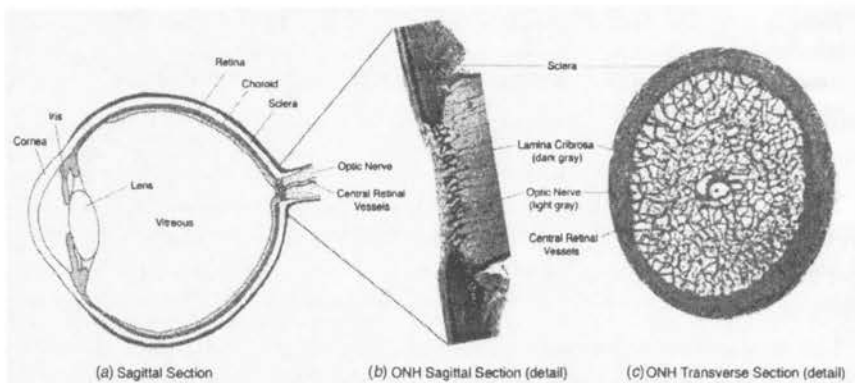

FIGURE 16. (a) Diagram of the anatomy of the eye, showing the location of the scleral canal and the optic nerve head (ONH); (b) histologic sagittal section through the scleral canal and ONH showing the peripapillary sclera, lamina cribrosa and retinal ganglion cell axons, and (c) histologic transverse section through the scleral canal and ONH showing the connective tissue structure of the scleral canal, lamina cribrosa and central retinal vessels, after Downs et al. [142].
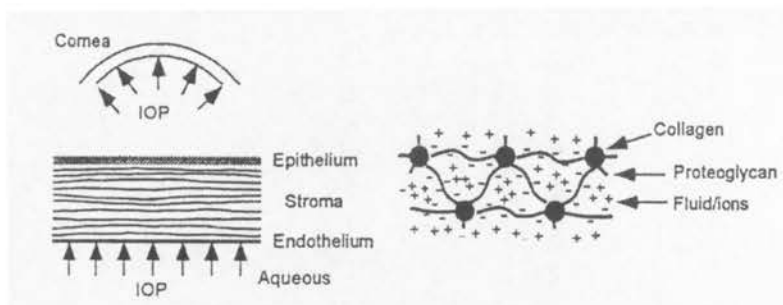
FIGURE 17. Idealized structure of the human cornea. The cornea is a semispherical shell loaded by the intraocular pressure (IOP; top left). The corneal stroma consists of parallel layers (lamellae) of collagen fibres (bottom left). The epithelium and endothelium are cellular layers bounding the stroma. Each lamella (right) consists of parallel collagen fibres embedded in a matrix of polyanionic proteoglycans and surrounded by water and ions, after Bryant and McDonnell [61].

The *sclera* is the principal load-bearing tissue of the eye and consists primarily of collagen. The primary function of the sclera is to resist intraocular pressure (IOP), provide attachment sites for the ocular musculature and support the *retina* in the spheroid shape for focused vision. The thickness and predominant collagen fibril orientation of this tissue are dependent on location in globe. However, whether the fibril orientation has a large effect on scleral material properties remains controversial, cf. the relevant references in Downs et al. [142].

The scleral shell is pierced by the *scleral canal*, an elliptical hole (1–2.5 mm in diameter) in the posterior portion of the globe, through which the *retinal ganglion cell axons* pass on their path to form *orbital optic nerve* (Fig. 16). The scleral canal is spanned by a series of thin, fenestrated connective tissue sheets known as *lamina cribosa* (Fig. 16 b, c). The latter provides structural and nutritional support to the retinal ganglion cell axons as they pass through the scleral canal. The tissue within the scleral canal are collectively known as *papilla* or *optic nerve head* (ONH).

IOP-related stress in the tissues of the ONH and sclera is considerable even at normal levels of intraocular pressure (10–20 mm Hg), and the deformation resulting from those stresses may be affected by factors such as scleral canal geometry, lamina cribrosa tissue density and geometry, extracellular matrix composition, and other factors that vary significantly among individuals, cf. the relevant references in [142].

The corneal stroma in its normal state has a strong tendency to imbibe fluid. The stroma is composed of lamellae of parallel fibres embedded in a matrix of polyanionic proteoglycans (cf. Fig. 17), which give rise to the fixed charge density of the tissue, like in the articular cartilage, cf. the relevant references in Bryant and McDonnell [61].

2.2.9. Skin. One of the major functions of the skin is to prevent the excessive loss of water from the body. Other functions are to protect the body by preventing the penetration of undesirable substances or radiation, and cushioning it against mechanical shocks. Skin is also of importance in maintaining the heat balance of the body and in the immunologic response to foreign materials. Other functions are the synthesis of vitamin D, interconversion of steroids and the excretion of ingested toxins.

Water loss through the skin consists of two processes: sweating and insensible perspiration. Water loss due to sweating is an active process aimed at loosing excessive heat. At rest it occurs only at relatively high ambient temperature (28–30°C, cf. Elsner et al. [158]). Insensible perspiration is a passive process caused by the difference in water content between the body and the

environment. Skin forms a very effective barrier against perspirational water loss, which is often called transepidermal water loss (TEWL). The effectiveness of the barrier is indicated by the fact that the ratio of water loss from the body with skin and the water loss from the body without skin, which can be equalled to a free water surface is less than 0.04.

The skin has a stratified structure consisting of two main layers: an exterior epithelial covering called the *epidermis* (ca. 75–150 μm), and beneath this, a connective tissue layer, the *dermis* (ca. 1–4 mm). These thicknesses may vary considerably over the surface of the body. Dermis and epidermis are separated by the basement membrane. A schematic cross-section of the skin is given in Fig. 18.
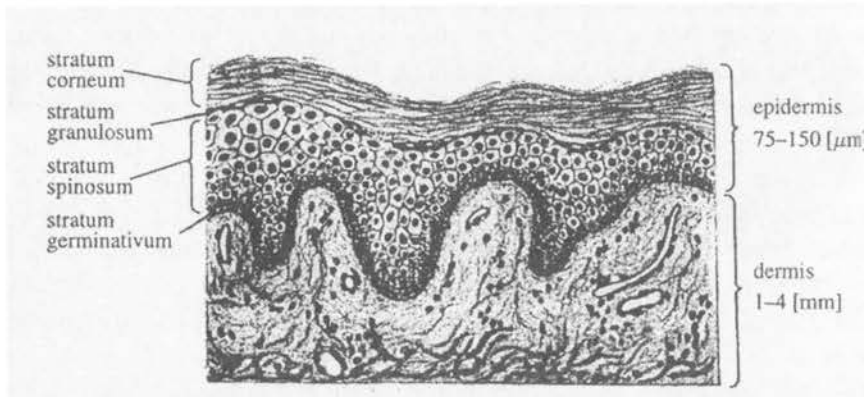

FIGURE 18. A schematic cross-section of the skin, after Guyton [212].

The epidermis is a differentiated, stratified, keratinising epithelium largely composed of keratinocytes which move progressively from attachment to the basement membrane towards the skin surface (turn-over time ca. 50 days, cf. Elsner et al. [158] and the relevant references cited in van Kemenade [593]) forming several well-defined layers: *stratum germinativum, stratum spinosum, stratum granulosum* and *stratum corneum*. The deepest layer of the epidermis is the *stratum germinativum* in which cell division occurs. The cells are cuboidal in shape. Nuclei, cytoplasm and cytoskeletal tonofilament bundles are present in the cells. The stratum spinosum lies immediately above the stratum germinativum. The keratinocytes become cuboidal and there are numerous desmosomal connections between adjacent keratinocytes. Desmosomes are laminated structures with intercellular and intracellular components. Cytoskeletal tonofilaments attach close to the desmosomes, providing stability across cells and cell layers. In the upper layers of the stratum spinosum, so-called lamellar bodies arise. These lamellar bodies are lipid syn-

thesizing organelles in the keratinocyte. The stratum spinosum is succeeded by the stratum granulosum. In this layer the lamellar bodies migrate towards the periphery of the cell and eventually discharge their lipid components into the intercellular space. The outermost layer is stratum corneum. The cells (now called corneocytes) are flattened and have lost their nuclei. The thickness of the stratum corneum varies regionally, becoming maximal on the palm and sole. Over most of the body surface the thickness of the stratum corneum varies between 8–15 μm. There are 15 to 20 layers of corneocytes. Between the flat corneocytes there are lipid bilayers originating from the lamellar bodies. This means that the stratum corneum consists of (protein rich) corneocytes embedded in a lipid rich matrix. This structural organization is often called the brick and mortar model. Dry stratum corneum (without any water) consists of approximately 75–85% proteins (mostly keratins), 5–15% lipids and 5–10% substances of low molecular weight, cf. Elsner et al. [158] and the relevant references cited in van Kemenade [593].

The stratum corneum has the ability to swell to several times its normal thickness. Generally, increasing environmental relative humidity causes an increase in stratum corneum hydration. The water content of the stratum corneum (mass of water per total mass) is important for the properties and external appearance, such as pliability and smoothness. Normally it is about 10–15% in the outer layers increasing to 65% at the bottom of the stratum corneum. The nature of water in the stratum corneum is different at different water contents. At a water content below 10% the water present is tightly bound, presumably to the polar sites of the proteins. At water contents between 10 and 40% there is also less tightly bound water present (hydrogen bonded). Above 50%, the water is present as bulk (free) water.

The dermis is a layer of connective tissue lying underneath the epidermis. It contains blood vessels, lymph vessels nerves and the skin appendages such as hairs, sebacous glands, and sweat glands. The thickness of the dermis varies between 1 mm (scalp) and 4 mm (back). The dermis consists of two regions, above a loose superficial layer, called a *papilary dermis* (10% of the total dermis), and beneath a dense layer, called the *reticular dermis* (90% of the total dermis). At the junction between the papillary and reticular dermis, there exists a *subpapillary* (also called *superficial*) *plexus* of blood vessels. The deep plexus of blood vessels lies at the bottom of the reticular dermis. The dermis is composed of connective tissue which contains a supporting matrix or ground substance. This ground substance is also bound to water. Two kinds of protein are also found: collagen with great tensile strength (ca. 75% dry weight), and elastin which has considerable elasticity (ca. 4% dry weight). Below this dermis is a layer containing predominantly fat cells, called the *subcutaneous tissue* or *hypodermis*.

2.2.10. Lungs. The main function of the lungs is (rapid) gas exchange. This is accomplished by a well-coordinated interaction of the lungs with the central nervous system, the diaphragm and chest wall musculature and the circulatory system, see Fung [176] and Godwin [193]. Total lung mass is about 300–400 g. Upper and lower lobes are anterior, while the lower lobes are posterior, cf. Fig. 19. Development of each lobe results in division into 19 bronchopulmonary segments which are relatively constant and often have pathophysiologic correlates, i.e. secondary tuberculosis is seen in the apical segments.
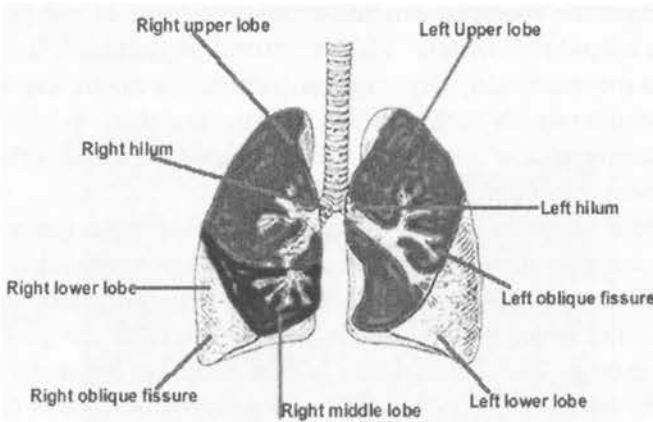

FIGURE 19. Gross structure of the lungs, after http://hsc.uwe.ac.uk/radiography/RAnatomy/resp/gross_structure.htm

To oxygenate the blood and to remove CO_2 nature chooses to do this by diffusion and chemical reaction, and for this purpose blood is spread out into very thin layers or sheets so that the blood-gas interfacial area becomes very large. In an adult human lung with a pulmonary capillary blood volume on the order of 150 ml, the pulmonary capillary blood-gas exchange area is of the order of $70\,m^2$, so that the average computed thickness of the sheets of blood in the pulmonary capillaries is only about $4\,\mu m$. The thin membrane that separates the blood from the air is less than $1\,\mu$ thick; it consists of a layer of endothelial cells, an interstitium, and a layer of epithelial cells. Each sheet of blood, bounded by two membranes, forms an *interalveoral septum*. Several billion septa form a space structure, which may be compared with a honeycomb or a bowl of soap bubbles, cf. Fung [176]. The smallest unit of space bounded by *interalveolar septa* is called the *alveolus*. In an adult human there are about 300 million alveoli. Each alveolus is polyhedral. It is bounded by interalveolar walls, with one or more sides missing in order to ventilate to the atmosphere.

Only about 10% of the lung is occupied by solid tissue, whereas the remainder is filled with air and blood. Supporting structures of the lung must be delicate to allow gas exchange, yet strong enough to maintain structural integrity, that is sustain alveolar structure.

From the trachea distally, the respiratory tree divides into paired branches of unequal length and diameter and is, therefore, described as having an arborizing branching pattern of irregular dichotomy, cf. Figs. 20, 21.
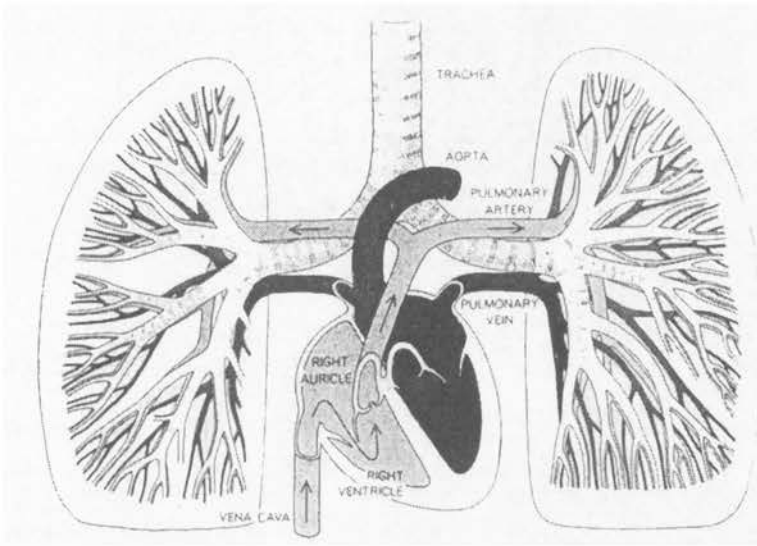

FIGURE 20. Relationship between the heart and lung in humans. Note that the pulmonary arteries lie close to the bronchi, whereas the pulmonary veins stand alone. Only the first few generations of the large pulmonary blood vessels and bronchi are shown in the figure, after Fung [176].

There are approximately 23 airway divisions to the level of the alveoli. The division include main bronchi, lobar bronchi, segmental bronchi (to designated bronchopulmonary segments), and so on to the smallest bronchioles which do not have alveoli and are lined completely by bronchial epithelium, the terminale bronchioles.

Respiratory bronchiole is the first bronchiole along which alveoli appear. There are 2–5 'generations' of respiratory bronchioles. Since these bronchioles are lined by cuboidal epithelium and have no muscular walls, they function primarily as conducting tubes, and probably account for minimal gas exchange.

Alveolar ducts are completely lined by alveoli, have no muscle in their walls and are covered by attenuated squamous epithelium.
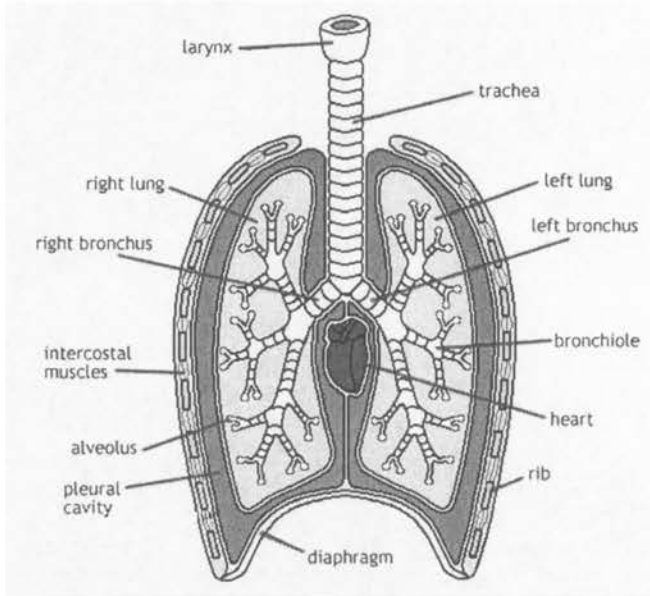
- **Larynx** – the voice box. Flaps of tissue vibrate to create sounds.
- **Trachea** – a tube made rigid by rings of cartilage. This makes the trachea keep its shape to allow free movement of air into and out of the lungs.
- **Bronchus** – there are two bronchi, branching from the trachea. One bronchus enters the left lung while the other enters the right lung.
- **Bronchioles** – smaller branches of the bronchi.
- **Alveolus** – there are around 70 million alveoli in each lung. These are tiny air sacs. It is here that oxygen enters the blood and carbon dioxide leaves it.
- **Pleural cavity** – the space in the chest where the lungs fit. It is lubricated to prevent the lungs from sticking to the rib cage.
- **Intercostal muscles** – muscle in-between each rib. When they contract they pull the rib cage upwards and outwards. This increases the volume of the chest.
- **Diaphragm** – a dome shaped sheet of muscle under the lungs. When it contracts it pulls down. This increases the volume of the chest.

FIGURE 21. Schematic lung structure, after www.longleypublications.co.uk /biology/KS3Biology/lungs.htm.

Alveolar sacs represent the termini of alveolar ducts and are completely lined by alveoli. The alveolar sacs and alveoli are lined by attenuated squamous epithelium. The normal alveolus is angular.

The *acinus* is the functional or terminal respiratory unit of the lung and includes all structures from the respiratory bronchiole to the alveolus (alveolar ducts, alveolar sacs, and alveoli). An acinus averages 0,75 mm in diameter. Each person has about 20 000 accini (and about 300 million alveoli).

The *lobule* is a less well-defined anatomic unit which includes 3-5 terminal bronchioles and their distal structures.

The conducting airways are compliant tubes lined by respiratory mucosa and containing variable amounts of *muscle* and/or *cartilage* in their wall. Airways are for conducting air and for clearance and filtering of foreign particles that are in the approximately 10 000 litres of inspired air per day. Bronchi are distinguished from bronchioles primarily by the presence of cartilage in their walls. Bronchioles also lack submucosal glands.

Pseudostratified ciliated columnar cells mucuous (goblet) cells are the two major components of the epithelium. The ciliated cells predominate in number. Both derive from basel cells. Circumferential layer of smooth muscles constitute the layer being deep to the mucosa (except in the trachea, where it is only the posterior, membranous wall), and becomes increasingly prominent as airway diameter and cartilage decrease. Circular smooth muscle is most prominent in the terminal bronchioles.

Cartilage lies outside the submucosa and decreases in amount as the caliber of the airway decreases. It is present distally in the bronchi, and is not in the bronchioles. The trachea has a C-shaped ring of cartilage in the wall, anteriorly. The lobar and segmental bronchi have haphazard and discontinuous plates of cartilage, circumferentially. Cartilage can be compressed by external pressure (e.g. a cough)

Anatomically most of the alveolar wall is comprised of the capillary. At any given time the total lung capillary volume is about 75 ml, spread over an area of 80 m^2 which result in a very thin layer of blood. Gases are exchanged between this channel of blood and the alveolar space. The entire surface of the alveolus is normally covered by epithelial cells. The alveolar wall has 2 basement membranes (BM), one associated with endothelial cells and one with epithelial cells. Where the wall becomes very thin these two (endothelial and epithelial) BM's fuse into a single BM.

The alveolar interstitium contains other cells (fibroblasts and lymphoid cells).

As we already know, Fig. 20 shows the relationship between the heart and lung. Blood flows from the right ventricle to the pulmonary artery, then to capillary blood vessels, the veins, and finally to the left atrium (LA). Figure 22 shows an enlarged view of capillary blood vessels in the interalveolar septa.

For a schematic diagram of a lobule the reader is referred to Fig. 6.2:3 in the book by Fung [176]. This author claims that the topology of the network of the pulmonary capillary blood vessels is definitely not treelike; it is sheetlike. The dense network of the capillary blood vessels in an alveolar wall of the frog is shown in Fig. 23.
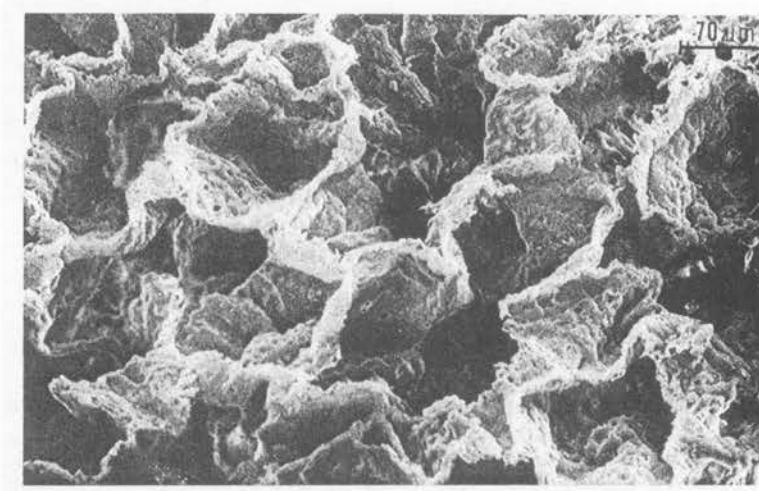
FIGURE 22. Scanning electron micrograph of cat lung illustrating how each interalveolar septum is shared by two alveoli. These septa are sheets of pulmonary capillary blood vessels. The wrinkly appearance of the septa is an artefact due to the cutting of the specimen and relieving of the stresses, thereby causing the contraction of elastin fibres, which cannot be fixed by commonly known fixing agents; after Fung [176].
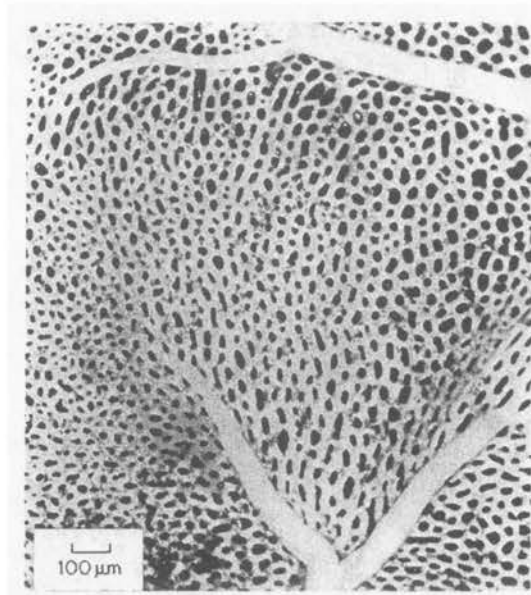
FIGURE 23. Photograph of a network of capillary blood vessels in the frog, after Maloney and Castle [370].

A similar picture of the cat lung is represented as Fig. 6.3:2 in the book by Fung [176].

Figure 24 visualizes the vascular space in the pulmonary alveolar sheet. The epithelium is lifted from the interstitium and pulled back. The elastin and collagen fibres in the interstitium are indicated, but not drawn in detail. The cross section of an individual capillary blood vessel may appear like a tube in certain directions, but overall the vascular space is represented as a sheet. From the point of view of fluid mechanics, the sheet representation is advantageous, since the streamlines will occupy the vascular space of a tube model, cf. Fig. 6.3:6 in the book by Fung [176].
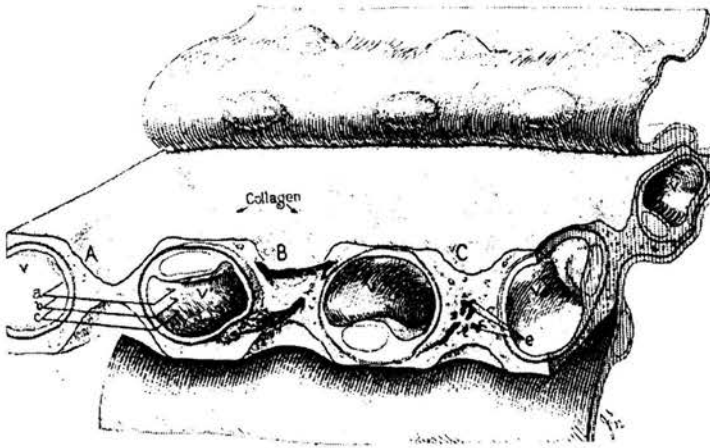

FIGURE 24. Composite drawing of the pulmonary interalveolar wall of the dog showing the interalveolar microvascular sheet, composed of a vascular compartment (V) (the capillary bed) and the avascular (intercapillary) posts (A, B, C). The alveolar epithelium has been pulled back to show the connective tissue matrix of the wall. Collagen converges on the post from the surrounding capillary wall. In post B collagen fibre bundles pass around within the post in a curving arrangement, after Rosenquist et al. [490].

2.2.11. Kidney. According to Jamison [270], Jacob Henle's crowning achievement was the three-volume Handbook of Systematic Anantomy, published in 1866 [225]. Figure 25 from the Handbook (see also Fig. 1 in the paper by Jamison [270]) is the cross section of the human kidney hand-drawn by Henle. The kidney is divided into lobules. Each consists of a cortex and medulla. Kidneys of all mammals and birds contain one or more such lobules. The rat kidney has one lobule, the human kidney—fourteen and the whale more than a thousand, but the basic structure is the same.
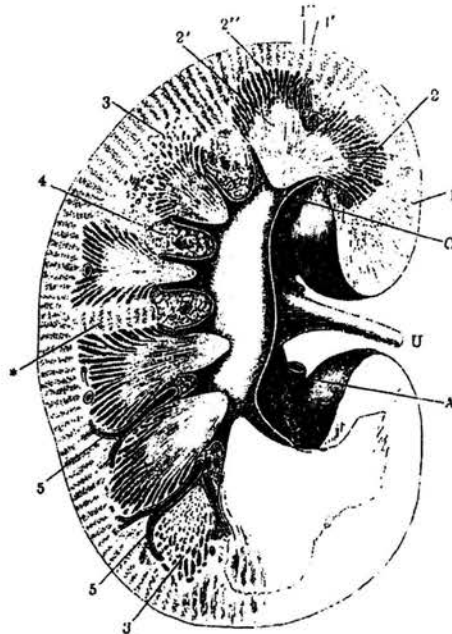
Figure 25. Saggittal section of a human kidney drawn by hand by Jacob Henle (1866). The legend beneath the figure is translated as follows: frontal section through the kidney, the renal pelvis and a number of renal calyces. A Branch of the renal artery. U ureter. C Renal calyx. 1 substance of the cortex. 1' Extension of the renal pyramid. 1" Actual substance of the cortex. 2 substance of the medulla. 2' Actual substance of the medulla. 2" Boundary layer of the same. 3 Section of the boundary layer perpendicular to the axis of the tubules. 4 renal sinus fat. 5 Branches of renal arteries. * Extension of pyramid running cross-wise, after Jamison [270].

Figure 26 depicts the two fundamental functional units of the kidney — nephron and blood vessel. There are two types of nephrons, those with short loops of Henle and those with long loops. The long loop nephron differs from the short loop nephron in three ways.

1. The glomerulus of the long loop nephron is confined to the region in the cortex next to the medulla.

2. Its tubule folds into a hairpin turn, the loop of Henle, that penetrates into the inner medulla. The Henle's loop of the short loop nephron turns in the outer medulla.

3. Its loop of Henle contains a thin ascending as well as thin descending segment. The short loop lacks a thin ascending segment.

All nephrons empty into collecting ducts, that fuse two ducts into one
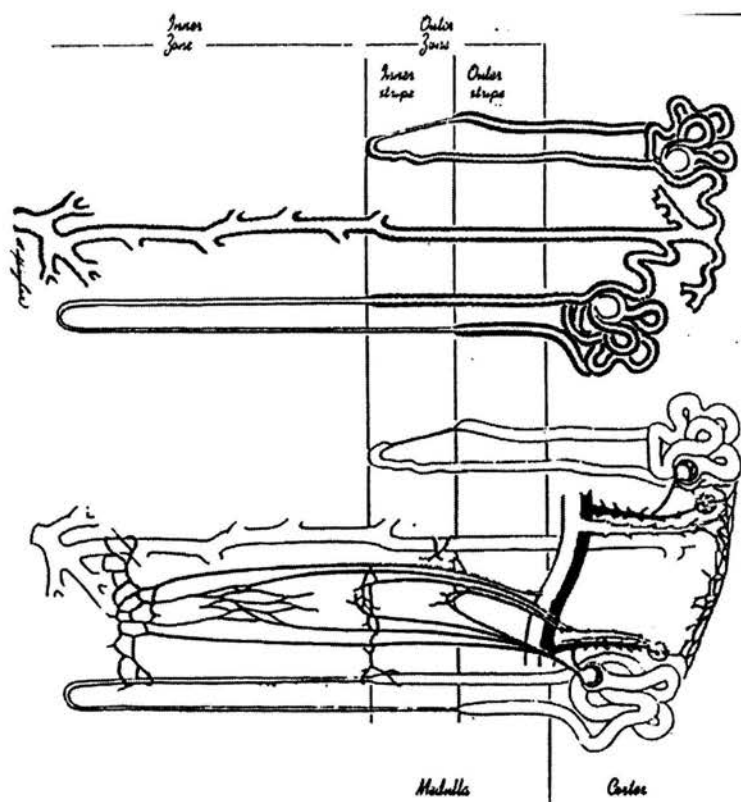
FIGURE 26. The two major units of the kidney. On the left, the two principal types of nephron are shown relative to their location in the renal cortex, outer medulla (Outer Zone) (subdivided into an Outer Stripe and an Inner Stripe) and inner medulla (Inner Zone). The short loop nephron (extreme left) whose loop of Henle turns at the junction of the outer medulla and inner medulla, has a descending thin segment but no ascending thin segment. The glomerulus of the long loop nephron is located in the region adjacent to medulla, and has a much longer loop of Henle, with both a thin descending and thin ascending segment. The thick ascending segment returns to a region adjacent to its own glomerulus to become the distal tubule. The distal tubules of both nephrons join the collecting duct system in the cortex, which is characterized by a series of fusions of two ducts into one, primarily in the inner medulla. On the right, the microcirculation of the kidney is superimposed on the nephrons and collecting duct. The arterial system is solid black, the venous system is open. The microcirculation consists of two capillary networks in series. The first capillary network, the glomerular capillaries, reunite in the efferent arteriole, which breaks up into the second capillary network, the peritubular capillaries, to supply blood to the cortex. The glomerular capillaries of the long loop nephrons reunite in the efferent arteriole, which breaks up into descending vasa recta to supply blood to the renal medulla. Ascending vasa recta return the blood to veins in the cortex, after Gottschalk [195].

7 or 8 times. The collecting ducts provide the final conduit for the remaining glomerular filtrate (or urine) to empty into the renal pelvis.

The book edited by Layton and Weinstein [335] presents current views on complex transport phenomena in the kidney. Surprisingly, nothing is said about kidney deformability as of a soft tissue. For the latter problem we refer the reader to a paper by Wachenbruch and Diller (1992) where a network thermodynamic model has been devised to describe the *coupled* movement of water and permeable additive within a kidney during perfusion under the *combined* action of diffusive, hydrodynamic, and mechanical processes. From our point of view kidney is a complex hierarchical porous biological material. Anyway, in contrast to say arteries and myocardium, mechanical modelling of kidney (the same pertains to liver) is scarce.

2.2.12. Brain. A short survey of structure of soft tissues exhibiting non-linear behavior and mechanical loads should necessarily include brain. There are many reasons for biomechanical studies of the brain. Let us just mention head injury, a critical problem worldwide, with approximately 1.5 million cases (50 000 fatal) each year in the United States alone, see Manson et al. [402].

Figures 27–28 present the brain in a lucid manner.

The human brain is a soft tissue yielding structure that is not as stiff as a gel or as plastic as a paste, cf. Akkas [5], Ommaya [438]. The soft tissue consists of gray matter, containing neuronal cell bodies, and white matter, containing interconnecting fibres between areas of gray matter, cf. Fig. 29.

FIGURE 27.   Photograph of the underside of the brain, looking up-wards. The eye balls and start of the spinal cord are clearly seen, see http://www.brain-tumour.net/reference/thebrain/photo1.htm
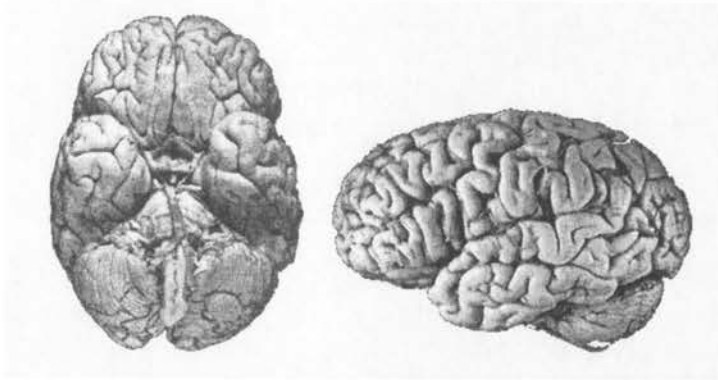
FIGURE 28. Left: simple presentation of the brain, with no spinal tissue visible. The lobes are reasonably distinguishable. Right: A 'slice' through the entire head showing clearly the location of the brain within the skull, see http://www.brain-tumour.net/reference/thebrain/photo1.htm
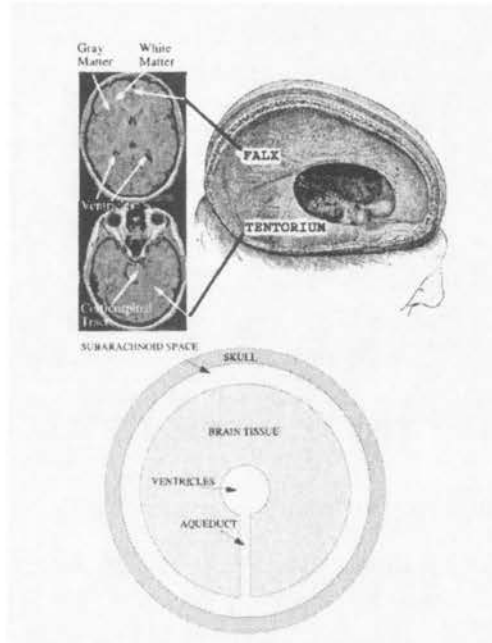
FIGURE 29. An illustration of some major features of the anatomy of the human brain. Top panel: the falx and tentorium membranes divide the brain into two cerebral hemispheres and the cerebellum; they are relatively stiff membranes, and they constrain the potential deformations of the soft tissue. The parenchyma is composed of white and gray matter; ventricles are cavities that are filled with CSF. Bottom panel: a simplified scheme of the connection between the subarachnoid space and ventricles; features have been exagerrated for illustrative purposes, after Kyriacou et al. [319].

The soft tissue is covered by the dura, arachnoid, and pia membranes with the space between the arachnoid and pia (subarachnoid space) filled with the cerebrospinal fluid (CSF), a clear, colourless fluid. The subarachnoidal space communicates with the four ventricles, which are cavities filled with CSF.

3. Basic structural elements: collagen, actin, and elastin

In a brief description of collagen types we largely follow Fung [175], Kucharz [314] and Mow and Ratcliffe [410]. Collagen is a protein present in the majority of species throughout the animal kingdom, including the vertebrates. It is the most abundant protein of human and other mammalian bodies. It is not a single protein, as thought until 1970s, and the family of collagen proteins has increased rapidly in recent two decades due to discoveries of new, genetically distinct types. The biological role of collagens is not limited to supporting the scaffold, rather the function of nearly all systems and organs of the body is related to collageneous structures. On the other hand, the biological functions of collagens should not be considered in isolation since they are constituents of the connective tissue and remain in close mutual relationships with other components of the extracellular matrix.

The term 'collagen' was introduced into histological works in the nineteens century and was derived from the break works 'kolla' and 'genos', which mean 'glue' and 'formation'. The earliest observations were related to the ability of collagen to produce glue (gelatin) when tissues, usually hide, were extracted with boiling water. This first property of collagen known in antiquity (Bogue, 1922). In modern times, the first studies on collagen were carried out by chemists involved in leather tanning and gelatin production. The book by Kucharz [314] provides a historical outline of collagen research.

3.1. Structure and types of collagens

Collagens represent a number of closely related but chemically distinct macromolecules. All forms are made up of three left-handed polypeptide chains. These chains are coiled in a right-handed direction about a common axis to form the rope-like molecule. The major part of collagen molecule has triple-helical structure. The nonhelical domains are present at both ends of the chains, and in some types of collagen the helical part is interrupted by nonhelical domains. The presence of a sizeable part of the molecule with the triple-helical conformation is a basic feature for classification of the proteins as collagens. Those containing only a small portion of the molecule in the form of the triple–helical conformation are termed proteins containing a collagen sequence.

The polypeptide chains are termed α-chains. The chains with different primary structure are numbered with arabic numerals, e.g., $\alpha 1, \alpha 2$. They may be identical or different within the same molecule. The distinct collagens are called 'types' and are numbered with roman numerals. The same numerals are added to the chains in brackets, following the arabic number of the chain. For example, the composition of the most common type 1 collagen is $[\alpha 1(I)]_2 [\alpha 2(I)]$, i.e., its molecule consists of two identical $\alpha 1(I)$ chains and one chain $\alpha 2(I)$. It is important to remember that chains with the same arabic number of different types of collagen are not identical, i.e., the chain $\alpha 1(I)$ has different primary structure than the chain $\alpha 1(II)$, etc. The term 'collagen types' is sometimes substituted with the term 'collagen systems', cf. Kucharz [314] p.5.

Collagen, as seen in the extracellular space, is synthesized from a precursor protein form. The polypeptide chains in nascend form are termed preprocollagen chains and are abbreviated as prepro α with appropriate numerals. After cleavage of the signal peptide, the preprocollagen chains form procollagen chains. They are subject to a number of posttranslational modifications, and three procollagen chains assemble into the procollagen molecule. Conversion of procollagen to collagen is associated with removing the propeptide from all three chains on both ends. The final molecule, which is the basic unit for fibril and other collageneous structures, is called collagen. This is synonymous with the old term tropocollagen.

The structure of the collagen molecule was discovered on the basis of X-ray diffraction studies followed by examination of synthetic polypeptides. The principal feature, which effects in the helix formation, is a high content of glycine and imino acid residues and the sequence of repeating residues Gly-X-Y, where X and Y can be any amino acid, often proline and hydroxyproline. We recall that glycine is the most simple amino acid, not containing any side chains, see Turner et al. [586]. For more details on amino and imino acids the reader is refered to Hames et al. [217]. An individual chain has a left-handed helical structure which is not stable when the chains are separated. The presence of glycine at every third residue is an absolute requirement for the triple-helix formation because glycine is the only amino acid without a side chain. Three glycine residues alternately from three chains form a shallow helix up the centre of the superhelical structure. The side chains of residues of amino acids other than glycine are directed outwards. Three left-handed helical chains form a 'supercoil' with a pitch of approximately 8.6 nm. The distance between amino acids within each chain is 0.291 nm, and the relative twist is $10°$. Thus the distance between each third glycine residue is 0.87 nm, see Fig. 30.
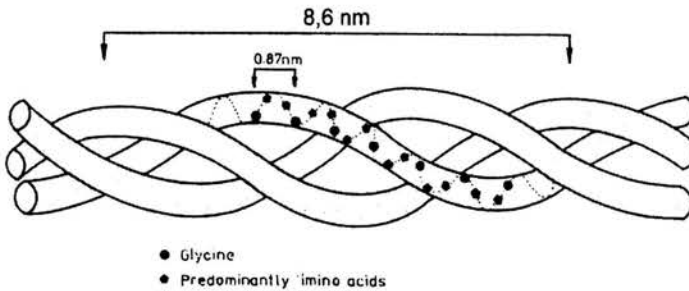
FIGURE 30. The collagen triple helix, after Kucharz [314].

The total amount of collagen is estimated at 25%–30% of the total body proteins; thus collagen is most abundant protein in the mammalian body. In adult mice collagen was found to make up 28.8% of the body weight at death. Measurements carried out in mice showed that about 40% of the total body collagen is in the skin, which forms only 17.6% of the body weight. In human skin, collagen constitutes about 75% of total nitrogen content. The musculoskeletal system of mice was found to contain 52%, and viscera accounted for only 3% of the total body collagen. The highest relative content of collagen (85%) has been found in tendons. The collagen content in various tissues is shown in Table 3.

TABLE 3. Collagen content in tissues of rat and mouse, after Kucharz [314].

Tissue	Collagen (mg/g dry weight)
Liver	8–10
Lungs	90–110
Kidney	20–30
Spleen	25–30
Aorta	200–260
Skin	600–720
Bone	150–250
Cartilage	310
Tendon	810–850

The distribution of collagens of various types has only partially been explored. Details are given in the book by [314], whilst an overview is summarized in Table 4.

We observe that Mow and Ratcliffe [410], mention that there exist still more collagen types, namely 18.

TABLE 4. Chain composition and distribution of collagens, after Kucharz [314].

Coll. type	Chain composition	Distribution
I	$[\alpha 1(I)]_2 \alpha 2(I)$	Skin, tendon, bone, cornea, dentin, fibrocartilage, large vessels, intestine, uterus
I-trimer	$[\alpha 1(I)]_3$	dentin, dermis, tendon
II	$[\alpha 1(II)]_3$	Hyaline, cartilage, vitreous, nucleus pulposus, notochord
III	$[\alpha 1(III)]_3$	Large vesels, uterine wall, dermis, intestine, heart valve, gingiva
IV	$[\alpha 1(IV)]_2 \alpha 2(IV)$	Basement membranes
V	$[\alpha 1(V)]_2 \alpha 2(V)$, $[\alpha 1(V)]_3$, $[\alpha 3(V)]_3$, $\alpha 1(V)\alpha 2(V)\alpha 3(V)$	Cornea, placental membranes, bone, large vessels, hyaline, cartilage, gingiva
VI	$\alpha 1(VI)\alpha 2(VI)\alpha 3(VI)$, $[\alpha 1(VI)]_3$	Descemet's membrane, skin, nucleus pulposus, heart muscle
VII	$[\alpha 1(VII)]_3$	Skin, placenta, lung, cartilage, cornea
VIII	Unknown	Produced by endothelial cells, Descemet's membrane
IX	$\alpha 1(IX)\alpha 2(IX)\alpha 3(IX)$	Cartilage
X	$[\alpha 1(X)]_3$	Produced by hypertrophied chondrocytes during the process of endochondral osscification
XI	$\alpha 1(XI)\alpha 2(XI)\alpha 3(XI)$	Hyaline cartilage, intervertebral disc, vitreous humor
XII	$[\alpha 1(XII)]_3$	Chick embryo tendon, bovine periodontal ligament
XIII	Unknown	Fetal skin, bone, intestinal mucosa

3.2. Tendon and related structures

The structure of tendon (and ligament) has already been presented in Section 2. Let us supplement this by addition of a brief description seen from a specific point of view.

As we already know a tendon is an elongated, cylindrical structure that attaches striated muscle to bone and through which the tension of a muscle is transmitted to the skeleton. Tendons are the most common example of dense, regular connective tissue and consist almost entirely of parallel, closely packed bundles of fibres. The fibres are separated by a small amount of amorphous matrix. Externally, the tendon is surrounded by a sheath of dense connective tissue, the paratenon. Under this layer another sheath is present, the epitenon, which continues the endotenon, separating the fascicles as well as carrying the blood hierarchical structure, cf. Figs. 8 and 9.

The tendon consists of fascicles separated by endotenon. Each fascicle is build up of many fibrils, among them fibroblasts are located. Fibroblasts are collageneous structures with a subordinate hierarchy including subfibrils and microfibrils. The most elementary component of all is the molecule of collagen (tropocollagen). The structural hierarchies in collagen from the molecule through the fibril level are shown in Fig. 31

Hulmes and Miller [249] performed reinterpretation of the X-ray data which leads to a model for a crystalline regions of the fibril, based on quasi-hexagonal molecular packing without microfibrillar substructure, and hence having the character of a molecular crystal, cf. Fig. 32.
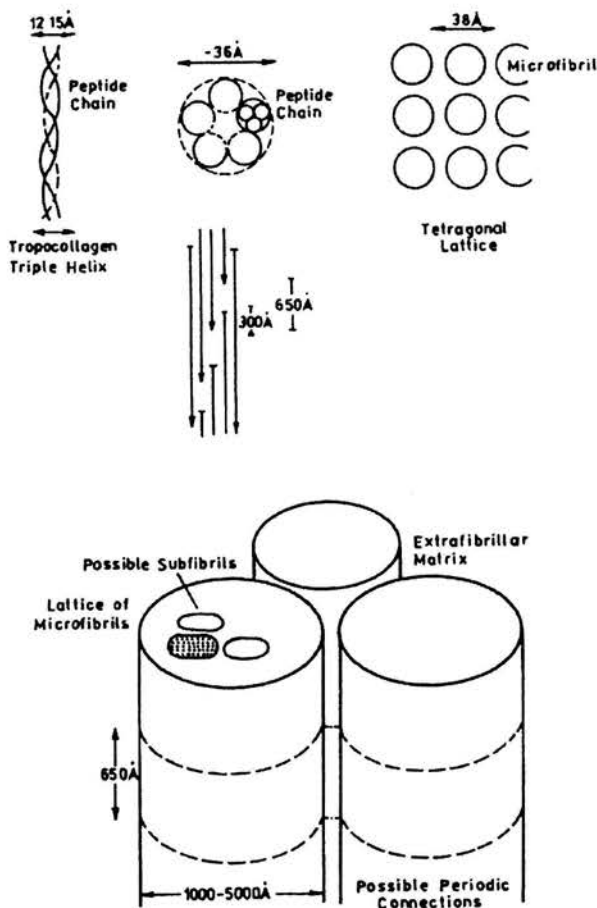
FIGURE 31. Structural hierarchies in collagen from the molecule through the fibril level: tropocollagen (collagen), microfibril, lattice formed by microfibrils, and collagen fibril, after Kucharz [314].
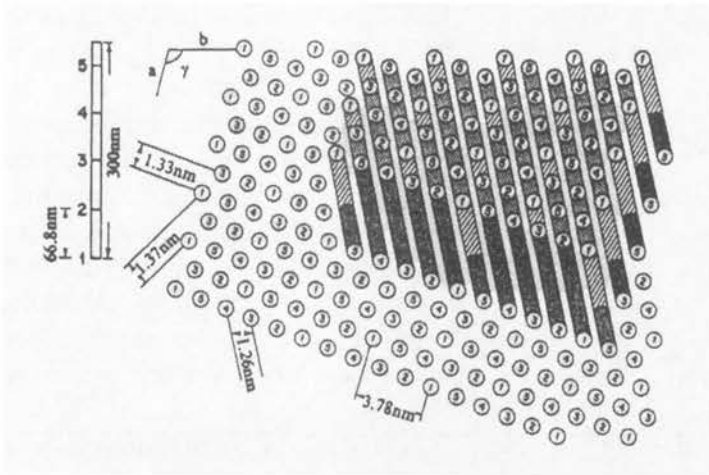
Figure 32. Possible structure in one region of a collagen fibril, shown in projection down the fibril axis. Numbers refer to molecular segments (see upper left) in one 66.8 nm (D) thick transverse section. Thick shaded lines show molecular tilt and connectivity between upper (bold type) and lower (regular type) surfaces of the section. The molecular polarity and sign of the tilt ($\sim 5°$) are arbitrary. In this example the lateral shift of the unit cell origin in height D is $\Delta a = a/10, \Delta b = -3b/10$. The same unit cell dimensions could also arise by regular combinations of two 1D (and 4D) staggers and one 2D (and 3D) stagger in the three principal directions, as well as by more irregular patterns of intermolecular $n \times D$ staggers, after Hulmes and Miller [249].

3.3. Mechanical properties of collagen

Of earlier results on mechanical properties of tendon fibres the paper by Yannas and Huang (1972) is worth of being mentioned.

Tendon fibres, about $200\,\mu$ diameter, were teased out of tails of 3-month old Sprague-Dawley rats [150]. These fibers are covered with a noncollagenous reticular membrane which was removed by immersion in 0.5 M NaH_2PO_4 at 23°C over a 2-hr period. Fibres which had been treated over a fraction of this period with NaH_2PO_4 were examined with the scanning microscope in order to note various characteristics of membrane as well as confirm its removal. Several membrane-free fibres were subsequently treated at room temperature over varying period of time with 0.05 M acetic acid and were also examined with the microscope in order to discern intermediate steps in the dissolution process.

Freshly teased fibres contain about 65% water by weight, but attain a water content of ca. 15 % when exposed to the laboratory atmosphere for about 1/2 hr. Depending on factors such as the age of the animal, the solubility

of these fibres often exceeds 90% of speciment weight as long as the water content does not fall below about 1%. Highly dehydrated specimens were prepared by heating at 105°C at a pressure of 10^{-3} mm Hg for 48 hr; at the end of such a treatment, the water content drops below 1%, whilst the solubility of both gelatin and collagen specimens drops to zero, indicating that these specimens have been transformed into covalently linked three-dimensional networks. Nevertheless, the characteristic of the collagen triple helix remains unchanged after such a severe treatment, as shown by the wide-angle X-ray pattern of the fibres and by optical rotatory dispersion of nonbirefringent collagen films. Moreover, determination of amino acid composition before and after dehydration, under the conditions described above, shows no change in the levels of all amino acids. These observations led to the conclusion that the sharp improvement in resolution obtained by dehydration was apparently gained only at the expense of increasing the density of crosslinks in the specimens.

Following adjustment of their water content to the desired value, tendon fibres were fractured in an Instron Tester, in which the stress-strain curves at constant extension rate were also obtained for several representative specimens. Fracture specimens were coated with an approximately 150 Å thick layer of gold and examined with a Cambridge Stereoscan Electron Microscope, operating at accelerating voltage of 200 kV. The moisture content of dehydrated specimens was determined by titration with Fischer reagents.

The stress-strain curves of wet and dehydrated tendon fibres are shown in Fig. 33.
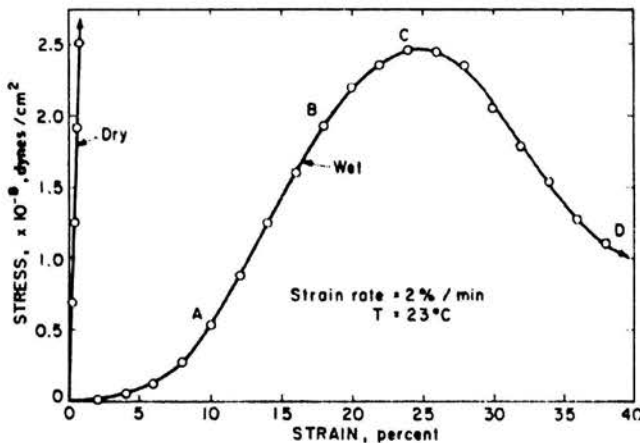

FIGURE 33. Stress-strain curve of wet and dehydrated rat tail tendon fibres. Strain rate, 2% /min, temperature, 23°C. Fracture occurs beyond point D, after Yannas and Huang (1972).

The stress-strain curve of the wet fibre is made up of three regions. In the region up to the point A the stress rises very slowly with extension and the deformation is immediately and completely recoverable. It corresponds to the uncrimping or straightening out of the waviness of the fibres. In the region A through B, the stress rises approximately linearly with strain and deformation incurred is partially recoverable, the amount of irrecoverable deformation increases with strain. This region probably corresponds to a combination of slippage and extension of the straightened fibres. The occurrence of slippage in wet fibres is directly confirmed in the scanning electron photomicrographs. Specimen failure occurs progressively beyond point C of the stress-strain curve.

Mechanical behaviour of collagenous tissues subject to compressive loads is important for tissues like cartilage and skin. The lectures by Huyghe contained in this volume deal with various aspects of soft tissues behaviour, when treated as porous materials. For instance, Khoska and Pinder (1984) performed compression tests on specially prepared collagen discs prepared from bovine Achilles tendon. This earlier study involves linear Darcy's law. Unfortunately, such a filtration law does not take into account the dependence of filtration on deformation of collagenous matrix.

Comminou and Yannas (1976) adopted the sine waveform to model the collagen fibres. The collagen fibre was regarded as a long sinusoidal beam (Reissner beam). The derived theoretical model was exploited by Manschot and Brakkee (1986) to obtain the relation between the collagen stiffness of the fibril E_f and the stiffness of the collagen of the skin E_c:

$$E_c = E_f \frac{NA_f}{A}.$$

Here N represents the total number of fibrils, A_f denotes cross-section of the whole skin (stress $\sigma = F/A$.)

The experimental measurements performed by Manschot and Brakkee (1986) exhibited anisotropy in two directions: along and across the tibial axis (these authors tested human calf skin). We recall that the diameter of the fibrils varies within a range of 20 to 40 nm, depending on the animal species and the tissue. Bundles of fibrils form fibres, which have diameters in range from 0.2 to 12 μm, cf. [175]. In a series of papers Sasaki and his coworkers studied mechanical properties of collagen from bovine Achilles tendon (BAT), cf. [502, 503, 504].

Sasaki et al. [504] investigated the relation between the structure of hydrated collagen and observed the characteristic humidity-sensitive reflection, d, as a function of water content and temperature. The intensity of SAXS

(= small angle X-ray scattering) patterns from hydrated and dried collagen was analyzed in order to estimate roughly the size of the extrafibrillar space.

Sasaki and Odajima [502, pp.655–658] estimated the Young modulus of collagen molecule, cf. Table 5.

TABLE 5. Young modulus of collagen molecule, after Sasaki and Odajima [502].

Collagen	State	Young modulus [GPa]
Bovine Achilles tendon	State solid in 0.15 M NaCl solution	2.9+0.1
Rat tail tendon[1]	Solid state in 0.15 M NaCl solution	9.0
Rat tail tendon[2]	Solid state in 0.15 M NaCl solution	5.1
Lathyritic rat skin[3]	Acetate/NaCl/glycerol solution	4.1
Dermosparic calf skin[4]	0.5 M acetic acid glycerol solution	5.1 – 3.0

[1] Harley et al. (1977), [2] Cusack and Miller (1979), [3] Nestler et al. (1983), [4] Hoffmann et al. (1984).

WAXD (=wide-angle X-ray diffraction) measurements were performed. The WAXD pattern of collagen enables one to observe a reflection corresponding to the distance between neighbouring amino acids along the helical axis. This distance, d, can be a measure of molecular deformation along the macroscopic tensile force. We define the microscopic strain about d in tendon collagen as

$$\epsilon_d = (d - d_o)/d_o, \tag{3.1}$$

where d_o is the d without a tensile force and is ~ 0.29 nm. From the obtained stress-strain curve for a collagen molecule, its Young's modulus was estimated and was compared with the modulus measured by other methods in the literature.

In the subsequent paper Sasaki and Odajima [503, pp. 1131–1136] investigated the elongation mechanism of tendon collagen on the basis of the hierarchical structure of the tissue (about 20 months old bovine Achilles tendon). Figure 34 depicts the force-strain curves for collagen molecule, a fibril structure, and a macroscopic tendon.

Sasaki et al. (1999) continued the previous research on tendon collagen. Particularly, these authors investigated molecular rearrangement and its relation to viscoelestic properties. Earlier, Sasaki et al. (1993) found that the relaxation modulus of bone and collagen was found to be well described by a linear combination of Kohlrausch-Williams-Watts (KWW) function and a simple exponential decay (Debye) function:

$$E(t) = E_0\{A_1 \exp[-(t/\tau_1)^\beta] + A_2 \exp(-t/\tau_2)\}, \tag{3.2}$$

where $A_1 + A_2 = 1, 0 < \beta \leq 1$.. E_0 is an initial value of the relaxation modulus
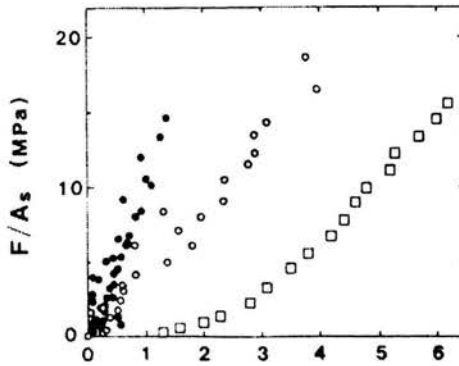
FIGURE 34. Comparison of applied force-strain curves of a collagen molecule (•), a collagen fibril (○) and a tendon (□). The vertical axis is the force per unit cross-sectional area of the specimen, after Sasaki and Odajima [503, pp. 1131-1136].

$E(0)$; A_1 and A_2 are fractions of the KWW and the Debye-type relaxations, respectively; τ_1 and τ_2 are relaxation times of respective relaxations. β is a parameter describing the shape of the relaxation modulus at the immediate decay part. For a dry collagen, τ_1 is determined to about 1000 s (Sasaki et al., 1993). Figure 35 shows the relaxation modulus for tendon collagen in saline solution measured by Azuma and Hasegawa (1971). The solid line represents Eq. (3.2) with $\beta = 0.6$, $\tau_1 = 11$ s, $\tau_2 = 10^4$ s, and $A_1 = 0.23$.
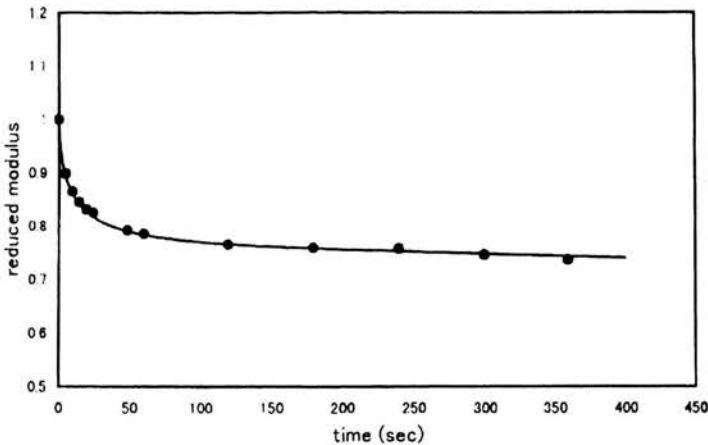
FIGURE 35. Normalized relaxation modulus, $E_r = E(t)/E(0)$, for tendon collagen in saline solution. Data points were reproduced after Azuma and Hasegawa (1971). Solid line represents Eq. (3.2) where $\beta = 0.6$, $\tau_1 = 11s$, $\tau_2 = 10^4s$, and $A_1 = 0.23$.

Roeder et al. (2002) reported polymerisation of purified type I collagen of different collagen concentrations and pH values to form 3-D matrices differing both structurally and mechanically. Confocal reflection microscopy was used to establish and compare 3-D microstructural differences between the matrices in their native, hydrated state. This information was then correlated with features of the stress-strain relationship, including linear modulus, failure stress and failure strain derived from tensile mechanical tests.

The book edited by Elsner et al. [158] offers a lot of information on skin collagen properties, including pathological cases.

3.4. Actin

Actin molecules are present in all muscles, leukocytes, red blood cells, endothelial cells, and many other cells. The measurement of the strength of a single actin filament is based on the fact that a single actin filament ($\sim$ 7 nm in diameter) can be clearly seen by video-fluorescence microscopy (Fung [175, p. 243]). Actin monomers are globular. They polymerise into filaments. Both ends of a single actin filament are caught using two kinds of microneedles connected to micromanipulators under a fluoerescence microscope. In the experiment performed by Kishino and Yanagida (1988) one of the needles, used for measuring was very flexible, and the other, used for pulling acting filaments, was stiff. Before the experiments, the needles were coated with monomeric myosin to increase their affinity with actin. The stiff needle was pulled until the filament broke. Force was calculated from the bending of the flexible needle. For filaments of length 4 to 32 μm, the tensile force of the actin filament was found to be 108±5 (s.d., n=61) pN without breaking and almost independent of the filament length. This force is comparable with the force exerted on a single thin element in muscle cells during isometric contraction. The tensile strength of the actin filament is at least $2.2 \times 10^6 \, \text{N/m}^2$, or 2.2 MPa.

3.5. Elastin

Elastin is the most "linearly" elastic biosolid material known. If a cylindrical specimen of elastin is prepared and subjected to uniaxial load in a tensile testing machine, a tension-elongation curve as shown in Fig. 36, is obtained, cf. Fung [175, p. 244]

The abscissa is the tensile strain defined as the change of length divided by the initial (unloaded) length of the specimen. The ordinate is the stress defined as the load divided by the initial cross-sectional area of the specimen at zero stress. We observe that the loading curve is almost a straight line.
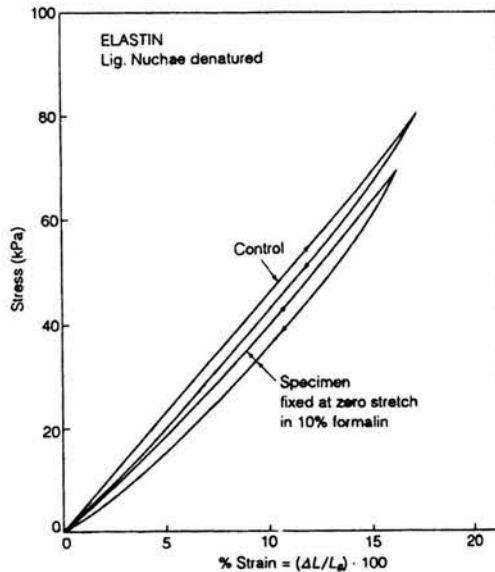
FIGURE 36. The stress-strain curve of elastin. The material is ligamentum nuchae of cattle, which contains a small amount of collagen that was denaturated by heating a 100°C for an hour. Such heating does not change the mechanical properties of elastin. The specimen is cylindrical with rectangular cross section. Loading is uniaxial. The curve labelled "control" refers to native elastin. The curve labelled "10% formalin" refers to a specimen fixed in formalin solution for a week without initial strain, after Fung [175].

Loading and unloading lead to two different curves, but the difference is small. Such elastic characteristics remain valid at least up to $\lambda = 1.6$.

Elastin is a protein found in vertebrates. It is present as thin strands in the skin and in alveolar connective tissue. It forms quite a large proportion of the material in the walls of arteries and veins, particularly near the heart. It is a prominent component of the lung tissue. The ligamentum nuchae, which runs along the top of the neck of horses and cattle, is almost pure elastin. Samples for laboratory testing can be prepared from the ligamentum nuchae of ungulates (but cat, dog, and man have very small ligamentum nuchae). These ligaments also contain a small amount of collagen, which can be denaturated by heating to 66°C or above. Heating to this temperature and cooling again does not change the mechanical properties of elastin.

The function of the ligamentum nuchae in the horse is clear: it holds up the heavy head and permits it movement with little energy cost. If the horse depended entirely on muscles to hold its head up, energy for maintaining tension in the muscle would be needed.

Elastin in the arteries and lung parenchyma provides elasticity to these tissues. In skin it keeps the tissue smooth.

4. Biaxial and shear tests, selected miscellaneous recent experimental tests

In contrast to inorganic materials, biosolids are much more difficult from the experimental point of view. The aim of this section is mainly to provide some recent examples of biaxial and shear tests. Comments on other tests of various soft tissues will also be given. For earlier results on soft tissues testing the reader is referred to the books by Fung [175] and Humphrey [255]. For instance, the last author described: (i) a cyclic inflation of aorta at a fixed length, (ii) the first computer-controlled device designed specifically for testing arteries via simultaneous inflation, extension and torsion. In sections which follow we shall also discuss other experimental setups and results.

4.1. Measuring shear modulus of aorta

One of frequently studied soft tissues are arterial walls since their biomechanical properties are crucial for understanding the alterations in the cardiovascular system due to age, arteriosclerosis, hypertension and dialysis, cf. Humphrey [255], Demiray and Vito (1991), Holzapfel and Ogden (2002). As we know from the Section 2.2.2, a vascular tissue is a highly complex material containing collagen, elastin and smooth muscle. For the literature related to experimental investigations of blood vessels the reader is referred to Humphrey [255] and to the relevant references cited by Vossoughi and Tözeren [601].

Vossoughi and Tözeren showed why the study of shear deformations is important both for healthy and pathologic arteries. For instance, during bending and rotation of the head, the carotid artery experiences shear deformation. In pathologic conditions, arteries are even more sheared, if compared to healthy vessels. For example, atherosclerosis and calcification are typically, localized, therefore certain portions of the wall are hardened in contrast to the rest of the wall, which may be not atherosclerotic or have calcified lesions. Under pulsatile action, the healthy portion of the wall can naturally stretch considerably, while the diseased portions may not be able to stretch as much, and therefore shearing may occur at the boundary between the diseased and healthy portions of the wall.

In clinical interventions, such as balloon angioplasty, implantation of stents, valves and arterial grafts and patches, significant wall shearing may

take place. In vessel transplantation, shear deformation is important. For instance, in using femoral vessel for a coronary bypass, the straight vessel must be bent to match the curvature of coronary vessel in which it is subjected to shear deformations.

Vossoughi and Tözeren [601] introduced a procedure whereby rectangular aortic and rubber specimens are subjected to shear. Using photoelasticity method on polyurethane rubber specimens, it was shown that the resulting stress distribution is uniform in central region of the specimen. By using a finite element procedure and the Mooney strain energy function, cf. Ciarlet [83],

$$W = c_1(I_1 - 3) + c_2(I_2 - 3), \tag{4.1}$$

where c_1[psi] or [kPa] and c_2[psi] or [kPa] are the material constants and I_1 and I_2 are the first and second strain invariants given by:

$$\begin{aligned} I_1 &= \lambda_1^2 + \lambda_2^2 + \lambda_3^2, \\ I_2 &= \lambda_1^2\lambda_2^2 + \lambda_2^2\lambda_3^2 + \lambda_3^2\lambda_1^2, \end{aligned} \tag{4.2}$$

it is shown that the shear stress in the central region is proportional to the intensity of the applied force. Here λ_i, $i = 1, 2, 3$, are the extension ratios along the principal direction, cf. Section 5 of these Notes.

Specimens from bovine thoracic aorta were tested. Primarily, bovine thoracic aorta was cleaned off from all the loose connective tissues. Two types of specimens were prepared, cf. Fig. 37.

The animals were sacrificed for other research purposes and the aortas removed within half an hour postmortem. The tissue was immediately immersed in physiologic cold salt solution with composition (in nM) of: 116.5 NaCl, 22.5 NaHCO$_3$, 1.2 NaH$_2$PO$_4$, 2.4 Na$_2$SO$_4$, 4.5 KCl, 1.3 MgSO$_4$, 2.5 CaCl$_2$, and 5.6 dextrose. All the tests were performed at room temperature (22–24°C).

Specimens dimensions were: width 0.50–2 inches, height 1.25–2.25 inches, thickness 1.15 inches. Figure 38 schematically shows a rectangular specimen with guidelines and dots imprinted on the face of specimen.

Figures 39 and 40 show the specimen attached to the clamps before and after the test.

It was found that the relationship between shear stress and shear strain, for all the aortic specimens tested, were linear, cf. Figs. 41 and 42. An average value of shear modulus is 76 kPa.

We observe that the relationship between the normal stress and normal strain is highly nonlinear, cf. Fig. 43.

Dokos et al. [140] described a shear test device for soft biological tissue capable of applying simple shear deformation simultaneously in two orthogonal

directions, while measuring the resulting forces generated in three directions. The system was designed to apply shear in more than one principal direction so that the degree of anisotropy of the test specimen could be directly addressed.

Weiss et al. [617] characterized the material response of the MCL (medial colateral ligament) to simple shear loading. Scheme of the test device was included and experimental data were discussed. For material parameters estimation, the ligament was represented as a fibre-reinforced composite with transversely isotropic symmetry using a hyperelastic strain energy that uncoupled deviatoric behaviour, cf Weiss et al. [618].

Kirpalani et al. [302] characterized the velocity and wall shear stress patterns in a model of human right coronary artery (RCA) under steady and unsteady conditions. Such studies are important for understanding atherosclerotic lesions which mostly develop in the proximal region of RCA. The performed tests showed that in the proximal region, flow separation was not produced and the axial shear stress along the inner wall was much lower than that on the outer wall. The large difference between outer and inner wall shear stresses appeared to be unique to the proximal region.
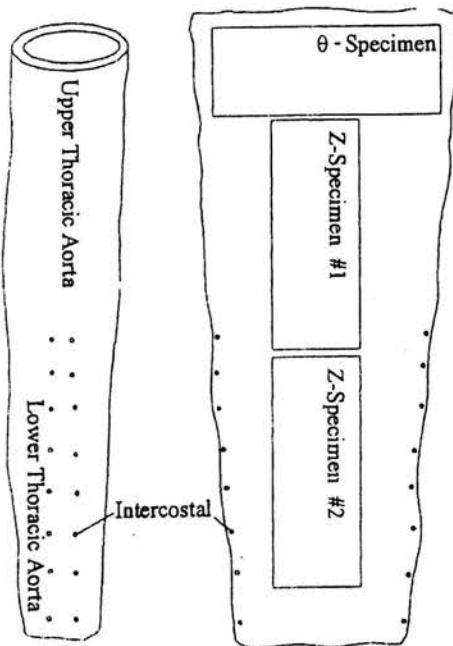
FIGURE 37. Schematic diagram showing preparation of rectangular specimens from a tubular aorta (a). The θ and Z-specimens cut from the aortic sheet are shown in (b), after Vossoughi and Tözeren [601].
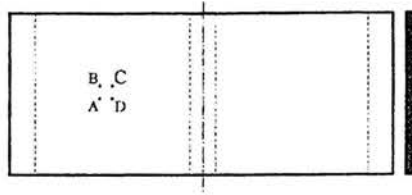
FIGURE 38. Schematic diagram showing a rectangular specimen with four guidelines and four dots imprinted on the face of the specimen, after Vossoughi and Tözeren [601].

The book edited by Elsner et al. [158] summarizes, among others, various experimental methods of testing the skin. The methods described include: hardware and basic principles of the dermal torque meter, extensometers, the cutometer (for the measurement of the viscoelastic properties of the skin *in vivo*), the gas-bearing electrodynamometer and linear skin rheometer, the Dermaflex A (to measure the stiffness of the skin in scleroderma), the DermaLab skin elasticity measurer, the Dermagraph device for measuring skin distensibility and relaxation, the IDRA (Integrated Dynamic Rebound Analyzer) ballistometer (this device employs a dynamic technique for assessing intrinsic viscoelastic properties of skin) — to mention but a few.

Skin breakdown is a significant clinical problem in rehabilitation (prosthetic use, wheelchair use). Thus it is appropriate to pursue methods for enhancement of skin large tolerance. Understanding normal skin adaptive changes at the microstructural level is an initial step in such an effort. Initial
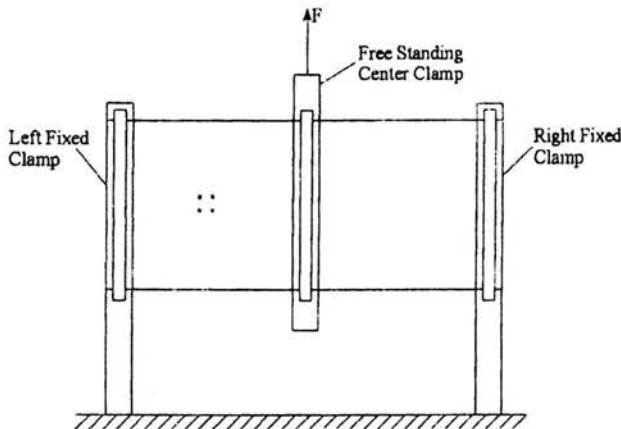
FIGURE 39. Schematic diagram showing the rectangular specimen attached to the clamps, after Vossoughi and Tözeren [601].
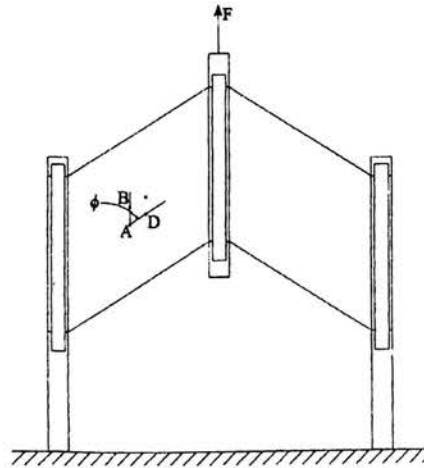
FIGURE 40. Schematic diagram showing the rectangular specimen after it is sheared, after Vossoughi and Tözeren [601].

qualitative assessment by Sanders and Goldstein [499] demonstrated larger mean fibril diameters, reduced mean fibril densities, decreased dermal and epidermal thickness, increased cell density for stressed compared with control samples. Pigs' skin was subjected to cyclic compressive and shear stresses. Pigs were selected because many characteristics of their thick, rigidly adherent and well-vascularizes skin are similar to human skin, cf. the relevant references cited in Sanders and Goldstein [499].
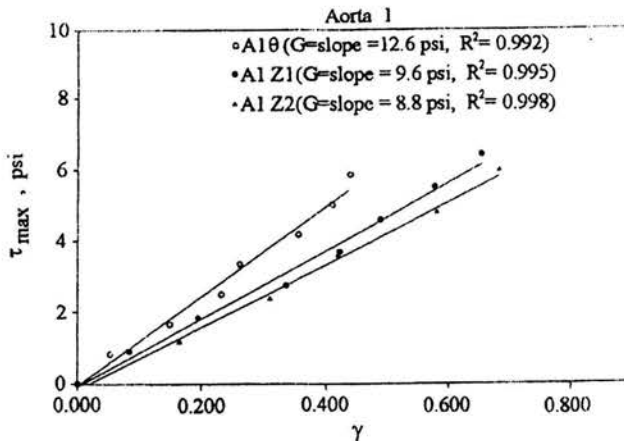
FIGURE 41. Typical shear stress versus shear strain diagrams for aorta No 1. both for θ and Z-specimens. Slopes of the least squared lines provided the effective shear modulus for the material of the aorta, after Vossoughi and Tözeren [601].
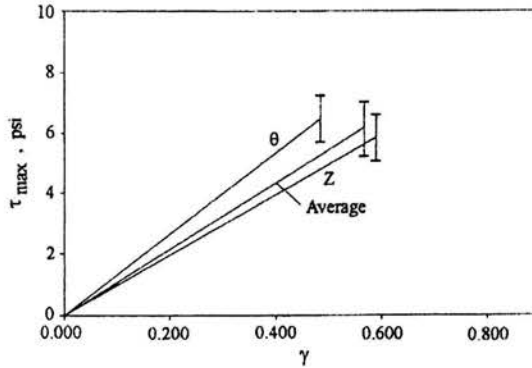
FIGURE 42. An average shear stress versus shear strain curve for bovine aorta. The average curves represent 5 specimen in θ-direction and 13 in Z-direction, after Vossoughi and Tözeren [601].
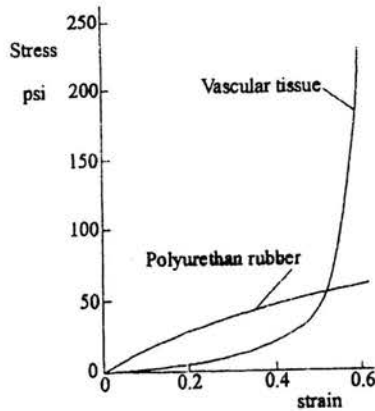
FIGURE 43. A typical normal stress versus normal strain curve for bovine aortic tissue exhibiting highly nonlinear behavior. In addition, such stress–strain curve for polyurethane rubber is also shown. Both curves are nonlinear but one concave and one convex, after Vossoughi and Tözeren [601].

The mechanics of microneedle insertion into the skin of human subjects was investigated by Davis et al. [118]. Many microneedle designs were proposed, yet not all are capable of inserting into the skin, cf. the relevant references in Davis et al. [118]. To provide quantitative predictions of microneedle insertion, these authors experimentally measured and theoretically modelled the effect of microneedle geometry on the force required to insert microneedles into the skin (0.08-3.04 N) of human subjects and the force needles can withstand before fracturing (up to about 6 N).

4.2. Example of biaxial extension device

Ortt et al. [440] describes the design and construction of a new device capable of both in-plane biaxial thermoelestic testing and measurement of the orthogonal components of the spatial thermal diffusivity tensor. Figure 44 presents this biaxial extension device.

Related to the last paper is the contribution by Jun et al. [292]. These authors reported a new optico-thermo-mechanical system for: (i) simultaneously measuring optical and mechanical properties, and (ii) examining the
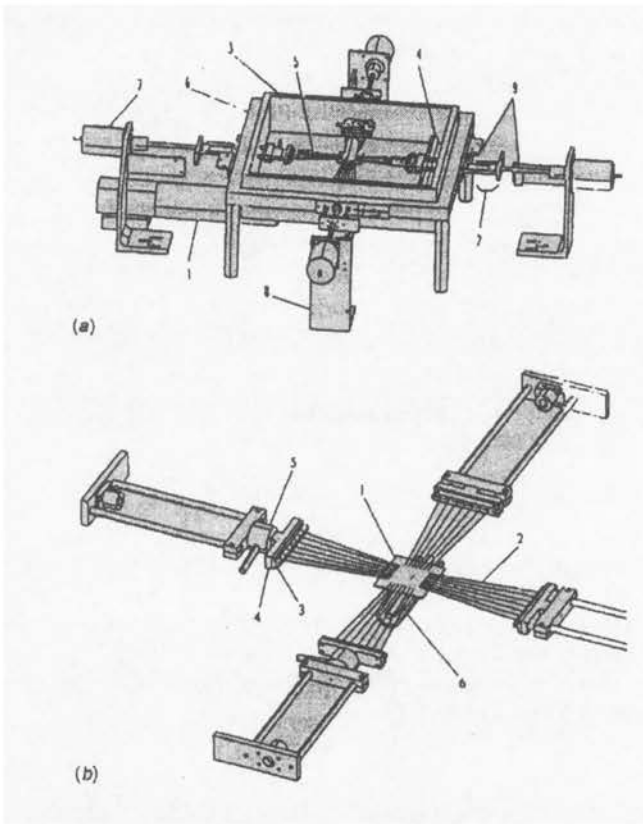
FIGURE 44. Biaxial extension device. Panel (a) is an oblique view of the device where (1) camera, (2) load carriage, (3) environmental chamber, (4) heater, (5) Kevlar threads, (6) load frame, (7) motors, (8) motor supports, and (9) limit switches; in plane directions defined as 1 and 2. Panel (b) is a schema of (1) the specimen with centrally placed tracking markers, (2) Kevlar threads, (3) T-bar, (4) coupling bar, (5) load cell and (6) flash-bulb and reflector, as seen from below, after Ortt et al. [440].

effect of thermal denaturation on changes in the optical properties of a collagen tissue under various *multiaxial* mechanical loads

The objective of the experimental study by Billiar and Sacks [41] was to specialize *biaxial testing techniques* for both the natural and glutaraldehyde-treated *porcine aortic valve* (AV), and to apply those methods to generate sufficient planar mechanical property data for constitutive modelling. Further, a technique was developed to examine the inter-relationship between the local fibre architecture and the principal strain field quantitatively. This technique allowed the authors to test the hypothesis that the highly aligned AV fibre architecture, rather than the local stress concentration induced by tethering, dominated the local strain field. Indices of extensibility and anisotropy were defined for specimen comparison, and special characteristics of the mechanical behaviour of the aortica valve cusps were discussed. A detailed description of the *biaxial testing device*, including modifications to allow the test specimen to undergo in-plane shear, has been previously presented by Sacks and Chuong [495].

4.3. Selected miscellaneous tests

Liao et al. [349] developed a *modified porous media* model with the consideration of both convection and diffusion by coupling lumen-side flow, shell-side flow, and transmembrane flow. Navier-Stokes equations were employed to simulate lumen-side flow, Darcy equations were employed to simulate shell-side flow, and Kedem-Katchalsky equations were used to compute transmembrane flow. The developed model describes the process of hemodialysis where an artificial kidney (also called hemodialyzer) is usually cylindrical in shape with about 2–5 cm in diameter and 15–30 cm in length, containing between 6000 and 12000 hollow fibres. The hollow fibres have an inner diameter of about 200 μm and a wall thickness between 15 and 50 μm. The hemodialyzer is used to remove waste product, such as excess plasma water, uremic solutes, and toxins from blood. Dialysate (fresh dialysis solution) flows outside hollow fibres (shell-side flow), while blood goes inside hollow fibres (lumen-side flow). Because the pressure and solute concentration between blood and dialysate sides are different, the waste products can be removed from blood to dialysate side through the wall of hollow fibres made of synthetic porous membrane (such as cellulose triacetate, polysulfone, polyethersulfone, and polyarylethersulfone). These hollow fibres act as semipermeable membranes (semipermeable barrier) for the mass transfer of uremic solutes and excess plasma water from blood to dialysate solution.

Experiments were performed to validate model predictions from numerical simulations. Such a study is useful for further design of optimal *artificial*

kidney. Experimental setup, schematically presented by Liao et al. [349], permits to evaluate clearance (K) as an important measure of the performance of the artificial kidney. The physical meaning of K is the equivalent volume flow rate at which the toxic solutes are cleaned completely from the blood, which can be easily used to calculate the dialysis time for patients. K is calculated from the following equation:

$$K = \frac{Q_{\text{bin}}C_{\text{bin}} - Q_{\text{bout}}C_{\text{bout}}}{C_{\text{bin}}}.$$

Here Q_{bin} and Q_{bout} are blood (lumen-side) flow rates in blood (lumen-side) inlet and outlet, respectively; C_{bin} and C_{bout} are solute concentrations in blood (lumen-side) inlet and outlet, respectively.

Poh et al. [450] presented nonintrusive MRI (magnetic resonance imaging) experimental studies on the effect of flow baffles on the dialysate-side flow distribution of hollow-fibre hemodialysers.

Rassier and Herzog [476] made an attempt to clarify the contradicting results observed in shortening-stretch tests in single *skeletal muscle fibres*. The experiments were performed with 10 single muscle fibres ($\approx 2\,\text{mm}$ length) dissected from lumbrical muscles of the *frog Rana Pipiens*. The results obtained suggest that stretch-induced force enhancement is partly caused by a passive element that is engaged at the length of initial fibre activation.

Brain tissue, composed of white and gray matter, is a complex material. Gray matter of the cerebral hemispheres consists of a mixture of neuronal cell bodies, their unmyelinated processes and neurogilia. White matter, found in subcortical regions, consists of myelinated axonal fibres surrounded by supporting cells (oligodendrocytes, astrocytes, ependyma and microglia) and blood vessels. Mechanical properties of brain tissue have been measured in vitro under compression, tension, shear, and oscillatory loading, cf. the relevant references in Gefen and Margulies [186]. Generally, brain tissue is nonlinear, viscoelastic material. Properties have been shown to vary over 10-fold depending on the different testing methods, and parameters (e.g., loading rates, strain magnitudes), location, orientation and preparation of samples, interspecies differences, developmental age, and importantly, on postmortem conditions. The aim of the study performed by Gefen and Margulies was to determine, by means of high-precision indentation testing, (1) the mechanical behaviour of an in-vivo brain (with its pressurized vasculature) and compare it to that of an in situ brain, (2) the effect of preconditioning on in vivo and in situ brain tissue, (3) the effect of the mechanical boundary conditions imposed by the skull in situ on measured mechanical properties with respect to the in vitro (excised brain) condition and (4) the sensitivity of indentation measurements to small changes in velocity of penetration. We recall that

indentation is a well-established method for mechanical characterization of many soft tissues such as brain, muscle, lung parenchyma and the plantar fat pad, cf. the relevant references in Gefen and Margulies [186]. The indentor used by the last authors is presented in Fig. 45
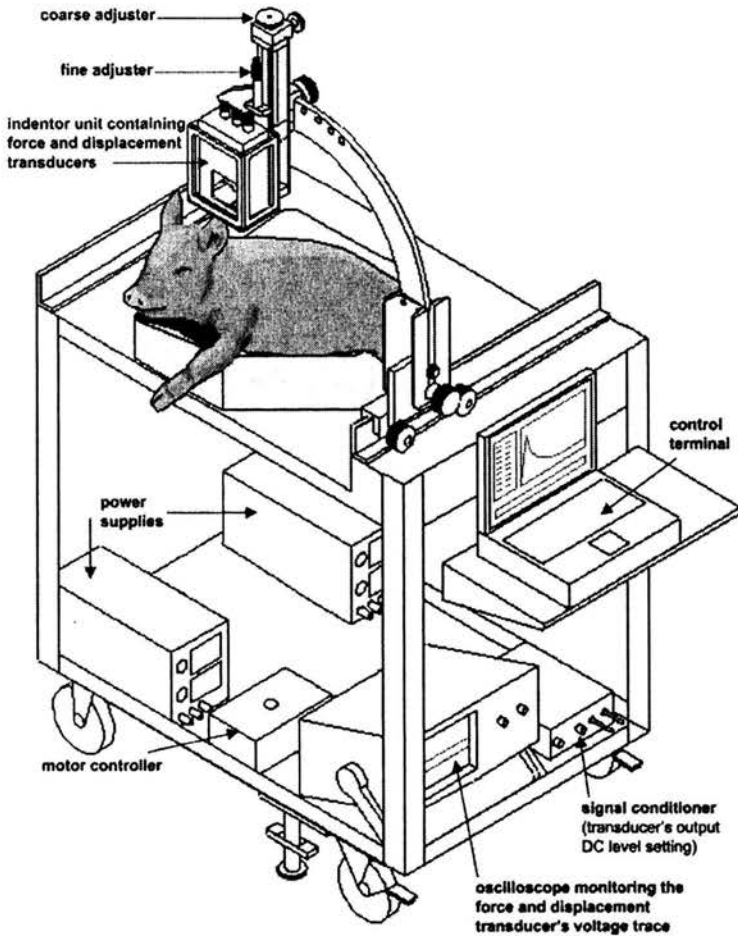
FIGURE 45. Scheme of the electromechanical indentor and linked instrumentation, after Gefen and Margulies [186].

The indentor comprised of a miniature linear stepper motor (with minimum displacement of 0.0023 mm), force transducer (with load capacity of 150 G) and a linear variable displacement transducer. It was used to repetitively indent the *exposed brain tissue*. The indentor tip was machined to a hemisphere to reduce micro-tears in the delicate brain tissue at the sites of indentation. The indenter is pressed against the tissue and shear moduli are

calculated from the applied load and extent of tissue deflection. Properties were obtained in the pig. Short- and long-term shear moduli as well as relaxation time courses $G(t)$ of brain tissue were measured in 4-week-old piglets ($N = 10$) in vivo, in situ and in vitro.

4.4. Ultrasound imaging and measurements

For vascular imaging different technical modalities have been introduced successfully to clinical practice such as conventional angiography and digital subtraction angiography (DSA), respectively, contrast-enhanced computed tomographic (CT) angiography and colour coded duplex Doppler ultrasonography (US), cf. Arlart et al. [14], Jensen [285], Nowicki and Karłowicz [423], Nowicki and Litniewski [424]. Ultrasound techniques have also been successfully used to assess bone properties and in imaging of organs like heart, kidney, liver, etc. Let us provide some examples of applications of ultrasound in the study of arteries and cartilage.

Cardiovascular disease is characterized by accumulation of lipids, collagen, muscle fibres, macrophages, calcium and necrotic tissue in the vascular wall, atherosclerosis reduces blood flow through stenosis or thrombotic occlusion. To predict the clinical outcome following intervention one needs to understand the physical properties of the vascular wall. Vascular mechanics improves our understanding of plaque development, progression and rupture, as well as optimizing the clinical assessment of vascular grafts and interventional procedures. For previous studies on basic vascular behaviour, including constitutive models the reader is referred to the relevant references cited in Humphrey [255], Holzapfel et al. [239], Tajaddini [557], Veress et al. [597] and the subsequent section of this paper. It seems that few studies have examined the validity of *in-vivo* deductions from *ex-vivo* studies, due to difficulty of testing the same tissue in both settings, cf. Tajaddini et al. [557]. Coronary arteries, the site of most acute problems, are difficult to study since they are small and relatively inaccessible, with numerous bifurcations. Their *in-vivo* study is further complicated by cardiac anatomy and motion.

Advances in the use of ultrasound have made *intravascular ultrasound* (IVUS) a reliable tool for directly visualizing vascular walls and plaques, cf. Nowicki and Litniewski [424]. IVUS provides precise *in-vivo* images of small vessels such as the coronaries, with minimal disturbance to the body. IVUS uses a catheter-mounted ultrasound transducer to acquire cross-sectional images of an artery with a spatial resolution of 80–100 μm radially and 150–200 μm circumferentially. Current IVUS catheters are as small as 0.9 mm and can interrogate most areas of the coronary tree, including coronary arteries in the range of 1.5–5 mm in diameter. IVUS provides detailed images of the

plaque and vessel wall, both *in vitro* and *in vivo*, thus providing a means to quantify lesions geometry. Tajaddini et al. [557] used IVUS in conjunction with mechanical testing to examine vascular properties of intact porcine coronary artery *ex-vivo* and *in-vivo* in non-diseased and stenotic vessels from an injury model mimicking human post-interventional restenosis. *Ex-vivo* behaviour of a human left anterior descending coronary artery (LAD) segment was also assessed for comparison.

Veress et al. [597] developed and utilized a technique referred to as 'Warping', for strain estimation from sequences of images, cf. the relevant references cited by these authors. The technique uses pointwise differences in image pixel intensities between template and target image datasets to generate a distributed body force that deforms a finite element (FE) model of the template so that it registers with the target image. The main objectives of the study performed were to test the efficacy of Warping for determination of strain distribution in plaques from IVUS images by assessing its sensitivity to errors in material model selection, material parameter estimation and simulated noise in the image data. The strain energy function emlpoyed will be discussed in Section 5.

The aim of the study due to Augst et al. [20] was to estimate the accuracy and reproducibility of CFD (computational fluid dynamics) predictions based on images acquired using 3D ultrasound. More precisely, a human carotid bifurcation phantom was scanned three times using 3D ultrasound. According to Augst et al. [20] wall shear stress delivered from CFD using this technique in a silicone phantom have acceptable reproducibility and agree reasonably well with predictions based on the true geometry.

Consider now some recent results of application of ultrasound to cartilage.

An ultrasound indentation system for the assessment of the biomechanical properties of soft tissues has been developed earlier, cf. the relevant references cited in Töyräs et al. [584]. The ultrasound indentation technique was utilized to characterize changes in the acoustic and mechanical properties of articular cartilage after enzymatic proteoglycan removal, cf. the reference by Youn et al. (1999) in Töyräs et al. [584]. Changes in the indentation stiffness as well as in ultrasound velocity wave sensitively detected after enzymatic digestions, revealing the potential of this technique. Ultrasound measurements also enable accurate determination of cartilage thickness. Cartilage thickness allows aspect-ratio (the ratio of indenter radius to cartilage thickness) correction of the indentation measurement. In the study performed by Töyräs et al. [584], both indentation and ultrasound measurements of bovine humeral articular cartilage were conducted in situ to demonstrate how the effect of variable cartilage thickness on the measured indenter forces could be minimized. Reference unconfined compression measurements were carried out with the same

tissue in vitro. By combining ultrasound and the instantaneous indentation with the hand-held arthroscopic instrument, the estimation of intrinsic tissue stiffness was improved and new diagnostically valuable information about cartilage thickness was obtained.

An alternative approach to the determination of cartilage thickness was proposed by Suh et al. [549]. These authors developed an in situ calibration method for an ultrasound transducer, which allows an accurate measurement of the true ultrasound speed in articular cartilage in situ, from which the thickness of the tissue can be readily determined. With a simultaneous implementation of indentation testing protocol using the ultrasound transducer as an indenter, this method can also provide an accurate measurement of indentation stiffness of articular cartilage. Suh et al. [549] used 40 osteochondral plugs (1 cm×1 cm×1 cm) obtained from the facets of the patellar groove and the femoral condyles of ten young fresh bovine knee joints. Twenty specimens were used to validate the accuracy of the in situ calibration method to measure the true ultrasound speed and the thickness of articular cartilage. The remaining 20 specimens were used to measure the indentation stiffness of normal and proteoglycan depleted OA-like cartilage (OA=osteoarthritis).

When investigating cartilage mechanical behaviour, and especially when comparing to predictions of theoretical models, the direct measurement of internal physical profiles such as solid deformation or fluid velocity would be of great utility. Novel instrumentation developed towards this goal could also be useful for clinical diagnosis. Fortin et al. [168] proposed a new technique and showed that it is capable of imaging solid matrix displacement internal to articular cartilage during the dynamics of loading. The method uses high frequency ultrasound (US) techniques and is inspired by recent work in elastography. In this technique an ultrasound transducer is pulsed during tissue deformation and a series of echoes, named A-scans, is acquired. A-scans are signals representing the pressure applied on the face of the transducer by the reflected echoes as a function of time and are related to the position of acoustic inhomogeneities, which in cartilage are at least partly related to collagen fibrils, cf. the relevant references cited in Fortin et al. [168]. Thus, by cross-correlating consecutive A-scans, one can follow the displacement of the solid matrix of the tissue to obtain time evolving solid displacement profiles. Fortin et al. [168] described the application of elastography to articular cartilage attached to bone and showed the time-dependence and depth-dependent heterogeneity of the internal solid radial displacement profiles in cartilage/bone disk subjected to unconfined compression. Cartilage disks (n=3) were isolated from the humeral head of 1–2 years-old steers in a manner that retained a thin layer of subchondral bone.

4.5. Magnetic resonance imaging (MRI)

As a noninvasive alternative to colour coded duplex Doppler US (ultra-sonography) magnetic resonance imaging (MRI) has been introduced into clinical routine more than ten years ago revealing continuous improvements up to now. By using suitable examination sequences both angiomorphologic and perivascular informations (having in mind angiography) can be obtained successfully with the MR technique promising a variety of advantages over US. Moreover, acquired functional quantitative MR based informations of blood flow allow a reliable evaluation of vascular pathologies.

An impressive volume edited by Arlart et al. [14] provides a comprehensive overview of the current state of the development in *vascular* MR imaging and MR angiography in order to demonstrate the clinical usefulness of this technique, of interest also in biomechanical modelling. In different chapters anatomic and physiologic informations of the normal arterial and venous system are presented. A general description of different vascular diseases and pathophysiology, the basic principles of physics in MR, flow-related and contrast-enhanced imaging techniques are reviewed. Information on different MR contrast materials, display and postprocessing techniques, hardware conceptions and its recent developments, quantification of blood flow, and potential artifacts and limitations in MR angiography are given. A well established concept of providing the clinical overview of MR angiography in different vascular areas includes chapters about the intra and extracranial cerebral vasculature, the different arterial systems of the chest and the abdomen, and the arteries of the extremities. In addition, the venous systems of the body are presented in two chapters. A large number of representative MR angiograms based on current acquisition techniques is provided to illustrate normal and pathologic vascular findings.

The aim of the experimental investigation carried out by Moreno et al. [405] was to quantify the amount of well-known effect of *elliptical deformation* present in the aortas of healthy subjects (2 male volunteers, aged 26 and 27 years old) in order to determine whether this effect should be considered in future hemodynamic studies. Indeed, the magnitude of the cross-sectional elliptic deformation of the aorta has been observed and quantified. A discrete Fourier transform of the radius versus angle MRI data provided significant information concerning the amount of elliptical deformation present throughout the cardiac cycle. The magnitude of the elliptic deformation exceeded even 7.5 percent (at the beginning of systole).

Nieminen et al. [421] tested the hypothesis that *quantitative MRI parameters*, as potential probes for revealing tissue composition and structure, could be used to asses the mechanical characterization of *articular cartilage in vitro*.

Biomechanical testing in the form of static and dynamic loading experiments in unconfined compression and the direct optical measurement of Poisson's ratio were used as reference techniques to reveal mechanical characteristics of cartilage samples from bovine humeral patellofemoral joints. Adjacent samples were analyzed using high-resolution MRI at 9.4 T, and the results from reference and MRI measurements were correlated to reveal the accuracy of quantitative MRI for prediction of mechanical properties of articular cartilage (the tissue Young's modulus, aggregate modulus, dynamic modulus and Poisson's ratio).

Jenkyn et al. [284] introduced a novel MR technique for quantifying muscle tension called MR elastography (MRE). This method was applied to functionally antagonistic ankle muscles to examine two mechanisms of muscle tension production: voluntary isometric contraction and passive stretching.

5. Elements of nonlinear elasticity

In this Section we introduce indispensable notions from finite elasticity. Section 5.1 owes much to Ogden's books [427, 432] whilst Sections 5.2 and 5.3 are based on the papers by Jemioło and Telega [278, 279].

The mathematical framework for describing the mechanical behaviour of biological soft tissues has much in common with that used in rubber elasticity, but there are significant differences in the structures of these materials and in the way that soft tissues and rubber respond under applied stresses. Figure 46 compares, for example, the typical simple tension stress-stretch response of rubber (left-hand figure) with that of soft tissue. An important characteristic of soft tissues is the initial large extension achieved with relatively low levels of stress and the subsequent stiffening at higher levels of extension, this being associated with the recruitment of collagen fibres as they become uncrimped and reach their natural lengths, whereupon their significant stiffness comes
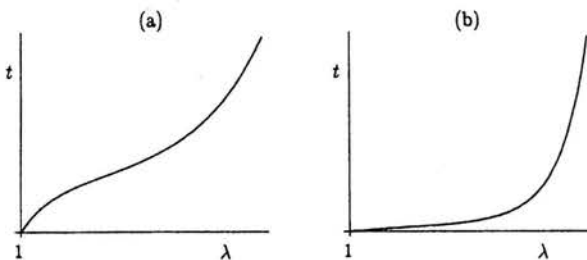
FIGURE 46. Typical simple tension response of (a) rubber and (b) soft tissue. Nominal stress $t \geq 0$ plotted against stretch $\lambda \geq 1$.

into play and overrides that of the underlying matrix material. The distribution of collagen fibres leads to the pronounced anisotropy in soft tissues, which distinguishes them from the typical (isotropic) rubber.

A more detailed picture of the response of soft tissue is illustrated in Fig. 47. This shows results from *in vitro* experiments on a human iliac artery which is subjected to extension and inflation. Figure 47 (a) shows a plot of the internal pressure against the circumferential stretch for a series of fixed values of the axial load. The curves show the typical stiffening referred to above. In Fig. 47(b) the pressure is plotted against the axial stretch, again for fixed values of the axial load. An interesting feature here is that a transitional
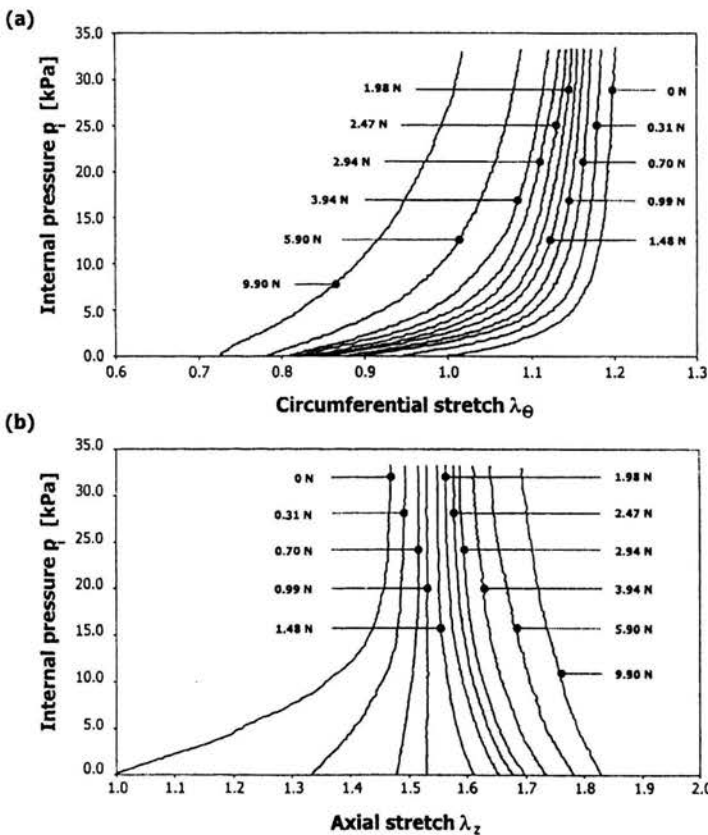
FIGURE 47. Typical characteristics of the response of a human iliac artery under pressure and axial load. Dependence of the internal pressure p_i on (a) the circumferential stretch and (b) the axial stretch at values of the axial load up to 9.9 N held constant during the deformation process, after Schulze-Bauer et al. (2001).

value of the axial stretch (approximately 1.53) is identified, as the *in vivo* value of the axial stretch. This value is unaffected by changes in pressure and corresponds to an axial load of 0.99 N. For lower (higher) values of the stretch the pressure stretch curves have a positive (negative) gradient, and the transitional value may therefore be referred to as an *inversion point*.

The data in Fig. 47 are from an external iliac artery of a 52 year old female without any cardiovascular risk factors. The artery was healthy in the sense that it was not stenotic. By contrast, data from the other specimens considered by Schulze-Bauer et al. (2001), from individuals ranging from 57 to 87 years old (with cardiovascular risk factors), have qualitative characteristics similar to those shown in Fig. 47, but there are some numerical differences. In particular, the value of the axial stretch at the inversion point is typically between 1.07 and 1.25, significantly less than the value seen in Fig. 47.

Generally, soft tissue material can be regarded as incompressible and anisotropic. The degree and type of anisotropy depends very much on the tissue considered and its topographic location. For example some tissues (such as tendon and ligament) are transversely isotropic and others (such as arteries) orthotropic. Moreover, their stress-strain response is highly nonlinear, with the typical rapid stiffening (locking) with pressure arising from the recruitment of collagen fibrils and giving rise to the markedly anisotropic behaviour, as is illustrated in Fig. 47. In some situations the mechanical response can be treated as purely *elastic*. For example, the *passive* behaviour of large *proximal* (close to the heart) arteries such as the aorta, and the iliac arteries can be regarded as essentially elastic, while the response of *distal* arteries, on the other hand, is viscoelastic. These notes are concerned mostly with elasticity and its application to some basic problems and geometries relevant to the characterization of the elastic response of soft tissues. The theory applies to many different soft tissues, but, for purposes of illustration, we confine much of the discussion to the analysis of the elasticity of soft tissues, though viscous behaviour is also discussed.

In Section 5.1 we summarize the basic equations and notation of nonlinear elasticity theory necessary for the continuum description of the mechanical properties of soft tissues.

5.1. Basic notions

Let $\mathbf{X}$ and $\mathbf{x}$, respectively, denote the position vector of a material point in some reference configuration, denoted $\mathcal{B}_r$, and the (deformed) current configuration, denoted $\mathcal{B}$, which may vary with time t. The *motion* (or *time-dependent deformation)* from $\mathcal{B}_r$ to $\mathcal{B}$ is known when $\mathbf{x}$ is specified as a func-

tion of $\mathbf{X}$ and t, and we write this in the form

$$\mathbf{x} = \text{Grad } \chi(\mathbf{X}, t), \tag{5.1}$$

where χ is the function describing the motion. For each t, χ is invertible and satisfies appropriate regularity conditions.

The *deformation gradient tensor*, denoted $\mathbf{F}$, is given by

$$\mathbf{F} = \text{Grad } \mathbf{x} \tag{5.2}$$

and has Cartesian components $F_{ij} = \partial x_i / \partial X_j$, where Grad is the gradient operator in $\mathcal{B}_r$ and x_i and X_j, are the components of $\mathbf{x}$ and $\mathbf{X}$, respectively, $i, j \in \{1, 2, 3\}$. Local invertibility of the deformation requires that $\mathbf{F}$ be non-singular, and the usual convention that

$$J \equiv \det \mathbf{F} > 0 \tag{5.3}$$

is adopted, wherein the notation J is defined.

Let $\mathbf{N}$ denote the unit outward normal to the boundary $\partial \mathcal{B}_r$ of $\mathcal{B}_r$; similarly $\mathbf{n}$ stands for the unit outward normal to $\partial \mathcal{B}$.

We shall frequently use Nanson's formula:

$$\mathbf{n} dA_t = J\mathbf{F}^{-T} \mathbf{N} dA. \tag{5.4}$$

The velocity $\mathbf{v}$ and acceleration $\mathbf{a}$ of a material particle are given, respectively, by

$$\mathbf{v} = \frac{\partial \chi}{\partial t}(\mathbf{X}, t), \quad \mathbf{a} = \frac{\partial^2 \chi}{\partial t^2}(\mathbf{X}, t), \tag{5.5}$$

these being the first and second material time derivatives of χ.

The (unique) *polar decompositions*

$$\mathbf{F} = \mathbf{RU} = \mathbf{VR}, \tag{5.6}$$

then follow, $\mathbf{R}$ being a proper orthogonal tensor and $\mathbf{U}$, $\mathbf{V}$ positive definite and symmetric tensors (the *right* and *left stretch tensors*, respectively). In spectral form $\mathbf{U}$ and $\mathbf{V}$ have the *spectral decompositions*

$$\mathbf{U} = \sum_{i=1}^{3} \lambda_i \mathbf{u}^{(i)} \otimes \mathbf{u}^{(i)}, \quad \mathbf{V} = \sum_{i=1}^{3} \lambda_i \mathbf{v}^{(i)} \otimes \mathbf{v}^{(i)}, \tag{5.7}$$

respectively, where $\lambda_i > 0, i \in \{1, 2, 3\}$, are the *principal stretches*, $\mathbf{u}^{(i)}$ are the (unit) eigenvectors of $\mathbf{U}$, called the *Lagrangian principal axes*, $\mathbf{v}^{(i)}$ the (unit) eigenvectors of $\mathbf{V}$, called the *Eulerian principal axes*, and $\otimes$ denotes the tensor product.

The *left* and *right Cauchy-Green deformation tensors*, denoted respectively by $\mathbf{B}$ and $\mathbf{C}$, are defined by

$$\mathbf{B} = \mathbf{FF}^T \equiv \mathbf{V}^2, \quad \mathbf{C} = \mathbf{F}^T\mathbf{F} \equiv \mathbf{U}^2 \qquad (5.8)$$

and the principal invariants of $\mathbf{B}$ (equivalently of $\mathbf{C}$) are defined by

$$I_1 = \mathrm{tr}\mathbf{B}, \ I_2 = \frac{1}{2}[I_1^2 - \mathrm{tr}(\mathbf{B}^2)], \ I_3 = \det\mathbf{B} \equiv (\det\mathbf{F})^2. \qquad (5.9)$$

The tensor $\mathbf{U}$ is often introduced as the square root of $\mathbf{C}$, cf. Ciarlet [83],

$$\mathbf{U} = \sqrt{\mathbf{C}}.$$

The Green strain tensor, defined by

$$\mathbf{E} = \frac{1}{2}(\mathbf{C} - \mathbf{I}), \qquad (5.10)$$

where $\mathbf{I}$ is the identity tensor, will be required in the following sections.

If the material is incompressible, which is usually taken to be the case both for rubber and for soft tissues, then the *incompressibility constraint*

$$J = \det\mathbf{F} = \lambda_1\lambda_2\lambda_3 = 1, \quad I_3 = 1 \qquad (5.11)$$

must be satisfied.

5.1.1. Stress and the equations of motion.
The equation of motion may be expressed in the form

$$\mathrm{Div}\mathbf{P} + \rho_r\mathbf{b} = \rho_r\mathbf{a} \equiv \rho_r\mathbf{x}_{,tt}, \qquad (5.12)$$

where $\mathbf{P}$ is the nominal stress tensor (the first Piola-Kirchhoff stress tensor), ρ_r is the mass density of the material in $\mathcal{B}_r$ and $_{,t}$ signifies the material time derivative. Body forces are given by $\rho_r\mathbf{b}$. Equation (5.12) is the Lagrangian version of the equation of motion, with $(\mathbf{X}, t)$ used as the independent variables. The global counterpart of the local balance equation (5.12) may be written

$$\int_{\mathcal{B}_r} \rho_r\mathbf{b}dV + \int_{\partial\mathcal{B}_r} \mathbf{P}\mathbf{N}dA = \frac{d}{dt}\int_{\mathcal{B}_r} \rho_r\mathbf{v}dV, \qquad (5.13)$$

where $\mathbf{N}$ is the unit outward normal to the boundary $\partial\mathcal{B}_r$ of $\mathcal{B}_r$, dA is the area element on $\partial\mathcal{B}_r$ and dV the volume element in $\mathcal{B}_r$. This serves to identify the *traction vector* $\mathbf{P}\mathbf{N}$ per unit area of $\partial\mathcal{B}_r$ (also referred to as the *load* or *stress vector*).

The equation of motion (5.12) may, equivalently, be written in the Eulerian form.

$$\text{div}\boldsymbol{\sigma} + \rho\mathbf{b}(\mathbf{x}, t) = \rho\mathbf{a}, \qquad (5.14)$$

where the symmetric tensor $\boldsymbol{\sigma}$ is the Cauchy stress tensor, div is the divergence operator with respect to $\mathbf{x}$, and ρ is the material density in $\mathcal{B}$, with $(\mathbf{x}, t)$ as the independent variables and treated, through the inverse of (5.1), as a function of $\mathbf{x}$ and t.

The two densities are connected through

$$\rho_r = \rho J. \qquad (5.15)$$

If the material is incompressible $\rho_r = \rho$.

The nominal and Cauchy stress tensors are related by

$$\mathbf{P} = J\boldsymbol{\sigma}\mathbf{F}^{-T}. \qquad (5.16)$$

The *Biot stress tensor*, denoted $\boldsymbol{\tau}$, and the *second Piola-Kirchhoff stress tensor*, denoted $\mathbf{T}$, which are both symmetric, are also often used. They are defined by

$$\boldsymbol{\tau} = \frac{1}{2}(\boldsymbol{\mathcal{S}}\mathbf{R} + \mathbf{R}^T\boldsymbol{\mathcal{S}}), \quad \mathbf{T} = \mathbf{F}^{-1}\mathbf{P} = J\mathbf{F}^{-1}\boldsymbol{\sigma}\mathbf{F}^{-T}, \quad \boldsymbol{\mathcal{S}} = \mathbf{P}^T \qquad (5.17)$$

and connected through

$$\boldsymbol{\tau} = \frac{1}{2}(\mathbf{TU} + \mathbf{UT}). \qquad (5.18)$$

5.1.2. Conjugate pairs of stress and strain tensors. Using *Nanson's formula* (5.4) the traction on an area element $\mathbf{n}dA_t$ in the current configuration can be written as follows

$$\mathbf{t}dA_t = \boldsymbol{\sigma}\mathbf{n}dA_t = J\boldsymbol{\sigma}\mathbf{F}^{-T}\mathbf{N}dA \equiv \mathbf{P}\mathbf{N}dA. \qquad (5.19)$$

We observe that Ogden [431, 432] prefers to consequently use as the *nominal stress tensor* the tensor $\boldsymbol{\mathcal{S}} = \mathbf{P}^T$.

The first Piola-Kirchoff stress tensor measures the force per *unit reference area* while $\boldsymbol{\sigma}$ measures the force per *unit deformed area*.

The symmetry of $\boldsymbol{\sigma}$ gives

$$\mathbf{P}\mathbf{F}^T = \mathbf{F}\mathbf{P}^T. \qquad (5.20)$$

Remark 1. Note a difference in notation used in this book and the books by Ogden [431, 432]. In our notation, $(\text{div}\boldsymbol{\sigma})_i = \partial\sigma_{ij}/\partial x_j$, while Ogden prefers to write $(\text{div}\boldsymbol{\sigma})_i = \partial\sigma_{ji}/\partial x_j$, etc.

The power of forces acting on $R_t \subset \mathcal{B}$ is converted into kinetic energy and $P_{\text{in}}(R_t)$.

In the reference configuration the integral for P_{in} becomes

$$\int_R J\mathrm{tr}(\boldsymbol{\sigma}\mathbf{D})dV, \tag{5.21}$$

where

$$\mathbf{D} = \frac{1}{2}(\mathbf{L} + \mathbf{L}^T), \quad \mathbf{L} = \mathrm{grad}\,\mathbf{v}. \tag{5.22}$$

The last integrand presents the *rate of working of the stresses* per *unit reference volume*, i.e., the stress power density. Using the symmetry of $\boldsymbol{\sigma}$ together with (5.16), (5.22) we obtain

$$\begin{aligned} J\mathrm{tr}(\boldsymbol{\sigma}\mathbf{D}) = J\mathrm{tr}(\boldsymbol{\sigma}\mathbf{L}) &= \mathrm{tr}(\mathbf{F}\mathbf{P}^T\mathbf{L}) = \\ &= \mathrm{tr}(\mathbf{P}^T\mathbf{L}\mathbf{F}) = \mathrm{tr}(\mathbf{P}^T\dot{\mathbf{F}}) = \mathrm{tr}(\boldsymbol{S}\dot{\mathbf{F}}), \end{aligned} \tag{5.23}$$

since $\dot{\mathbf{F}} = \mathbf{L}\mathbf{F}$. Hence we conclude that the stress power is also given by $\mathrm{tr}(\boldsymbol{S}\dot{\mathbf{F}})$. We say that $\boldsymbol{S}$ and $\mathbf{F}$ constitute a pair of *conjugate* stress and deformation tensors.

Furthermore, by setting $\mathbf{E} = \mathbf{E}^{(2)}$ we write

$$\mathbf{E}^{(2)} = \frac{1}{2}(\mathbf{F}^T\mathbf{F} - \mathbf{I}) = \mathbf{E}. \tag{5.24}$$

Hence by using (5.22) and (5.24) we get

$$\dot{\mathbf{E}}^{(2)} = \frac{1}{2}(\mathbf{F}^T\dot{\mathbf{F}} + \dot{\mathbf{F}}^T\mathbf{F}) \equiv \mathbf{F}^T\mathbf{D}\mathbf{F}. \tag{5.25}$$

The stress power is written as

$$\begin{aligned} \mathrm{tr}(\mathbf{P}^T\dot{\mathbf{F}}) = \mathrm{tr}(\boldsymbol{S}\dot{\mathbf{F}}) &= \mathrm{tr}(\boldsymbol{S}\mathbf{F}^{-\top}\mathbf{F}^T\dot{\mathbf{F}}) = \\ &= \mathrm{tr}(\boldsymbol{S}\mathbf{F}^{-\top}\dot{\mathbf{E}}^{(2)}) = \mathrm{tr}(\mathbf{T}^{(2)}\dot{\mathbf{E}}^{(2)}), \end{aligned} \tag{5.26}$$

where

$$\mathbf{T}^{(2)} = \mathbf{T} \equiv \boldsymbol{S}\mathbf{F}^{-\top} = J\mathbf{F}^{-1}\boldsymbol{\sigma}\mathbf{F}^{-\top} \tag{5.27}$$

is the *second (symmetric) Piola-Kirchhoff stress tensor*, i.e. $\mathbf{T} = \mathbf{T}^T$. The first and second Piola-Kirchoff stress tensors are interrelated by

$$\mathbf{P} = \mathbf{F}\mathbf{T}. \tag{5.28}$$

The stress and strain pair $(\mathbf{T}, \mathbf{E})$ or $(\mathbf{T}^{(2)}, \mathbf{E}^{(2)})$ is a pair of conjugate stress and strain tensors.

The *Kirchhoff stress tensor*, being the 'weighted' Cauchy stress $J\boldsymbol{\sigma}$, is denoted by

$$\boldsymbol{\tau} = J\boldsymbol{\sigma}. \tag{5.29}$$

We already know that $\mathbf{F}^T\mathbf{F} = \mathbf{U}^2$, cf. $(5.8)_2$. Hence we also have

$$\dot{\mathbf{E}}^{(2)} = \frac{1}{2}(\mathbf{U}\dot{\mathbf{U}} + \dot{\mathbf{U}}\mathbf{U}).$$

Using the symmetry of $\mathbf{T}^{(2)}$ and of $\dot{\mathbf{U}}$ we obtain

$$\operatorname{tr}(\mathbf{T}^{(2)}\dot{\mathbf{E}}^{(2)}) = \operatorname{tr}(\mathbf{T}^{(2)}\mathbf{U}\dot{\mathbf{U}}) = \operatorname{tr}\left[\frac{1}{2}(\mathbf{T}^{(2)}\mathbf{U} + \mathbf{U}\mathbf{T}^{(2)})\dot{\mathbf{U}}\right].$$

Thus we may introduce the definition of the *Biot stress tensor* $\mathbf{T}^{(1)} = \boldsymbol{\tau}$, *conjugate* to the strain tensor

$$\mathbf{E}^{(1)} \equiv \mathbf{U} - \mathbf{I}, \tag{5.30}$$

as

$$\mathbf{T}^{(1)} = \frac{1}{2}(\mathbf{T}^{(2)}\mathbf{U} + \mathbf{U}\mathbf{T}^{(2)}). \tag{5.31}$$

Indeed, $\dot{\mathbf{E}}^{(1)} = \dot{\mathbf{U}}$ and consequently the stress and strain pair $(\mathbf{T}^{(1)}, \mathbf{E}^{(1)})$ constitute a pair of conjugate stress and strain tensors.

By using the polar decomposition (5.6), the Biot stress tensor takes the form

$$\boldsymbol{\tau} = \mathbf{T}^{(1)} = \frac{1}{2}(\boldsymbol{\mathcal{S}}\mathbf{R} + \mathbf{R}^T\boldsymbol{\mathcal{S}}^T) = \frac{1}{2}(\mathbf{P}^T\mathbf{R} + \mathbf{R}^T\mathbf{P}). \tag{5.32}$$

Summarizing, we have the connections

$$J\operatorname{tr}(\boldsymbol{\sigma}\mathbf{D}) = \operatorname{tr}(\boldsymbol{\mathcal{S}}\dot{\mathbf{F}}) = \operatorname{tr}(\mathbf{T}^{(2)}\dot{\mathbf{E}}^{(2)}) = \operatorname{tr}(\mathbf{T}^{(1)}\dot{\mathbf{E}}^{(1)}). \tag{5.33}$$

Moreover, $\boldsymbol{\mathcal{S}} = \mathbf{P}^T$, $\mathbf{T}^{(2)} = \mathbf{T}$, and $\mathbf{P}$ and $\mathbf{T}$ denote the first and second Piola-Kirchhoff stress tensor, respectively. The strain measure $\mathbf{E}^{(2)}$ is usually denoted by $\mathbf{E}$.

More generally, the symmetric stress tensor $\mathbf{T}^{(m)}$ conjugate to the strain tensor $\mathbf{E}^{(m)} \equiv (\mathbf{U}^{(m)} - \mathbf{I})/m$ may be defined via the identity

$$\operatorname{tr}(\mathbf{T}^{(m)}\dot{\mathbf{E}}^{(m)}) = \operatorname{tr}(\mathbf{T}^{(1)}\dot{\mathbf{E}}^{(1)}) = \operatorname{tr}(\mathbf{T}^{(1)}\dot{\mathbf{U}}). \tag{5.34}$$

The limit case $m \to 0$ is much more complex. For $m = 0$ we have the logarithmic strain $\ln\mathbf{U}$. Below we discuss the stress conjugate to this strain. It is worth noting that the notion of pairs of conjugate stress and strain tensors is *independent* of any material constitutive law.

For a discussion of the stress tensors conjugate to $\ln \mathbf{U}$ and $\ln \mathbf{V}$ the reader is referred to Shillor et al. [516]. The last two strain tensors are often used in the mechanical literature. For its properties the reader is referred to Dłużewski [138] and Dłużewski et al. [139], and to the references cited therein. For instance, the logarithmic strain tensor possesses simple additive decomposition into bulk strain and dilatation.

The results on the stresses conjugate to $\ln \mathbf{U}$ and $\ln \mathbf{V}$ seem to be scattered throughout the relevant literature. Also, it has often been claimed that the logarithm of the left stretch, i.e. $\ln \mathbf{V}$, does not, in general, have a conjugate stress. As an exception one gives isotropic elastic materials. In fact, the problem is more subtle and one can find the stress conjugate to $\ln \mathbf{V}$.

The problem of finding the stress conjugate to the strain $\ln \mathbf{U}$ was finally resolved by Hoger (1987). For earlier investigations the reader is referred to the relevant references in Hoger (1987) and Xiao et al. (1993), cf. also Shillor et al. [516].

Remark 2. As we have already noted, the problem of finding the stress conjugate to $\ln \mathbf{V}$ is more subtle than the previous one. Earlier, some authors claimed that the Eulerian logarithmic strain $\ln \mathbf{V}$ does not have a conjugate stress, in general. For a discussion the reader is referred to Lehmann et al. (1991, 1993). It was claimed, that a conjugate stress only exists (and that is the Cauchy stress $\boldsymbol{\sigma}$) if this stress tensor and $\mathbf{V}$ are coaxial as, for instance, in the case of isotropic materials. That is true if (non objective) material time derivative D/Dt is used. In fact, to obtain explicit expressions for different (Eulerian) stress tensors, say $\overline{\boldsymbol{\sigma}}$ conjugate to the logarithmic strain $\ln \mathbf{V}$ one has to introduce objective time derivatives. They reduce to the Cauchy stress $\boldsymbol{\sigma}$ in coaxial deformation processes and in the case of isotropy.

5.1.3. Hyperelasticity.

We consider an elastic material for which the material properties are characterized in terms of a *strain-energy function* (per unit volume), denoted $W = W(\mathbf{F})$ and defined on the space of deformation gradients. This theory is known as *hyperelasticity*. For an inhomogeneous material, i.e. one whose properties vary from point to point, W depends on $\mathbf{X}$ in addition to $\mathbf{F}$, but we often do not indicate this dependence explicitly in what follows. For an unconstrained hyperelastic material the nominal stress is given by

$$\mathbf{P} = \mathbf{H}(\mathbf{F}) \equiv \frac{\partial W}{\partial \mathbf{F}}, \tag{5.35}$$

wherein the notation $\mathbf{H}$ is defined. The tensor function $\mathbf{H}$ is referred to as the *response function of the material relative to the configuration* $\mathcal{B}_r$ with respect to the nominal stress tensor. In components, the derivative in (5.35)

is written $S_{ij} = \partial W/\partial F_{ij}$, which provides the convention for ordering of the indices in the partial derivative with respect to $\mathbf{F}$.

For an incompressible material the counterpart of (5.35) is

$$\mathbf{P} = \frac{\partial W}{\partial \mathbf{F}} - p\mathbf{F}^{-T}, \quad \det\mathbf{F} = 1, \tag{5.36}$$

where p is the Lagrange multiplier associated with the incompressibility constraint and is referred to as the *arbitrary hydrostatic pressure* (determined by solving the boundary or boundary-initial value problem). The Cauchy stress tensor corresponding to (5.35), on use of (5.16), is then seen to be given by

$$\boldsymbol{\sigma} = \mathbf{G}(\mathbf{F}) = J^{-1}\frac{\partial W}{\partial \mathbf{F}}\mathbf{F}^{T}, \tag{5.37}$$

wherein the response function $\mathbf{G}$ associated with $\boldsymbol{\sigma}$ is defined. As for $\mathbf{H}$, the form of $\mathbf{G}$ depends on the choice of reference configuration, and $\mathbf{G}$ is referred to as the *response function* of the material *relative* to $\mathcal{B}_r$ associated with the Cauchy stress tensor. Unlike $\mathbf{H}$, however, $\mathbf{G}$ is a *symmetric*, tensor-valued function. For incompressible materials (5.37) is replaced by

$$\boldsymbol{\sigma} = \frac{\partial W}{\partial \mathbf{F}}\mathbf{F}^{T} - p\mathbf{I}, \quad \det\mathbf{F} = 1. \tag{5.38}$$

If the configuration $\mathcal{B}_r$ is stress free then it is referred to as a *natural configuration*. Here, we take W and the stress to vanish in $\mathcal{B}_r$, so that, for an unconstrained material,

$$W(\mathbf{I}) = 0, \quad \frac{\partial W}{\partial \mathbf{F}}(\mathbf{I}) = (\mathbf{0}) \tag{5.39}$$

with appropriate modifications in the case of an incompressible material. If the stress does not vanish in $\mathcal{B}_r$ then this configuration is said to be *residually stressed*. In such a configuration the traction must vanish at all points of the boundary, so that, *a fortiori*, residual stress is inhomogeneous in character (i.e., it cannot be uniform). Residual stresses are important in the context of biological tissues and the restriction (5.39) will be removed later, where we consider the consequences of residual stress for the constitutive law and response of the material, cf. also Telega and Stańczyk [570].

5.1.4. Objectivity. The elastic stored energy is required to be independent of rigid motions of the form

$$\mathbf{x}^{\star} = \mathbf{Q}(t)\mathbf{x} + \mathbf{c}(t), \tag{5.40}$$

superimposed on the motion $\mathbf{x} = \chi(\mathbf{X}, t)$. Here $\mathbf{Q}$ is a proper orthogonal (rotation) tensor, $\mathbf{c}$ is a translation vector. It follows that

$$W(\mathbf{QF}) = W(\mathbf{F}), \qquad (5.41)$$

for *all* rotations $\mathbf{Q}$. A strain-energy function satisfying this requirement is said to be *objective*. This may also be expressed by referring to W as being indifferent to observer transformations. Use of the polar decomposition (5.6) and the choice $\mathbf{Q} = \mathbf{R}^T$ in (5.41) shows that

$$W(\mathbf{F}) = W(\mathbf{U}). \qquad (5.42)$$

Thus, W depends on $\mathbf{F}$ only through the stretch tensor $\mathbf{U}$ and may therefore be defined on the class of positive definite symmetric tensors. Equivalently, through (5.8) and (5.10), W may be regarded as a function of the Green strain $\mathbf{E}$.

Expressions analogous to (5.35) and (5.36) can therefore be written down for the Biot and second Piola-Kirchhoff stresses. Thus,

$$\tau = \frac{\partial W}{\partial \mathbf{U}}, \quad \mathbf{T} = \frac{\partial W}{\partial \mathbf{E}} \qquad (5.43)$$

and

$$\tau = \frac{\partial W}{\partial \mathbf{U}} - p\mathbf{U}^{-1}, \qquad \det\mathbf{U} = 1, \quad \mathbf{T} = \frac{\partial W}{\partial \mathbf{E}} - p\mathbf{C}^{-1}, \quad \det\mathbf{C} = 1, \quad (5.44)$$

for unconstrained and incompressible materials respectively, where $\mathbf{C} = \mathbf{I} + 2\mathbf{E}$. Note that when expressed as a function of $\mathbf{U}$ or $\mathbf{E}$ the strain energy automatically satisfies the objectivity requirement.

5.1.5. Material symmetry. Mathematically, there is no restriction so far, other than (5.39) and (5.41) on the form that the function W may take. However, the predicted stress-strain behaviour based on the form of W must, on the one hand, be acceptable for the description of the elastic behaviour of real materials and, on the other hand, make mathematical sense.

Further restrictions on the form of W arise if the material possesses symmetries in the configuration $\mathcal{B}_r$. Material symmetry (relative to a given reference configuration) is identified by transformations of the reference configuration that do not affect the material response. Consider a change from the reference configuration $\mathcal{B}_r$ (in which material points are identified by position vectors $\mathbf{X}$) to a new reference configuration $\mathcal{B}'_r$ (with material points identified by $\mathbf{X}'$), let $\mathbf{F}'$ denote the deformation gradient relative to $\mathcal{B}'_r$ and let Grad $\mathbf{X}'$ be denoted by $\bar{\mathbf{F}}$. If the material response is unchanged then

$$W(\mathbf{F}'\bar{\mathbf{F}}) = \mathbf{W}(\mathbf{F}'), \qquad (5.45)$$

for *all* deformation gradients $\mathbf{F}'$. This states that the strain-energy function is unaffected by a change of reference configuration with deformation gradient $\bar{\mathbf{F}}$. The collection of $\bar{\mathbf{F}}$ for which (5.45) holds forms a group, which is called the *symmetry group of the material relative to* $\mathcal{B}_r$. As we already know biological soft tissues are distinguished by the anisotropy of their structure. We will examine the appropriate type of anisotropy in Section 5.3, but initially we shall, for simplicity, focus on the development of the theory in the case of isotropy.

5.1.6. Isotropy. To be specific we now consider *isotropic elastic materials,* for which the symmetry group is the *proper orthogonal group*. Then, we have

$$W(\mathbf{FQ}) = W(\mathbf{F}), \qquad (5.46)$$

for *all* rotations $\mathbf{Q}$. Bearing in mind that the $\mathbf{Q}$'s appearing in (5.41) and (5.46) are independent the combination of these two equations yields

$$W(\mathbf{QUQ^T}) = W(\mathbf{U}), \qquad (5.47)$$

for all rotations $\mathbf{Q}$, or, equivalently, $W(\mathbf{QVQ^T}) = W(\mathbf{V})$. Equation (5.47) states that W is an *isotropic function* of $\mathbf{U}$. It follows from the spectral decomposition (5.7) that W depends on $\mathbf{U}$ only through the principal stretches $\lambda_1, \lambda_2, \lambda_3$. To avoid introducing additional notation we express this dependence as $W(\lambda_1, \lambda_2, \lambda_3)$; by selecting appropriate values for $\mathbf{Q}$ in (5.47) we may deduce that W depends symmetrically on $\lambda_1, \lambda_2, \lambda_3$, i.e.,

$$W(\lambda_1, \lambda_2, \lambda_3) = W(\lambda_1, \lambda_3, \lambda_2) = W(\lambda_2, \lambda_1, \lambda_3). \qquad (5.48)$$

A consequence of isotropy is that the Biot stress $\boldsymbol{\tau}$ is *coaxial with* $\mathbf{U}$ and, equivalently, the Cauchy stress $\boldsymbol{\sigma}$ is coaxial with $\mathbf{V}$. Hence, in parallel with (5.7), we have

$$\boldsymbol{\tau} = \sum_{i=1}^{3} \tau_i \mathbf{u}^{(i)} \otimes \mathbf{u}^{(i)}, \quad \boldsymbol{\sigma} = \sum_{i=1}^{3} \sigma_i \mathbf{v}^{(i)} \otimes \mathbf{v}^{(i)}, \qquad (5.49)$$

where τ_i are the *principal Biot stresses* and σ_i are the *principal Cauchy stresses*. For an unconstrained material,

$$\tau_i = J\lambda_i^{-1}\sigma_i\frac{\partial W}{\partial \lambda_i}, \quad J\sigma_i = \lambda_i\frac{\partial W}{\partial \lambda_i}, \qquad (5.50)$$

while for incompressible material these are replaced by

$$\tau_i = \frac{\partial W}{\partial \lambda_i} - p\lambda_i^{-1}, \quad \sigma_i = \lambda_i\frac{\partial W}{\partial \lambda_i} - p, \quad \lambda_1\lambda_2\lambda_3 = 1. \qquad (5.51)$$

Note that in (5.50) and (5.51) there is no summation over the repeated index i.

For an isotropic material the symmetric dependence (5.48) of W on the principal stretches is equivalent to W being regarded as a function of the (symmetric) principal invariants I_1, I_2, I_3 defined by (5.9). In terms of the invariants I_1, I_2, I_3 the Cauchy stress tensor for an unconstrained isotropic elastic material may be written

$$\boldsymbol{\sigma} = \alpha_0 \mathbf{I} + \alpha_1 \mathbf{B} + \alpha_2 \mathbf{B}^2, \tag{5.52}$$

where the coefficients $\alpha_0, \alpha_1, \alpha_2$ are functions of I_1, I_2, I_3 given by

$$\alpha_0 = 2I_3^{1/2} \frac{\partial W}{\partial I_3}, \quad \alpha_1 = 2I_3^{-1/2} \left(\frac{\partial W}{\partial I_1} + I_1 \frac{\partial W}{\partial I_2} \right), \quad \alpha_2 = -2I_3^{-1/2} \frac{\partial W}{\partial I_2}, \tag{5.53}$$

with W now regarded as a function of I_1, I_2, I_3. For an incompressible material the corresponding expression is

$$\boldsymbol{\sigma} = -p\mathbf{I} + \alpha_1 \mathbf{B} + \alpha_2 \mathbf{B}^2, \tag{5.54}$$

where p is the arbitrary hydrostatic pressure, α_1 and α_2 are again given by (5.53) (but with $I_3 = 1$), and W is now regarded as a function of I_1 and I_2 alone.

5.2. Further relationships for isotropic hyperelastic materials

Prior to passing to transverse isotropy we shall discuss some general forms of isotropic constitutive relationships.

5.2.1. On general form of the stored energy function.
As usual, by $\mathbf{C} = \mathbf{F}^T \mathbf{F}$ we denote the right Cauchy-Green strain tensor, cf. [33, 50, 83, 426]. The objectivity principle yields the stored energy function in the form cf. [83, 426]

$$W = \breve{W}(\mathbf{C}). \tag{5.55}$$

Let us denote by $\mathbf{T}$, $\boldsymbol{\sigma}$ the second (symmetric) Piola-Kirchhoff and Cauchy stress tensors, respectively. We have

$$\mathbf{T} = \frac{1}{2} \left(\frac{\partial \breve{W}(\mathbf{C})}{\partial \mathbf{C}} + \frac{\partial \breve{W}(\mathbf{C})}{\partial \mathbf{C}^T} \right), \quad \boldsymbol{\sigma} = \frac{1}{J} \mathbf{F} \mathbf{T} \mathbf{F}^T. \tag{5.56}$$

The first (unsymmetric) Piola-Kirchhoff stress tensor $\mathbf{P}$ is related to $\mathbf{T}$ by $\mathbf{P} = \mathbf{F} \mathbf{T}$. For isotropic hyperelastic materials $\breve{W}$ satisfies

$$\forall \mathbf{Q} = O(3) \quad \breve{W}(\mathbf{C}) = \breve{W}(\mathbf{Q} \mathbf{C} \mathbf{Q}^T). \tag{5.57}$$

Here $O(3)$ denotes the full orthogonal group in space dimension 3.

We assume the existence of a stress and strain-free state (natural configuration) such that

$$\breve{W}(\mathbf{I}) = \mathbf{0}, \quad \mathbf{T} = \breve{\mathbf{T}}(\mathbf{I}) = \mathbf{0}, \tag{5.58}$$

where $\mathbf{I}$ is the identity tensor. By now it has been well-established that in many soft tissues residual stresses and strains are present cf. [3, 123, 191]

Consequently, assumption $(5.58)_2$ for such tissues is, in a general case, a simplification. Fortunately, an isotropic body can support no residual stress, [235]. Thus, for an ideal case of isotropic soft tissues, assumption (5.58) remains valid.

Having in mind FEM it is convenient to choose the invariants of $\mathbf{C}$ compatible with the multiplicative decomposition of $\mathbf{F}$ in parts related to volumetric and distorsional deformations as well as with the polar decomposition, the last being expressed by the well-known relation $\mathbf{F}=\mathbf{R}\mathbf{U}= \mathbf{V}\mathbf{R}$. Then one can formulate in a uniform manner the constitutive relationships for compressible and incompressible materials. Accordingly, we write

$$\mathbf{F} = J^{1/3}\overline{\mathbf{F}} = J^{1/3}\mathbf{R}\overline{\mathbf{U}} = J^{1/3}\overline{\mathbf{V}}\mathbf{R}, \quad \det\overline{\mathbf{F}} = \det\overline{\mathbf{U}} = \det\overline{\mathbf{V}} = 1. \tag{5.59}$$

Consequently, the stored energy function (5.55) satisfying (5.57) can be written as follows, cf. [273]

$$W = \breve{W}(\mathbf{C}) = \breve{W}(\mathbf{B}) = \overline{W}(\overline{I}_1, \overline{I}_2, J), \tag{5.60}$$

where

$$\overline{I}_1 = \mathrm{tr}\overline{\mathbf{B}} = \mathrm{tr}\overline{\mathbf{C}}, \ \overline{I}_2 = \mathrm{tr}\overline{\mathbf{B}}^{-1}= \mathrm{tr}\overline{\mathbf{C}}^{-1},$$
$$J = \sqrt{\det\mathbf{B}} = \sqrt{\det\mathbf{C}} = \det\mathbf{F} \tag{5.61}$$

and

$$\mathbf{B} = \mathbf{F}\mathbf{F}^T, \quad \overline{\mathbf{B}} = \overline{\mathbf{F}}\overline{\mathbf{F}}^T, \quad \overline{\mathbf{C}} = \overline{\mathbf{F}}^T\overline{\mathbf{F}}. \tag{5.62}$$

We observe that

$$\overline{I}_1 = J^{-2/3}I_1, \qquad\qquad I_1 = \mathrm{tr}\mathbf{C} = \mathrm{tr}\mathbf{B}, \quad \overline{I}_2 = J^{-4/3}I_2,$$
$$I_2 = \frac{1}{2}(I_1^2 - \mathrm{tr}\mathbf{C}^2), \qquad \mathrm{tr}\mathbf{C}^2 = \mathrm{tr}\mathbf{B}^2. \tag{5.63}$$

We also recall that the invariants I_1, I_2 and J^2 are the so called basic invariants, well-known in the theory of tensor functions representation, cf. [273].

After standard calculations, from relationships (5.56) and (5.60) we get the general constitutive equation for isotropic hyperelastic materials in the Eulerian description

$$\boldsymbol{\sigma} = \frac{\partial\overline{W}}{\partial J}\mathbf{I} + \frac{2}{J}\left(\frac{\partial\overline{W}}{\partial\overline{I}_1}\overline{\mathbf{B}}_D - \frac{\partial\overline{W}}{\partial\overline{I}_2}\overline{\mathbf{B}}_D^{-1}\right) = \beta_0\mathbf{I} + \beta_1\overline{\mathbf{B}}_D + \beta_{-1}\overline{\mathbf{B}}_D^{-1}, \tag{5.64}$$

where

$$\overline{\mathbf{B}}_D = \overline{\mathbf{B}} - \frac{1}{3}\overline{I}_1\mathbf{I}, \quad \overline{\mathbf{B}}_D^{-1} = \overline{\mathbf{B}}^{-1} - \frac{1}{3}\overline{I}_2\mathbf{I}. \qquad (5.65)$$

The form $(5.60)_3$ of the stored energy function enables one to classify hyperelastic isotropic materials as follows:

(i) incompressible materials $(J - 1 = 0)$ where

$$\bar{W} = W_D(\overline{I}_1, \overline{I}_2), \qquad (5.66)$$

(ii) nearly incompressible materials described by

$$\bar{W} = W_D(\overline{I}_1, \overline{I}_2) + W_I^\varepsilon(J), \qquad (5.67)$$

(iii) compressible materials described by the elastic potential $(5.60)_3$.

More precisely, the function W_I has the following form, cf. [83, 559]

$$W_I^\varepsilon(J) = \frac{1}{\varepsilon}h(\det\mathbf{F}).$$

The function h satisfies:

(H_1) $h : R^+ \longrightarrow R$ is convex,

(H_2) $\lim\limits_{\delta\to 0^+} h(\delta) = \lim\limits_{\delta\to +\infty} h(\delta) = +\infty$ and $h(\delta) = 0$ if and only if $\delta = 1$.

Ciarlet [83] provides an example of the function h:

$$h(\delta) = c\delta^2 - d\log\delta, \quad c > 0, d > 0.$$

Obviously, in the case of incompressible materials the stored energy function (5.66) *is not an elastic potential*, since the hydrostatic part of the Cauchy stress tensor is not defined and the constitutive relationship is given by

$$\boldsymbol{\sigma} = -p\mathbf{I} + \overline{\beta}_1\overline{\mathbf{B}} + \overline{\beta}_{-1}\overline{\mathbf{B}}^{-1}, \qquad (5.68)$$

where

$$\overline{\beta}_1 = 2\frac{\partial W_D}{\partial \overline{I}_1}, \quad \overline{\beta}_{-1} = -2\frac{\partial W_D}{\partial \overline{I}_2}. \qquad (5.69)$$

The above classification is convenient when FEM system ABAQUS [1] is used, as in our case. Obviously, in the case of incompressible materials the coupling between distorsional and volumetric stored energies is absent.

Let us denote by λ_i, $\overline{\lambda}_i$, $(i = 1, 2, 3)$ the eigenvalues of $\mathbf{U}$ and $\overline{\mathbf{U}}$ respectively, or of $\mathbf{V}$ and $\overline{\mathbf{V}}$. We have

$$\lambda_i = J^{1/3}\overline{\lambda}_i; \quad i = 1, 2, 3. \qquad (5.70)$$

In general, only two eigenvalues of $\overline{\lambda}_i$ are independent. We may write

$$\overline{\lambda}_3 = \left(\overline{\lambda}_1 \overline{\lambda}_2\right)^{-1}. \tag{5.71}$$

Consequently, we have, cf. Eq. (5.60),

$$\overline{W}(\overline{I}_1, \overline{I}_2, J) = \widehat{W}(\overline{\lambda}_1, \overline{\lambda}_2, J). \tag{5.72}$$

The function $\widehat{W}$ is symmetric in the variables $\overline{\lambda}_1, \overline{\lambda}_2$. For the notion of symmetric function in the context of nonlinear hyperelasticity the reader is referred to Ciarlet [83].

5.2.2. Stored energy functions for isotropic hyperelastic soft tissue.
The aim of this section is to provide several specific stored energy functions as well as numerical examples.

Let us consider the following stored energy function, being a generalisation of Fung's proposal cf. [175]

$$\bar{W}(\bar{I}_1, \bar{I}_2, J) = \frac{C}{a} \left(e^{a\psi(\bar{I}_1, \bar{I}_2, J)} - 1 \right), \tag{5.73}$$

where and C and a are material coefficients while the invariants $\bar{I}_1, \bar{I}_2$ and J have been defined previously. Now the Cauchy stress tensor is expressed by (5.64) and

$$\beta_0 = Ce^{a\psi}\frac{\partial\psi}{\partial J}, \quad \beta_1 = \frac{2}{J}Ce^{a\psi}\frac{\partial\psi}{\partial\bar{I}_1}, \quad \beta_{-1} = -\frac{2}{J}Ce^{a\psi}\frac{\partial\psi}{\partial\bar{I}_2}. \tag{5.74}$$

According to relation (5.58), we assume

$$\psi(3,3,1) = 0, \quad \mathbf{T} = \widetilde{\mathbf{T}}(\mathbf{I}) = 0. \tag{5.75}$$

In other words, in the undeformed configuration the hyperelastic solid is stress-free. The function appearing in Eq. (5.73) has one of the following forms

(a) $\qquad \psi = \psi(\overline{I}_1, \overline{I}_2),$
(b) $\qquad \psi = \psi_1(\overline{I}_1, \overline{I}_2) + \psi_2(J),$
(c) $\qquad \psi = \psi_1(\overline{I}_1, \overline{I}_2, J).$

It is reasonable to consider the following form of ψ:

$$\psi = a_1(\bar{I}_1 - 3) + a_2(\bar{I}_2 - 3) + a_3(J - 1) + a_4(\bar{I}_1\bar{I}_2 - 9) + \ldots, \tag{5.76}$$

where the parameters $a_1, a_2, \ldots$ are material coefficients.

In the present section we will discuss only the models (a) and (c) of soft tissues. For such models the material parameters are known. Also, an implementation in the finite element system ABAQUS will be discussed. In the case of incompressible materials the following particular form of the function (5.73), now denoted by W, is assumed:

$$W(\bar{I}_1) = \frac{\mu_0}{2\gamma} \left[e^{\gamma(\bar{I}_1 - 3)} - 1 \right],\tag{5.77}$$

where μ_0 denotes the shear modulus and is a positive material parameter.

For compressible materials we consider the following stored energy function (the bar over W is deleted):

$$W(\bar{I}_1, \bar{I}_2, J) = \frac{C_0}{a} \left[e^{aC_1(\bar{I}_1 - 3) + C_2(\bar{I}_1 - 3) + C_3(J-1)^2} - 1 \right],\tag{5.78}$$

where C_0, C_i ($i = 1, 2, 3$) are positive material parameters, see [524, 525]. We observe that material parameters appearing in Eqs. (5.77), (5.78), and more generally in (5.76), can be determined by performing simple test (one- and two-dimensional) and next minimizing the approximation error (similarly to the case of other hyperelastic materials, cf. [431]).

Also, function (5.77) is a particular case of (5.78). However, from the numerical and mechanical point of view it is convenient to treat both models as independent. For the sake of simplicity, models (5.77) and (5.78) will be denoted by IM and CM, respectively.

In the case of the model IM the constitutive relationship is given by

$$\boldsymbol{\sigma} = -p\mathbf{I} + \mu_0 e^{\gamma(\bar{I}_1 - 3)} \bar{\mathbf{B}}.\tag{5.79}$$

For three-dimensional and plane strain problems an application of FEM to incompressible materials requires hybrid finite elements (or a modification of models (a) and (b)).

For the plane stress problem the situation is different, since then the incompressibility constraint can easily be handled. We observe that for incompressible material in the state of plane stress, the stretch in the direction orthogonal to the plane is determined from the equation $J = 1$; hence

$$\lambda_3 = \tilde{J}^{-3}.\tag{5.80}$$

Here the tilde refers to two-dimensional quantities. It means that $\tilde{J}$ denotes the determinant of plane deformation tensor. From Eq. (5.79), for the plane stress state, we have

$$p = \mu_0 e^{\gamma(\tilde{I} + \tilde{J}^{-2} - 3)} \tilde{J}^{-2}.\tag{5.81}$$

Thus

$$\widetilde{\sigma} = \mu_0 e^{\gamma(\widetilde{I}+\widetilde{J}^{-2}-3)} \left(-\widetilde{J}^{-2}\widetilde{\mathbf{I}} + \widetilde{\mathbf{B}}\right),$$ (5.82)

where $\widetilde{I} = \mathrm{tr}\widetilde{\mathbf{B}} = \mathrm{tr}\widetilde{\mathbf{C}}$.

The derivation of the constitutive relationship in the case of the stored energy function (5.78) is left to the reader as an easy exercise.

Implementation of IM and CM models in the ABAQUS system

The model IM requires programming, within the general structure of the interface UHYPER (see Jemioło and Szwed [272]), of only the first and second order derivatives with respect to the invariant $\bar{I}_1$ of the function (5.77). On the other hand, CM model requires programming of the following derivatives of the function (5.78)

$$\frac{\partial W}{\partial \bar{I}_1} = \frac{1}{2}C_0C_1e^\phi, \quad \frac{\partial W}{\partial \bar{I}_2} = \frac{1}{2}C_0C_2e^\phi, \quad \frac{\partial W}{\partial J} = C_0C_3e^\phi(J-1),$$

$$\frac{\partial^2 W}{\partial \bar{I}_1^2} = \frac{1}{2}C_0C_1^2e^\phi, \qquad\qquad \frac{\partial^2 W}{\partial \bar{I}_2^2} = \frac{1}{2}C_0C_2^2e^\phi,$$

$$\frac{\partial^2 W}{\partial J^2} = C_0C_3e^\phi\left[1 + 2C_3(J-1)^2\right], \quad \frac{\partial^2 W}{\partial \bar{I}_1\partial \bar{I}_2} = \frac{1}{2}C_0C_1C_2e^\phi,$$

$$\frac{\partial^2 W}{\partial \bar{I}_1\partial J} = C_0C_1C_3e^\phi(J-1), \quad \frac{\partial^2 W}{\partial \bar{I}_2\partial J} = C_0C_2C_3e^\phi(J-1),$$

$$\frac{\partial^3 W}{\partial \bar{I}_1^2\partial J} = C_0C_1^2C_3e^\phi(J-1), \quad \frac{\partial^3 W}{\partial \bar{I}_2^2\partial J} = C_0C_2^2C_3e^\phi(J-1),$$ (5.83)

$$\frac{\partial^3 W}{\partial \bar{I}_1\partial \bar{I}_2\partial J} = C_0C_1C_2C_3e^\phi(J-1),$$

$$\frac{\partial^3 W}{\partial \bar{I}_1\partial J^2} = C_0C_1C_3e^\phi\left[1 + 2C_3(J-1)^2\right],$$

$$\frac{\partial^3 W}{\partial \bar{I}_2\partial J^2} = C_0C_2C_3e^\phi\left[1 + 2C_3(J-1)^2\right],$$

$$\frac{\partial^3 W}{\partial J^3} = 2C_0C_3^2e^\phi\left[3 + 2C_3(J-1)^2\right](J-1),$$

where

$$\phi = C_1(\bar{I}_1 - 3) + C_2(\bar{I}_2 - 3) + C_3(J-1)^2.$$ (5.84)

Numerical examples: IM model

Our aim now is to provide illustrative example for the IM model. We observe that, in general, it is more difficult to obtain satisfactory numerical results for this model than for the CM model. As one can guess, the difficulty is linked with the incompressibility condition.

Example 1. Simple shear (plane stress problem)
Now we have

$$\sigma_{11} = \mu_0 \xi^2 e^{\gamma \xi^2}, \quad \sigma_{22} = 0, \quad \sigma_{12} = \mu_0 \xi e^{\gamma \xi}, \quad \sigma_{33} = \sigma_{13} = \sigma_{23} = 0.$$
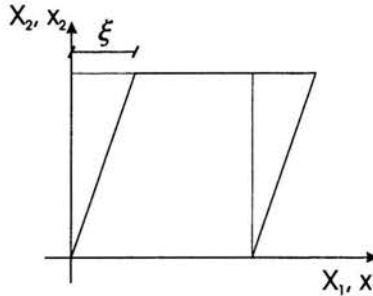
FIGURE 48. Simple shear.

For the notation the reader is referred to Fig. 48. Figure 49 represents a comparison of analytical and numerical results. The last has been obtained by using the interface UHYPER with the implemented IM model. Both the Poynting effect (nonvanishing normal stress) and Kelvin effect (nonvanishing trace of the stress tensor) are exhibited. The results presented in Fig. 49 are
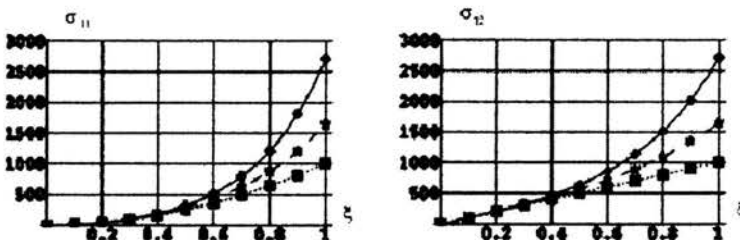
FIGURE 49. Simple shear Comparison of analytical and numerical results for simple shear (plane stress state); $\mu_0 = 1000$; the coefficient γ for the curves 1, 2, 3 is equal to: $\gamma = 1$, $\gamma = 0,5$, $\gamma = 0.01$.
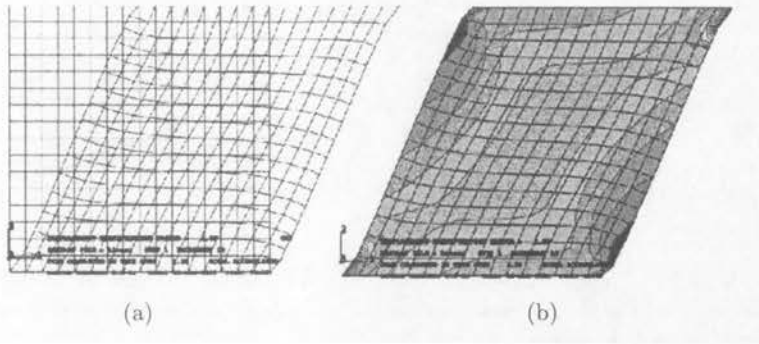
FIGURE 50. Shear: a) FEM mesh and the final configuration, b) level lines for the Cauchy stress σ_{12} ; $\mu_0 = 10^6, \gamma = 1$.

valid provided that the state of simple shear is realized. This can be achieved if simultaneously displacements and forces on the boundaries are controlled. Otherwise, the situation depicted in Fig. 50 may happen. For instance, in Fig. 50 a, only the displacements on the upper boundary are controlled.

Example 2. Thick cylinder subject to internal pressure (plane stress)

The internal and external radii of cylinder in Fig. 51a are equal to $R_i = 10$ and $R_0 = 20$ (length units), respectively. The cylinder is subject to such an internal pressure that its boundary undergoes the displacement equal to 5 length units. The results of calculation are depicted in Figs.51 b, c, 52.
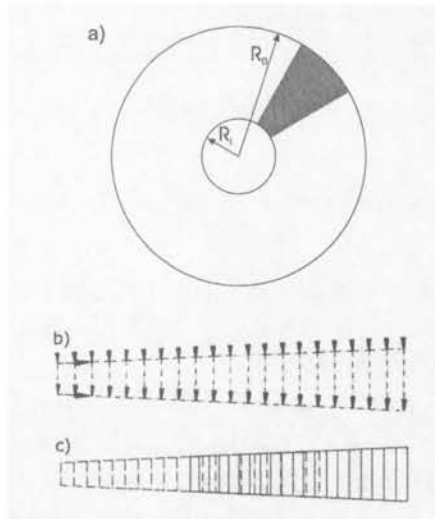
FIGURE 51. Thick cylinder in plane stress state: a,b) FEM mesh and boundary condition, c) initial and final configurations.
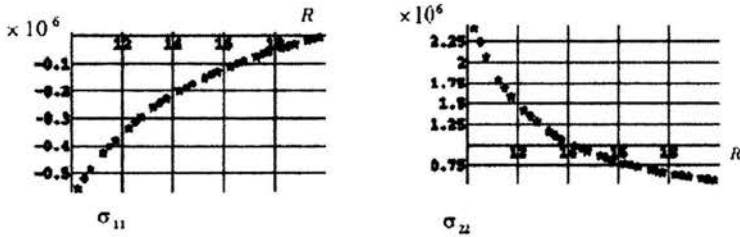
FIGURE 52. Thick cylinder in plane stress state (10 or 20 finite elements); $\mu_0 = 10^6, \gamma = 1$. Cauchy's stresses σ_{11} and σ_{22} represent values averaged (centrally) over the finite elements.

Numerical examples: CM model

The results which follow have been performed for the following values of the coefficients: $C_0 = 8133\,\text{Pa}$, $C_1 = 0.907$, $C_2 = 0.002475$, $C_3 = 20$ These values are taken from paper by Simon et al. [525] and characterize a rabbit aorta.

Example 3. Simple shear (plane strain or 3D problem)
In this case, from Eqs. (5.74) and (5.78) we get

$$\sigma_{11} = C_0 e^{\xi^2(C_1+C_2)} \left[\frac{1}{3}\xi^2(2C_1 + C_2)\right],$$

$$\sigma_{12} = C_0 e^{\xi^2(C_1+C_2)}(C_1 + C_2)\xi,$$

$$\sigma_{22} = C_0 e^{\xi^2(C_1+C_2)} \left[-\frac{1}{3}\xi^2(C_1 + 2C_2)\right],$$

$$\sigma_{33} = C_0 e^{\xi^2(C_1+C_2)} \left[-\frac{1}{3}\xi^2(C_1 - C_2)\right].$$

The results of calculation are depicted in Fig. 53. Numerical calculations were performed by using the interface UHYPER with the model CM implemented according to (5.83), (5.84).

Example 4. Consider now the slab with a central hole with the unit thickness. The length of the side of the square is 2 length units. The diameter of the hole is 0.2 length units. The slab is subject to tension in one direction, such that its length increases fivefolds. The vertical displacement on AB and CD is constrained. To get numerical results, the slab was divided into 512 finite elements CPS4. The results presented in Fig. 54 were obtained after 15 iterations.
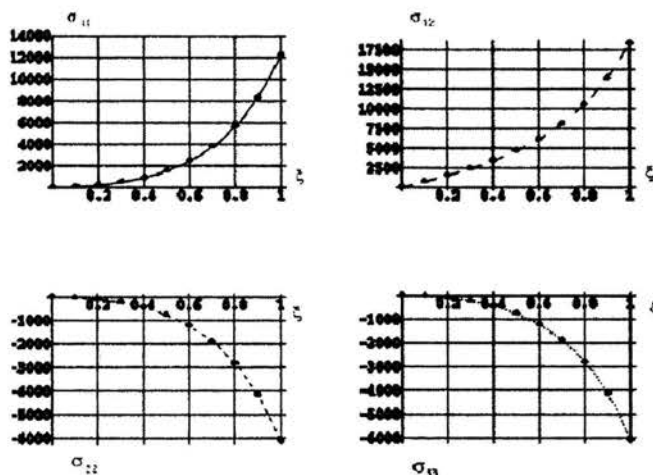
FIGURE 53. Comparison of analytical and numerical results for simple shear (plane strain state or 3D problem).
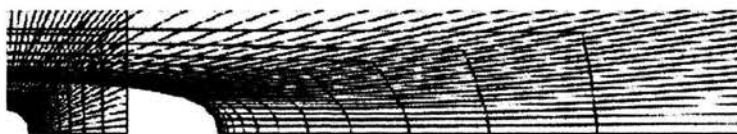
FIGURE 54. The initial and final configurations of square slab with a hole.

5.3. Transverse isotropy

In the present section we shall discuss an important case of transverse isotropy where one direction is privileged (imagine skeletal muscle fibres).

5.3.1. General relations. To describe the transverse isotropy we introduce a parametric tensor $\mathbf{M} = \mathbf{m} \otimes \mathbf{m}$. The tensor $\mathbf{M}$ is prescribed in the initial (Lagrangian) configuration. The unit vector $\mathbf{m}(\mathbf{X})$ coincides with direction of material fibres in the initial configuration; $\mathbf{X}$ denotes the Lagrangian variable of a material point. Let

$$S = \left\{ \mathbf{Q} \in O\left(3\right) \mid \mathbf{M} = \mathbf{QM}\,\mathbf{Q}^{T} \right\}, \qquad (5.85)$$

where $O(3)$ stands for the full orthogonal group in the three-dimensional case, cf. Jemioło and Telega [273]. The stored energy density function W

satisfies

$$W\left(\mathbf{E},\mathbf{M},r\right) = W\left(\mathbf{Q}\mathbf{E}\mathbf{Q}^{T},\mathbf{M},r\right) = \tilde{W}\left(\mathbf{C},\mathbf{M},r\right)$$
$$= \tilde{W}\left(\mathbf{Q}\mathbf{C}\mathbf{Q}^{T},\mathbf{M},r\right), \quad \forall \mathbf{Q} \in S. \quad (5.86)$$

Here the function $r\left(\mathbf{X}\right)$ describes the inhomogeneity of the material. From the point of view of tensor functions and constitutive equations the variable r is not essential. Therefore we shall only consider homogeneous materials.

The theory of representation of transversely isotropic functions yields, cf. Jemioło and Telega [273],

$$W\left(\mathbf{E},\mathbf{M}\right) = \check{W}\left(N_i\right) = \tilde{W}\left(\mathbf{C},\mathbf{M}\right) = \hat{W}\left(I_i\right); \quad i = 1,\ldots,5. \quad (5.87)$$

Here $\{N_i\}$ and $\{I_i\}$ denote the so-called *basic invariants* of the tensors $\mathbf{E}$ and $\mathbf{C}$, respectively. The constitutive equations are

$$\mathbf{T} = \check{\mathbf{T}}(\mathbf{E}) = \frac{1}{2}\left(\frac{\partial \check{W}}{\partial \mathbf{E}} + \frac{\partial \check{W}}{\partial \mathbf{E}^T}\right) = \frac{1}{2}\sum_{i=1}^{5} \frac{\partial \check{W}}{\partial N_i}\left(\frac{\partial N_i}{\partial \mathbf{E}} + \frac{\partial N_i}{\partial \mathbf{E}^T}\right)$$
$$= \sum_{i=1}^{5} \alpha_i \mathbf{G}_i^{(\mathbf{E})}, \quad (5.88)$$

$$\mathbf{T} = \hat{\mathbf{T}}\left(\mathbf{C}\right) = \frac{1}{2}\left(\frac{\partial \hat{W}}{\partial \mathbf{C}} + \frac{\partial \hat{W}}{\partial \mathbf{C}^T}\right)$$
$$= \frac{1}{2}\sum_{i=1}^{5} \frac{\partial \hat{W}}{\partial I_i}\left(\frac{\partial I_i}{\partial \mathbf{C}} + \frac{\partial I_i}{\partial \mathbf{C}^T}\right) = \sum_{i=1}^{5} \beta_i \mathbf{G}_i^{(\mathbf{C})}. \quad (5.89)$$

The symmetric tensors of the second-order $\mathbf{G}_i^{(\mathbf{E})}$ and $\mathbf{G}_i^{(\mathbf{C})}$ are the so-called generators, cf. Jemioło and Telega [273].

We assume the existence of a natural state where

$$W\left(\mathbf{0},\mathbf{M}\right) = \tilde{W}\left(\mathbf{I},\mathbf{M}\right) = 0, \quad \check{\mathbf{T}}\left(\mathbf{0}\right) = \hat{\mathbf{T}}\left(\mathbf{I}\right) = \mathbf{0}. \quad (5.90)$$

The basic invariants of the function $\check{W}\left(N_i\right)$ are well-known, cf. Jemioło and Telega [273]. We write

$$\check{W}\left(N_i\right) = \check{W}\left(\mathrm{tr}\mathbf{E}, \mathrm{tr}\mathbf{E}^2, \mathrm{tr}\mathbf{E}^3, \mathrm{tr}\mathbf{E}\mathbf{M}, \mathrm{tr}\mathbf{E}^2\mathbf{M}\right), \quad i = 1,\ldots,5. \quad (5.91)$$

The quadratic approximation of the last function leads to the transversely isotropic Saint-Venant Kirchhoff stored energy function. We denote this stored energy function by W_{SVK}. We have

$$\check{W}\left(N_i\right) = W_{\mathrm{SVK}}\left(N_i\left(\mathbf{E}\right)\right) + O\left(\|\mathbf{E}\|^3\right), \quad i = 1,2,4,5. \quad (5.92)$$

Similarly to the isotropic Saint-Venant Kirchhoff model [83], the function W_{SVK} is assumed to be convex with respect to $\mathbf{E}$, i.e., the following fourth-order tensor

$$\frac{1}{4}\left(\frac{\partial^2 W_{SVK}\left(N_i\left(\mathbf{E}\right)\right)}{\partial \mathbf{E} \otimes \partial \mathbf{E}} + \frac{\partial^2 W_{SVK}\left(N_i\left(\mathbf{E}\right)\right)}{\partial \mathbf{E}^T \otimes \partial \mathbf{E}} + \frac{\partial^2 W_{SVK}\left(N_i\left(\mathbf{E}\right)\right)}{\partial \mathbf{E} \otimes \partial \mathbf{E}^T}\right.$$
$$\left. + \frac{\partial^2 W_{SVK}\left(N_i\left(\mathbf{E}\right)\right)}{\partial \mathbf{E}^T \otimes \partial \mathbf{E}^T}\right), \quad i = 1,2,4,5, \quad (5.93)$$

has to be positive definite. The stored energy function W_{SVK} is given by

$$\tilde{W}_{\text{SVK}}\left(\mathbf{E}\right) = W_{\text{SVK}}\left(N_i\left(\mathbf{E}\right)\right) = a_1\left(\text{tr}\mathbf{E}\right)^2 + a_2\text{tr}\mathbf{E}^2 + a_3\left(\text{tr}\mathbf{E}\mathbf{M}\right)^2$$
$$+ a_4\text{tr}\mathbf{E}\text{tr}\mathbf{E}\mathbf{M} + a_5\text{tr}\mathbf{E}^2\mathbf{M}. \quad (5.94)$$

Isotropic Saint-Venant Kirchhoff stored energy function is recovered for $a_1 = \lambda$, $a_2 = 2\mu$, $a_3 = a_4 = a_5 = 0$.

Substituting (5.94) into (5.88) we find the constitutive relationship for transversely isotropic Saint-Venant Kirchhoff material in the Lagrangian description. The reader is advised to find the classical relationship $\mathbf{T} = \mathbf{C}\mathbf{E} = (C_{ijkl}E_{kl})$ in arbitrary coordinates. We observe that, for incompressible, transversely isotropic Saint-Venant Kirchhoff materials only four material coefficients amongst $a_1, \ldots, a_5$ are independent.

5.3.2. New constitutive relationships for transversely isotropic hyperelastic materials. In this section we are going to present new models of transversely isotropic hyperelastic materials.

The stored energy function $\hat{W}$ for compressible materials can equivalently be written as follows:

$$\hat{W}\left(I_i\right) = \hat{W}\left(\text{tr}\mathbf{C}, \text{tr}\text{Cof}\,\mathbf{C}, \det \mathbf{C}, \text{tr}\left(\mathbf{M}\mathbf{C}\right), \text{tr}\left(\mathbf{M}\text{Cof}\,\mathbf{C}\right)\right), \quad (5.95)$$

where

$$\text{Cof}\,\mathbf{C} = \left(\det \mathbf{C}\right)\mathbf{C}^{-1}. \quad (5.96)$$

Hence

$$\mathbf{T} = \beta_1\mathbf{I} + 2\beta_2\left(I_2\mathbf{I} - \text{Cof}\,\mathbf{C}\right)\mathbf{C}^{-1} + \left(\beta_3 I_3 + \beta_5 I_5\right)\mathbf{C}^{-1} + \beta_4\mathbf{M}$$
$$- \beta_5 I_3\left(\mathbf{M}\mathbf{C}^{-1} + \mathbf{C}^{-1}\mathbf{M}\right). \quad (5.97)$$

The scalar functions β_i depend on I_i, $i = 1, \ldots, 5$.

In the Eulerian description we have

$$\boldsymbol{\sigma} = \left(\frac{I_2}{J}\beta_2 + J\beta_3 + \frac{I_5}{J}\beta_5 \right) \mathbf{I} + \frac{\beta_1}{J}\mathbf{B} - \beta_2 J\mathbf{B}^{-1} + \beta_4 \tilde{\mathbf{M}}$$
$$- J\beta_5 \left(\tilde{\mathbf{M}}B^{-1} + \mathbf{B}^{-1}\tilde{\mathbf{M}} \right), \quad (5.98)$$

where

$$\mathbf{B} = \mathbf{F}\mathbf{F}^T, \quad \tilde{\mathbf{M}} = \mathbf{F}\mathbf{M}\mathbf{F}^T. \quad (5.99)$$

According to $(5.99)_2$ the material fibres are rotated and stretched.

We now propose two new stored energy functions for transversely isotropic materials:

$$\hat{W}(I_i) = \sum_{i+j+k+l \neq 0} A_{ijkl} (I_1 - 3)^{a_i} (I_2 - 3)^{b_j} (I_4 - 1)^{c_k} (I_5 - 1)^{d_l} + \Gamma(I_3),$$
$$(5.100)$$

$$\hat{W}_1(I_i) = \sum_{i+j+k+l \neq 0} B_{ijkl} (I_1^{a_i} - 3) \left(I_2^{b_j} - 3 \right) (I_4^{c_k} - 1) \left(I_5^{d_l} - 1 \right) + \Gamma(I_3).$$
$$(5.101)$$

Here the coefficients A_{ijkl} and B_{ijkl} are not the components of tensors but merely material parameters. The coefficients a_i, b_j, c_k and d_l are additional parameters which have to be determined by using experimental data and nonlinear optimization. The function $\Gamma(I_3)$ with $\Gamma(1) = 0$ is convex and tends to infinity for I_3 tending to zero and infinity.

Having in mind applications and finite element algorithms (see the relevant references in Jemioło and Telega [277]), it is convenient to choose transversely isotropic invariants of $\mathbf{C}$ for incompressible materials in a manner enabling to formulate the constitutive relationships in a uniform manner. Recalling that $\mathbf{F} = \mathbf{R}\mathbf{U} = \mathbf{V}\mathbf{R}$ and performing the multiplicative decomposition of $\mathbf{F}$ on volumetric and distorsional parts we write

$$\mathbf{F} = J^{1/3}\bar{\mathbf{F}} = J^{1/3}\mathbf{R}\bar{\mathbf{U}} = J^{1/3}\bar{\mathbf{V}}\mathbf{R}, \quad \det\bar{\mathbf{F}} = \det\bar{\mathbf{U}} = \det\bar{\mathbf{V}} = 1. \quad (5.102)$$

The stored energy function is postulated as follows

$$\bar{W}(\bar{I}_j, J) = \bar{W} \left(\mathrm{tr}\bar{\mathbf{C}}, \mathrm{tr}\mathrm{Cof}\,\bar{\mathbf{C}}, \mathrm{tr}(\mathbf{M}\bar{\mathbf{C}}), \mathrm{tr}(\mathbf{M}\mathrm{Cof}\,\bar{\mathbf{C}}), J \right),$$
$$j = 1, \ldots, 4, \quad (5.103)$$

where

$$\bar{I}_1 = \operatorname{tr}\bar{\mathbf{B}} = \operatorname{tr}\bar{\mathbf{C}} = J^{-\frac{2}{3}}I_1, \quad I_1 = \operatorname{tr}\mathbf{C} = \operatorname{tr}\mathbf{B}, \quad \mathbf{B} = \mathbf{FF}^T,$$

$$\bar{I}_2 = \operatorname{tr}\bar{\mathbf{B}}^{-1} = \operatorname{tr}\bar{\mathbf{C}}^{-1} = J^{-\frac{4}{3}}I_2, \quad I_2 = \operatorname{tr}\operatorname{Cof}\mathbf{C} = \frac{1}{2}\left(I_1^2 - \operatorname{tr}\mathbf{C}^2\right),$$

$$\bar{I}_3 = \operatorname{tr}\left(\mathbf{M}\bar{\mathbf{C}}\right) = J^{-\frac{2}{3}}\operatorname{tr}\left(\mathbf{MC}\right) = J^{-\frac{2}{3}}\operatorname{tr}\tilde{\mathbf{M}}, \quad \operatorname{tr}\mathbf{C}^2 = \operatorname{tr}\mathbf{B}^2, \qquad (5.104)$$

$$\bar{I}_4 = \operatorname{tr}\left(\mathbf{M}\operatorname{Cof}\bar{\mathbf{C}}\right) = J^{-\frac{4}{3}}\operatorname{tr}\left(\mathbf{M}\operatorname{Cof}\mathbf{C}\right) = J^{-\frac{4}{3}}\operatorname{tr}\left(\operatorname{Cof}\tilde{\mathbf{M}}\right),$$

$$\tilde{\mathbf{M}} = \mathbf{FMF}^T.$$

The invariants I_1, I_2 and J^2 are the so-called basic invariants used for isotropic materials.

After standard calculations one can derive the corresponding constitutive relationships in the Lagrangian and Eulerian descriptions. Details are left to the reader.

We now propose two stored energy functions for incompressible and nearly incompressible transversely isotropic, hyperelastic materials.

$$\bar{W}\left(\bar{I}_j, J\right) = \sum_{i+j+k+l\neq 0} \bar{A}_{ijkl}\left(\bar{I}_1 - 3\right)^{\alpha_i}\left(\bar{I}_2 - 3\right)^{\beta_j}\left(\bar{I}_3 - 1\right)^{\gamma_k}\left(\bar{I}_4 - 1\right)^{\delta_l}$$
$$+ \bar{\Gamma}\left(J\right), \quad (5.105)$$

$$\bar{W}_1\left(\bar{I}_j, J\right) = \sum_{i+j+k+l\neq 0} \bar{B}_{ijkl}\left(\bar{I}_1^{\alpha_i} - 3\right)\left(\bar{I}_2^{\beta_j} - 3\right)\left(\bar{I}_3^{\gamma_k} - 1\right)\left(\bar{I}_4^{\delta_l} - 1\right)$$
$$+ \bar{\Gamma}\left(J\right). \quad (5.106)$$

For incompressible materials $\bar{\Gamma}\left(J\right) = \lambda\left(J - 1\right)$, where λ denotes the Lagrange multiplier associated with the condition $J = 1$.

For incompressible and nearly incompressible transversely isotropic materials like soft tissues one can use the following stored energy function,

$$\bar{W}_{NTF}\left(\bar{I}_i\right) = \sum_{j=1}^{N} \bar{a}_j\left(e^{\bar{\psi}_j\left(\bar{I}_i\right)} - 1\right) + \bar{\Gamma}\left(J\right), \quad \bar{a}_j > 0. \qquad (5.107)$$

In the case of incompressible materials and vanishing invariants $\bar{I}_3$ and $\bar{I}_4$, the relation (5.107) reduces to known models of incompressible soft tissues, cf. Section 5.2 of these Notes.

5.3.3. Generalization of isotropic Ogden's model to transversely isotropic hyperelastic materials. Our approach permits to extend the well-known Ogden's model [83, 426] to transversely isotropic materials. We propose the following stored energy function:

$$
\begin{aligned}
W_{\mathrm{OG}}\left(\mathbf{C}, \mathbf{M}\right) &= \sum_{k=1}^{K} \hat{a}_k \left(\mathrm{tr}\,\mathbf{C}^{\alpha_k} - 3\right) + \sum_{l=1}^{L} \hat{b}_l \left(\mathrm{tr}\,\mathrm{Cof}\,\mathbf{C}^{\beta_l} - 3\right) \\
&+ \sum_{m=1}^{M} \hat{c}_m \left[(\det \mathbf{C})^{\chi_m} - 1\right] + \sum_{n=1}^{N} \hat{d}_n \left(\mathrm{tr}\,\mathbf{M}\mathbf{C}^{\delta_m} - 1\right) \\
&+ \sum_{p=1}^{P} \hat{e}_p \left(\mathrm{tr}\,\mathbf{M}\mathrm{Cof}\,\mathbf{C}^{\varepsilon_p} - 1\right) + \sum_{q=1}^{Q} \hat{f}_q \left[\left(\mathrm{tr}\,\mathbf{M}\mathbf{C}^{\phi_q}\right)\left(\mathrm{tr}\,\mathbf{M}\mathbf{C}^{\varphi_q}\right) - 1\right] \\
&+ \sum_{s=1}^{S} \hat{g}_s \left[(\mathrm{tr}\,\mathbf{M}\mathrm{Cof}\,\mathbf{C}^{\gamma_s})(\mathrm{tr}\,\mathbf{M}\mathrm{Cof}\,\mathbf{C}^{\eta_s}) - 1\right]. \quad (5.108)
\end{aligned}
$$

Ogden's stored energy function for the isotropic hyperelastic materials is recovered provided that $\hat{d}_n = 0$, $\hat{e}_p = 0$, $\hat{f}_q = 0$, $\hat{g}_s = 0$, $n = 1, \ldots, N$; $p = 1, \ldots, P$; $q = 1, \ldots, Q$; $s = 1, \ldots, S$, see [83, 428, 431]. We observe that the stored energy function (5.108) is not, in general, polyconvex in Ball's sense. The notion of polyconvexity for isotropic, transversely isotropic and orthotropic materials will be introduced in Section 5.4.

One can easily demonstrate, similarly to the case of isotropy, that the strain energy (5.94) describing transversely isotropic materials, is not polyconvex. Moreover, this function is also not rank-one convex, cf. [83] for the case of isotropy. We observe that the convexity of the function (5.94) with respect to $\mathbf{E}$ renders the passage to the classical Hooke's law consequent. The elastic moduli a_i, $i = 1, \ldots, 5$, are the same as in the linear theory.

For incompressible isotropic Ogden's materials we have $\mathrm{tr}\,\mathrm{Cof}\,\bar{\mathbf{C}}^{\beta_l} = \mathrm{tr}\,\bar{\mathbf{C}}^{-\beta_l}$. Consequently, for such materials the stored energy function is simplified.

The reader is advised to derive general form of constitutive relationships in the Lagrangian and Eulerian descriptions, provided that the stored energy function is given by (5.108).

Let us provide an example of the stored energy function applicable to modelling incompressible and nearly incompressible transversely isotropic materials:

$$\bar{W}_{\mathrm{OG}}\left(\bar{\mathbf{C}}, J; \mathbf{M}\right) = \sum_{k=1}^{K} \bar{a}_k \left(\mathrm{tr}\bar{\mathbf{C}}^{\alpha_k} - 3\right) + \sum_{l=1}^{L} \bar{b}_l \left(\mathrm{tr}\mathrm{Cof}\,\dot{\bar{\mathbf{C}}}^{\beta_l} - 3\right)$$

$$+ \sum_{n=1}^{N} \bar{d}_n \left(\mathrm{tr}\mathbf{M}\bar{\mathbf{C}}^{\delta_n} - 1\right) + \sum_{p=1}^{P} \bar{e}_p \left(\mathrm{tr}\mathbf{M}\mathrm{Cof}\,\bar{\mathbf{C}}^{\varepsilon_p} - 1\right)$$

$$+ \sum_{q=1}^{Q} \bar{f}_q \left[\left(\mathrm{tr}\mathbf{M}\bar{\mathbf{C}}^{\phi_q}\right)\left(\mathrm{tr}\mathbf{M}\bar{\mathbf{C}}^{\varphi_q}\right) - 1\right]$$

$$+ \sum_{s=1}^{S} \bar{g}_s \left[\left(\mathrm{tr}\mathbf{M}\mathrm{Cof}\,\bar{\mathbf{C}}^{\gamma_s}\right)\left(\mathrm{tr}\mathbf{M}\mathrm{Cof}\,\bar{\mathbf{C}}^{\eta_s}\right) - 1\right] + \bar{\Gamma}\left(J\right). \quad (5.109)$$

5.3.4. Comments on insufficiency of some models of soft tissues.

Tong and Fung (1976) proposed the following stored energy function for soft tissues:

$$W\left(\mathbf{E}\right) = \alpha\left(\mathbf{E}\right) + a_0\beta\left(\mathbf{E}\right) e^{\psi(\mathbf{E})}, \quad (5.110)$$

where

$$\alpha(\mathbf{E}) = \frac{1}{2}\mathbf{E}\cdot\boldsymbol{\mathcal{A}}\cdot\mathbf{E}, \quad \beta(\mathbf{E}) = \frac{1}{2}\mathbf{E}\cdot\boldsymbol{\mathcal{B}}\cdot\mathbf{E},$$

$$\psi(\mathbf{E}) = \mathrm{tr}\left(\boldsymbol{\mathcal{A}}\mathbf{E}\right) + \frac{1}{2}\mathbf{E}\cdot\boldsymbol{\mathcal{C}}\cdot\mathbf{E} + \ldots. \quad (5.111)$$

Here $\boldsymbol{\mathcal{A}}$, $\boldsymbol{\mathcal{B}}$ and $\boldsymbol{\mathcal{C}}$ are fourth-order tensors which are determined by material parameters obtained from appropriate experiments. The function (5.110) is not, in general, polyconvex, and has too many material parameters with similar mechanical interpretation. Also, it can be shown that this model exhibits drawbacks similar to the hyperelastic model of Saint-Venant Kirchhoff; these have been discussed by Ciarlet [83]. To yield reasonable results, the function $\psi\left(\mathbf{E}\right)$ should involve tensors of order higher than four. The paper by Tong and Fung (1976) has nevertheless played a role in revealing the possibility of modelling nonlinear behaviour of soft tissues by means of exponential functions.

Our previous considerations suggest that a reasonable stored energy function for transversely isotropic hyperelastic soft tissues can be assumed in the following form

$$W\left(I_i\right) = \sum_{j=1}^{N} a_j \left(e^{\psi_j(I_i)} - 1\right), \quad a_j > 0. \quad (5.112)$$

We observe that if the functions ψ_j are postulated as being independent of material parameters, then a_j can be determined by using linear optimization

methods. Also, the function (5.112) is polyconvex provided that each function ψ_j is polyconvex.

Let us pass to the models proposed in Lin and Yin (1998) and May-Newman and Yin [375]. In the first of these papers the stored energy function is given by

$$W = C_1 \left(e^\psi - 1 \right), \tag{5.113}$$

where

$$\psi = C_2 \left(I_1 - 3 \right)^2 + C_3 \left(I_1 - 3 \right) \left(I_4 - 1 \right) + C_4 \left(I_4 - 1 \right)^2. \tag{5.114}$$

Here C_i, $i = 1, \ldots, 4$, are material coefficients and $C_1 > 0$. The constitutive equation in Eulerian description is expressed as follows:

$$\sigma = -p\mathbf{I} + 2\beta_1 \mathbf{B} + 2\beta_4 \tilde{\mathbf{M}}, \tag{5.115}$$

where p denotes the Lagrange multiplier (pressure) and

$$\beta_1 = \frac{\partial W}{\partial I_1} = C_1 e^\psi \left[2C_2 \left(I_1 - 3 \right) + C_3 \left(I_4 - 1 \right) \right],$$
$$\beta_4 = \frac{\partial W}{\partial I_4} = C_1 e^\psi \left[C_3 \left(I_1 - 3 \right) + 2C_4 \left(I_4 - 1 \right) \right].$$

Obviously the material is incompressible. The quadratic approximation of (5.113) yields

$$W = C_1 C_2 (\mathrm{tr}\mathbf{E})^2 + C_1 C_3 \mathrm{tr}\mathbf{E}\mathrm{tr}\mathbf{E}\mathbf{M} + C_1 C_4 (\mathrm{tr}\mathbf{E}\mathbf{M})^2 + O\left(\|\mathbf{E}\|^3 \right). \tag{5.116}$$

Function (5.116) does not contain a sufficient number of material parameters to predict mechanical properties of incompressible, transversely isotropic material in the range of relatively small deformations, in the case of 3D problems. From the representation theory of so-called plane (two-dimensional) tensor function follows that function (5.116) is an irreducible quadratic function of 2D tensor $\mathbf{E}$, cf. [273]. On the basis of material parameters given in Liu and Yin (1998) for rabbit myocardium Jemioło and Telega (2001) found, among others, the level sets depicted in Figs. 55, 56, and the stored energy function for one-dimensional deformations presented in Fig. 57. To construct these figures these authors exploited the data given in Lin and Yin (1998) and gathered in Table 6. The scatter of the reported values is significant. Figure 57 shows that for relatively small values of stretches the stored energy function, constructed in Liu and Yin (1998), may even assume negative values. We conclude that the constitutive modelling proposed in Liu and Yin (1998) is not sufficiently accurate.
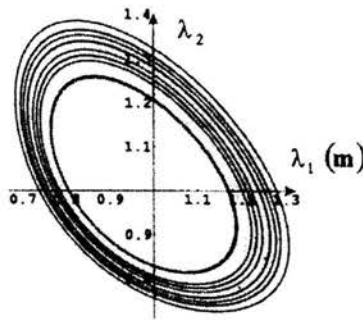
FIGURE 55. Comparison of level sets for the stored energy function (5.113), (5.114) (dotted curves) with its quadratic approximation (5.116) (continuous curves) in the case of averaged values for 7 samples studied in Lin and Yin (1998). The curves correspond to two-dimensional tests in the principal axes of anisotropy, after Jemioło and Telega (2001).
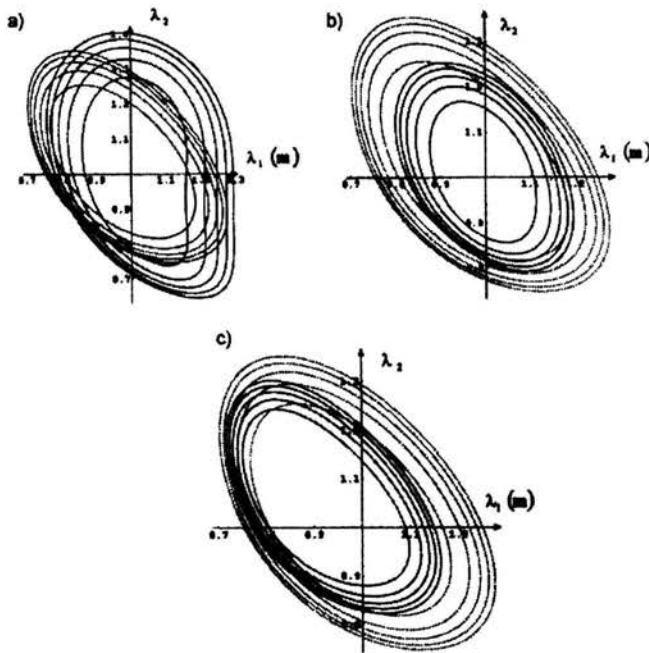
FIGURE 56. Level sets for three samples and the stored energy function (5.113), (5.114); λ_1, λ_2 are principal stretches (two-dimensional tests) and the samples orientation coincides with the unit vector **m** describing the orientation of fibres: a) sample 1, b) sample 2, c) sample 3. The dotted lines correspond to 'averaged' material parameters, after Jemioło and Telega (2001).
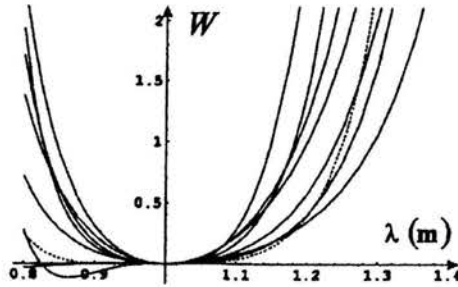
FIGURE 57. The stored energy function (5.113) with ψ given by (5.114) and dotted line as previously for one-dimensional deformation. For the sample 3 the function W assumes negative values in a certain range of compression (inadmissible form of W), after Jemioło and Telega (2001).

TABLE 6. Material parameters of the stored energy function (5.113) with ψ specified by (5.114) according to Liu and Yin (1998) (rabbit myocardium). The material parameters appearing in (5.116) are also given, after Jemioło and Telega (2001).

No.	C_1	C_2	C_3	C_4	C_1C_2	C_1C_3	C_1C_4
1.	1.01	3.05	-2.24	1.92	3.0805	-2.2624	1.212
2.	2.42	12.13	0.63	1.05	29.3546	1.5246	2.541
3.	9.86	4.62	2.37	0.09	45.5532	23.3682	0.8875
4.	2.92	3.21	-2.60	2.01	9.3732	-7.592	5.8692
5.	2.62	2.40	-0.89	2.01	6.288	-2.3318	5.502
6.	1.67	1.70	1.90	0.38	2.839	3.173	0.6346
7.	6.85	2.88	-0.76	0.38	19.728	-5.206	2.603
8. (averaged)	1.05	9.13	2.32	0.08	9.5865	2.436	0.084

Similar conclusion applies to the model studied in [375], where

$$W = C_0 \left(e^{\tilde{\psi}} - 1 \right) \tag{5.117}$$

and

$$\tilde{\psi} = C_1 \left(I_1 - 3 \right)^2 + C_2 \left(I - 1 \right)^4, \quad I = \sqrt{I_4} = \sqrt{\mathrm{tr} \mathbf{CM}} = \sqrt{\mathbf{m} \cdot \mathbf{C} \cdot \mathbf{m}}. \tag{5.118}$$

The hyperelastic potential (5.117) was used to model the valve tissue of pig, which provides a good substitute for similar human tissue. The material parameters, taken from [375], are gathered in Table 7. Now the material functions involved in constitutive relationship (5.115) have the following form

$$\beta_1 = \frac{\partial W}{\partial I_1} = 2C_0 C_1 e^{\tilde{\psi}} \left(I_1 - 3 \right), \quad \beta_4 = \frac{\partial W}{\partial I_4} = \frac{2C_0 C_2}{I} e^{\tilde{\psi}} \left(I - 1 \right)^3. \tag{5.119}$$

TABLE 7. Material parameters of the stored energy function (5.117), (5.118)$_1$ for the valve tissue of pig, according to May-Newman and Yin [375]. The material parameters appearing in (5.116) are also given, after Jemioło and Telega (2001).

No.	C_0 [kPa]	C_1	C_2	$C_0 C_1$ [kPa]	$C_0 C_2$ [kPa]
1	2	3	4	5	6
1.	1.010	2.59	1376.9	2.61590	1514.59
2.	0.079	1.25	1320.6	0.09875	104.3274
3.	0.181	7.01	626.5	1.26881	113.3965
4.	0.214	4.90	1602.9	1.04860	343.0206
5.	0.105	5.23	1991.6	0.54915	209.118
6.	0.203	1.76	833.0	0.35728	169.099
7.	0.053	6.31	1943.2	0.33443	102.9896
8.	2.171	2.19	1408.8	4.75449	3058.5048
9. (averaged)	0.399	4.325	1446.5	1.725675	577.1535

We observe that even for relatively large deformations the stored energy function (5.117) with $\tilde{\psi}$ specified by (5.118)$_1$ can be approximated by the following polynomial in I_1 and I

$$ W = C_0 C_1 \left(\mathrm{tr}\mathbf{E} \right)^2 + C_0 C_2 \left(\sqrt{(\mathrm{tr}\mathbf{E}M) - 1} - 1 \right)^4 . \tag{5.120} $$

Here the independent material parameters $C_0 C_1$ and $C_0 C_2$ can be determined by using linear optimization methods. For the model (5.117) and (5.118)$_1$ the quadratic approximation with respect to the measure $\mathbf{E}$ is useless since it yields an isotropic stored energy function with the first term appearing in (5.120). Figure 58 depicts typical relations between stresses and deformations in one-dimensional test.

In the paper [618] the following stored energy function has been implemented in FEM

$$ \bar{W} \left(\bar{I}_1, \bar{I}_2, \bar{I}_3 \right) = C_1 \left(\bar{I}_1 - 3 \right) + C_2 \left(\bar{I}_2 - 3 \right) + C_3 \left[e^{(\bar{I}_3 - 1)} - \bar{I}_3 \right] , \tag{5.121} $$

where C_1, C_2 and C_3 are material coefficients whilst the invariants $\bar{I}_i$, $i = 1, 2, 3$, are defined by (5.104). This model constitutes a simple generalization of the well-known Mooney-Rivlin potential [83, 431] the latter being valid for incompressible isotropic materials. Since the formula (5.121) does not incorporate the invariant $\bar{I}_4$ and there is no coupling between the invariants $\bar{I}_1$ and $\bar{I}_3$, therefore the model (5.121) cannot properly describe incompressible transversely anisotropic materials in the range of small deformations. It seems that the stored energy function (5.121) should be confined to plane problems. Weiss et al. [618] devised their model to describe the mechanical behaviour of tendon and cartilage. We observe that from the point of FEM the paper
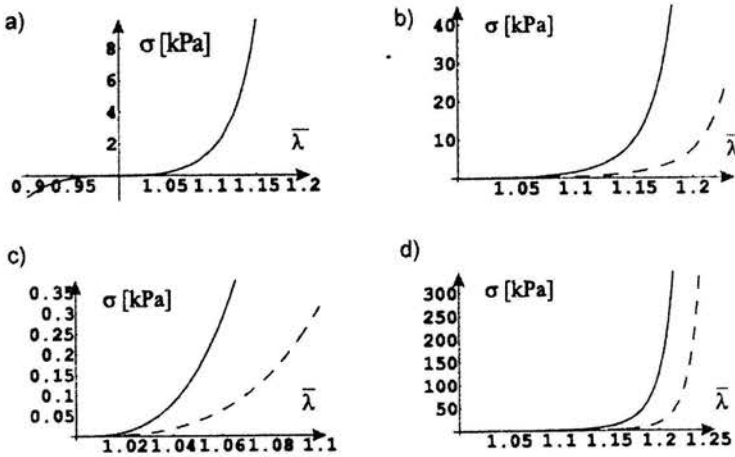
FIGURE 58. Cauchy stress-elongation relationships for the one-dimensional extension; the stored energy function is given by (5.117), (5.119). The material parameters are taken from Table 7: continuous line in (a) – (d) after row 9, (b) - sample 3 (dotted line), (c) and (d) – sample 2 (dotted line). The sample orientation coincides with $\mathbf{m}$

[618] constitutes a first attempt of numerical implementation of the model describing transversely isotropic, hyperelastic and incompressible materials.

5.4. Orthotropy

In the case of orthotropy we have three privileged directions, say $\mathbf{m}_i$, $i = 1, 2, 3$. Let us assume that $\{\mathbf{m}_i\}$ constitute an orthonormal privileged frame. The orthonormal vectors $\mathbf{m}_i$ may depend upon the location (fibres are not necessarily straight). Consider the three tensors

$$\mathbf{M}_1 = \mathbf{m}_1 \otimes \mathbf{m}_1, \quad \mathbf{M}_2 = \mathbf{m}_2 \otimes \mathbf{m}_2, \quad \mathbf{M}_3 = \mathbf{m}_3 \otimes \mathbf{m}_3. \tag{5.122}$$

We say that $\mathbf{M}_i$, $i = 1, 2, 3$, are the *structural tensors* for orthotropy, cf. Boehler [49], Jemioło and Telega [273] and Zheng [650].

Let $\mathbf{A}$ be a symmetric, second-order tensor, the so-called *agency*. For instance $\mathbf{A}$ may represent the right Cauchy-Green strain tensor $\mathbf{C}$ or the Green strain tensor $\mathbf{E}$.

Since

$$\mathbf{M}_1 + \mathbf{M}_2 + \mathbf{M}_3 = \mathbf{I}, \tag{5.123}$$

therefore the general scalar orthotropic function is a function of the following invariants:

$$\mathrm{tr}\mathbf{A}, \ \mathrm{tr}\mathbf{A}^2, \ \mathrm{tr}\mathbf{A}^3, \ \mathrm{tr}\mathbf{M}_1\mathbf{A}, \ \mathrm{tr}\mathbf{M}_1\mathbf{A}^2, \ \mathrm{tr}\mathbf{M}_2\mathbf{A}, \ \mathrm{tr}\mathbf{M}_2\mathbf{A}^2. \tag{5.124}$$

We observe that the first three invariants are the same as in the case of isotropy.

An equivalent manner of the formulation of orthotropic scalar and tensor functions consists in using so-called fabric tensors, cf. Cowin [97], Jemioło and Telega [274, 275, 280], Shillor et al. [516].

Having at our disposal the strain energy function of the invariants (5.124) one can easily derive the relevant constitutive equations both in the case of compressible and incompressible materials. It suffices to use the general rules outlined in Section 5.

An alternative approach to the formulation of constitutive equations for transversely isotropic materials and orthotropic biotissues was proposed by Crisione et al. [105, 106]. In essence, in the first paper a novel set of 5 strain invariants for transversely isotropic materials has been proposed through analysis of physical attributes of deformation. The strain attributes are to be distinguished from strain invariants. Central to the proposed approach is the identification of six rotation invariant scalars α_{1-6} that define the strain in materials that have one family of parallel fibres arranged in laminae (like in myocardium), cf. Criscione et al. [106]. In the last paper orthotropic behaviour (two families of fibres), has also been considered. Advantages of this alternative approach, by no means algebraically simple, remain to be proved. Moreover it seems that the criticism presented in Appendix A of the paper [106], and pertaining to orthotropy, is not justified. These authors overlook the fact that relations between invariants and tensor components are nonlinear and, in general there is no one-to-one correspondence between these two sets of quantities.

Remark 3. Consider the situation in which there are two distinct preferred directions in the reference configuration. Let $\mathbf{m}_1$ and $\mathbf{m}_2$ denote the associated unit vectors, not necessarily orthogonal. The strain energy then depends on the following invariants, cf. Boehler [49], Jemioło and Telega [273]

$$\text{tr}\mathbf{C}, \ \text{tr}\mathbf{C}^2, \ \text{tr}\mathbf{C}^3, \ \mathbf{m}_1 \cdot \mathbf{C}\mathbf{m}_1, \ \mathbf{m}_1 \cdot \mathbf{C}^2\mathbf{m}_1,$$

$$\mathbf{m}_2 \cdot \mathbf{C}\mathbf{m}_2, \ \mathbf{m}_2 \cdot \mathbf{C}^2\mathbf{m}_2, \ \mathbf{m}_1 \cdot \mathbf{C}\mathbf{m}_2. \quad (5.125)$$

We observe that the energy also depends explicitly on the angle between the directions, as determined by the product $\mathbf{m}_1 \cdot \mathbf{m}_2$ (independent of the deformation). The term $\mathbf{m}_1 \cdot \mathbf{C}^2\mathbf{m}_2$ is absent since it can be shown that it depends on the other invariants and on $\mathbf{m}_1 \cdot \mathbf{m}_2$. The invariant $\mathbf{m}_1 \cdot \mathbf{C}\mathbf{m}_2$ is not changed with respect to the reversal of $\mathbf{m}_1$ or $\mathbf{m}_2$ separately but it can be made so by multiplying by $\mathbf{m}_1 \cdot \mathbf{m}_2$

The reader is advised to derive the general form of constitutive relationships for compressible and incompressible materials, cf. Ogden [431, 432].

5.5. Polyconvexity of stored energy function: isotropy and anisotropy

It seems that mathematical properties of stored energy function used in the modelling of soft tissues have not been discussed. 'Good' energy function should exhibit certain mathematical properties, being in fact a generalisation of convexity. Convexity is typical for materials undergoing small deformations. In contrast, it is well known that the stored energy function $W(\mathbf{X}, \mathbf{F})$ characterizing finitely deformed materials cannot be convex, cf. Ball (1977), Ciarlet [83]. For other notions like quasiconvexity and rank-one convexity, more general than polyconvexity the reader is referred to Dacorogna [110] and Ponte Castañeda et al. [453].

Let us briefly discuss the polyconvexity introduced by Ball (1977). For generalizations and more detailed treatment the reader is referred to Ciarlet [83] and Dacorogna [110].

A stored energy function $W : \Omega \times \mathbb{M}^3_+ \to \mathbb{R}$ is *polyconvex* if for each $\mathbf{X} \in \bar\Omega$, there exists a convex function

$$g(\mathbf{X}, \cdot, \cdot, \cdot) : \mathbb{M}^3 \times \mathbb{M}^3 \times (0, +\infty) \to \mathbb{R}$$

such that

$$W(\mathbf{X}, \mathbf{F}) = g(\mathbf{X}, \mathbf{F}, \operatorname{Cof} \mathbf{F}, \det \mathbf{F}), \qquad (5.126)$$

for each $\mathbf{F} \in \mathbb{M}^3_+$. Here $\mathbb{M}^3$ is the set of all real square matrices of order 3, $\mathbb{M}^3_+ = \{\mathbf{A} \in \mathbb{M} | \det \mathbf{A} > 0\}$, $\operatorname{Cof} \mathbf{A}$ denotes the cofactor matrix of $\mathbf{A}$ ($\operatorname{Cof} \mathbf{A} = (\det \mathbf{A})\mathbf{A}^{-T}$ if $\mathbf{A}$ is invertible). Sometimes instead of $\operatorname{Cof} \mathbf{F}$ its transpose, the adjugate matrix $\operatorname{adj} \mathbf{F}$ is used. We recall that $\mathbb{R} = \mathbb{R}^1$ stands for the set of real numbers and $\bar\Omega$ denotes the closure of a domain occupied by a body, like say tissue or organ.

Remark 4. Since the convex set $\mathbb{M}^3 \times \mathbb{M}^3 \times (0, +\infty)$ is open in $\mathbb{M}^3 \times \mathbb{M}^3 \times \mathbb{R}$, the convex function $g(\mathbf{X}, \cdot, \cdot, \cdot) : \mathbb{M}^3 \times \mathbb{M}^3 \times (0, +\infty) \to \mathbb{R}$ is continuous, Ekeland and Temam [155]. On the other hand, the function

$$\bar g : (\mathbf{X}, \mathbf{F}, \mathbf{H}, \delta) \in \mathbb{M}^3 \times \mathbb{M}^3 \times \mathbb{R} \to \begin{cases} g(\mathbf{X}, \mathbf{F}, \mathbf{H}, \delta) & \text{if } \delta > 0, \\ +\infty & \text{if } \delta \le 0, \end{cases}$$

with values in the set $\mathbb{R} \cup \{+\infty\}$, is convex but it need not be continuous for $\delta = 0$, unless the function g is that, cf. Ciarlet [83, p.175]

$$\left. \begin{array}{c} (\mathbf{F}_k, \mathbf{H}_k) \to (\mathbf{F}, \mathbf{H}) \text{ in } \mathbb{M}^3 \\ \delta_k \to 0^+ \end{array} \right\} \Rightarrow g(\mathbf{X}, \mathbf{F}_k, \mathbf{H}_k, \delta_k) \to +\infty$$

as $k \to \infty$. Note, however, that this property implies, but is not necessarily implied by, the property $W(\mathbf{X}, \mathbf{F}) \to +\infty$ as $\det \mathbf{F} \to 0^+$.   □

An important example of polyconvex stored energy function is provided by

$$W(\mathbf{F}) = \sum_{i=1}^{M} a_i \mathrm{tr} \mathbf{C}^{\gamma_i/2} + \sum_{j=1}^{N} b_j \mathrm{tr}(\mathrm{Cof}\,\mathbf{C})^{\delta_j/2} + h(\det \mathbf{F}), \qquad (5.127)$$

where $\mathbf{C} = \mathbf{F}^T\mathbf{F}$, $a_i > 0$, $\gamma_i > 1$, $b_j > 0$, $\delta_j \geq 1$, and $h : (0, +\infty) \to \mathbb{R}$ is a convex function satisfying $h(\delta) \to +\infty$ as $\delta \to 0^+$ and subjected to suitable growth conditions as $\delta \to +\infty$. Such stored energy function was proposed by Ogden in 1972, cf. Ball (1977), Ciarlet [83], Ogden [431, 432]. Obviously, the function W may depend on $\mathbf{X}$ (for inhomogeneous materials like biotissues). The exponential (or logarithmic) stored energy functions, often used in constitutive modelling of soft tissues, may be approximated by function of type (5.127).

The reader interested in existence theorems for various boundary value problems of isotropic finite elasticity in the case of polyconvex stored energy functions is referred to Ball (1977) and Ciarlet [83], cf. also Dacorogna [110].

Remark 5. Isotropic Saint-Venant Kirchhoff stored energy function.
An isotropic material is a Saint-Venant Kirchhoff material if its response function for the second (symmetric) Piola-Kirchhoff stress has the following form

$$\mathbf{T} = \lambda(\mathrm{tr}\mathbf{E})\mathbf{I} + 2\mu\mathbf{E}, \qquad (5.128)$$

where λ and μ are Lamé constants, cf. Ciarlet [83]. Though relation (5.128) is linear, yet $\mathbf{E}(\mathbf{u})$ is nonlinear. We recall that

$$\mathbf{E}(\mathbf{u}) = \frac{1}{2}(\nabla\mathbf{u} + \nabla\mathbf{u}^T + \nabla\mathbf{u}^T\nabla\mathbf{u}).$$

In fact, Saint-Venant Kirchhoff material belongs to the simplest among the nonlinear models, and is quite popular in computations.

It can easily be shown that the inverse relation is of the form

$$\mathbf{E} = \frac{\lambda}{2\mu(3\lambda + 2\mu)}(\mathrm{tr}\mathbf{T})\mathbf{I} + \frac{1}{2\mu}\mathbf{T}. \qquad (5.129)$$

As usual, $\mathbf{I} = (\delta_{ij})$.

The stored energy function for the Saint-Venant Kirchhoff material takes the form

$$\mathcal{W}(\mathbf{E}) = \frac{\lambda}{2}(\mathrm{tr}\mathbf{E})^2 + \mu\mathrm{tr}\mathbf{E}^2. \qquad (5.130)$$

It can be shown that the function

$$\tilde{\mathcal{W}}(\mathbf{F}) = \mathcal{W}(\mathbf{E}) \qquad (5.131)$$

is neither polyconvex, nor quasiconvex, nor rank-one convex, cf. Ciarlet [83]. This surprising result means that the stored energy function $\tilde{\mathcal{W}}$ falls out of the region of functions with now well-understood mathematical behaviour.

It is evident (cf. Section 5.3) that near a stress-free state the constitutive equation of an isotropic nonlinear material should necessarily be of the form

$$\mathbf{T} = \lambda(\mathrm{tr}\mathbf{E})\mathbf{I} + 2\mu(\mathbf{E}) + o(\mathbf{E}),$$

obtained by a quadratic approximation, cf. Ciarlet [83].

In Section 7, studying passive and active stresses, the function of type (5.130) will intervene in the experimental stored energy function.

Transverse isotropy

The transversely isotropic strain energy $\mathcal{W}(\mathbf{X}, \mathbf{F}) = \mathcal{W}(\mathbf{X}, \mathbf{C}; \mathbf{M})$ is *polyconvex* provided that for each $\mathbf{X} \in \bar{\Omega}$, there exists a *convex function*:

$$g(\mathbf{X}, \cdot, \cdot, \cdot, \cdot, \cdot) : \mathbb{M}^3 \times \mathbb{M}^3 \times \mathbb{M}^3 \times \mathbb{M}^3 \times (0, +\infty) \to \mathbb{R}$$

such that

$$\mathcal{W}(\mathbf{X}, \mathbf{F}) = g(\mathbf{X}, \mathbf{F}, \mathrm{Cof}\,\mathbf{F}, \mathbf{MF}, \mathbf{MCof}\,\mathbf{F}, \det\mathbf{F}), \qquad (5.132)$$

for all $\mathbf{F} \in \mathbb{M}_+^3 = \{\mathbf{F} \in \mathbb{M}_+^3 | \det\mathbf{F} > 0\}$. Obviously $\mathbf{MF}$ denotes the projection of $\mathbf{F}$ by the structural tensor $\mathbf{M}$, and similarly for $\mathbf{MCof}\,\mathbf{F}$. Hence it suffices to define the function g appearing in (5.132) on $\mathbb{M}^3 \times \mathbb{M}^3 \times \mathbf{M}\mathbb{M}^3 \times$ $\times\mathbf{M}\mathbb{M}^3 \times (0, +\infty)$. Obviously, the operation Cof has to be performed prior to projection by $\mathbf{M}$ in the fourth term of the Cartesian product.

Example 5.

(i) Compressible transversely isotropic Mooney-Rivlin material:

$$\mathcal{W}(\mathbf{X}, \mathbf{F}) = W(\mathbf{X}, \mathbf{C}; \mathbf{M}) = a||\mathbf{F}||^2 + b||\mathrm{Cof}\,\mathbf{F}||^2 + c||\mathbf{MF}||^\alpha$$
$$+ d||\mathbf{MCof}\,\mathbf{F}||^\beta + h(\det\mathbf{F}), \quad (5.133)$$

where $a > 0$, $b > 0$, $c > 0$, $d > 0$ may depend on $\mathbf{X} \in \bar{\Omega}$, and $\alpha \geq 2$, $\beta \geq 2$, whilst the convex function h possesses the properties specified earlier; $||\mathbf{F}||^2 = \mathrm{tr}\mathbf{F}^T\mathbf{F} = \mathrm{tr}\mathbf{C}$.

(ii) Compressible transversely isotropic Ogden material:

$$\mathcal{W}_{OG}(\mathbf{X}, \mathbf{F}) = W_1(\mathbf{X}, \mathbf{C}) + W_2(\mathbf{X}, \mathbf{C}; \mathbf{M}),$$

where $W_1(\mathbf{X}, \mathbf{C})$ (isotropic part) is given by

$$W_1(\mathbf{X}, \mathbf{F}) = \sum_{i=1}^M a_i \mathrm{tr}\mathbf{C}^{\gamma_i/2} + \sum_{j=1}^N b_j \mathrm{tr}(\mathrm{Cof}\,\mathbf{C})^{\delta_j/2} + h(\det\mathbf{F}) \quad (5.134)$$

with $a_i > 0$, $\gamma_i \geq 1$, $b_j > 0$, $\delta_j \geq 1$. Obviously the material coefficients and the function h may depend on $\mathbf{X} \in \bar{\Omega}$. A simple example of transversely isotropic part $\mathcal{W}_2(\mathbf{X}, \mathbf{F}) = W_2(\mathbf{X}, \mathbf{C}; \mathbf{M})$ is provided by

$$\mathcal{W}_2(\mathbf{X}, \mathbf{F}) = c||\mathbf{MF}||^\alpha + d||\mathbf{MCof}\,\mathbf{F}||^\beta \qquad (5.135)$$

with $c > 0$, $d > 0$, $\alpha \geq 2$, $\beta \geq 2$.

Polyconvex orthotropic strain energy function

The stored energy function

$$\mathcal{W}(\mathbf{X}, \mathbf{F}) = W(\mathbf{X}, \mathbf{C}; \mathbf{M}_1, \mathbf{M}_2),$$

is polyconvex provided that for each $\mathbf{X} \in \bar{\Omega}$, there exists a convex function

$$g(\mathbf{X}, \cdot, \cdot, \cdot, \cdot, \cdot, \cdot, \cdot) : \mathbb{M}^3 \times \mathbb{M}^3 \times \mathbb{M}^3 \times \mathbb{M}^3 \times \mathbb{M}^3 \times \mathbb{M}^3 \times (0, +\infty) \to \mathbb{R}$$

such that

$$\mathcal{W}(\mathbf{X}, \mathbf{F}) = g(\mathbf{X}, \mathbf{F}, \mathrm{Cof}\,\mathbf{F}, \mathbf{M}_1\mathbf{F}, \mathbf{M}_1\mathrm{Cof}\,\mathbf{F}, \mathbf{M}_2\mathbf{F}, \mathbf{M}_2\mathrm{Cof}\,\mathbf{F}, \det\mathbf{F}), \quad (5.136)$$

for all $\mathbf{F} \in \mathbb{M}_+^3$.

Comments provided earlier for polyconvex transversely isotropic stored energy function can easily be extended to orthotropy by simply taking $\mathbf{M}_\alpha\mathbf{F}$ and $\mathbf{M}_\alpha\mathrm{Cof}\,\mathbf{F}$ ($\alpha = 1, 2$) instead of $\mathbf{MF}$ and $\mathbf{MCof}\,\mathbf{F}$.

Example 6.

(i) Compressible orthotropic Mooney-Rivlin material:

$$\begin{aligned}
\mathcal{W}(\mathbf{X}, \mathbf{F}) = W(\mathbf{X}, \mathbf{C}; \mathbf{M}_1, \mathbf{M}_2) &= a||\mathbf{F}||^2 + b||\mathrm{Cof}\,\mathbf{F}||^2 \\
&+ c_1||\mathbf{M}_1\mathbf{F}||^{\alpha_1} + d_1||\mathbf{M}_1\mathrm{Cof}\,\mathbf{F}||^{\beta_1} \\
&+ c_2||\mathbf{M}_2\mathbf{F}||^{\alpha_2} + d_2||\mathbf{M}_2\mathrm{Cof}\,\mathbf{F}||^{\beta_2} + h(\det\mathbf{F}), \quad (5.137)
\end{aligned}$$

with $a > 0$, $b > 0$, $c_1 > 0$, $c_2 > 0$, $d_1 > 0$, c_2, $\alpha_1 \geq 2$, $\alpha_2 \geq 2$, $\beta_1 \geq 2$, $\beta_2 \geq 2$, and h as previously.

(ii) Compressible orthotropic Ogden material:

$$\mathcal{W}_{OG}(\mathbf{X}, \mathbf{F}) = W_1(\mathbf{X}, \mathbf{C}) + W_2(\mathbf{X}, \mathbf{C}; \mathbf{M}_\alpha).$$

The isotropic part is given by (5.134). A simple example of the orthotropic part is provided by

$$\begin{aligned}
\mathcal{W}_2(\mathbf{X}, \mathbf{F}) = W_2(\mathbf{X}, \mathbf{C}; \mathbf{M}_\alpha) &= a_1||\mathbf{M}_1\mathbf{F}||^{\alpha_1} + b_1||\mathbf{M}_1\mathrm{Cof}\,\mathbf{F}||^{\beta_1} \\
&+ a_2||\mathbf{M}_2\mathbf{F}||^{\alpha_2} + b_2||\mathbf{M}_2\mathrm{Cof}\,\mathbf{F}||^{\beta_2} \quad (5.138)
\end{aligned}$$

with $a_\alpha > 0$, $b_\alpha > 0$, $\alpha_1 \geq 2$, $\alpha_2 \geq 2$, $\beta_1 \geq 2$, $\beta_2 \geq 2$.

Remark 6. For incompressible materials (both isotropic and anisotropic) one has to delete the function h and take into account the incompressibility condition $\det \mathbf{F} = 1$; for instance by introducing Lagrange multiplier.

6. Effective properties of soft tissues

As we already know, soft tissues exhibit complete hierarchical structure. From the theoretical point of view, one could probably derive macroscopic equations by using the so-called reiterated homogenisation cf. Braides and Defranceschi [52], Telega and Bielski [568] and references cited therein. Each level is then characterised by a small parameter. Obviously, lower level is characterised by a smaller parameter. Consider, for simplicity, two scales characterised by $\varepsilon_1(\varepsilon) = \varepsilon$ and $\varepsilon_2(\varepsilon) = \varepsilon^2$, $\varepsilon > 0$. Then we have

$$\lim_{\varepsilon \to 0} \varepsilon_2/\varepsilon_1 = 0. \tag{6.1}$$

The principle of type (6.1) called 'the separation of scales', can readily be extended to tissues with multilevel architecture. It suffices to imagine the microstructure of skeletal muscle or cartilage. For both these tissues scales range from nanometers to centimeters. Practically, however, we still cannot derive, usually nonlinear, equations describing macroscopic behaviour of soft tissues starting from the lowest level. Therefore simplifications are needed.

In this section we intend to outline application of micromechanical modelling to soft tissues. It seems that most popular is the approach typical for mixture theory, cf. also the lectures by Huyghe in this volume. From the point of view of mathematical homogenisation (Braides and Defranceschi [52], Cioranescu and Donato [84], Telega [567]), the mixture theory has its disadvantages. For instance, within the framework of this theory it is not easy to cope with fluctuations and derivation of macroscopic constitutive equations. Homogenisation methods lead naturally to macroscopic relationships, though still one has to solve the so-called basic cell problem. Except one-dimensional cases, the last problem can only be solved approximately. Very popular are also the methods allowing to find bounds, cf. the relevant papers contained in [453].

6.1. Orientational averaging to constitutive modelling of fibrous connective tissues

In 1983 Lanir [327] proposed a method which is nothing else as 'orientational averaging'. For a systematic presentation of that method and its applications to elastic and inelastic composites the reader is referred to the

book by Lagzdiņš et al. [322]. In the present section we shall briefly discuss the approach devised by Lanir [327] and available biomechanical applications. Lanir [327] defines fibrous tissues as materials consisting of several networks of different types of fibres embedded in a fluid matrix. The matrix is bound to the fibres. The stress vector and the stress tensor are defined as their mean values; yet in Lanir's paper [327] this notion remains somewhat intuitive (from the point of view of the probability theory). Alternatively the stress vector can be defined as the total load that must be applied on a unit area to counteract the sum of tractions of all the tissue components crossing it. This stress vector is associated with appropriate stress tensor components in a general coordinate system (ξ_i), $i = 1, 2, 3$.

Structure is defined in term of the fibre orientation in the tissue space. To each type of fibre K a *density distribution* function $R_K(\mathbf{m})$ is associated (in general a random quantity), where $\mathbf{m}$ is a unit vector tangent to the fibre. Thus $R_K(\mathbf{m}) \cdot \Delta\Omega$ is the volumetric fraction of fibres of type K which are oriented in the direction $\mathbf{m}$ and occupy a spatial angle $\Delta\Omega$.

Lanir [327] considered first the case of homogeneous tissue with straight fibres subjected to homogeneous strain. An extension to cases of nonhomogeneous tissues, undulated fibres and nonhomogeneous strains is then straightforward.

General assumptions are as follows:

 (i) Each fibre is thin and perfectly flexible. It has no compressive strength and if contracted will buckle under zero load.

 (ii) The effect of the matrix flow during deformation is that of hydrostatic pressure. The flow stops at the point when the forces binding the matrix counteract the effect of the pressure.

(iii) Each fibre is subjected to uniaxial strain which is the tensorial transformation of the overall strain in the direction of the fibre (affine transformation).

Kinematics of tissue considered is formulated in a general coordinate system (ξ^i), $i = 1, 2, 3$. Then we have, cf. Green and Adkins [199].

$$\mathbf{X} = \hat{\mathbf{X}}(\xi^i, t). \tag{6.2}$$

The metric tensors in the undeformed and deformed configurations are given by

$$G_{ij} = \left(\partial X_n/\partial\xi^i\right)\left(\partial X_n/\partial\xi^j\right), \tag{6.3}$$

$$g_{ij} = \left(\partial x_n/\partial\xi^i\right)\left(\partial x_n/\partial\xi^j\right), \tag{6.4}$$

respectively. Then $J = (g/G)^{1/2}$, where g and G are the determinants of (g_{ij}) and (G_{ij}) respectively. The covariant strain tensor γ_{ij} which is associated

with the squared difference of distance between each two close points in the body due to deformation is defined by

$$\gamma_{ij} = (g_{ij} - G_{ij})/2. \tag{6.5}$$

We observe that the notation (g_{ij}) and (G_{ij}) is the reverse to the one used by Green and Adkins [199] and Lanir [327]. Our notation is usually used in solid mechanics.

If the strain is referred to rectangular coordinates then $(G_{ij}) = (\delta_{ij})$ and $\gamma_{ij} = E_{ij}$.

Let us denote the strain energy function of the fibres per unit of unde-formed volume by $W(\gamma_{ij})$. The contravariant stress components in general coordinates $(\xi^i) = (\xi_i)$ are given by

$$\tau_{\text{G-A}}^{ij} = J^{-1} \partial W / \partial \gamma_{ij} + p g^{ij}, \tag{6.6}$$

where p is the hydrostatic pressure associated with the matrix. Green and Adkins [199], and consequently Lanir, use (τ^{ij}) for the stress tensor appearing in (6.6) and measured per unit area of the deformed body. We have previously used (τ_{ij}) for the Kirchhoff stress tensor, cf. formula (5.29); hence the distinction.

In (6.6) we should precisely write $(\partial W / \partial \gamma_{ij} + \partial W / \partial \gamma_{ji})/2$ instead of $\partial W / \partial \gamma_{ij}$.

To better grasp the stress tensor $\tau_{\text{G-A}}^{ij}$, let us denote, after Green and Adkins [199] (s^{ij}) a symmetric stress tensor measured per unit area of the undeformed body. It can be shown that

$$s^{ij} = \frac{1}{2} \left(\frac{\partial W}{\partial \gamma_{ij}} + \frac{\partial W}{\partial \gamma_{ji}} \right) = J \tau_{\text{G-A}}^{ij}, \tag{6.7}$$

for a compressible body and, and

$$s^{ij} = \frac{1}{2} \left(\frac{\partial W}{\partial \gamma_{ij}} + \frac{\partial W}{\partial \gamma_{ji}} \right) + p g^{ij}, \tag{6.8}$$

for an incompressible body.

The tensor (s^{ji}) is the (symmetric) second Piola-Kirchhoff stress tensor expressed in curvilinear coordinates (ξ^i); thus in Cartesian coordinates $s_{ij} = T_{ij}$.

Lanir [327] considered first the homogeneous elastic case. Then the fibres are elastic and the matrix hydrostatic pressure is a unique function of the strain. To simplify the presentation, let us assume that the fibres are straight. An extension to more realistic case of undulating (wavy) fibres is not difficult, cf. Lanir [327].

W appearing in (6.6) is the sum of the strain energies in the fibres. Each type of fibre K has an associated uniaxial strain energy function w_K. Without loss of generality we can express w_K in terms of the stretch ratio λ. The load per unit undeformed cross-sectional area in the fibre is given by

$$f_K(\lambda) = \partial w_K(\lambda)/\partial\lambda, \quad \lambda > 1 \tag{6.9}$$

and vanishes (see assumption (i)) if $\lambda \le 1$. The total energy of all the fibres of type K in an unstrained volume unit is

$$W_K = \sum_{\mathbf{m}} \Phi_K R_K(\mathbf{m})w_K(\lambda)\Delta\Omega, \quad \text{(no summation over } K), \tag{6.10}$$

where Φ_K is the volumetric fraction (out of the total volume) of fibres of type K in the unstrained state. The summation is performed over the whole range of fibre orientations.

The total strain energy in the fibres W in a unit unstrained volume is thus given by

$$W = \sum_{K,\mathbf{m}} \Phi_K R_K(\mathbf{m})w_K(\lambda)\Delta\Omega. \tag{6.11}$$

To specify the constitutive relationship (6.6), let (ξ_i') denote a special coordinate system for a straight fibre in the undeformed body, such that ξ_1' coincides with the direction of the fibre. Then, there are (locally) unique relations such that

$$\xi_i = \hat{\xi}_i(\xi_j'), \quad j = 1, 2, 3$$

and

$$\xi_i' = \hat{\xi}_i'(\xi_j).$$

The strain along the fibre is calculated as follows

$$\gamma_{11}' = \frac{\partial\xi^i}{\partial\xi_1'}\frac{\partial\xi^j}{\partial\xi_1'}\gamma_{ij}. \tag{6.12}$$

From (6.6), (6.11) and (6.12) we get

$$\tau_{G-A}^{ij} = J^{-1}\sum_{K,\mathbf{m}} \Phi_K R_K(\mathbf{m})(1/\lambda)f_K(\lambda)[\partial\gamma_{11}'/\partial E_{ij}]\Delta\Omega + pg^{ij}, \tag{6.13}$$

where (E_{ij}) is the strain in the tissue (assumption (iii)). The stretch ratio λ of the fibre is

$$\lambda = \frac{ds}{ds_0} = (2\gamma_{11}' + 1)^{1/2}.$$

Let us recall that the squared change of distance between each two 'close' points in the body due to the deformation is given by

$$ds^2 - ds_0^2 = 2\gamma_{ij}d\xi^i d\xi^j.$$

In the case of a 'large' number of fibres per unit volume (or unit area in the case of, for instance, membranes) the summation can be replaced by integration, cf. Lagzdiņš et al. [322]. In fact then the summation over **m** is the integration over a unit sphere (or its part).

For extension of the outlined averaging method to tissues with undulating fibres, viscoelastic case and nonhomogeneously structured tissue the reader is referred to the same paper by Lanir [327], where specific cases were also discussed (for instance membranes).

Similar averaging method was also used to the derivation of constitutive equation for the lung tissue; cf. Lanir [326]. The lung tissue is idealized as a cluster of a very large number of irregular hollow polyhedrons (alveoli) with membranous walls, cf. Section 2.2.10. Each of the polyhedrons is open in part of its surface and connected via this opening to the outer atmosphere. The strain energy function of the membrane has two components: one is associated with the tissue itself, whilst the other reflects the effect of the interfacial tension. For details of the developments and elastic and viscoelastic constitutive equations the reader is referred to Lanir [326].

The same author [328, 329] considered soft tissues as osmotically active binary systems of solid fibres in a fluid-like matrix, cf. also the lectures by Huyghe in this volume and the references therein. The strain energy function of the entire network of fibres was expressed as a function of the strain tensor **E**, obtained by integration over two angles (spherical coordinates; recall that $|\mathbf{m}| = 1$ in the reference configuration). At equilibrium the total Cauchy stress tensor is written as follows

$$\boldsymbol{\sigma}(\mathbf{E}, c) = \boldsymbol{\sigma}_f(\mathbf{E}) - \Psi(c)\mathbf{I}, \qquad (6.14)$$

where $\boldsymbol{\sigma}_f(\mathbf{E})$ is the stress due to the bulk-averaged effect of the axial stresses in the tissue fibres (the solid stress), and $\Psi(c)$ is an osmotic pressure depending on the proteoglycan concentration c. In fact such an approach is typical to mixture theory.

We recall that from the mechanical point of view, soft tissues consist of networks of fibres (the solid), of large macromolecules of proteoglycans and of a fluid. The proteoglycans contain negatively charged groups in their structure cf. Mow and Ratcliffe [410], Telega and Wojnar [576]. These negative charges are neutralized electrostatically by excessive concentration of cations in the tissue fluid. By virtue of their size, the proteoglycan molecules are effectively immobilized by the fibres structure. Hence, the tissue

acts as a polyelectrolyte which gives rise to a swelling potential represented by the 'osmotic pressure'. Swelling is accompanied by stretching of the tissue fibres and a concomitant increase of the fluid hydrostatic pressure required for mechanical balance. The reader is referred to the comprehensive paper by Telega and Wojnar [576] on various aspects of charged tissue behaviour.

Consequences of known restrictions on the behaviour of swelling tissues were examined by Lanir in the case of isotropy [328] and anisotropy [329]. In the last case the 'Generalized Coleman Noll' (GCN) inequality and strong ellipticity (S-E) condition were exploited. In fact, as we have already mentioned earlier, further research on mathematical structure of constitutive equations used in biomechanical modelling is needed.

Remark 7. Less general approach was developed by Ault and Hoffman [21]. These authors exploited formulae for macroscopically transversely isotropic material, well-known in composite mechanics, cf. Nemat-Nasser and Hori [418]. The model is confined to linear elastic behaviour of (isotropic) matrix and fibres. Perfect bonding is assumed to exist between the fibres and the matrix. Such an assumption can be weakened (Lipton and Vernescu, [353]), thus allowing for slip between the fibres and the matrix. The theoretical model was next applied by Ault and Hoffman [22] to two types of connective tissue: rat tail tendon and the posterior knee joint capsule of the cat. It seems that composite models like that advanced by Ault and Hoffman have confined range of applicability since nonlinearities exhibited by mechanical behaviour of tissues described have not been taken into account, see also the next subsection

Remark 8. Let us provide comments on possible applicability of recently proposed non-affine micro-sphere model of rubber elasticity elaborated by Miehe et al. [387], to connective tissues. In this model the free energy of the single chain in a cross-linked network is governed by *two micro-kinematic variables: the stretch* and *the tube contraction.*

Now we proceed to introducing those microvariables. In the statistical treatment of a single polymer chain, in our case it would be a fibre of connective tissue, its geometrical structure is idealized to be composed of N segments of equal length l, the so-called Kuhn segment length. The contour length L of the chain is $L = Nl$. In the classical statistical treatments of a single polymer chain, the single chain is unconstrained and has an entirely random orientation in space as visualised in Fig. 59a, which a priori ignores a dependency on the motion of neighbouring chains, cf. the references cited in Miehe et al. [387]. We recall that in the case of connective tissues fibres exhibit certain order.
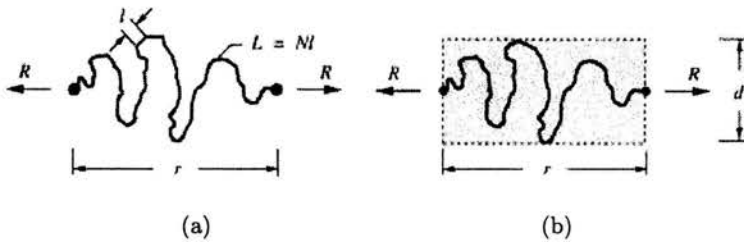
FIGURE 59. Geometry of a simple polymer chain. (a) Free single chain consisting of N segments with lengths l, end-to-end distance r and contour length $L = Nl$. (b) Chain topology constrained by a straight tube of diameter d, after Miehe et al. [387].

The key phenomenological kinematic variable of the single chain is the current end-to-end distance r depicted in Fig. 59a. For an unconstrained free chain this distance assumes the random-walk-type root-mean-square value $r_0 = \sqrt{N}l$. Alternative dimensionless kinematic variables to measure the deformation of the chain are the stretch λ or the relative stretch λ_r defined as

$$\lambda = \frac{r}{r_0} \quad \text{and} \quad \lambda_r = \frac{r}{L} = \frac{\lambda}{\sqrt{N}} \tag{6.15}$$

respectively, with $\lambda \in [0, \sqrt{N})$ and $\lambda_r \in [0,1)$. The maximum values of these measures are obtained when the end-to-end distance r approaches the contour length L.

Classical treatments of polymers consider a free free motion of a single chain in the cross-linked network. These theories do not take into account the constraints between different molecules which form the network. Concept from molecular statistics that takes these effects into account are the so-called *constraint junction* and *constrained segment theories*. A recent development associated with the latter group is the so-called *tube model* of rubber elasticity, cf. the relevant references in Miehe et al. [387]. The tube model characterizes the cross-links and entanglement topology of a polymer network by a set of worm-like network chain paths. The basic physical argument for the tube approach is the large degree of coil interpenetrations of network chains. These interpenetrations can be viewed as obstacles that impose constraint on the free motion of the chain. An important (and simple) assumption introduced by Miehe et al. [387], consists of confining the polymer chain to a *tube of constant diameter d* as visualized in Fig. 59b, with both ends fixed at the centre of the end cross sections. This simplified geometry constrains the number of allowed conformations of the chain to the free space inside of the tube. Then it is assumed that the network constraint to

the simple chain under consideration can be described by the dimensionless kinematic variable:

$$\nu = (d_0/d)^2, \tag{6.16}$$

with $\nu \in (0, \infty)$, denoted as the *tube area contraction*. Here, d_0 is the initial diameter of the tube, which can be considered as a material parameter of the undeformed network. For references related to estimates of d_0 in terms of the length l and the number of segments per unit volume the reader is referred to Miehe et al. [387]. Obviously, here we mean estimates in the case of polymers. It seems that in the case of soft fibres, such estimates will depend on the type of tissue (cartilage, ligament, tendon, artery, heart, etc.). Thus, in the presented model, the allowed conformations of the single chain are determined by the two *micro-kinematic* variables λ and ν, just introduced.

The second feature of the model due to Miehe et al. [387] is a new non-affine micro-to-macro transition that defines the three-dimensional overall response of the polymer network based on an averaging procedure of micro-state variables defined on the micro-sphere of space orientations. This micro-to-macro transition links the two micro-kinematic variables λ and ν in a non-affine format to line-stretch $\bar{\lambda}$ and area-stretch $\bar{\nu}$ of the (isotropic) macro-continuum. We observe that the entropy and free energy of a single chain in a straight micro-tube are determined by using classical notions of statistical mechanics.

Let us provide now a critical comment linked with micro-to-macro transition. Though Miehe et al. [387] claim that they perform 'a characteristic homogenization procedure', yet this is not true. Their procedure of finding the overall quantities is just a *specific averaging procedure*. Here we would like to mention that there is an essential difference in performing homogenization of convex and nonconex problems, cf. Braides and Defranceschi [52], Telega [567] and references therein. More precisely one has to distinguish between deterministic and stochastic homogenization. For convex deterministic periodic problems (microperiodic distribution of microinhomogeneities like fibres or cells) the effective properties can be derived by solving a so-called basic cell problem. In all other cases (convex-stochastic, deterministic-nonconvex, stochastic-nonconvex) rigorous derivation of effective properties requires solving counterpart of the basic cell problem, now involving the whole space $\mathbb{R}^3$ (or the two-dimensional space $\mathbb{R}^2$ in the case of the plane problems). Practically samples of the materials can only be finite. Hence the idea of RVE (representative volume element). Then the effective properties depend on the dimensions of the RVE. Unfortunately, Miehe et al. [387] did not mention that, in fact, they deal with nonconvex stored energy functions (finitely deformed rubber materials). Consequently, one cannot resort to the paper by

Ponte Castañeda and Suquet [452] which deals with nonlinear homogenization problems, but not with nonconvex ones.

An open problem, which naturally arises, is how to extend the model proposed by Miehe et al. [387] to modelling of tissues? As we know, biological tissues (both bones and soft tissues) contain various chains. The assumption of straight confining tube may not be directly applicable (for instance consider myofilaments). In reality, as we know, biological tissues are macroscopically anisotropic. It means that already at the microscopic level the energy of a single fibre would have to depend on the direction, similarly to the approach proposed by Lanir [327].

In the case of macroscopically orthotropic tissues three families of fibres are determined by three (possibly location dependent) independent unit vectors, tangent to the fibres: $\mathbf{m}_1$, $\mathbf{m}_2$, and $\mathbf{m}_3$.

Also it is important to take into account limited extensibility of fibres (rubber-like materials may undergo much higher stretch than fibrous connective tissues), cf. Section 6.2.1.

As a step towards realization of formulation of orthotropic constitutive equations in terms of molecular chain model one can mention the papers due to Bischoff et al. [44, 45].

6.2. Some specific cases of fibres alignment

In this section three specific microstructural models are presented.

6.2.1. Modification of Voigt's model.
In micromechanics, the so called Voigt and Reuss models are well known. These are the simplest models of obtaining lower and upper bounds for effective properties of composites, cf. Allaire [9], Jikov et al. [287], Lewiński and Telega [345], Nemat-Nasser and Hori [418]. The bounds obtained in this way are most narrow.

Wren and Carter [631] modified the Voigt model elaborated for polycrystalline composites in a manner applicable to soft skeletal connective tissues. More precisely, tissue is described as a two-phase composite consisting of fibres dispersed in a matrix materials representing the ground substance (glycosaminoglycan matrix, etc.). A fibre volume fraction is denoted by V_f whilst a matrix valume fraction $V_m = 1 - V_f$. The matrix is assumed to be isotropic while the fibres contribute tensile stiffness and strength in the direction in which they are aligned. For simplicity tissue homogeneity is assumed. In describing the model, we assumed that we have a tissue specimen to which we apply known strain in the axial direction ϵ_a.

In fact, such a specimen is nothing else than RVE (representative volume element). We refer to the direction of strain application as the axial direction

and, when referencing a particular fibre, we refer to the direction of fibre alignment as the fibre direction. The elaborated model predicts the relation $\sigma_a = \hat{\sigma}_a(\epsilon_a)$ associated with the applied strains ϵ_a. Time-dependent effects are not incorporated.

The question now is in what consists the modification of the Voigt model. According to this model, the axial strain induced in a polycrystalline composite by an axial applied strain ϵ_a is:

$$\sigma_a = E\epsilon_a = (V_f E_f + V_m E_m)\epsilon_a = V_f \sigma_f + V_m \sigma_m, \qquad (6.17)$$

where $\sigma_f = E_f \epsilon_a$ and $\sigma_m = E_m \epsilon_a$ are the stresses induced in the two phases. For soft skeletal connective tissues, the relationships $\sigma_f = E_f \epsilon_a$ and $\sigma_m = E_m \epsilon_a$ no longer suffice. Wren and Carter [631] proposed new relations for σ_m and σ_f applicable to soft skeletal connective tissues. Those new relations are to be used in Eq. (6.17) in place of the stresses for polycrystalline solids. Wren and Carter [631] proposed the following simple relationship for the axial matrix stress:

$$\sigma_m(\epsilon_a) = \begin{cases} E_m \epsilon_a & \text{if } \epsilon_a < \epsilon_m^{\text{fail}}, \\ 0 & \text{if } \epsilon_a \geq \epsilon_m^{\text{fail}}. \end{cases} \qquad (6.18)$$

Here E_m denotes the matrix elastic modulus and ϵ_m^{fail} is the matrix failure stress. The modelling of mechanical behaviour of fibres is a little bit more complex. One has to consider three cases: single fibre aligned with loading, fibre rotation fully unconstrained and fibre rotation fully constrained. Anyway, a single fibre i fails at the stretch ratio $\lambda_i^{\text{fail}} = L^f/L^0$ (in the case of fibre aligned with loading), where L^0 denotes the length of the fibre when maximally crimped and L^f is its length when it fails.

The derived macroscopic formula $\sigma_a = \hat{\sigma}_a(\epsilon_a)$ was applied to rabbit patellar tendon, tissue from the deep region of bovine menisci and specimens from the zone surface of bovine humeral articular cartilage. The results obtained compare favourably with experimental data. Toe region of the stress-strain curve is also visible.

6.2.2. Microstructural model for description of low load behaviour of fibrous connective tissue.
In this and in the next subsection we shall present two different approaches to modelling uniaxial extension of fibrous connective tissues like tendon and ligament. For such tissues an important problem consists in defining the reference length. Reference length is the basis for biomechanical description, yet is not selected in a consistent manner throughout the literature, cf. Hurschler et al. [263]. Reference length of a tendon or ligament is often determined empirically by increasing elongation until

a measurable load is detected. More precisely, a small arbitrarily selected preload is assigned, or an inflection is observed in the load-deformation curve, cf. the relevant references in Hurschler et al. [263].

Tendon and ligament specimens, however are compliant at the onset of load bearing such that small changes in load result in relatively large variations in reference length. In addition, relatively large preloads are sometimes applied that mask much of the toe-in region of the load-deformation response. Consequently, different choices of preload can introduce bias into biomechanical measures such as stretch, strain, strain to failure, or tangent modulus.

Another important problem is to identify the transition from the stress-stiffening 'toe-region' to the more 'linear region' commonly observed in the stress-strain diagrams of fibre recruiting soft tissues. The definitions of such a point is essential in the study of low load behaviour in normal and pathologic connective tissues.

Hurchler et al. [263] proposed solution to these two problems. More precisely, these authors introduced the location parameter (γ) as a preload independent parameter to establish a reference length in biomechanical evaluations of fibrous connective tissues, such as ligaments and tendons. Moreover, they established a method for quantifying the toe-to-linear region transition-point in strain-stiffening soft fibrous tissues.

Hurchler et al. [263] applied the probabilistic microstructural model developed earlier by Hurchler et al. [262]. Let us pass to a brief presentation of the model. The unloaded tissue is assumed to be dominantly composed of crimped collagen fibres that need to be extended to various lengths before they begin to bear a tensile load. Fibres are assumed to be oriented predominantly along the longitudinal axis of the ligament or tendon. The straightening stretch ratio (SSR), defined as the tissue stretch at which an individual fibre begins to bear load, is defined as $\lambda_s = l_s/l_0$ (fibre length divided by tissue reference length). The load borne by the fibre is assumed to behave according to a constitutive relationship based on collagen fibril microstructure. The stress in the tissue is determined by the overall tissue stretch (stretch ratio= $\lambda_t = l/l_0$ =deformed tissue length divided by tissue reference length) and the deformation state, and hence load bearing contribution of the fibre population. Thus, the longitudinal normal tissue stress σ_t can be computed by integrating the contribution of all fibres over all possible SSR(λ_s):

$$\sigma_t(\lambda_t) = \int\limits_{\gamma}^{\lambda_t} P_w(\lambda_s)\sigma_{33}(\lambda_t/\lambda_s)d\lambda_s, \quad \lambda_t > \gamma. \qquad (6.19)$$

Here P_w is the Weibull probability density function (PDF) as a function

SSR, σ_{33} is the longitudinal normal stress in a fibre, and γ is the location parameter of the Weibull distribution and defines the onset of fibre loading. Hence $\sigma_t(\lambda_t) = 0$ when $\lambda_t \leq \gamma$, since none of the fibres are loaded below the threshold γ. We observe that γ can be less or greater than one, depending on whether the tissue is initially in a preloaded or 'slack' configuration, respectively. The form of the Weibull PDF used in Eq. (6.19) is

$$P_w(\lambda_s) = \begin{cases} \frac{\beta(\lambda_s-\gamma)^{\beta-1}}{\delta^2} \exp\left[-\left(\frac{\lambda_s-\gamma}{\delta}\right)\right], & \text{if } \lambda_s > \gamma, \\ 0, & \text{if } \lambda_s \leq \gamma. \end{cases} \qquad (6.20)$$

Here γ is the location parameter as stated above, and β and δ are the shape and scale parameters, respectively. The shape, scale, and location parameters are such that $\beta > 0$, $\delta > 0$, and $\gamma > 0$ since stretch ratio is defined to be greater than zero. Shape and scale parameters are related to the shape of the 'toe-region' whilst the location parameter is related to the stretch at which fibres begin to bear load. The Weibull PDF parameters (β, δ, and γ) for a given set of stress-stretch data are determined by a nonlinear least-squares minimization cf. Hurschler et al. [262].

According to Hurschler et al. [262, 263] the Weibull PDF [611] was chosen to represent fibre straightening in fibrous connective tissues like tendons and ligaments since in a slack configuration, no fibres have yet straightened to bear loads. We observe that the Weibull PDF is an asymmetric one-tailed function and has a zero probability of occurrence below a certain value. We recall that the Gaussian PDF, described by only two parameters (the mean and the standard deviation), does not have this property.

Figure 60 illustrates influence of the microstructure of fibrous connective tissue on the mechanical load-deformation and stress-stretch behaviour of the tissues.

6.2.3. One-dimensional, quasi-linear viscoelastic model of tendon accounting for the effects of preconditioning.

As we already know, the nonlinear stress-strain relationship of tendons starts with a 'toe' region at lower strain range, and the curve becomes linear at higher strain levels. We also know that the nonlinearity is attributed to gradual straightening of the original wavy collagen fibres. It is also important to include time-dependent aspects. Those have two components: viscoelasticity and preconditioning, cf. Fung [175]. They differ *in-vitro* in their recovery characteristics; while recovery from viscoelastic effects is complete and has time constants in the range of seconds to minutes, recovery from preconditioning *in-vitro* may be only partial and has time constants of the order of several hours, cf. the relevant
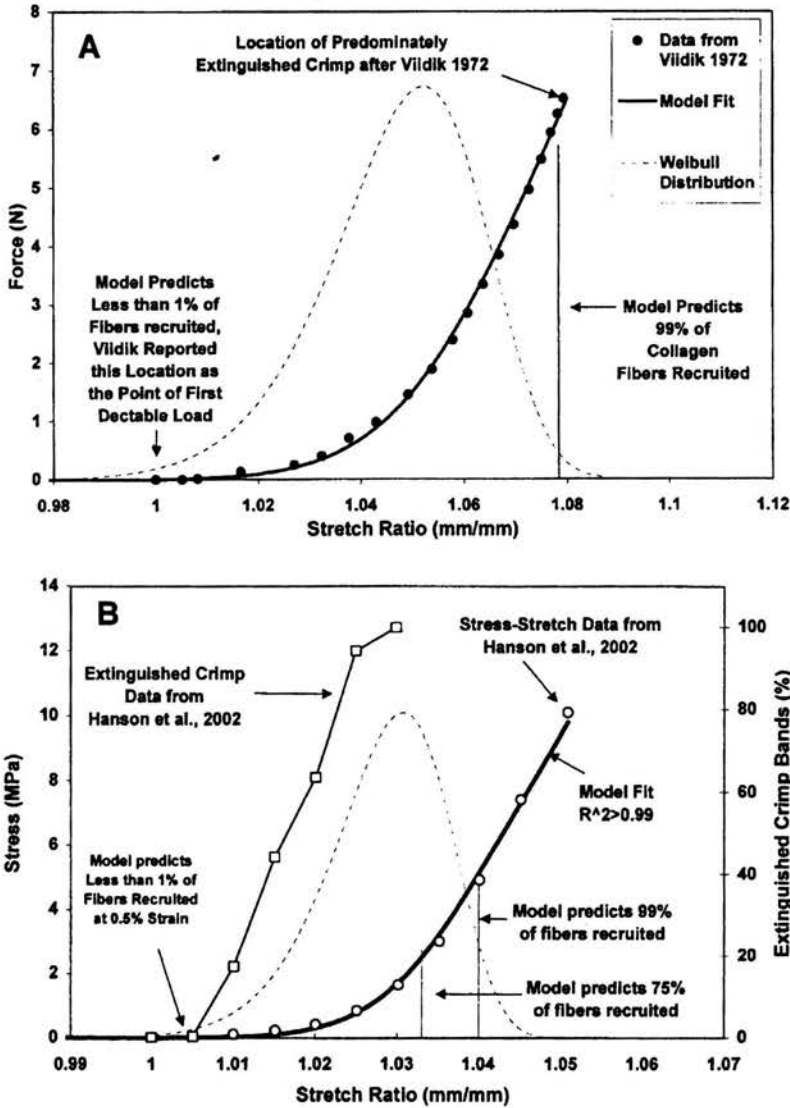
FIGURE 60. Model fits to data from: (A) Viidik [599] in which changes in collagen fibre crimp were examined with polarized light during tissue strain (measured grip to grip), and (B) Hanson et al. [216] in which changes in collagen fibre crimp were examined with optical coherence tomography during tissue strain (measured grip to grip). In both cases the original units of the studies were maintained with the exception of strain being converted to stretch ratio. In the case of the Viidik data the model agrees very well, in the case of Hanson et al. [216] data the model slightly underpredicts the stretch at which complete fibre straightening occurs, after Hurschler et al. [263].

references in Sverdlik and Lanir, [553]. The most apparent effect of precondi-
tioning is a shift of the stress-strain curve to the right, cf. Fig. 61. Sverdlik and
Lanir [553] performed a combined experimental and theoretical investigation
of tendon accounting for its waviness, viscoelasticity and preconditioning.
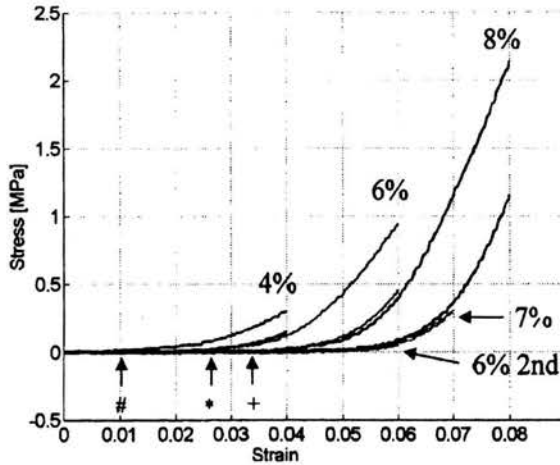
FIGURE 61. The stress-strain curve for the first and last stretches of each set.
Symbols: the reference strain e_{smin} for set 2 (#), set 3 (*), and set 4 (+). In
set 5, e_{smin} cannot usually be determined reliably due to high noise/signal ratio
resulting from the very low force signals at these sets, after Sverdlik and Lanir
[553].

The mathematical model is an extended one-dimensional version of the
3D (three-dimensional) structural formulation of Lanir [327], presented by
us in Section 6.1.

Let us briefly describe this 1D model. The single fibre is assumed to be
quasi-linear viscoelastic under tension. The second Piola-Kirchhoff stress of
the single fibre is then, cf. Fung [175]

$$T_f(e_f, t) = T_f^e G(t) + \int_0^t G(t - \tau) \frac{dT_f^e}{de_f} \frac{de_f(\tau)}{d\tau} d\tau, \qquad (6.21)$$

where $G(t)$ is the reduced relaxation function, e_f is the true strain in the
fibre, T_f^e is the 'immediate' elastic response of the fibre, which is assumed in
a simple nonlinear bimodal form (linear+nonlinear):

$$T_f(e_f) = Ae_f + Be_f^N. \qquad (6.22)$$

Here A, B, and N are material parameters. The reduced viscoelastic relaxa-

tion function $G(t)$ is assumed to be bi-exponential:

$$G(t) = k_0 + k_1 \exp(-t/\tau_1) + k_2 \exp(-t/\tau_2), \qquad (6.23)$$

with $k_0 + k_1 + k_2 = 1$; $k_0, k_1, k_2 > 0$. The relaxation times τ_1, τ_2 and the constants k_i $(i = 0, 1, 2)$ are material parameters.

The true strain e_f (in fibre) for every level of the tendon strain e depends on its waviness as follows (for obvious reasons we do not use E for 1D strain). The true stretch ratio in the fibre is given

$$\lambda_f = \frac{L}{L_s} = \frac{L}{L_0}\frac{L_0}{L_s} = \frac{\lambda}{\lambda_s}, \qquad (6.24)$$

where $\lambda = L/L_0$ is the stretch ratio of tendon, and $\lambda_s = L_s/L_0$ is the straightening stretch ratio of the fibre; L and L_s are the current and the straightening lengths of the fibre. Using the strain definition $e = (\lambda^2 - 1)/2$, the fibre strain $e_f = (\lambda_f^2 - 1)/2$, is expressed by

$$e_f = \frac{e - e_s}{1 + 2e_s}, \qquad (6.25)$$

where $e_s = (\lambda_s^2 - 1)/2$ is the straightening strain of the fibre. This straightening strain changes with time during preconditioning due to fibre elongation, the latter being a function of time and of the magnitude of true strain in the fibre. Two mechanisms of elongation are incorporated in the model: one is a first-rate reaction model for the increase of e_s as

$$\frac{de_s}{dt} = \begin{cases} P_1(e_f - P_2), & \text{if } e_f(t) > P_2 > 0, \\ 0 \text{ otherwise,} \end{cases} \qquad (6.26)$$

with the initial condition $e_s(0) = e_{s0}$. The parameter P_1 is a rate constant and P_2 is a threshold below which no viscous lengthening occurs. The second mechanism is of a 'plastic' nature, where the increase of e_s depends on e_f as in

$$\frac{de_s}{dt} = \begin{cases} \frac{de_f(t)}{dt}, & \text{if } e_f > P_3 > 0; \quad \frac{de_f(t)}{dt} > 0, \\ 0, & \text{otherwise.} \end{cases} \qquad (6.27)$$

Here P_3 is a threshold below which no 'plastic' lengthening occurs.

The initial waviness e_{s0} of the fibres is assumed to be distributed between the fibres of the tendon as a *beta density probability distribution*.

$$D(e_{s0}) = \frac{\Gamma(\alpha + \beta)}{\Gamma(\alpha)\Gamma(\beta)} \left(\frac{e_{s0}}{e_{s0\text{max}}}\right)^{\alpha-1} \left(1 - \frac{e_{s0}}{e_{s0\text{max}}}\right)^{\beta-1} \frac{1}{e_{s0\text{max}}} \qquad (6.28)$$

with $\alpha, \beta > 0$; $0 < e_{s0} < e_{s0max}$. Here the subscript '0' refers to the initial state; α, β are parameters which determine the shape of the beta function, e_{s0max} denotes the highest level of e_{s0}, and Γ is the gamma function. The rationale for using beta rather than normal distribution function is that the former is nonzero only within a finite region ($[0, e_{s0max}]$ in the present model), while the latter extends to infinity (physically unacceptable). Moreover, the beta distribution allows for asymmetry.

The overall response of the tendon is equal the sum of contributions of all its fibres. Thus, the second Piola-Kirchhoff stress of the tendon is given by

$$T(e,t) = \int_0^e D(e_s)T_f[e_f(e_s,t)]de_s = \int_0^e D(e_{s0})T_f[e_f(e_s,t)]de_{s0}, \qquad (6.29)$$

where the second equality results from the continuity condition $D(e_{s0})de_{s0} = D(e_s)de_s$. From Eqs. (6.21)–(6.23) and (6.29) we finally get the tendon stress in the form

$$T(e,t) = \int_0^e D(e_{s0}) \int_0^t \left[k_0 + k_1 \exp\left(\frac{-(t-\tau)}{\tau_1}\right) + k_2 \exp\left(\frac{-(t-\tau)}{\tau_2}\right) \right]$$
$$\times \left(A + NBe_f^{N-1}\right) \frac{de_f(\tau)}{d\tau} d\tau de_{s0} \quad (6.30)$$

in the last equation the effects of fibre lengthening during preconditioning are introduced via the time dependence of the strain in the fibre e_f, according to (6.25)–(6.27).

The proposed model is highly nonlinear and contains 13 parameters. One, e_{s0max}, is determined directly from the stress-strain curve at the first stretch for each specimen; the parameters A, B are determined from the data and the other parameters. The remaining ten parameters (N, α, β, k_1, k_2, τ_1, τ_2, P_1, P_2, P_4) can be estimated to fit the data best, in the least squares sense.

The theoretical model just presented was confronted with experimental data obtained for sheep tendons. More precisely twenty three below-knee forelimb sections of 3–4 year old female sheep weighting 60–80 kg were used by Sverdlik and Lanir [553] to obtain thirty five digital extensor tendons with typical lengths of about 120 mm. The test protocol consisted of sets of stress relaxation loadings, each with first increasing maximal strain levels (4,6,8 percentil sequence) and then decreasing strains (7,6 percent) at consecutive sets. The results obtained by Sverdlik and Lanir [553] indicate that the response of the tendon to stretch is modified by the stretch itself in a way that

depends on the level of strain, on the strain history and on the duration of the stretch, cf. Fig. 61.

The agreement of the model predictions with the measured stress-strain response (Fig. 62) is good, except for some deviation at the lowest strain level (set 1,4 percent strain).
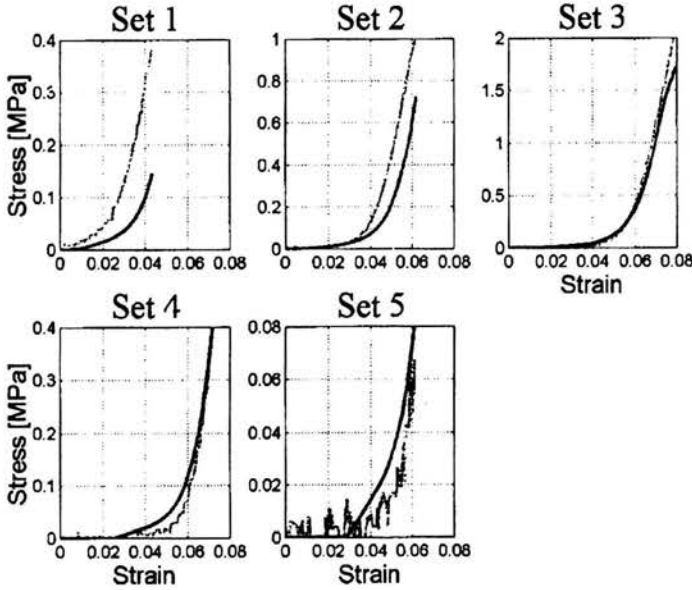
FIGURE 62. Comparison between simulation and experimental data of the stress-strain curves in the first stretch in each loading set. Gray line – experimental data, dark line – model prediction, after Sverdlik and Lanir [553].

Remark 9. An earlier structural model of parallel-fibred connective tissues such as tendons and ligaments was proposed by Kwan and Woo [318]. In essence, the stress-strain relationship of a single collagen fibril is assumed to be bilinear, with 1) an initial low modulus region, followed by 2) a high modulus region. For a tissue composed of multiple collagen fibrils, the fibrils may have variable initial lengths in their relaxed state and, thus, have crimps that can be removed at different strain levels. As each group of fibrils becomes taut at its respective strain level, there will be a gradual increase in tissue modulus. When all the fibrils become taut, the tissue modulus reaches a maximum value. Ultimately, as the loading continues, the fibrils begin to fail successively. Hence, we conclude that the model due to Kwan and Woo [318] is piecewise linear and contains many independent constants describing approximation of real nonlinear curve.

Remark 10. Unlike articular cartilage, the cornea has received relatively little attention from proponents of multiphase theories for soft tissue biomechanics. This may be because the cornea's principal function, unlike articular cartilage, is not mechanical but optical. The cornea does not regularly experience large deformations or loads, and its viscoelastic response is of secondary importance. However, these theories may be crucial to understanding: (1) the cornea's response to surgery, and (2) the physiology of corneal swelling. The latter topic was studied by Bryant and McDonnell [61]. The corneal stroma in its normal state has a strong tendency to imbibe fluid. The stroma is composed of lamellae of parallel collagen fibres embedded in a matrix of polyanionic proteoglycans, which gives rise to the fixed charge density of the tissue. At normal hydration, the stroma is roughly 80 percent water by weight, with most of the fluid contained in the spongy matrix of proteoglycans. Corneal swelling is typically explained in one of the three ways: by the behaviour of the corneal endothelium (e.g. the pump-leak hypothesis); in terms of the osmotic pressure of the corneal stroma (i.e. the Donnan view); or by the reference to experimental demonstration of cornea's swelling behaviour (e.g. swelling pressure and inhibition experiments), cf. the relevant references in Bryant and McDonnel [61].

The swelling pressure is defined as the pressure applied in confined compression to a sample of stromal tissue immersed in a saline bath. This pressure decreases exponentially with corneal hydration. The inhibition pressure is measured *in-vivo* by inserting a small cannula, filled with 0.15 M saline and connected to a closed reservoir containing a pressure transducer into the stroma, cf. Fig. 3 in Bryant and McDonnell [61]. The inhibition pressure is recorded as the suction pressure in the cannula.

In the intact cornea, the water-absorbing tendency of the stroma is counterbalanced by the endothelial 'fluid pump' which is actually one or more active ion transport processes residing in the posterior cellular layer (endothelium), including Na^+–K^+ ATPase, cf. the relevant references in Bryant and McDonnell [61]. It is known that a swollen cornea will deturgesce in proportion to the fluid exudation from the endothelium and that this fluid exudation is linked to the metabolic processes in the endothelium. Most conceptual models of the endothelial metabolic pump mechanism describe a net flow of ions from the stroma to the aqueous, although a complete picture of how active ion transport effects corneal deturgescence has been lacking.

One of the most prevalent explanations is the *pump-leak hypothesis*, which proposes a balance between the pressure-driven and osmotic fluid flows across the endothelium. The IOP (interocular fluid pressure) is postulated to be higher than the hydrostatic fluid pressure in the stroma, cf. the relevant references in Bryant and McDonnell [61].

The last authors developed a biomechanical model of the cornea that can explain the different views of corneal swelling. These authors use the *triphasic theory* proposed in 1991 by Lai et al. (see Mow and Ratcliffe [410]), supplemented by boundary conditions representing the steady-state fluid and ion flow across the corneal endothelium. The equations were solved in cylindrical coordinates for the problem of confined compression and in spherical coordinates to represent the intact cornea. Moreover, expressions were derived for the inhibition and swelling pressures, and it was shown how the model addresses both the Dunnan and pump-leak hypothesis. The material of the stroma was modelled as a linear, transversely isotropic solid, in which the axis of material symmetry is normal to the corneal surface.

6.3. Cartilage and other soft tissues as multiphase materials

6.3.1. General comments. Both bone and soft biological tissues are multiphase porous materials. In this section we shall provide some comments on modelling of cartilage and present available results on micro-macro transition.

In essence, there are three views used to describe the biomechanics of soft tissues, using continuum models that include mobile tissue fluid, cf. also the lectures by Huyghe in this volume. These models include the response of soft tissues by either considering the material to be a porous elastic (or viscoelastic) solid that is saturated by a pore fluid which flows relative to the deforming solid or, equivalently considering the material to be a continuum mixture of a deformable solid phase and a fluid phase, cf. De Boer [119], Coussy [96], Cowin and Huyghe [100], Rajagopal and Tao [473], Simon [523], and references therein. When applied to biomechanical studies, the poroelastic and biphasic mixture models are equivalent. For a discussion the reader is referred to the review article by Simon [523].

The third approach to soft tissue modelling, viewed as porous multiphase material, consists in using various micro-macro averaging techniques.

It seems that the prevailing part of a huge number of studies pertaining to soft hydrated tissues covers annulus fibrosus, articular cartilage and meniscus. These tissues were investigated both from the mechanical and electrochemical point of view, cf. Adams et al. [4], Ateshian et al. [18], Charlebois et al. [69], Chen et al. [72], Dimicco and Sah [135], Freeman [172], Frijns et al. [170], Gu et al. [203], Huyghe and Janssen [267], Iatridis and Gwynn [268], Lai et al. [323], Loboa et al. [358], Levenston et al. [484], Mow and Ratcliffe [410], Mow et al. [409], Stoltz [547], Telega and Wojnar [576], Urban et al. [587], van Meerweld et al. [595], Wang et al. [607], and the references therein and in Cowin and Huyghe [100]. The studies performed exhibit non-

linear and anisotropic behaviour of articular cartilage. This tissue is modelled as a biphasic, triphasic, even quadriphasic mixture. Gu et al. [203] modelled mechano-electrochemical behaviours of charged hydrated soft tissues containing multi-electrolytes as a mixture composed of $n + 2$ constituents (1 charged solid, 1 noncharged solvent phase, and n ion species). For results pertaining to influence of mechanical loads (fluid flow, hydrostatic pressure, shear stress) on behaviour of chondrocytes the reader is referred to Edlich et al. [152] and Stoltz [547].

The procedure of the formulation of the mixture model of material consists of three essential steps: 1) the formulation of balance equations, 2) imposing mechanical and thermodynamical constraints (if needed – like incompressibility, entropy inequality, etc.), 3) the choice of the constitutive relationship. For a general case, the reader is referred to the last section of our paper.

In the case of non-isothermal models, the problem of the definition of the macroscopic temperature(s) arises. For instance, it is discussed whether a biphasic material has one or two temperatures. The micro-macro transition solves this problem rather easily. Indeed, the micro-macro transition (like homogenization methods) requires the knowledge of geometry (deterministic or random) and constitutive equations of components. By performing homogenization (averaging) macroscopic equations are obtained, say Biot-type equations, cf. Telega and Wojnar (2005) and the relevant papers in Auriault et al. [23].

Studying biomechanical literature one perceives that the classical Darcy law of filtration is used in dynamical problems similarly to the case of steady-state flows. In reality, in dynamic flows through porous media the Darcy law is *nonlocal in time*, cf. the relevant references in Auriault et al. [23]. For instance, if the flow is harmonic, the permeability tensor depends on the frequency ω.

In charged-hydrated biological tissues streaming potential plays a crucial role, see many references cited previously. Their mathematical modelling is usually based on the (direct current) *Helmholtz-Smoluchowski equation* (Reppert and Morgan [481], Reppert et al. [482]

$$\Delta V = \frac{\varepsilon \zeta}{\eta \sigma} \Delta P, \tag{6.31}$$

where ε is the permittivity of the fluid, η is the viscosity of the fluid, ζ is the zeta potential, and σ is the conductivity of the fluid. ΔV, ΔP are the voltage and pressure measured across the sample, respectively.

This equation was extended by Packard [441] to frequency-dependent streaming potentials in capillaries. Next, Pride [459] proposed a generalized

theory for frequency-dependent streaming potentials in porous media. Comparison of both models was performed by Reppert and Morgan [481] and Reppert et al. [482]. It seems that the frequencies of physiological load of, say, articular cartilage are too low, even during fast running, to justify the need of using the frequency-dependent model of Pride.

Remark 11. There are two viscoelastic models that are widely used to describe soft tissue viscoelastic behaviour: the quasi-linear viscoelastic (QLV) model [630] and the biphasic mixture model due to Mow et al. [409], cf. also the relevant references in Mow and Ratcliffe [410]. We observe that the models described in Section 6.2 only partially belong to such a classification.

The QLV model stems from the basic assumption that the nonlinear stress-strain response is decoupled from the linear relaxation function, and stress is defined as the convolution of these two functions. The biphasic model considers the tissue as a mixture of two phases: a solid matrix and an interstitial fluid. In its essence, this model quantifies viscoelasticity as due to fluid flow and frictional losses due to the relative motion between solid and fluid phases.

Yin and Elliott [643] applied the transversely isotropic biphasic mixture model previously developed by Cohen et al. [90] – a model of cartilage in unconfined compression loading – to tendon in uniaxial, unconfined tensile loading. To cope with the nonlinear behaviour, incremental analysis was performed. Yet, the toe region was not quite adequately described and preconditioning was not investigated.

Remark 12. van Kemenade [593] and van Kemenade et al. [594] used the triphasic mixture model for skin (solid+fluid+ionic component) to study the transepidermal water loss. In essence the approach consists of a skin and an air model coupled by equating corresponding chemical potentials of water at the surface of the skin to vapour chemical potentials just above the skin surface.

6.3.2. Effective properties of cartilage. Influence of chondrocytes.
Though the amount of papers dealing with modelling of cartilage behaviour is really huge (see comments in the last section of our paper), yet no really general model of cartilage, accounting for its complex microstructure, seems to be available.

We pass now to the presentation of typical partial results.

Soulhat et al. [537] developed a simple fibre-reinforced composite poroelastic model of cartilage to explore its applicability in unconfined compression via comparison with experimental data accounting for transient and drained behaviour. This composite model is an extension of the isotropic homoge-

neous biphasic model. As a first approach it was assumed that the fibrils (collagen) are distributed homogeneously in the r, θ, z directions. The matrix is biphasic and isotropic (proteoglycans and water). The fibrils in the network behave linearly under tension with no resistance to compression (piecewise linear behaviour). The model does not take into account depth-dependent orientation of fibrils.

Broom [55] proposed two- and three- dimensional honeycomb arrangements of fibrils in articular cartilage. The 2D mesh is presented in Fig. 63. Specific feature of this mesh is that it is depth-dependent.

A   B   C
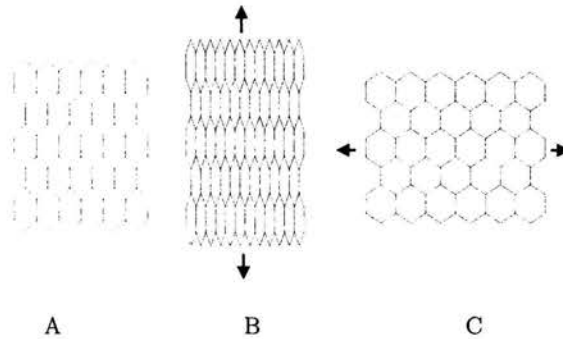
FIGURE 63. Two-dimensional honeycomb mesh analogue of the interconnecting geometry of radial elements modelling the arrangements of fibrils in the matrix of articular cartilage. Note the rapid strain-locking in the radial direction (A and B) versus considerable extension permitted in the transverse direction (A and C), after Broom [55].

Gałka et al. [181] exploited the above regular geometrical model and derived effective (homogenized) elastic moduli. The basic cell, and consequently also these moduli, change with depth. The general formulae for these moduli (2D case) are in the comprehensive paper by Telega et al. [573].

Bursać et al. [65] modelled the cartilage collagen lattice as a simple pressurized two-dimensional cable network. The model was designed to show that tissue equilibrium behaviour in confined compression could be described by considering only the contribution of the tensed collagen network and Donnan osmotic pressure. Two different structural geometries were considered: a hexagonal network and a triangular network. The author claims that: 'In the absence of experimental data, tensile behaviour of individual fibres was assumed to be equivalent to the tensile stress-strain characteristic of a pig tendon'. From Section 6.2 of our paper we know that such an assumption cannot lead to reliable results.

Telega and Wojnar [575] proposed a general linear model of stationary flows of two-ionic electrolytes through porous piezoelectric media. Elaborat-

ing the model, the authors thought of possible application to bone tissue, cf. also Telega and Wojnar [576] and the relevant references therein. It is worth noting that the filtration now described by the so-called Wiedemann-Darcy law, is driven not only by mechanical forces (the gravity forces and pressure gradient) but also by the gradient of electric potential and gradient of the density of ions. To apply the model to soft tissues, one has to drop the piezo effect and include nonlinear behaviour of the matrix (fibrils). By exploiting known filtration laws for, say, cartilage one can try to construct a nonlinear Wiedemann-Darcy law. We observe that for nonstationary flows the Wiedemann-Darcy law becomes nonlocal in time, cf. the paper by Gałka et al. in Auriault et al. [23].

Influence of chondrocytes on cartilage and vice versa

In the 19th century, it was generally believed that articular cartilage was inert and without structure, cf. the relevant references in Guilak et al. [208]. However, by the turn of the century, many investigators had hypothesized that not only articular cartilage had form and structure but that changes in the normal physical environment of the joint could alter the composition and morphology of the tissue. By the mid-1900s, it was suggested that specific relationship existed between the structural characteristics and functional history of articular cartilage, and with increased knowledge of the composition and structure of cartilage, investigators began to hypothesize how the properties may be affected by alterations in the mechanical environment *in vivo*. Further, it was suggested that physiological loading was necessary for the proper maintenance of the joint and the deviations from the normal loading patterns could be a source of significant joint degeneration, cf. Guilak et al. [208] and the relevant references therein.

Let us now pass to a concise presentation of studies aiming at explaining the deformation behaviour of chondrocytes in cartilage and influence of chondrocytes on macroscopic properties of cartilage. The chondrocyte perceives its mechanical environment through biological, mechanical, and physicochemical interactions with cartilage extracellular matrix. In addition to zonal variations in composition and structure, this matrix consists of several distinct regions based on proximity to the chondrocyte. These regions have been termed the pericellular, territorial, and interterritorial matrices, cf. the relevant references in Guilak [207]. The bulk of the tissue is made up of the interterritorial matrix, which consists primarily of water dissolved with small electrolytes, like K^+, Na^+, Cl^-, Ca^{2+}. The pericellular matrix of chondrocytes consists of a distinct tissue region that contains large amounts of Type VI collagen and a high concentration of proteoglycans. In addition to

defining the physicochemical environment of the chondrocyte, the pericellular matrix interacts physically with the chondrocyte through the cell–surface receptors (e.g. integrins, annexin V) which bind to matrix proteins such as fibronectin, hyaluronic acid, and various collagens in the pericellular region. The chondrocyte together with this pericellular region and a surrounding capsule have been termed *chondron*, cf. the relevant references in Guilak et al. [207]. According to the last author, the functional significance of this distinct structural unit is as yet unknown. In our opinion, such a structure of cartilage ensures that it is a sort of a *biological functionally graded material* (in the language of modern micromechanics).

Guilak [207] synthesized a number of studies that have characterized the mechanical environment of the chondrocyte by quantifying the mechanical properties and deformation behaviour of chondrocytes and by theoretically modelling the cell within the pericellular and extracellular matrices. These studies combined theoretical methods (constitutive modelling, finite element analysis), as well as biomechanical and microscopic experiments. From more practical point of view, the aim of these investigations was to elucidate the sequence of biomechanical and biochemical events through which mechanical stress influences chondrocyte activity in both health and disease. For instance, to theoretically model chondrocyte-matrix interactions, the linear biphasic theory proposed earlier for studying cartilage in a penalty finite element formulation was used to quantify the transient stress-strain and fluid flow environment of the chondrocyte during compression. This model represented the various components of cartilage (chondrocytes and the pericellular and extracellular matrices) as biphasic media whose viscoelastic behaviour is governed predominantly by interactions between solid and fluid phases. An important feature is the two order of magnitude difference in the geometric scales between the level of the tissue explant and the level of the individual cell. By dividing the analysis into two separate problems, a multiple scaling algorithm was used to calculate the strain-stress environment in the neighbourhood of the cell, see Fig. 64.

Since the linear model was assumed, therefore stresses and strains in the chondrocytes were underestimated. The important issue, still left aside, is that in seriously diseased diathroidal joints (rheumatoid arthritis, osteoarthrosis) cartilage undergoes destruction; it finally can become completely destroyed. Thus, more realistic investigations of diseased cartilage should take into account damage processes of cartilage, including its thinning.

Effective moduli of cartilage viewed as a material composed of extracellular matrix and small cells (inclusions) were investigated by Wu et al. [633] and Wu and Herzog [634]. Prior to passing to a discussion of those results we
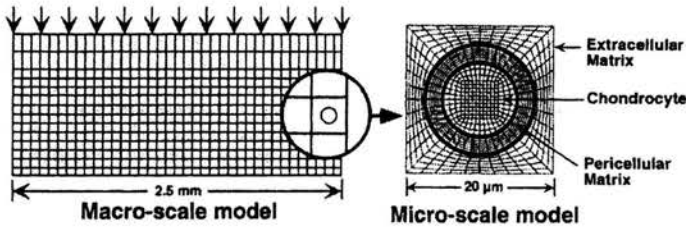
FIGURE 64. A biphasic multi-scale finite element method was used to model the mechanical environment of a single cell within the cartilage extracellular matrix. The 'macro-scale' response of a cartilage explant in a state of unconfined compression was first modelled. From this solution, a linear interpolation of the time history of the kinematic boundary conditions within a microscopic region were then applied to a 'micro-scale' finite element mesh of a $100\,\mu$m$\times 100\,\mu$m region of cartilage that incorporated a chondrocyte ($10\,\mu$m diameter) and its pericellular matrix ($2.5\,\mu$m thick) embedded within and attached to the extracellular matrix. A $20\,\mu$m$\times 20\,\mu$m region of the micro-scale mesh is shown here, after Guilak [207].

recall that the elastic modulus of chondrocyte is smaller by three orders of magnitude while the permeability of chondrocytes is greater by five orders of magnitude, than those of the extracellular matrix, cf. Guilak [207] and the relevant references in Wu et al. [633] and Wu and Herzog [634].

Wu et al. [633] consider both matrix and chondorcytes as isotropic, linear biphasic materials:

$$\begin{aligned}
&\boldsymbol{\sigma}^{s,i} = -\Phi^{s,i}p\mathbf{I} + \boldsymbol{\sigma}_e^{s,i}, \quad \boldsymbol{\sigma}_e^{s,i} = \lambda_i(\mathrm{tre})\mathbf{I} + 2\mu\mathbf{e}, \\
&\boldsymbol{\sigma}^{f,i} = -\Phi^{f,i}p\mathbf{I}, \\
&\boldsymbol{\sigma}^{t,i} = \boldsymbol{\sigma}^{s,i} + \boldsymbol{\sigma}^{f,i} = -p\mathbf{I} + \boldsymbol{\sigma}_e^{s,i}, \quad i = c,m,
\end{aligned} \tag{6.32}$$

where $\mathbf{I} = (\delta_{ij})$; $\boldsymbol{\sigma}^s$, $\boldsymbol{\sigma}^f$ and $\boldsymbol{\sigma}^t$ represent the stresses in the solid phase, in the interstitial fluid, and in the total tissue; λ and μ are the Lamé constants; p, $\mathbf{e}$ are fluid pressure and small strain tensor; $\Phi^{s,i}$ and $\Phi^{f,i}$ ($\Phi^{s,i} + \Phi^{s,i} = 1$) are the solid and fluid volume fractions, respectively; moreover $c = $ cell, $m = $ matrix.

Effective elastic moduli were obtained in two cases: (i) the concentration of cells is small (dilute solution), i.e. the interaction between cells is negligible, (ii) the concentration of cells is large. We recall that in real cartilage, cell volume concentration may reach values as large as 10%.

The formulae for the effective shear modulus of the cartilage μ and the effective bulk modulus K (macroscopic isotropy) were obtained by a direct application of formulae well-known in the composite mechanics, cf. the relevant references in Wu et al. [633]. The effective permeability was also devised

under the assumption of steady state flow. The authors claim that in transient deformations, it depends also on $\dot{e}_v$, the rate of volumetric strain in the solid phase. Unfortunately, within the linear approach such a dependence is not possible. In fact, in the dynamic case the permeability (tensor for macroscopic anisotropy) is *nonlocal in time*. Deformation-dependent permeability is possible provided that the mechanical response of the matrix is nonlinear. Unfortunately, no result of this type seems to be available. Obviously, we mean here an approach based on micro-macro modelling.

A more developed effective mechanical model of cartilage was proposed by Wu and Herzog [634]. The macroscopic model is still *linear*, but this time transversely isotropic. Articular cartilage was assumed to be a four-phasic composite comprised of a proteoglycan matrix (elastic) and inclusions (vertically and horizontally distributed collagen fibres, spheroidal chondrocytes). The effective transversely isotropic elastic moduli were obtained by a specification of general formulae due to Qiu and Weng (1999). Such an approach can be used for a nondilute solution of inclusions and is applicable to cartilage layers with large volumetric concentrations of collagen fibres and chondrocytes, cf. Fig. 65
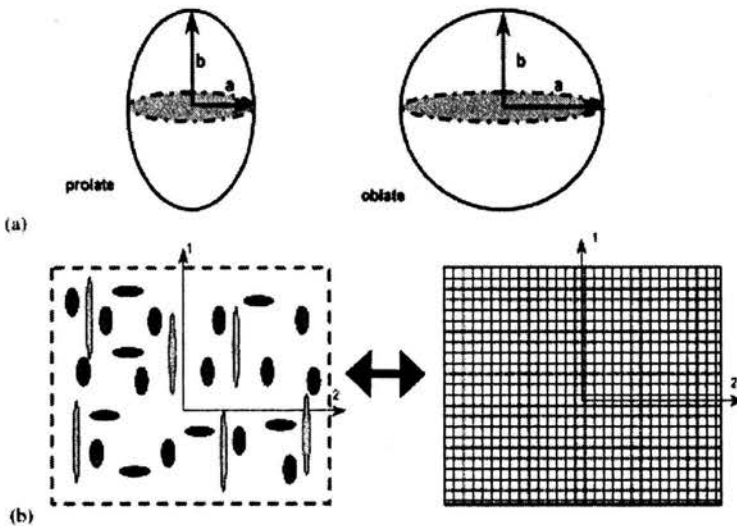
FIGURE 65. Cartilage modelled as a composite with aligned, spheroidal inclusions, after Wu and Herzog [634].

Remark 13. Barocas and Tranquillo [28] proposed an anisotropic, *nonlinear biphasic viscoleastic model* that describes the mechanical interaction between cells and the extracellular matrix (ECM), in particular accounting for the biomechanical feedback loop wherein cells deform the surrounding

network of ECM fibres, inducing network alignment in cases of inhomogeneous deformation, which in turn induces cell alignment (contact guidance). This results in cell traction and migration preferentially in the direction of cell alignment, affecting how the cells further deform the network. The theory leads to a set of coupled integro-partial differential equations. In the biphasic model due to Barocas and Tranquillo [28], a collagen network phase contains also the cells and an interstitial solution phase contains mainly water. The cells exert traction on the surrounding network, which is balanced by the network viscoelasticity and interstitial flow. A finite element solution method was applied by Barocas and Tranquillo [29] to a specific isotropic model, yet still nonlinear.

6.4. Gas transport in the lungs. Alveolar duct model

The aim of this section is twofold; first we present recent developments in pulmonary gas diffusion with special emphasis on volume averaging method. Second, nonlinear mechanical models of lung alveolar duct are discussed.

6.4.1. Volume averaging and gas diffusion in the lungs. The structure of the lung has been presented in Section 2.2.10. A challenging problem is the study of the gas transport within the alveolar region. Following precisely the internal alveoli structure and the erythrocytes (RBC – red blood cells) within the lung is a task beyond existing mathematical tools. Hence the need for micro-macro approach.

Koulich et al. [312] derived the macroscopic diffusion equation by applying the method of volume averaging. For a detailed presentation of this method the reader is referred to the book by Whitaker [622]. It is worth noticing that, until now, the method has only been applied to transport problems (no deformability of matrix or skeleton).

The derivation of the model due to Koulich is simple and runs as follows. We consider a representative elementary volume element (Fig. 66c). The alveolar region has earlier been presented in Fig. 22. Here, in Fig. 66A we see a similar structure of the lung (dog). The main constituents of the porous region are (Fig. 66B): the alveolus region (a), the alveolus membrane (m), the interstitial fluid region (f), the capillary membrane (c), the plasma region (p), the red blood cell membrane (r), and the red blood cell interior (h). It is usual to lump regions (m), (c), and (p) into one single representative region, denominated here by the tissue region (t), mainly because these constituents have comparable molecular gas diffusivities, cf. Hsia et al. [245]. The gas diffusion transport is driven by the gas concentration along the outer boundary of the alveolar region and the gas concentration within each RBC interior (inner boundary).
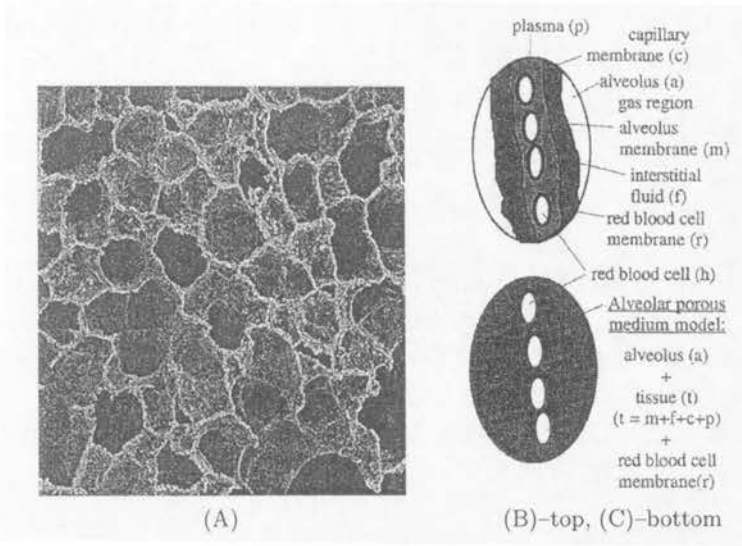
FIGURE 66. (A) scanning electron micrograph of the lung alveaolar region, (B) microscopic level, with all individual constituents, (C) intermediate level, as a representative elementary volume (REV), after Koulich et al. [312].

The microscopic equation modelling the isothermal diffusion of an ideal gas within each alveolar constituent is written as follows:

$$\frac{M}{RT}\frac{\partial P}{\partial t} = -\operatorname{div}\mathbf{j}, \qquad (6.33)$$

where M is the molecular mass of the gas, R is the universal gas constant, T is the absolute temperature of the gas, P is the partial pressure of the gas, and $\mathbf{j}$ is the flux of solute (gas). We observe that from the ideal gas law, $P = c(RT/M)$, where c is the representative gas concentration.

Assuming a Fickean-type diffusion we have

$$\mathbf{j} = -\frac{DM}{RT}\nabla P, \qquad (6.34)$$

where D is the gas molecular diffusivity (D accounts also for the solubility of the gas in a nongaseous medium, e.g. within the tissue region; in this case D becomes the so-called *Krogh diffusion coefficient* which is the product of both the Fick diffusion coefficient and the solubility coefficient). From (6.33) and (6.34) we get

$$\frac{\partial P}{\partial t} = D\Delta P, \qquad (6.35)$$

where Δ denotes the laplacian ($\Delta = \nabla^2$).

For a *three-constituent model* of the alveolar region (alveolus (a), tissue (t), and RBC membrane (r)), one can write the diffusion equation and appropriate boundary, interface and initial conditions. For instance, for the alveolus (a)–region we write

$$\frac{\partial P_a}{\partial t} = D_a \Delta P_a, \tag{6.36}$$

where P_a and D_a are the partial pressure and the molecular diffusivity of the gas within the alveolus region. The notation D_t, D_r, P_t, and P_r is obvious.

Denoting by V the REV, and by V_i the domain in V occupied by constituent 'i' ('i' can be (a)–region, (t)–region, or the RBC membrane (r)–region), we introduce an intrinsic average of the partial pressure P_i as follows:

$$\langle P \rangle_i = \frac{1}{|V_i|} \int\limits_{V_i} P_i dV, \tag{6.37}$$

where $|V_i|$ = the volume of V_i. We now write $P_i = \langle P_i \rangle + \tilde{P}_i$, where $\tilde{P}_i$ denotes *the fluctuation* of P_i from the averaged-volume $\langle P_i \rangle$. Using now the procedure of volume averaging and solving the so-called *closure problem*, cf. Whitaker [622] we finally obtain

$$\frac{\partial \langle P \rangle}{\partial t} = D_{\text{eff}} \Delta \langle P \rangle, \tag{6.38}$$

where D_{eff} is the effective diffusivity coefficient of the lung given by

$$\begin{aligned} D_{\text{eff}} = &\frac{1}{|V|} \left(|V_a| D_a + |V_t| D_t + V_r| D_r| \right) \\ &+ \frac{1}{|V|} \left[(D_a - D_t) d_a + (D_t - D_r) d_t \right]. \end{aligned} \tag{6.39}$$

Here d_i are scalar coefficients appearing in the closure equation:

$$\int\limits_{A_{ij}} \mathbf{n}_{ij} P_i dA = d_i \nabla \langle P \rangle, \tag{6.40}$$

(no summation over i). A_{ij} are interfaces and $\mathbf{n}_{ij}$ normal unit vectors; for instance A_{at} denotes the alveolus-tissue interface, with the normal unit vector $\mathbf{n}_{at}$.

We observe that the literature on the estimation of D_{eff} in the context of composite and micromechanics is vast, cf. Cherkaev and Kohn [80], Jikov et al. [287], Milton [396], Tokarzewski and Telega [582], Torquato [583], Whittaker [622] and the relevant references therein. Unfortunately, the problem of

the determination of D_{eff} for porous materials becomes more complex since Eq. (6.39) requires the knowledge of regions (and their boundaries) occupied by each constituent within the alveolar domain. To overcome this difficulty, the effective diffusivity D_{eff} is calculated indirectly by using the *lung diffusing capacity* D_L.

The lung diffusing capacity obtained in laboratory results from unsteady processes, such as the diffusion during the single-breath technique (Comroe et al. [91]). This technique consists of having a gas mixture with a low concentration of CO inhaled, held for a certain period of time (usually ten seconds) and then exhaled. During this single-breath process CO diffuses from the gas region of the alveolus to the RBC's. The process is unsteady because the potential gradient (i.e. the CO concentration within the gas region) driving the diffusion varies (decays) in time.

The lung diffusing capacity D_L of the alveolar region can be obtained from the single-breath technique results using the Krogh equation (Comroe et al. [91]):

$$\langle P \rangle(t) = \langle P \rangle_0 e^{-(D_L P_{\text{ref}}/V_A)t}, \tag{6.41}$$

where $\langle P \rangle$ is the result of volume-averaging $\langle P \rangle$ over the entire REV-domain, and $\langle P \rangle_0 = \langle P \rangle(0)$ (i.e. for $t = 0$). The reference pressure P_{ref} is chosen as the total pressure of dry gases ($P_{\text{ref}} = 9.51 \times 10^4 \, \text{Pa} = 713 \, \text{mm Hg}$), and V_A is the alveolar volume equal to the inspired volume plus the residual lung volume (a representative, normal, value is $V_A = 4.93 \times 10^{-3} \, \text{m}^3$).

From Eq. (6.41) we readily obtain

$$D_L = \frac{V_A}{t P_{\text{ref}}} \ln \left[\frac{\langle P \rangle_0}{\langle P \rangle(t)} \right]. \tag{6.42}$$

During clinical single-breath tests, Eq. (6.42) is used for determining the lung diffusing capacity by measuring the gas partial-pressure in the inhaled mixture $\langle P \rangle_0$, the total test time t and the gas partial-pressure in the exhaled mixture $\langle P \rangle(t)$. The relationship between D_L and D_{eff} was discussed in Koulich et al. [312]. The order-of-magnitude estimates of these coefficients are: $P_{\text{ref}} \sim 10^5 \, \text{Pa}$, $D_L \sim 10^{-9} \, \text{m}^3/\text{s Pa}$, $D_{\text{eff}} \sim 10^{-7} \, \text{m}^2/\text{s}$. RBC distribution within the alveolar domain was also investigated. For instance, Fig. 67 depicts the time evolution of the diffusion process for the case of centre-cluster distribution. The RBC's are clustered inside the centred cube shown in the top-left frame, where the partial pressure is always zero ($\langle P \rangle = 0.0 \, \text{Torr}$). Each frame, corresponding to a certain time during the single-breath test, shows the isosurface corresponding to $\langle P \rangle = 0.1 \, \text{Torr}$ (this value is ten percent of the initial partial pressure value). We observe how the isosurface $\langle P \rangle = 0.1 \, \text{Torr}$ (1 Torr=133.3 Pa) moves away from the RBC cluster (at the centre of the
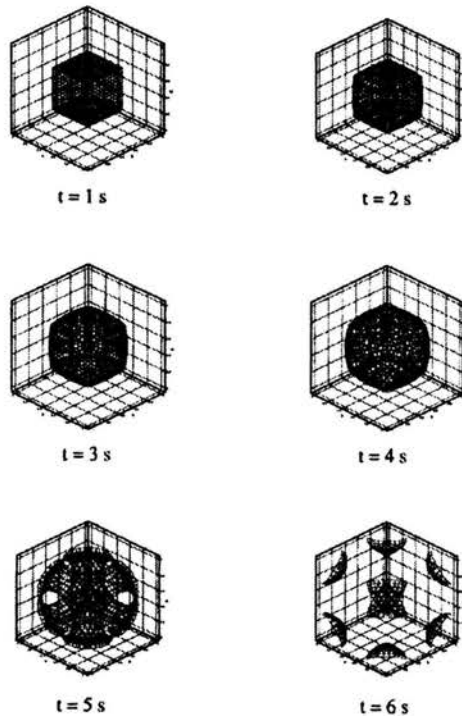
FIGURE 67. Time-evolution of isoconcentration surface $\langle P \rangle = 0.1$ Torr, for the case of RBC's clustered in the centre of the domain (REV). As the CO is progressively consumed by the RBC's in the cluster, the isoconcentration surface expands toward the boundaries of the domain where the gas concentration is higher, after Kulish et al. (2002).

domain where the partial pressure is initially higher (i.e. $\langle P \rangle = 1.0$ Torr). This evolution indicates the directional depletion of CO within the domain, from low (centre) to high (boundaries) partial pressure (or concentration) regions.

Remark 14. Whiteley et al. [623] proposed a mathematical model of pulmonary gas transport that takes account of dissolved oxygen, oxygen bound to haemoglobin, dissolved carbon dioxide bound to reduced haemoglobin, hydrogen ions and bicarbonate ions. An individual red blood cell together with the surrounding plasma and membrane is shown in Fig. 68. The governing equations comprise the alveolar membrane, red blood cell, and plasma (plus boundary and initial conditions). Only transport equations were investigated (no deformability).

Alvelar Gas

Alveolar Membrane a_T

Plasma

Red Blood Cell

a_R a_c

y

x l
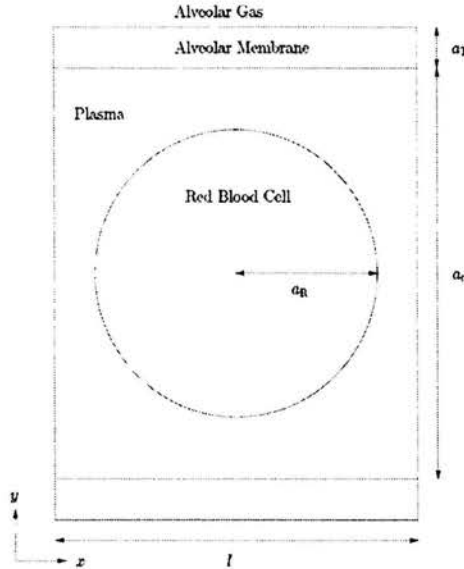
FIGURE 68. Model of red blood cell and the surrounding constituents, after Whiteley et al. [623].

6.4.2. Tissue-gas interaction in lung. The mechanical behaviour of mammalian lung tissue (parenchyma) is nonlinear. From Section 2.2.10 we know that its geometric structure is very complex. Models of parenchymal elasticity have been widely used to investigate micromechanical propertiesof the mammalian lung. The models can be classified as those consisting purely of alveoli and those consisting of an alveolar duct unit: a ductal airspace surrounded by alveoli with alveolar mouths open to the duct lumen, see the relevant references in Denny and Schroter [130]. According to the last authors, a weakness in purely alveolar models is that they simplify parenchymal structure by neglecting the presence of a duct lumen surrounded by alveolar mouths through which the alveoli are ventilated. The assumption that parenchyma is comprised solely of septa covered with a liquid lining ignores important interactive coupling effects between the connective tissue in the alveolar mouths and the tissue plus surface tension in the septa. Hence the need for more elaborate mathematical models. A brief outline of earlier investigations was sketched by Denny and Schroter [130]. The authors themselves proposed a new micromechanical alveolar duct model (Denny and Schroter [128, 130]. The model is volume filling, it contains a duct lumen surrounded by alveolar mouths through which the surrounding alveoli are ventilated, it allows the septal tissue to make a contribution to the recoil pressure, and it yields a pressure-volume (P–V) behaviour that qualitatively compares well

with experimental data. Now we proceed to the presentation of the model developed by Denny and Schroter [128, 130].

Alveolar duct geometry

The alveolar duct unit is modelled as an assemblage of 36 truncated octahedra. The four central polyhedra have all their faces open to form a longitudinal duct lumen surrounded by 32 alveolar polyhedra, each with either a square, or hexagonal, or both a square and a hexagonal face open to the duct, cf. Fig. 69. Such an idealization renders the alveolar duct a complex cellular material.

(a)   (b)
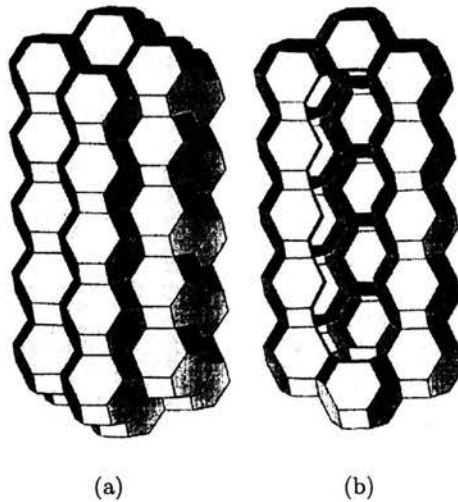
FIGURE 69. (a) An assembly of truncated octahedra modelling an alveolar duct surrounded by alveoli; (b) front facing polyhedra are removed to reveal the internal structure of the longitudinal duct airspace, after Denny and Schroter [130].

The network of elastin and collagen connective tissue fibre bundles is represented by pin-jointed line elements lying around the alveolar mouths, along the septal junctions, and across the alveolar walls, cf. Fig. 70.

The volume of each polyhedron and the length densities of its line elements are uniquely defined by L_s, the length of each edge or septal border segment. The cross-sectional areas of elastin and collagen associated with the line elements, jointly with their respective length densities, determine the volume densities and distribution of the connective tissue. We observe that the model does not include the septal border features formed by the junction of two septal walls. According to Denny and Schroter [130] such a simplification still yields acceptable results.
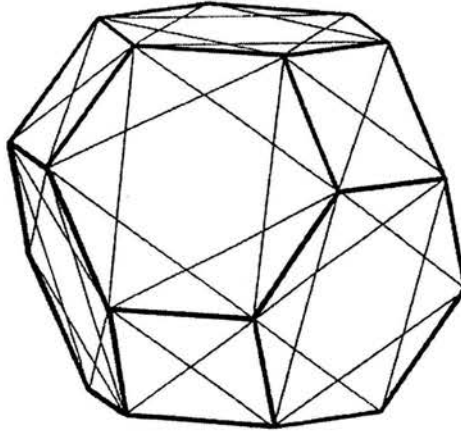
FIGURE 70. Geometry of a single truncated octahedron showing the idealized arrangement of the fibre bundles along the septal faces, after Denny and Schroter [130].

Alveolar duct dimensions and connective tissue fibre bundle cross-sectional areas

At maximum inflation, L_s is taken to be $82\,\mu m$, implying a maximum alveolar caliper diameter of $200\,\mu m$. The connective tissue cross-sectional areas are given in Table 8.

TABLE 8. Amounts and distributions of connective tissue line elements in the alveolar duct model, after Denny and Schroter [130].

	Fibre Bundle Element Type	
	Alveolar Mouth (AM)	Alveolar Septa (AS)
Length Density	$30L_s/56\sqrt{2}L_s^3$	$(54+126\sqrt{3}+30\sqrt{2})L_s/56\sqrt{2}L_s^3$
Collagen Fibres		
cross sectional area (μm^3)	19.64	8.77
distribution (%)	17.6	82.4
Elastin Fibres		
cross sectional area (μm^3)	14.03	4.74
distribution (%)	22.0	78.0

At maximum inflation, the volumetric strain of the alveolar duct unit, defined as $(V_{\max} - V_0)/V_0$, is set to be 5, where $V_{\max}$ and V_0 refer to the maximum volume and volume at $0\,cm\,H_2O$, respectively. Assuming that the fibre volumes remain constant and that the alveolar dimensions vary as $V^{1/3}$, the alveolar mouth elastin and collagen fibre bundle diameters can be estimated to be $4.2\,\mu m$ and $5\,\mu m$, respectively, at $0\,cm\,H_2O$ inflation pressure.
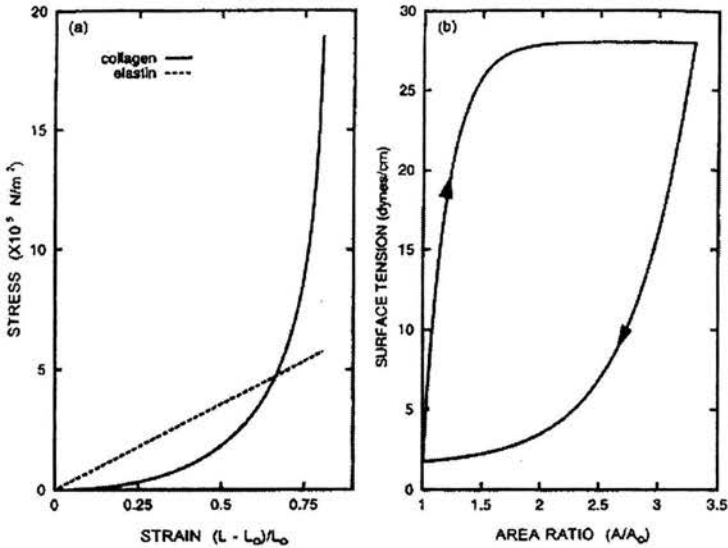
FIGURE 71. Assumed mechanical characteristics of the load-bearing components contained in the model: (a) the stress-strain relationships for the network of elastin and collagen fibre bundles; (b) the area-dependent relationship used to model the surface tension of the air-liquid interface, after Denny and Schroter [130].

Connective tissue stress-strain relationships

Though morphological investigations show that the collagen and elastin fibre bundles are often to some extent interwoven (cf. the relevant references in Denny and Schroter [130]), yet separate stress-strain laws can be chosen to reflect the functional independence of the elastin and collagen fibre networks. The Young modulus of elastin fibres is $7.1 \times 10^5 \, \mathrm{Nm^{-2}}$. It is known that elastin provides the stability to the alveolar septal configurations over wide ranges of lung volume, anchoring them in space. The high stiffness and low distensibility of the collagen fibres have the role of preventing lung rupture at maximal lung volumes. Individual collagen fibres fracture at strains as low as only 2 percent and have the considerably higher Young's modulus of $1 \times 10^9 \, \mathrm{N \, m^{-2}}$, cf. the relevant references in Denny and Schroter [130].

The stress-strain relationships are shown in Fig. 71(a). The line elements modelling the collagen fibre bundles exhibit a highly nonlinear behaviour:

$$T = c_1 \log \left[1 - \left(\frac{\exp(\lambda) - 1}{c_2} \right) \right] + c_3 \lambda, \qquad (6.43)$$

where T is the stress, $\lambda = (L - L_0)/L_0$, L and L_0 are the current fibre bundle length and its length at $0 \, \mathrm{cm \, H_2O}$. The constants are given by: $c_1 =$

$-22.5 \times 10^5 \, \text{N m}^{-2}$, $c_2 = 1.26$, $c_3 = -17.8 \times 10^5 \, \text{N m}^{-2}$. We observe that in Fig. 71(a), the maximum strain of 0.817 is equivalent to a maximum duct volumetric strain of 5.

Surface tension of the liquid-gas interface

The surface tension of the *liquid-gas interface* plays an important role in causing the difference between the inflation and deflation paths, cf. the relevant references cited in Denny and Schroter [130]. The surface tension relationship for the inflation path is modelled by

$$\gamma = \gamma_{\max} \left[1 - a_1 \exp \left(-a_2 \frac{S}{S_0} \right) \right], \tag{6.44}$$

whilst the deflation path is described by the following equation

$$\gamma = \gamma_{\min} \left[1 + b_1 \exp \left(b_2 \frac{S}{S_0} \right) \right]. \tag{6.45}$$

Here γ is the current value of surface tension, $\gamma_{\max} = 28.0 \, \text{dyn/cm}$ is its maximum value, $\gamma_{\min} = 1.5 \, \text{dyn/cm}$ is its minimum value, S is the current surface area, and S_0 is the initial surface area. The constants are given by $a_1 = 140.46$, $a_2 = 5.0$, $b_1 = 0.024$ and $b_2 = 2.0$. The relationships (6.44) and (6.45) are depicted in Fig. 70(b).

We observe that such a description of inflation and deflation is not complete since there is no criterion from passing from the inflation to deflation paths, cf. Kowalczyk and Kleiber [313]. The situation formally resembles pseudoelastic behaviour discussed in Section 8 of our Notes.

Using the introduced model, Denny and Schroter [130] presented the results of numerical calculations obtained by using a nonlinear large displacement formulation of the finite element method.

Remark 15.

(i) An alternative approach to modelling tissue-gas interaction in the lungs was earlier proposed by Kowalczyk and Kleiber [313]. These authors considered lung parenchyma as a two-phase medium, composed of fluid and solid phases. The fluid phase is a gas treated as an incompressible fluid or, in some cases, as a barotropic fluid. Filtration is described by the Darcy-type law where the permeability depends in a nonlinear manner on the porosity and $J^{(s)}$, where $J^{(s)}$ denotes the determinant of the gradient of deformation of the solid phase. The latter is made of nonlinear hyperelastic material. The approach employed by Kowalczyk and Kleiber [313] falls within the framework of nonlinear poroelasticity, cf. Coussy [96].

The reader is advised to compare the results due to Denny and Schroter [130] and Kowalczyk and Kleiber [313].

(ii) Basing on the results available in the literature, Romero et al. [483] proposed a model of the lung as a material composed of two phases, a continuous phase (matrix) that acts uninterruptedly and a second phase composed of fibre elements that are recruited progressively into the mechanical process. A nine-parameter model was elaborated, adopting standard linear viscoelastic elements both for the linear matrix and for each of the fibres. In essence, a given element is incorporated in the mechanical response of the lung once a threshold value is reached (recruitment). We have already met such a modelling used for ligaments and tendons. Now the lung model is nonlinear, in fact piecewise linear, and viscoelastic. The predictions of the model were compared with the experimental data obtained by studying only one 270 g male Wistar rat lung. For details the reader is referred to Romero et al. [483].

(iii) De Buhan et al. [63] proposed an approach to micro-macro modelling of fluid saturated hyperelastic porous materials. In essence, these authors extend to such materials the approach used earlier by Hill [234] and Ogden [425] for the determination of the overall response of microinhomogeneous elastic solids undergoing finite strains. The framework proposed can only be an approximate one since the overall response is obtained by averaging over a representative elementary volume (REV) with boundary conditions typical for the self-consistent method. The paper by de Buhan et al. [63] is not complete since the filtration equation, which should be a nonlinear Darcy-type law, was not derived. Also the notation used is sometimes surprising and sometimes confusing. For instance $\mathbf{\Delta}$ denotes the Green-Lagrange strain tensor (thus $\mathbf{\Delta} = \mathbf{E}$); $d\Omega_t$ denotes an elementary volume element at time t.

7. Description of active stresses in contractile soft tissues

In contractile soft tissues (skeletal, heart, and smooth muscles) the total stress is the sum of passive and active stresses.

7.1. Heart muscle

We will present two approaches. The first is due to Tanaka et al. [560]. These authors developed a transversely isotropic 3D model of ventricular walls, taking into account the excitation-contraction coupling. The phenomenon of excitation-contraction may be summarized as follows:

(i) The generation of tension or contraction of the cardiac muscle is controlled by the concentration of Ca^{2+} in the cell.

(ii) There are threshold and saturated values in the response for the concentration of Ca^{2+}.

(iii) In the process mentioned, the subsequent stage is caused by the preceding one, and time is needed for the reaction in each stage. In other words, a time delay is induced in each stage. Consequently, it may be supposed that the concentration of Ca^{2+} influences the rate, or higher time derivatives of the tension or contraction.

The mechanical behaviour of ventricular walls was simplified as follows:

1. Ventricular walls are incompressible.

2. Mechanical properties in the plane perpendicular to the muscle fiber are isotropic, i.e., ventricular walls are transversely isotropic.

3. Mechanical properties of ventricular walls are passive in the directions perpendicular to the muscle fibre. Thus the active properties are observed only in the muscle fibre direction.

4. Viscoelastic properties of ventricular walls can be neglected.

5. The stress acting on the ventricular walls is expressed as the sum of passive stress $\mathbf{T}^p$ and active stress $\mathbf{T}^a$; that is the second Piola-Kirchhoff stress tensor $\mathbf{T}$ is given by

$$\mathbf{T} = \mathbf{T}^p + \mathbf{T}^a. \tag{7.1}$$

The passive stress $\mathbf{T}^p$ can be expressed by,

$$\mathbf{T}^p = \frac{\partial(\rho_r W)}{\partial \mathbf{E}}.$$

The strain energy density function $\rho_r W$ is assumed in the form

$$\rho_r W(\mathbf{E}) = a \exp \Psi(\mathbf{E}) + p[\det(2\mathbf{E} + \mathbf{I}) - 1]. \tag{7.2}$$

We recall that ρ_r denotes the mass density in the undeformed configuration.

According to the previous assumption (3), the active stress $\mathbf{T}^a$ can be expressed by

$$\mathbf{T}^a = \tau^a \mathbf{M}, \tag{7.3}$$

where $\mathbf{M} = \mathbf{m} \otimes \mathbf{m}$ is the structural tensor and τ^a is the activated stress caused by the activation. The maximum value of τ^a depends on the length of the cardiac muscle because the maximum number of cross-bridges between myosin and actin filaments, which determines the maximum value of the

tension, differs with the length of the muscle. The magnitude of tension is also governed by the activity that expresses the ratio of bonding of troponin with Ca^{2+}, that is, the ratio of active filaments. The activity and the strain of muscle fibres are denoted by α and E_m, respectively. It can be shown that

$$E_m = \mathbf{Em} \cdot \mathbf{m}. \tag{7.4}$$

Suppose that the cardiac muscle is soaked in Ca^{2+} solution of a constant concentration for a sufficiently long time under the condition of constant length. Consequently, the active stress τ^a will tend to the asymptotic value τ^{as}. It may be assumed that

$$\tau^{as} = \hat{\tau}^{as}(E_m, \alpha) = \tau^{as}_{\max} F(E_m) A(\alpha). \tag{7.5}$$

Here $F(E_m)$ and $A(\alpha)$ are the normalized functions expressing the dependence of E_m and α on τ^{as}, respectively, and $\tau^{as}_{\max}$ is a constant representing the maximum value of active stress.

The current value of active stress is a solution of the following simple evolution equation

$$\dot{\tau}^a = \frac{d\tau^a}{dt} = b(\tau^{as} - \tau^a), \qquad \tau^a(0) = \tau_0, \tag{7.6}$$

where b is a material constant specifying the rate of change. The last equation describes physically observed delay existing between the generation of contractions and tension, which is not induced immediately after the change of action potential or the rise of the concentration of Ca^{2+}.

More general relation:

$$\dot{\tau}^a = f(t, \tau^{as} - \tau^a), \quad \tau^a(0) = \tau_0$$

can also be envisaged.

The functions F, A are assumed to be specified by

$$F(E_m) = \left\langle (1 + F_0) \exp\left\{ -\left[\frac{E_m - E_{m0}}{\Delta E_m} \right]^2 \right\} - F_0 \right\rangle, \tag{7.7}$$

$$A(\alpha) = \langle 1 - \exp[-m(\alpha - \alpha_{ths})] \rangle, \tag{7.8}$$

respectively. Here E_{m0} is the value of E_m at the maximum tension, ΔE_m is the half of the range of E_h generating the tension, and F_0 is the material coefficient. The symbol $\langle \cdot \rangle$ denotes the Macauley bracket. Moreover, m is the material constant and α_{ths} is the value corresponding to the threshold of Ca^{2+} that can generate the tension. The function $F(E_m)$ was determined

on the basis of the relationship between the sarcomere length and tension. $A(\alpha)$ was formulated with reference to the relationship between the tension and concentration of Ca^{2+} at the saturated state, cf. the relevant references in Tanaka et al. [560].

The evolution equation

$$\dot{\alpha} = c(\beta - \alpha), \tag{7.9}$$

yields satisfactory predictions for the experimental data. Here β denotes the concentration of Ca^{2+}, and c is the material coefficient. The last equation is viewed as describing the diffusion of Ca^{2+} and the bonding process of troponin.

The concentration β was assumed in the following form

$$\beta = \beta_0 t^k \exp(-lt), \tag{7.10}$$

where β_0, k and l are material constants.

The calculations were performed by assuming that $\Psi(\mathbf{E})$ is given by the transversely isotropic Saint-Venant Kirchhoff model. It seems that the calculations performed by Tanaka et al. [560] are reduced to isotropic model:

$$\Psi(\mathbf{E}) = \lambda(\mathrm{tr}\mathbf{E})^2 + 2\mu\mathrm{tr}\mathbf{E}^2. \tag{7.11}$$

The material constants were identified as follows (uniaxial case): $\lambda = 34.0$, $\mu = 5.0$, $a = 0.2\,\mathrm{kPa}$, $\tau_{max}^{as} = 107.9\,\mathrm{kPa}$, $E_{m0} = 0.322$, $\Delta E_m = 0.205$, $F_0 = 0.032$, $m = 0.16\,1/(\mathrm{mM})$, $\alpha_{ths} = 0.56\,\mathrm{mM}$, $\beta_0 = 0.0326\,\mathrm{mM}/(\mathrm{ms})^k$, $k = 1.0$, $l = 0.004\,(\mathrm{ms})^{-1}$, $b = 0.007\,(\mathrm{ms})^{-1}$, $c = 0.018\,(\mathrm{ms})^{-1}$. Typical results for $A(\alpha) = 1$ are presented in Fig. 72.

Consider now another approach, this time formulated in terms of Cauchy's stress tensor. We largely follow Huphrey [255]. Unlike skeletal muscle in which maximal active force generation occurs at a sarcomere length that optimizes myofilament overlap ($\sim 2.1\,\mu\mathrm{m}$), the isometric tension developed by isolated cardiac muscle continues to rise with increased sarcomere length in the physiologic range (1.6–$2.4\,\mu\mathrm{m}$). The increase with ventricular volume of end-systolic pressure and stroke work is reflected in isolated muscle as a monotonic increase in the peak isometric tension with sarcomere length, cf. Fig. 73

We observe that the active tension shown in this figure is the total tension minus the resting tension, which, unlike in the skeletal muscle, becomes significant at sarcomere lengths over $2.3\,\mu\mathrm{m}$.

The relationship between cytosolic calcium concentration $[Ca^{2+}]$ and muscle tension has been studied in skinned muscle.

Myofilaments are activated in a graded manner by increasing the micromolar concentrations of calcium, which binds to troponin C according to Michaelis-Menton kinetics (Rüegg [493], Humphrey [255]). Half-maximal tension in cardiac muscle is developed at calcium concentrations of 10^{-5} M (the median effective concentration (EC_{50})) depending on factors such as species and temperature (cf. Bers [35]). Then the relative isometric (one-dimensional) stress $\sigma_0/\sigma_{\max}$ may be modelled as follows, cf. Tözeren [585],

$$\frac{\sigma_0}{\sigma_{\max}} = \frac{[\mathrm{Ca}^{2+}]^n}{[\mathrm{Ca}^{2+}]^n + C_{50}^n}, \tag{7.12}$$

where the Hill coefficient $n = 2$ and C_{50} is the value of $[\mathrm{Ca}^{2+}]$ at which σ_0 equals one-half of $\sigma_{\max}$, the maximum stress generated at an unloaded length (i.e. fibre stretch $\lambda = 1$ and sarcomere length $L = 1.9\,\mu\mathrm{m}$). Furthermore, based on experimental data from rat cardiac muscle, the C_{50} in micromolars is (Guccione et al. [206]):

$$C_{50} = \frac{4.35}{\sqrt{e^{4.75(L-1.58)} - 1}}, \tag{7.13}$$

where L is the sarcomere length in microns.

General conclusion is that the active stress can be modelled as follows, cf. Hunter et al. [261],

$$\sigma(\lambda, [\mathrm{Ca}^{2+}]) = \frac{[\mathrm{Ca}^{2+}]^n}{[\mathrm{Ca}^{2+}]^n + C_{50}^n}\sigma_{\max}(1 + \beta(\lambda - 1)), \tag{7.14}$$
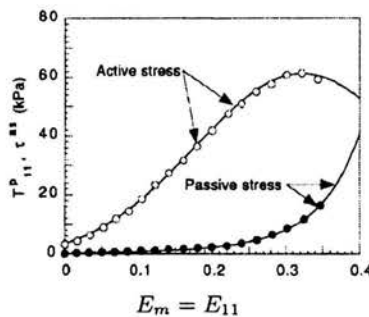
FIGURE 72. Passive stress versus cardiac muscle fibre strain relationship (*solid line*, calculated result; *solid circles*, experimental data) and relationship of maximum of the isometric tension versus cardiac muscle fibre strain (*solid line*, calculated result; *open circles*, experimental data) of the papillary muscles of a cat; after Tanaka et al. [560]. Experimental data were taken from the literature.
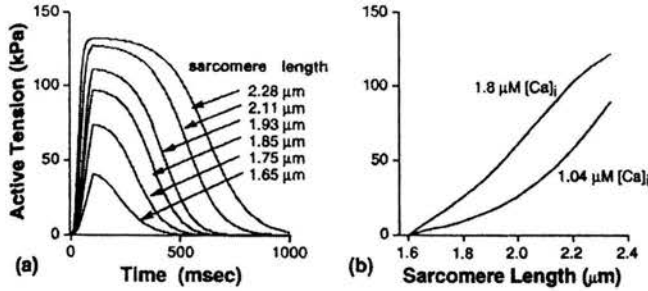
FIGURE 73. Active tension versus time at various sarcomere lengths and tension versus length at two concentrations of calcium, after McCulloch [376].

where β is a material parameter ($\beta = 1.45$ is evidence for length dependent binding of Ca^{2+}) and $\sigma_{max} \approx 100\,kPa$.

Closer inspection of the literature reveals that many formulations of cardiac muscle response are available. In essence, most employ the assumption that cardiac active stress is generated only in the direction of the muscle fibre. It means that the total Cauchy stress assumes the following general form, cf. (7.14),

$$\boldsymbol{\sigma} = \boldsymbol{\sigma}^p + \boldsymbol{\sigma}^a = -p\mathbf{I} + \mathbf{F}\frac{\partial W}{\partial \mathbf{E}}\mathbf{F}^T + \sigma(\lambda, [Ca^{2+}])\tilde{\mathbf{m}} \otimes \tilde{\mathbf{m}}, \qquad (7.15)$$

where $\tilde{\mathbf{m}}$ denotes the current muscle direction, i.e. $\tilde{\mathbf{m}} = \mathbf{Fm}$. We observe that the presence of $-p\mathbf{I}$ ignores changes in volume due to perfusion.

7.2. Active stresses in arteries (smooth muscle contractility)

A seminal paper by Rachev and Hayashi [469] started investigation pertaining to modelling active mechanical behaviour of arterial wall developed by the contraction of stimulated vascular smooth muscle cells. The active response results in a change of wall diameter and thickness, and obviously affects the stress and strain distribution in the wall. Arteries were assumed to be thick-walled orthotropic tubes made of nonlinear and incompressible elastic material. Influence of residual strains was also discussed. To model passive behaviour logarithmic strain energy function was employed. As we have already mentioned, a comprehensive presentation of residual strains and stresses will be given in our forthcoming paper [570].

Here we prefer to present a simpler model due to Rachev [467]. In this paper the author considers an artery as a circular membrane made of nonlinear elastic and incompressible orthotropic material. Exploiting some experimental data that in some cases an artery remodels without changing significantly its structure and composition, mechanical properties are considered

to be constant during the remodelling process, cf. the relevant references in Rachev [467]. Since the arterial wall is assumed to be an elastic membrane, the circumferential and axial stresses are considered to be uniformly distributed across the wall thickness, while the radial stress is assumed zero everywhere. Then the artery is in the zero-stress state. Consequently the assumptions made by Rachev [467] exclude the existence of residual strains and stresses in the arterial wall of the unloaded arterial segment. Hence we conclude that the state of no load when the smooth muscle is fully relaxed is accepted as a reference state. Under applied loads the artery undergoes an axisymmetric finite deformation. The mean stretch ratio in the longitudinal and circumferential directions are given by

$$\lambda_z = \frac{l}{L}, \quad \lambda_\theta = \frac{r}{R}, \tag{7.16}$$

where R and r are the mid-wall radii of the artery in the reference and deformed configuration, respectively. The nonvanishing components of the Green strain tensor are specified by

$$E_z = \frac{1}{2}(\lambda_z^2 - 1), \quad E_\theta = \frac{1}{2}(\lambda_\theta^2 - 1). \tag{7.17}$$

The passive axial and circumferential Cauchy stresses are specified by

$$\sigma_z^{(p)} = \lambda_z^2 \frac{\partial W}{\partial E_z}, \quad \sigma_\theta^{(p)} = \lambda_\theta^2 \frac{\partial W}{\partial E_\theta}, \tag{7.18}$$

where $W(E_z, E_\theta)$ is the strain energy function. For calculations, an anisotropic (orthotropic) function was assumed:

$$W = a_1 E_z^2 + a_2 E_\theta^2 + 2a_3 E_z E_\theta + a \exp(b_1 E_z^2 + b_2 E_\theta^2 + 2b_3 E_z E_\theta), \tag{7.19}$$

where a, a_i, b_i ($i = 1, 2, 3$) are material coefficients.

The active circumferential Cauchy stress is assumed in the form

$$\sigma_\theta^{(a)} = c\phi\lambda_z F(\lambda_z), \tag{7.20}$$

where $c = [\mathrm{Ca}^{2+}]$ is the calcium ion concentration, which exceeds the threshold concentration capable of initiating the active response (the contractile activity of smooth muscle cells occurs when the intercellular concentration of Ca^{2+} exceeds a threshold concentration of $10^{-7}\,\mathrm{M}$); ϕ is the ratio of area occupied by the smooth muscle cells to the total area, both having a normal in the circumferential direction; $F(\lambda_\theta)$ is a function that accounts for the length-active tension relationship. For fixed values of c and ϕ the function

$F(\lambda_\theta)$ is proportional to the circumferential Lagrangian stress (defined per unit undeformed area). The stretch ratio λ_θ in Eq. (7.20) accounts for the fact that the actual active Cauchy stress $\sigma_\theta^{(a)}$ is defined per unit of deformed area.

Equation (7.20) has to be completed with an evolution equation for c. For a specific form of such an equation the reader is referred to Rachev [467]. This author provided also examples of remodelling for the case of both increased and decreased flow.

Remark 16. Humphrey and Rajagopal [257] proposed a rather complex model applicable to growth and remodelling of large arteries. Critical discussion is deferred to our paper [570]. Here we provide only a general equation for the total Cauchy stress tensor $\boldsymbol{\sigma} = \boldsymbol{\sigma}^{(p)} + \boldsymbol{\sigma}^{(a)}$, being a sum of the passive part $\boldsymbol{\sigma}^{(p)}$ and active part $\boldsymbol{\sigma}^{(a)}$:

$$\boldsymbol{\sigma} = -p\mathbf{I} + \frac{1}{2}ae^{\Psi}\mathbf{F}\frac{\partial\Psi}{\partial\mathbf{E}}\mathbf{F}^T + \sigma_0(c)\lambda_\theta\left[1 - \left(\frac{\lambda_m - \lambda_\theta}{\lambda_m - \lambda_0}\right)^2\right]\mathbf{e}_\theta \otimes \mathbf{e}_\theta, \quad (7.21)$$

where $\Psi(\mathbf{E})$ is assumed to be quadratic in terms of the (physical) components of the Green strain (cylindrical orthotropy, nine material coefficients), a is also a material coefficient and λ_m and λ_0 are circumferential stretches at which the contraction of the vascular smooth muscle is maximum or zero, respectively; σ_0 depends on the intracellular calcium and quantifies the degree of smooth muscle contraction. We recall that $c = [Ca^{2+}]$, cf. the previous section and $\mathbf{e}_\theta$ is the unit vector in the circumferential direction of the deformed artery. A specific expression for σ_0 was discussed by Humphrey and Rajagopal [257].

Equation (7.21) was also used by Humphrey and Wilson [260] in a study of potential importance of the mechanics in the early stages of hypertension, before structural or functional changes occur. Particularly implications to the transmural distribution of stress due to an immediate vasoactive response to a step-increase in blood pressure was investigated. It was shown computationally that a vasodilation would exacerbate hypertension-introduced increases in wall stress whereas a vasoconstriction can reduce both the magnitude and the transmural gradient of the stress. Consequently Humphrey and Wilson [260] suggest that vasoconstriction may be one of the first means by an artery to restore its wall stress (or strain) to normal values. The growth-regulatory effects of the associated vasoactive molecules may then help to set into motion the altered gene expression, that ultimately results in the thickened wall and endothelial dysfunction.

For more details on muscle activation the reader is referred to the book by Mizrahi [399] and the relevant papers in Herzog [232].

Values of the activation function of the smooth muscle $\sigma_0([Ca^{2+}])$ in Eq. (7.21) typically range from 0 to 100 kPa.

7.3. Skeletal muscle

It seems that studies on modelling macroscopic response of skeletal muscles where total stress is a sum of passive and active parts are scarce in the available literature. Here we shall only present the ideas exploited by Meier and Blickham (2000). Unfortunately the paper lacks many important details, and consequently only main ideas can be discussed.

The passive stress is described by polynomial in strain invariants, isotropic stored energy function. The active stress in the muscle fibre direction is described as the product of the isometric stress, an activation function f_t, a velocity function f_v, and a length function f_l. The fibre direction of each element is defined by two input angles. The model offers a possibility of examination of the influence of muscle geometry and fibre recruitment. For instance, one can study inertia effects of muscle.

8. Pseudoelastic behaviour of soft tissues

Pseudo-elastic behaviour, known also as the Mullins effect, of polymeric materials is a well-known phenomenon, cf. [429, 430]. Collagenous tissues exhibit similar property, due to the presence of collagen fibres. In the present section we exploit this approach to modelling the pseudoelastic effect of soft tissues both for isotropic and anisotropic tissues. We largely follow the papers by Jemioło and Telega [278, 282].

8.1. Some examples of pseudoelastic behaviour of soft tissues

If the tissue is loaded at a finite strain rate and then, its length is held constant it exhibits the phenomenon of stress relaxation, cf. Fung [175]. An example is shown in Fig. 74, for an anterior cruciate ligament, cf. also Section 6.

Another feature is worth noting. If a tissue is taken from an animal, put in a testing machine, tested for a load-elongation curve by a cycle of loading and unloading at a constant rate of elongation, left alone at the unstressed condition for a resting period of 10 min. or so until it has recovered its relaxed length, and then tested the second time, following the same procedure, the load-elongation curve will be found to be shifted, cf. Fig. 75. If the test is repeated indefinitely, the difference between successive cycles is decreased, and eventually disappears. Then the specimen is said to be *preconditioned*.
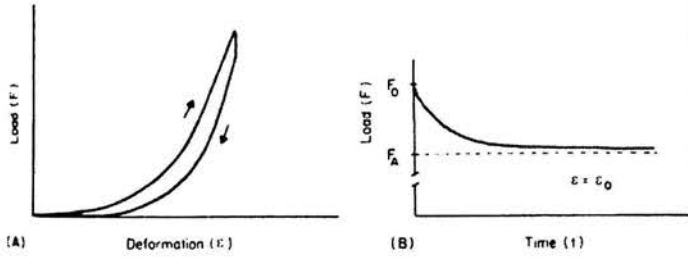
FIGURE 74. The load-elongation and relaxation curves of an anterior cruciate ligament specimen. In (A), the specimen was loaded to about one-third of its failure load and then unloaded at the same constant speed. In (B) the specimen was stretched at constant speed until the load reached F_0; then the stretching was stopped and the length was held constant. The load then relaxed, after Fung [175].
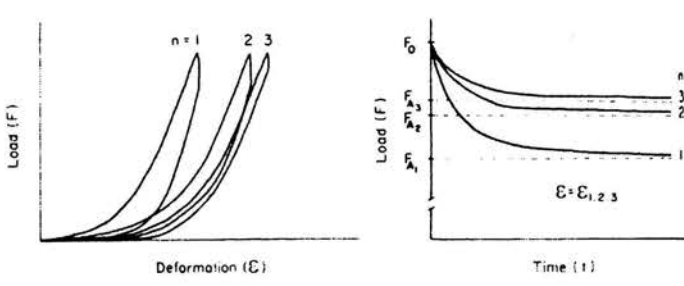
FIGURE 75. Preconditioning of an anterior cruciate ligament. The load-elongation and relaxation curves of the first three cycles are shown, after Fung [175].

Assuming that tissue is preconditioned, Fung [175] claims to have reduced the quasi-linear viscoelastic constitutive equation of a living tissue to a *pseudo-elastic* constitutive equation. Then, for the loading branch and the unloading branch separately, the stress-strain relationship is unique. According to Fung [175], since stress and strain are uniquely related in each branch of a specific cyclic process, we can treat the material as one elastic material in loading and another elastic material in unloading. In our opinion such an approach is misleading. In fact, we have always one material, and its cyclic behaviour is similar to the so-called Mullins effect in rubber-like materials, cf. Ogden and Roxburgh [429].

In the papers by Jemioło and Telega [278] and Jemioło et al. [282] a first step forward was done to avoid inconstistencies of Fung's approach.

Influence of prior temperature on pseudo-elastic behaviour of collageneous tissue was examined by Chen and Humphrey [75], cf. also Chen et

al. [71]. Heat-induced denaturation of collagen is an irreversible rate-process wherein the native helical structure is transformed into a more random coiled structure, cf. Chen and Humphrey [75] and the relevant references therein. The elasticity of soft tissues results primarily from changes in configurational entropy, not internal energy. Thus denaturation induces marked changes in the mechanical behaviour Chen and Humphrey [75] attempted to quantify these heat-induced changes in terms of the extend of prior thermal damage. For instance, the chemical outcome of heat-treated aneurysms, arteriovenous maltformations, artherosclerotic plaques, and corneas depends primarily on the post-heating structural integrity (e.g. properties) of the tissue.

Denaturation also results in an irreversible shrinkage of collagen, which is thereby a convenient measure of thermal damage. Chen et al. [71] performed measurements of heat-induced axial shrinkage ξ in chordae tendinae that was induced by various thermomechanical loads (i.e. isothermal heating at temperatures $T \in [65, 90]°$C, and constant uniaxial first Piola-Kirchhoff stresses $S \in [0, 0.65]$ MPa during heating). A single sigmoidal correlation between ξ and a nondimensional measure of heating time $\tau_h = \ln(\tau/\tau_2)$ for all 17 different thermomechanical loads where τ is the heating time and τ_2 a temperature and load dependent characteristic time. Chen and Humphrey [75] deduced that this suggests a time-temperature-load equivalency. These authors also found a time-dependent recovery of $\xi(\tau_r)$ towards an equilibrium value ξ_e, where τ_r is recovery time, when the tissue was returned to 37°C and $S = 0$ MPa following heating.

These findings led Chen and Humphrey [75] to conclusion that the stress-strain behaviour at 37°C, of collageneous tissue depends on the extent of prior thermal damage, not the specific thermomechanical history that induced the damage. This hypothesis was tested by the these authors for the case wherein the recovery achieves a near equilibrium. Cyclic uniaxial tests at 37°C on chordae tendinae before and well after 13 different thermomechanical heating protocols were performed. Changes in extensibility hysteresis and stiffness revealed that the effects due to prior heating can be parametrised by a single measure of thermal damage.

Details of the experimental device and methods for subjecting chordae tendinae to thermomechanical loads are to be found in Chen et al. [71].

The overall protocol consisted of (a) registering the original reference configuration, (b) collecting 10 cycles of load-controlled (i.e. S from 0 to 1 MPa) uniaxial data of $T_0 = 37°$C and 0.01–0.05 Hz, (c) allowing the specimen to "creep" for 20 min. at 37°C under a prescribed constant stress of $S \in [0, 0.65]$ MPa, (d) subjecting the specimen to isothermal heating at a $T \in [65, 90]°$C for $\tau \in [160 - 3600]$ s in the presence of an isotonic $S \in [0, 0.65]$ MPa, cf. Table 9.

TABLE 9. Thermomechanical histories that defined the 13 study groups: heating time (s) as a function of the isothermal temperature (in °C) and isotropic first Piola-Kirchhoff stress during heating (in MPa). Note that the recovery times were 20 min. for the free-shrinkage tests (i.e. $S = 0$ MPa) and 60 min. for all others, after Chen and Humphrey [75].

	0MPa	0.1 MPa	0.3 MPa	0.5 MPa	0.65 MPa
65 °C	160	1800			
70 °C		300	3600		
75 °C		300	600	900	
80 °C			420	600	900
85 °C				180	240
90 °C					180

Figure 76 visualizes this complex protocol via the configurations that the specimen assumes, where $\mathcal{B}_0$ denotes the original stress-free configuration, and $\mathcal{B}_s, \mathcal{B}_\tau, \mathcal{B}_{\tau_r}$ and $\mathcal{B}_c$ represents sequences of configurations during creep, heating, recovery, and cyclic mechanical loading, respectively. Deformation gradients are denoted by $\mathbf{F}$ with a subscript, and shrinkage by ξ. The 1-D
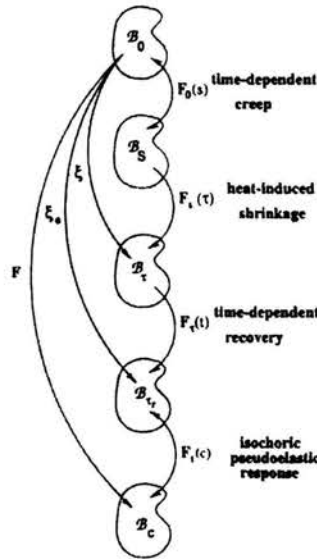
FIGURE 76. Scheme of the configurations assumed by a specimen during testing: s is creep time, τ heating time, τ_r recovery time, and c the sequence of equilibrium states under cyclic loading at 37°C. $\mathbf{F}_0(s)$ denotes the deformation gradient associated with the moving from $\mathcal{B}_0$ to $\mathcal{B}_s$, etc. Reversibility and irreversibility are denoted by double- and single-headed arrows, after Chen and Humphrey [75].

axial shrinkage ξ_l is based on the equilibrated $\mathcal{B}_{\tau_r}$ configuration relative to $\mathcal{B}_0$. The first Piola Kirchhoff stress P during cyclic loading is the one applied in $\mathcal{B}_c$ divided by the equilibrated cross-sectional are in $\mathcal{B}_{\tau_r}$, The axial stretch λ is defined as the current length in $\mathcal{B}_c$ divided by that in $\mathcal{B}_{\tau_r}$ whilst the axial stretch Λ — as the current length in $\mathcal{B}_c$ divided by that in $\mathcal{B}_0$. In the absence of creep and heating, $\mathbf{F}_0(s) = \mathbf{I}, \mathbf{F}_s(\tau) = \mathbf{I}$, and $\mathbf{F}_s(\tau_r) = \mathbf{I}$, whereby $\lambda = \Lambda$ and P are defined relative to $\mathcal{B}_0$ as usually done in soft tissue pseudoelasticity.

Chen and Humphrey [75] employed the following pseudoelastic constitutive relationship due to Fung et al. (1993):

$$P = b\left[e^{a(\lambda-1)} - 1 - a(\lambda - 1)\right] + c(\lambda - 1),$$

where a, b and c are material parameters. Some of the results are depicted in Figs. 76–79.
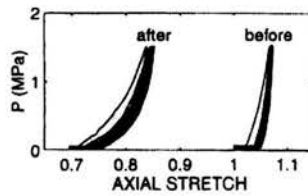
FIGURE 77. Stress–stretch response (P versus Λ) to 10 cycles of load-controlled uniaxial testing at 37°C both before and after the specimen incurred thermal shrinkage. Λ was measured with respect to β_0, and the equilibrium shrinkage $\xi_e = 30.7\%$ after heating, after Chen and Humphrey [75].
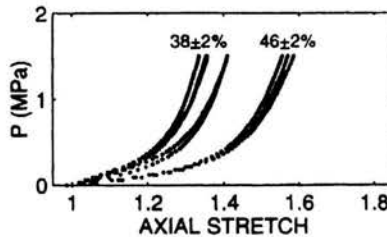
FIGURE 78. Stress–stretch response (P versus Λ) for groups of specimens (n=5–8 each) that were subjected to one of eight different thermal damage protocols: five protocols yielded $\xi_e = 38 \pm 2\%$ whereas three yielded $\xi_e = 46 \pm 2\%$, after Chen and Humphrey [75].
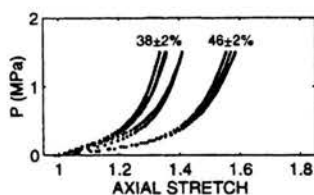
FIGURE 79. Mean stress–stretch response (P versus Λ) from the tenth cycle of uniaxial testing for pre–heated controls (dashed line) and groups of specimens that were subjected to one or five thermo–mechanical protocols (T, τ, P, t) that yielded $\xi_e = 13.8, 30.7, 41.1, 45.4$ or 51.2%, after Chen and Humphrey [75].

8.2. A pseudo–hyperelastic model of isotropic soft tissues

Living soft tissues cannot have a strain-energy function in the thermo-dynamic sense. However, in cyclic loading and unloading the stress-strain relationship after preconditioning does not vary much with the strain rate, cf. Fung [175]. If the strain-rate effect is ignored altogether; then the loading curve and the unloading curve (they are unequal) can be separately treated as a uniquely defined stress-strain relationship, which is associated with a strain-energy function. Each of these curves is a pseudo-elasticity curve. Pseudoelastic behaviour was assessed in various soft tissues (ligaments and tendons, arteries and veins, skin).

In biomechanical literature the pseudoelastic curves are described by two sets of material constants, one for the loading and one for the unloading branches of hysteresis loop, cf. Fung [175], Tanaka et al. [560] and the references therein. Tanaka et al. [560] claim that the notion of pseudoelasticity is applicable only for constant stress range or a constant strain range of hysteresis loop. In our opinion such a statement is unjustified. The approach to modelling the pseudoelastic behaviour of soft tissues has one serious drawback: so far no criterion has been proposed to describe the 'switching' loading-unloading. To remedy this lack of consistency we propose to exploit the modelling due to Ogden and Roxburgh [429]. These authors elaborated a pseudoelastic model having in mind applications to polymeric materials. However, the model is only applicable to the description of loading-unloading, and not to cyclic behaviour accounting for preconditioning.

8.2.1. Basic assumptions and constitutive relationships of pseudo-hyperelasticity. Similarly to the paper by Ogden and Roxburgh [429] we assume the existence of elastic pseudo-potential

$$\mathcal{P} = \breve{\mathcal{P}}\left(\mathbf{F}, \eta\right). \tag{8.1}$$

Here $\mathbf{F}$ denotes the deformation gradient with $J = \det\mathbf{F} > 0$, and $\eta \in (0, 1]$ is an additional parameter. This parameter may be called, after the damage mechanics, the 'degradation parameter'. The parameter η is related to the description of energy dissipation. During deformation, the parameter η should enable a continuous passage from active to passive processes. In active processes the material exhibits elastic properties with the energy density $\check{\mathcal{P}}(\mathbf{F}, \eta)$ where $\eta = const$. The potential (8.1) satisfies to the following conditions

$$\mathbf{P} = \frac{\partial \check{\mathcal{P}}(\mathbf{F}, \eta)}{\partial \mathbf{F}}, \quad 0 = \frac{\partial \check{\mathcal{P}}(\mathbf{F}, \eta)}{\partial \eta}, \quad \check{\mathcal{P}}(\mathbf{F}, 1) = \hat{W}(\mathbf{F}), \qquad (8.2)$$

where $\mathbf{P}$ denotes the first, unsymmetric, Piola-Kirchhoff stress tensor. The function $\hat{W}(\mathbf{F})$ is similar to the stored energy function of hyperelastic material (without degradation of its elastic properties). The conditions (8.2) ensure the fulfilment of mechanical balance and permit to interpret the passive process as a behaviour of an elastic material with the elastic energy different from that of the active process. The parameter η is then an implicit, continuous function of $\mathbf{F}$. An alternative form of the so-called model of degradation of elastic properties of materials within the framework of continuum damage approach was developed in De Souza Neto [538] cf. also the references therein. Function (8.1), satisfying the conditions (8.2), is called the pseudo-hyperelastic potential. We assume that

$$\check{\mathcal{P}}(\mathbf{F}, \eta) = \eta W(\mathbf{F}) + \Phi(\eta). \qquad (8.3)$$

According to the assumption of existence of the natural state and using (8.2) we get

$$W(\mathbf{R}) = 0, \quad \Phi(1) = 0, \quad \hat{\mathbf{S}}(\mathbf{R}, \eta) = \mathbf{0}. \qquad (8.4)$$

In (8.4) $\mathbf{R}$ stems from the polar decomposition $\mathbf{F} = \mathbf{R}\mathbf{U} = \mathbf{V}\mathbf{R}$. Equations $(8.2)_{1,2}$ and (8.3) yield

$$\mathbf{P} = \eta \frac{\partial \hat{W}(\mathbf{F})}{\partial \mathbf{F}}, \quad -\frac{d\Phi(\eta)}{d\eta} = \hat{W}(\mathbf{F}). \qquad (8.5)$$

The relation $(8.5)_2$ defines implicitly the parameter η as a function of $\mathbf{F}$. Since (8.5) implies

$$-\frac{d^2\Phi(\eta)}{d\eta^2} \eta \frac{d\eta}{d\mathbf{F}} = \hat{\mathbf{P}}(\mathbf{F}), \qquad (8.6)$$

therefore we assume that the unloading is associated with the decreasing of η, or in other words with the softening of the material. The function $\Phi(\eta)$ is assumed to be a concave function; then from Eq. $(8.5)_2$ we conclude that η is a uniquely defined function dependent on $\hat{W}(\mathbf{F})$. In the first, primary,

loading cycle we assume that $\eta = 1$ whilst the unloading occurs for a certain value $\mathbf{F}_m$. Then Eq. $(8.5)_2$ gives

$$-\frac{\mathrm{d}\Phi(1)}{\mathrm{d}\eta} = \hat{W}(\mathbf{F}_m) \equiv W_m. \tag{8.7}$$

The last relation means that η depends also on the value of energy W_m. For a complete unloading ($\mathbf{F} = \mathbf{R}$) we assume that η achieves a minimum value η_m. The pseudo-potential (8.3) assumes the residual value

$$\check{\mathcal{P}}(\mathbf{R}, \eta_m) = \Phi(\eta_m). \tag{8.8}$$

The residual or irreversible value of the energy is interpreted as the energy necessary to provoke the degradation of material. According to the second law of thermodynamics we assume that

$$\dot{\Phi}(\eta_m) \geqslant 0. \tag{8.9}$$

Here the dot denotes the derivative with respect to any time-like parameter.

Equation (8.5) and (8.7) imply that it is convenient to postulate a functional dependence for $\Phi(\eta)$ with respect to η, as a function of η and W_m. Let

$$-\frac{\mathrm{d}\Phi(\eta)}{\mathrm{d}\eta} = c_1 \, \mathrm{Erf}^{-1}\left[c_2(\eta - 1)\right] + W_m, \tag{8.10}$$

where c_1 and c_2 are positive constants, and $\mathrm{Erf}^{-1}(\cdot)$ stands for the inverse of the error function $\mathrm{Erf}(\cdot)$. From Eqs. (8.10) and $(8.5)_2$ we conclude that

$$\eta = 1 + \frac{1}{c_2}\mathrm{Erf}\left[\frac{1}{c_1}\left(\hat{W}(\mathbf{F}) - W_m\right)\right]. \tag{8.11}$$

The constants c_1 and c_2 were determined by performing tests.

8.2.2. An example of pseudo-hyperelastic model of isotropic soft tissues. Consider the simplest isotropic model of soft tissues. We assume that the tissue is incompressible, i.e.,

$$J - 1 = 0. \tag{8.12}$$

Consequently, the pseudo-potential (8.3) has to incorporate the constraint (8.12) with the Lagrange multiplier p, being the hydrostatic pressure or the spherical part of the Cauchy stress $\boldsymbol{\sigma}$. In the case of incompressible materials the stored energy function $\hat{W}(\mathbf{F})$ is a function of only two independent

invariants of isochoric deformations. The tensor $\mathbf{F}$ is decomposed into the isochoric and volumetric part as follows

$$\mathbf{F} = J^{1/3}\bar{\mathbf{F}} = J^{1/3}\mathbf{R}\bar{\mathbf{U}} = J^{1/3}\bar{\mathbf{V}}\mathbf{R}, \quad \det\bar{\mathbf{F}} = \det\bar{\mathbf{U}} = \det\bar{\mathbf{V}} = 1. \quad (8.13)$$

Since $\mathbf{P} = \mathbf{F}\mathbf{T}$ in the deformed configuration we have

$$\boldsymbol{\sigma} = \frac{1}{J}\mathbf{F}\mathbf{T}\mathbf{F}^T. \quad (8.14)$$

Here the conditions $(8.5)_1$ and (8.12) have been taken into account. Further, we introduce

$$\mathbf{C} = \mathbf{F}^T\mathbf{F}, \quad \mathbf{B} = \mathbf{F}\mathbf{F}^T, \quad \bar{\mathbf{B}} = \bar{\mathbf{F}}\bar{\mathbf{F}}^T, \quad \bar{\mathbf{C}} = \bar{\mathbf{F}}^T\bar{\mathbf{F}}, \quad (8.15)$$

where $\mathbf{C}$ denotes the Green strain tensor. Obviously, the quantities with bar refer to isochoric deformations, and $\mathbf{F}^T$ stands for the transpose of $\mathbf{F}$. For incompressible isotropic materials the stored function has the form,

$$W = \check{W}\left(\bar{\mathbf{C}}\right) = \check{W}\left(\bar{\mathbf{B}}\right) = \bar{W}\left(\bar{I}_1, \bar{I}_2\right), \quad (8.16)$$

where

$$\bar{I}_1 = \mathrm{tr}\bar{\mathbf{B}} = \mathrm{tr}\bar{\mathbf{C}}, \quad \bar{I}_2 = \mathrm{tr}\bar{\mathbf{B}}^{-1} = \mathrm{tr}\bar{\mathbf{C}}^{-1}. \quad (8.17)$$

From (8.5), (8.15) and (8.16) we obtain the following constitutive relationship of the pseudo-hyperelasticity in the reference configuration

$$\boldsymbol{\sigma} = -p\mathbf{I} + \eta\left(\bar{\beta}_1\bar{\mathbf{B}} + \bar{\beta}_{-1}\bar{\mathbf{B}}^{-1}\right), \quad -\frac{\mathrm{d}\Phi\left(\eta\right)}{\mathrm{d}\eta} = \bar{W}\left(\bar{I}_1, \bar{I}_2\right), \quad (8.18)$$

where

$$\bar{\beta}_1 = 2\frac{\partial\bar{W}\left(\bar{I}_1, \bar{I}_2\right)}{\partial\bar{I}_1}, \quad \bar{\beta}_{-1} = -2\frac{\partial\bar{W}\left(\bar{I}_1, \bar{I}_2\right)}{\partial\bar{I}_2}. \quad (8.19)$$

We observe that Eqs. (8.18) and (8.19) can be applied to arbitrary stored energy functions describing isotropic soft tissues. Such functions have been discussed in Section 5 of our paper. To illustrate a simple pseudo-hyperelastic model of soft tissues we take the following elastic stored energy function:

$$\bar{W}\left(\bar{I}_1\right) = \frac{\mu_0}{2\gamma}\left[e^{\gamma\left(\bar{I}_1-3\right)} - 1\right], \quad (8.20)$$

where μ_0 denotes the initial shear modulus and γ is a positive parameter. From Eqs. (8.18) and (8.20) we then get:

$$\boldsymbol{\sigma} = -p\mathbf{I} + \mu_0\eta e^{\gamma\left(\bar{I}_1-3\right)}\bar{\mathbf{B}}. \quad (8.21)$$

8.2.3. Example: analysis of homogeneous deformations for a pseudo-hyperelastic model of loading and unloading processes. The analysis of homogeneous deformations for loading and unloading processes is fundamental for experimental verification of the proposed model of soft tissues behaviour. We are going to provide examples by using the relation (8.20) and (8.21). For more elaborate models of isotropic soft tissues the analysis is similar to the one which follows. In the case of incompressible materials it suffices to investigate plane problems (the plane strain state and the plane stress state). For homogeneous deformations it is convenient to consider the function (8.20) as a function of eigenvalues of the tensor of isochoric stretch. By $\lambda_i, \bar{\lambda}_i$ ($i = 1, 2, 3$) we denote the eigenvalues of $\mathbf{U}$ and $\bar{\mathbf{U}}$, respectively (or of $\mathbf{V}$ and $\bar{\mathbf{V}}$). We have

$$\lambda_i = J^{1/3}\bar{\lambda}_i; \quad i = 1, 2, 3. \tag{8.22}$$

In the general case only two eigenvalues $\bar{\lambda}_i$ are independent:

$$\bar{\lambda}_3 = \left(\bar{\lambda}_1 \bar{\lambda}_2\right)^{-1}. \tag{8.23}$$

Consequently, we have

$$\bar{W}\left(\bar{I}_1\right) = \hat{W}\left(\bar{\lambda}_1, \bar{\lambda}_2\right). \tag{8.24}$$

The function $\hat{W}$ is a symmetric function.

We observe that both the uniaxial tension test and biaxial tension test are plane stress tests ($\sigma_3 = 0$). Then Eq. (8.12) yields

$$\lambda_3 = \tilde{J}^{-1}, \tag{8.25}$$

where $\tilde{J} = \det \tilde{\mathbf{F}}$ and $\tilde{\mathbf{F}}$ denotes the plane deformation gradient. For the plane stress state, from (8.21) and $\sigma_3 = 0$, we get

$$p = \mu_0 \eta \mathrm{e}^{\gamma(\tilde{I}+\tilde{J}^{-2}-3)}\tilde{J}^{-2}. \tag{8.26}$$

Moreover, the constitutive relationship takes the form

$$\tilde{\boldsymbol{\sigma}} = \mu_0 \eta \mathrm{e}^{\gamma(\tilde{I}+\tilde{J}^{-2}-3)}\left(-\tilde{J}^{-2}\tilde{\mathbf{I}} + \tilde{\mathbf{B}}\right), \tag{8.27}$$

where $\tilde{I} = \mathrm{tr}\tilde{\mathbf{B}} = \mathrm{tr}\tilde{\mathbf{C}}$. We observe that Eq. (8.27) can also be used for membranes and shells.

From Eqs. (8.10), (8.11), (8.14), (8.20), and (8.21) one gets the relations between nominal stresses and stretches in basic experimental tests.

Figure 80a depicts predictions of the model in the uniaxial tension test in the case of active process. Figure 80b presents the nominal stress versus stretch relation for uniaxial and biaxial tension and simple shear. The density of the elastic energy (8.20) is, in loading processes, sufficiently regular as can be concluded from the level lines in Fig. 81. The relevant diagrams for loading and unloading processes are presented in Fig. 82, where $\gamma = 5$ and for the unloading lines $c_1 = 1.5$, $c_2 = 1.2$. Figure 83a presents the diagram of the function (8.11) where Eq. (8.20) is taken into account for $\lambda_m = 1.4$ for the uniaxial test, see also Fig. 82a. As we already know, this function monotonically decreases from 1 to the value η_m corresponding to complete unloading of the sample after its preliminary elongation.
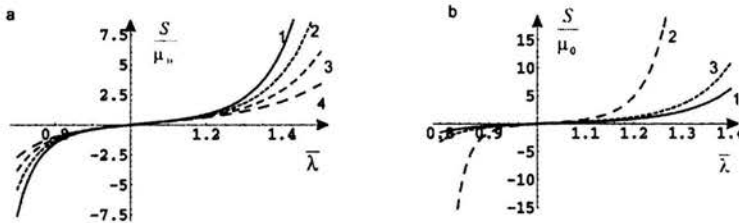
FIGURE 80. Nominal stress versus stretch for primary loading tests: a) uniaxial tension test, influence of γ; $\gamma = 5$(curve 1), $\gamma = 4$(curve 2), $\gamma = 3$ (curve 3), $\gamma = 2$ (curve 4); b) comparison of uniaxial tension test (curve 1) with uniform biaxial tension (curve 2) and shear (curve 3) for $\gamma = 5$, after Jemioło and Telega [278].
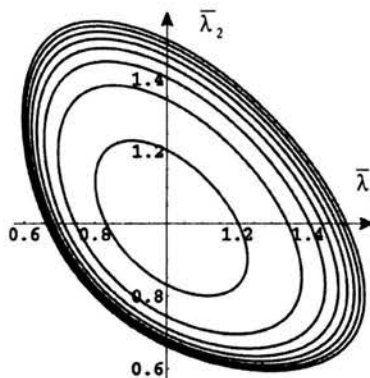
FIGURE 81. Subsequent lines of the elastic energy density (8.20) for $\gamma = 5$. The diagrams are normalized by the shear modulus, after Jemioło and Telega [278].

a

b
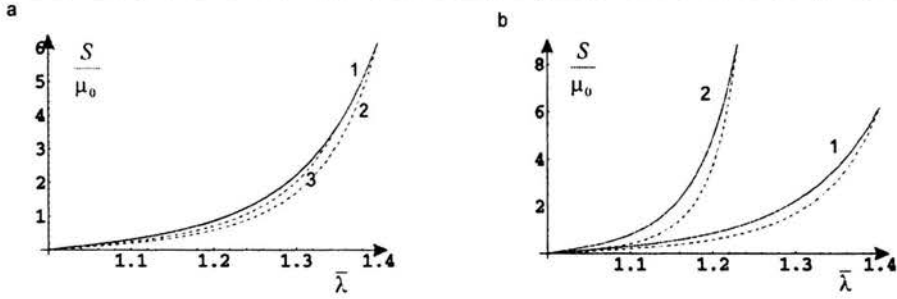
FIGURE 82. Loading and unloading diagrams: a) uniaxial tension tests, (curve 1) – the loading line, (curve 2) – the unloading line for the stretch 1.4, (curve 3) – the unloading line for the stretch 1.35, b) uniaxial tension test (loop 1) and biaxial uniform tension test (loop 2), after Jemioło and Telega [278].

a

b
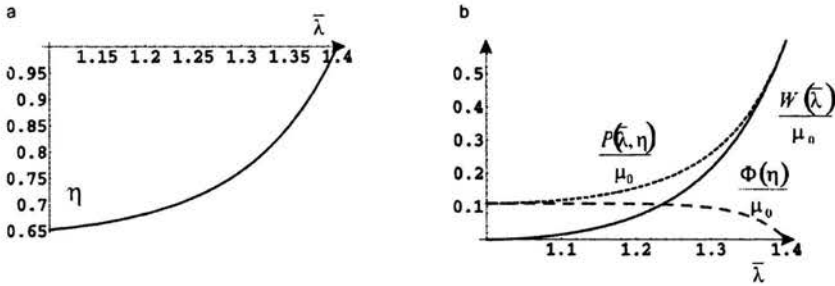
FIGURE 83. Diagrams of: a) damage parameter, b) pseudo–hyperelastic potential, the density of elastic energy in the first cycle of uniaxial tension, and function Φ, versus stretch

8.3. Pseudo–hyperelastic anisotropic models of soft tissues

The model presented in the previous section was extended to anisotropic soft tissues by Jemioło et al. [283].

8.3.1. Transverse isotropy. As we already know, soft tissues are usually anisotropic. Figure 84 shows a clear difference in stress-extension relations for left ventricular midwall specimen in the fibre and cross-fibre direction.

As previously, we assume the existence of elastic pseudo-potential:

$$\mathcal{P} = \check{\mathcal{P}}(\mathbf{C}, \mathbf{M}, \eta). \tag{8.28}$$

As usual, by $\mathbf{F}$ we denote the deformation gradient and $\mathbf{C} = \mathbf{F}^T\mathbf{F}$ is the right Cauchy-Green strain tensor. To describe the anisotropy we introduce a parametric tensor $\mathbf{M}$, cf. Section 5. The tensor $\mathbf{M}$ is prescribed in the initial
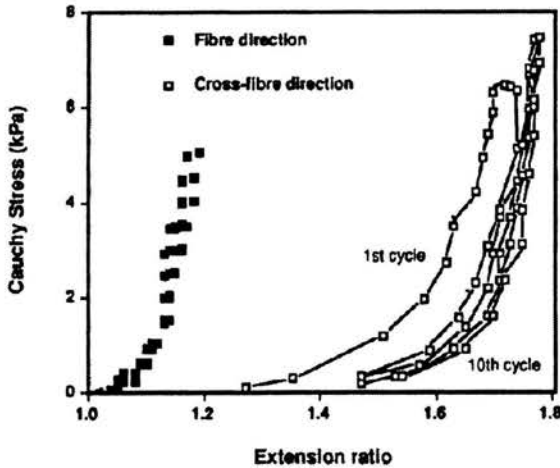
FIGURE 84. Stress–extension relations for left ventricular midwall specimen during 1st, 9th and 10th cycles of equibiaxial loading. Cycle period 30 sec. and specimen thickness 1.83 mm. The solid lines indicate the order of loading in the cross-fibre directions, after Smail and Hunter [530].

(Lagrangian) configuration. We assume that $J = \det \mathbf{F} > 0$, and $\eta \in (0, 1]$ as an additional parameter. During loading tissue exhibits elastic properties with the energy density $\mathcal{P}(\mathbf{C}, \mathbf{M}, \eta)$ where $\eta = const.$ The potential (8.28) satisfies the following conditions

$$\mathbf{T} = \frac{\partial \check{\mathcal{P}}(\mathbf{C}, \mathbf{M}, \eta)}{\partial \mathbf{C}} + \frac{\partial \check{\mathcal{P}}(\mathbf{C}, \mathbf{M}, \eta)}{\partial \mathbf{C}^T}, \quad 0 = \frac{\partial \check{\mathcal{P}}(\mathbf{C}, \mathbf{M}, \eta)}{\partial \eta},$$

(8.29)

$$\check{\mathcal{P}}(\mathbf{C}, \mathbf{M}, 1) = \hat{W}(\mathbf{C}, \mathbf{M}),$$

where $\mathbf{T}$ denotes the second, symmetric, Piola-Kirchhoff stress tensor. The function $\hat{W}(\mathbf{C}, \mathbf{M})$ is similar to the stored energy function of anisotropic hyperelastic material (without degradation of its elastic properties). Conditions (8.29) ensure the fulfilment of balance of mechanical energy and permit to interpret the unloading process as a behaviour of an elastic material with the elastic energy different from that of the loading process. The parameter is then an implicit, continuous function of $\mathbf{C}$ and $\mathbf{M}$. Function (8.28), satisfying the conditions (8.29), is called the pseudo-hyperelastic potential. We assume that

$$\check{\mathcal{P}}(\mathbf{C}, \mathbf{M}, \eta) = \eta \hat{W}(\mathbf{C}, \mathbf{M}) + \Phi(\eta). \tag{8.30}$$

According to the assumption of existence of the natural state and using (8.29)

we get

$$\hat{W}(\mathbf{I}, \mathbf{M}) = 0, \quad \Phi(1) = 0, \quad \hat{\mathbf{T}}(\mathbf{I}, \mathbf{M}, \eta) = 0. \tag{8.31}$$

Equations $(8.29)_{1,2}$ and (8.30) yield

$$\mathbf{T} = \eta \left[\frac{\partial \hat{W}(\mathbf{C}, \mathbf{M})}{\partial \mathbf{C}} + \frac{\partial \hat{W}(\mathbf{C}, \mathbf{M})}{\partial \mathbf{C}^T} \right], \quad -\frac{d\Phi(\eta)}{d\eta} = \hat{W}(\mathbf{C}, \mathbf{M}). \tag{8.32}$$

Relation $(8.32)_2$ defines implicitly the parameter η as a function of $\mathbf{C}$ and $\mathbf{M}$. We assume that the unloading is associated with the decreasing of η, or in other words, with the softening of material. The function $\Phi(\eta)$ is assumed to be a concave function; then from Eq. $(8.32)_2$ we conclude that η is a uniquely defined function dependent on $\hat{W}(\mathbf{C}, \mathbf{M})$. In the first, primary loading cycle we assume that $\eta = 1$ whilst the unloading occurs for a certain value $\mathbf{C}_m$. Then Eq. $(8.32)_2$ gives

$$-\frac{d\Phi(1)}{d\eta} = \hat{W}(\mathbf{C}_m, \mathbf{M}) \equiv W_m. \tag{8.33}$$

The last relation means that η depends also on the value of the energy W_m. For a complete unloading $(\mathbf{C} = \mathbf{I})$ we assume that η achieves a minimum value η_m. The pseudo-potential (8.30) assumes then the residual value

$$\check{P}(\mathbf{C}, \mathbf{M}, \eta) = \Phi(\eta_m). \tag{8.34}$$

The residual or irreversible value of the energy is interpreted as the energy necessary to provoke the degradation of material. According to the second law of thermodynamics we assume that

$$\dot{\Phi}(\eta_m) \geq 0. \tag{8.35}$$

Equations (8.32) and (8.34) imply that it is convenient to postulate a functional dependence for $\Phi(\eta)$ with respect to η, as a function of η and W_m. Let, cf. formula (8.10)

$$-\frac{d\Psi}{d\eta} = c_1 \mathrm{Erf}^{-1}[c_2(\eta - 1)] + W_m, \tag{8.36}$$

where c_1 and c_2 are positive constants. From Eqs. (8.36) and $(8.32)_2$ we conclude that

$$\eta = 1 + \frac{1}{c_2}\mathrm{Erf}\left[\frac{1}{c_1}(\hat{W}(\mathbf{C}, \mathbf{M}) - W_m)\right]. \tag{8.37}$$

The constants c_1 and c_2 were determined by performing tests.

Remark 17. Formulas (8.26)–(8.37) do not formally change if $\mathbf{M}$ denotes a set of structural tensors. Then we easily recover formulas for pseudo-hyperelastic behaviour of orthotropic soft tissues. The case of *two-dimensional stress state* is discussed below.

Example 7. Consider now a two-dimensional response, for instance of a biological membrane. Then the stored energy function has the form, cf. Jemioło and Telega [274]

$$\hat{W}(\tilde{\mathbf{C}}, \tilde{\mathbf{M}}) = \breve{W}(\tilde{I}_1, \tilde{I}_2, \tilde{J}), \tag{8.38}$$

where

$$\tilde{I}_1 = \mathrm{tr}\tilde{\mathbf{C}}, \quad \tilde{I}_2 = \mathrm{tr}\tilde{\mathbf{C}}\tilde{\mathbf{M}}, \quad \tilde{J} = \det \tilde{\mathbf{F}}. \tag{8.39}$$

Here tilde denotes two-dimensional entities. We recall that the scalar invariants appearing in (8.38) constitute a functional basis for the orthotropic scalar-valued function, cf. Table 4.10 in Jemioło and Telega [274]. In the 2D case $\tilde{\mathbf{M}}_1 + \tilde{\mathbf{M}}_2 = \tilde{\mathbf{I}}$. Hence $\tilde{\mathbf{M}}_2 = \tilde{\mathbf{I}} - \tilde{\mathbf{M}}_1$, and it suffices to consider $\tilde{\mathbf{M}}$.

To illustrate a simple pseudoelastic model of orthotropic soft tissue we propose the following elastic stored energy function:

$$\breve{W}(\tilde{I}_1, \tilde{I}_2, \tilde{J}) = a\left[\exp \phi(\tilde{I}_1, \tilde{I}_2, \tilde{J}) - 1\right] + \Gamma(\tilde{J}), \tag{8.40}$$

where a is a positive parameter and Γ is a convex function. It is reasonable to consider the following forms of ϕ and Γ:

$$\phi(\tilde{I}_1, \tilde{I}_2) = b_1(\tilde{I}_1 - 2) + b_2(\tilde{I}_2 - 1) + b_3(\tilde{I}_1\tilde{I}_2 - 2) + b_4(\tilde{I}^2 - 1) + \dots \tag{8.41}$$

$$\Gamma(\tilde{J}) = -d_1 \ln \tilde{J} + d_2(\tilde{J}^2 - 1), \qquad d_1 > 0, \quad d_2 > 0, \tag{8.42}$$

where the parameters b_i and d_i are material constants, and

$$b_3 = -\frac{1}{2}b_2, \qquad d_1 = a(2b_1 - b_2 + b_4) + 2d_2. \tag{8.43}$$

Once the explicit form of ϕ and Γ is known, we can describe the loading and unloading behaviour.

8.3.2. Orthotropy.

Constitutive relationships for hyperelastic orthotropic materials in the case of plane stress state and their interpretations

Deleting tilda over 2D entities, according to the general representation of 2D orthotropic scalar function, the stored energy function can be written as follows, cf. Jemioło and Telega [273].

$$w\left(\mathbf{E}, \mathbf{M}_1, \mathbf{M}_2\right) = \overline{w}(N_i) = W\left(\mathbf{C}, \mathbf{M}_1, \mathbf{M}_2\right) = \tilde{W}\left(J_i\right), \quad i = 1, 2, 3. \tag{8.44}$$

Here N_i are the so-called orthotropic invariants of the Lagrange strain measure $\mathbf{E} = (\mathbf{C} - \mathbf{I})/2$ whilst J_i denote the invariants of the right Cauchy-Green tensor $\mathbf{C} = \mathbf{F}^T\mathbf{F} = \mathbf{U}^2$. The sets of invariants $\{N_i\}$ and $\{J_i\}$ represent irreducible functional bases. The parametric tensors $\mathbf{M}_1$ and $\mathbf{M}_2$ appearing in (8.44) are defined as follows: $\mathbf{M}_1 = \mathbf{m}_1 \otimes \mathbf{m}_1$, $\mathbf{M}_2 = \mathbf{m}_2 \otimes \mathbf{m}_2$. The unit vectors $\mathbf{m}_1$ and $\mathbf{m}_2$ are orthogonal and coincide with the singled out directions of material in the reference configuration. The vectors may depend on position in the body considered. We recall that the sets $S_\alpha = \{\mathbf{Q} \in O(2) \,|\, \mathbf{M}_\alpha = \mathbf{Q}\mathbf{M}_\alpha\mathbf{Q}^T\}$, $\alpha = 1, 2$, determine the symmetry groups of parametric tensors, where $O(2)$ stands for the full 2D orthogonal group. Consequently, the material considered possesses a local symmetry $S = S_1 \cap S_2$, and thus is orthotropic. Obviously it may also be nonhomogeneous.

The constitutive relationships determining the second (symmetric) Piola-Kirchhoff stress tensor are given by

$$
\begin{aligned}
\mathbf{T} = \overline{\mathbf{T}}\,(\mathbf{E}, \mathbf{M}_1, \mathbf{M}_2) &= \left.\frac{\partial w}{\partial \mathbf{E}}\right|_{\mathbf{E}=\mathbf{E}^T} = \sum_{i=1}^{3}\frac{\partial \overline{w}}{\partial N_i}\left.\frac{\partial N_i}{\partial \mathbf{E}}\right|_{\mathbf{E}=\mathbf{E}^T} = \sum_{i=1}^{3}\alpha_i\mathbf{G}_i^{(\mathbf{E})} \\
&= \tilde{\mathbf{T}}\,(\mathbf{C}, \mathbf{M}_1, \mathbf{M}_2) = 2\left.\frac{\partial W}{\partial \mathbf{C}}\right|_{\mathbf{C}=\mathbf{C}^T} = 2\sum_{i=1}^{3}\frac{\partial \tilde{W}}{\partial J_i}\left.\frac{\partial J_i}{\partial \mathbf{C}}\right|_{\mathbf{C}=\mathbf{C}^T} = 2\sum_{i=1}^{3}\beta_i\mathbf{G}_i^{(\mathbf{C})}.
\end{aligned}
\tag{8.45}
$$

The symmetric tensors $\mathbf{G}_i^{(\mathbf{E})}$ and $\mathbf{G}_i^{(\mathbf{C})}$ are called *generators* of the constitutive relationships defined by $(8.45)_1$ and $(8.45)_2$ respectively.

According to the assumption of existence of natural state we additionally have:

$$
\begin{aligned}
w\,(\mathbf{0}, \mathbf{M}_1, \mathbf{M}_2) &= W\,(\mathbf{I}, \mathbf{M}_1, \mathbf{M}_2) = 0, \\
\overline{\mathbf{T}}\,(\mathbf{0}, \mathbf{M}_1, \mathbf{M}_2) &= \tilde{\mathbf{T}}\,(\mathbf{I}, \mathbf{M}_1, \mathbf{M}_2) = \mathbf{0}.
\end{aligned}
\tag{8.46}
$$

We also assume that the stored energy function (8.44) is at least of class C^2. For $\{N_i\}$ and $\{J_i\}$ we take polynomial bases and write

$$
\begin{aligned}
\overline{w}\,(N_i) &= \overline{w}\left(\mathrm{tr}\,(\mathbf{E}\mathbf{M}_1), \mathrm{tr}\,(\mathbf{E}\mathbf{M}_2), \mathrm{tr}\mathbf{E}^2\right), \\
\tilde{W}\,(J_i) &= \tilde{W}\left(\mathrm{tr}\,(\mathbf{C}\mathbf{M}_1), \mathrm{tr}\,(\mathbf{C}\mathbf{M}_2), \det\mathbf{C}\right).
\end{aligned}
\tag{8.47}
$$

We recall that in the 2D case, $\mathbf{M}_1 + \mathbf{M}_2 = \mathbf{I}$; hence we get $\mathrm{tr}\mathbf{E}\mathbf{M}_1 + \mathrm{tr}\mathbf{E}\mathbf{M}_1 = \mathrm{tr}\mathbf{E}$.

The choice of invariants in (8.47) is by no means accidental. The invariants N_i are convex functions of $\mathbf{E}$, thus allowing us to construct a convex stored energy function for orthotropic Saint-Venant-Kirchhoff (SVK) material. Furthermore, the invariants J_1 and J_2 are convex function of $\mathbf{C}$ whilst $J_3 = (\det\mathbf{F})^2$ is a convex function of $\det\mathbf{F}$.

Taking into account (8.45) in (8.47) we get

$$\mathbf{T} = \alpha_1 \mathbf{M}_1 + \alpha_2 \mathbf{M}_2 + 2\alpha_3 \mathbf{E} = 2\left(\beta_1 \mathbf{M}_1 + \beta_2 \mathbf{M}_2 + \beta_3 J_3 \mathbf{C}^{-1}\right). \qquad (8.48)$$

We recall that $\mathrm{Cof} \mathbf{C} = J_3 \mathbf{C}^{-1}$; in the 2D case we have $J_3 \mathbf{C}^{-1} = (\mathrm{tr} \mathbf{C}) \mathbf{I} - \mathbf{C}$. From (8.46) it follows that

$$\begin{aligned}
\overline{w}(0,0,0) = \tilde{W}(1,1,1) &= 0, \\
\alpha_i(0,0,0) &= 0, \quad i = 1, 2, \\
\beta_1(1,1,1) + \beta_2(1,1,1) + 2\beta_3(1,1,1) &= 0, \\
\beta_1(1,1,1) &= \beta_2(1,1,1).
\end{aligned} \qquad (8.49)$$

From the point of view of the theory of representation of anisotropic tensor functions, the constitutive relationships $(8.48)_1$ and $(8.48)_2$ are equivalent. We observe that $\mathbf{E} = (\mathbf{C} - \mathbf{I})/2$ is an isotropic tensor function in respect of $\mathbf{C}$ and the relations between the invariants of the tensors $\mathbf{E}$ and $\mathbf{C}$ are as follows:

$$\begin{aligned}
N_1 &= \frac{1}{2}(J_1 - 1), \quad N_2 = \frac{1}{2}(J_2 - 1), \\
N_3 &= \frac{1}{4}\left[(J_1 + J_2)^2 - 2J_3 - 2(J_1 + J_2) + 2\right].
\end{aligned} \qquad (8.50)$$

The invariants N_i given by (8.50) are convex functions of $\mathbf{C}$.

The constitutive relationships appearing in the equilibrium equation referred to the Lagrange description, and determining the first (unsymmetric) Piola-Kirchhoff stress tensor can be obtained from (8.48) and from the relation: $\mathbf{P} = \mathbf{FT}$. On the other hand, the constitutive relationships appearing in the Eulerian description, determining the (symmetric) Cauchy stress tensor $\boldsymbol{\sigma}$, are obtained from the relation: $\boldsymbol{\sigma} = \mathbf{SF}^T/J$. We recall that $J = \sqrt{J_3} = \sqrt{\det \mathbf{C}} = \sqrt{\det \mathbf{B}}$, where $\mathbf{B} = \mathbf{FF}^T = \mathbf{V}^2 = \mathbf{RCR}^T$ denotes the left Cauchy-Green strain tensor. Taking into account the above relations in (8.48) we get

$$\begin{aligned}
\boldsymbol{\sigma} &= \frac{1}{J}\left[\alpha_1 \bar{\mathbf{M}}_1 + \alpha_2 \bar{\mathbf{M}}_2 + 2(N_1 + N_2)\alpha_3 \mathbf{B}\right] = \\
&= \frac{2}{J}\left(\beta_1 \bar{\mathbf{M}}_1 + \beta_2 \bar{\mathbf{M}}_2\right) + 2\beta_3 J \mathbf{I},
\end{aligned} \qquad (8.51)$$

where

$$\bar{\mathbf{M}}_1 = \mathbf{FM}_1\mathbf{F}^T, \quad \bar{\mathbf{M}}_2 = \mathbf{FM}_2\mathbf{F}^T. \qquad (8.52)$$

The functions α_i, β_i (i=1,2,3) are scalar functions of the basic invariants.

From (8.52) and the polar decomposition theorem of $\mathbf{F}$ it follows that material fibers coinciding with the singled out directions of material undergo rotation and stretching.

We assume that each of the stored energy functions (8.44) can be, in the range of relatively small strains measured by $\mathbf{E}$, approximated by

$$\bar{w}\left(N_i\right) = w_{\text{SVK}}\left(N_i\right) + O\left(\|\mathbf{E}\|^3\right). \tag{8.53}$$

From (8.53) and (8.47)$_1$ we conclude that the stored energy function of the orthotropic SVK material has the following form:

$$w_{\text{SVK}}\left(N_i\right) = \frac{1}{2}\left[a_1\left(N_1\right)^2 + a_2\left(N_2\right)^2 + a_3 N_1 N_2 + a_4 N_3\right], \tag{8.54}$$

where a_k $(k = 1, \ldots, 4)$ are elastic constants. From (8.54) we get

$$\left.\frac{\partial^2 w_{\text{SVK}}\left(N_i\right)}{\partial \mathbf{E} \otimes \partial \mathbf{E}}\right|_{\mathbf{E}=\mathbf{E}^T} = \bar{\mathbf{C}}\left(a_k, \mathbf{M}_1, \mathbf{M}_2\right) \equiv \mathbf{C}, \tag{8.55}$$

where $\mathbf{C}$ is the stiffness tensor with the usual symmetry properties. For materials without kinematic constraints, it is assumed that $\mathbf{C}$ is positive definite. It can be shown that the elastic constants appearing in (8.54) are given by

$$a_1 = \frac{E_1}{1 - \nu_{12}\nu_{21}} - 2G, \qquad a_2 = \frac{E_2}{1 - \nu_{12}\nu_{21}} - 2G,$$

$$a_3 = \frac{E_1 \nu_{21} + E_2 \nu_{12}}{1 - \nu_{12}\nu_{21}}, \qquad a_4 = 2G, \tag{8.56}$$

$$\nu_{12} E_2 = \nu_{21} E_1. \tag{8.57}$$

Here we have introduced the standard notation for the Young, Poisson and shear moduli. The positive definiteness of the tensor (8.55) (the convexity of function (8.54) with respect to $\mathbf{E}$) imply that

$$E_1 > 0, \quad E_1 > 0, \quad G > 0, \quad 1 - \nu_{12}\nu_{21} > 0.$$

An orthotropic model of pseudo-hyperelasticity for plane stress problems

We propose the following generalization (GSVK) of the stored energy function for of SVK material (8.54):

$$\tilde{W}\left(J_i\right) = \frac{1}{8}\Big\{a_1\left(J_1 - 1\right)^2 + a_2\left(J_2 - 1\right)^2 + a_3\left(J_1 - 1\right)\left(J_2 - 1\right)$$

$$+ a_4\left[\left(J_1 + J_2\right)^2 - 2\left(J_1 + J_2\right)\right]\Big\} + \frac{1}{2}a_5\left(J_3 - 1\right)^2 - \frac{1}{4}a_4 \ln\left(J_3\right)$$

$$= \bar{w}\left(N_i\right) = w_{\text{SVK}}\left(N_i\right) + O\left(\|\mathbf{E}\|^3\right), \tag{8.58}$$

where a_k $(k = 1, ..., 4)$ are defined by (8.56) and a_5 is positive constant. Obviously, model (8.58) has to be tested experimentally. From Eq. (8.58) it follows that agreement of the model GSVK with experimental data will be similar to that resulting from the model SVK for relatively small deformations. On the other hand, proposing the model GSVK we eliminate the fundamental, unrealistic predictions of the model SVK for significant homogeneous deformations in the case of compression, cf. Fig. 85. For biaxial tension-compression tests with control of strains the level curves of the stored energy function (8.58) are boundaries of convex sets, cf. Fig. 86.
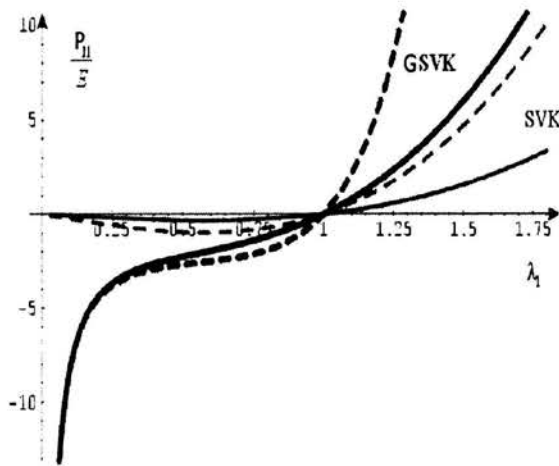
FIGURE 85. Comparison of orthotropic SVK and GSVK hyperelastic models. Loading diagrams ($E_1 = E$, $E_2 = 10E$, $G = 0.8E$, $\nu_{12} = 0.2$, $a_5 = E$): uniaxial, $\lambda_2 = 1$, (continuous curves) and biaxial, $\lambda_1 = \lambda_2$, (dotted curves) tension-compression tests, after [281].
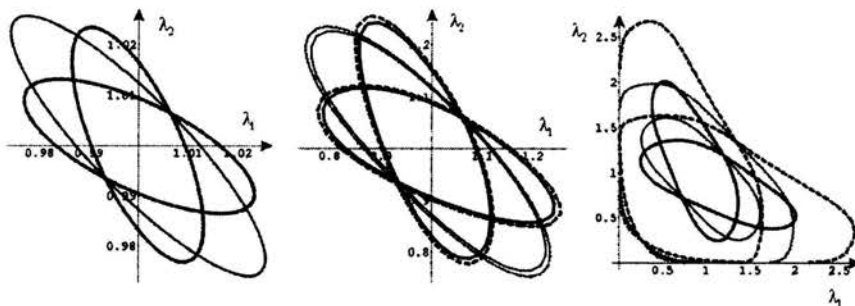
FIGURE 86. Comparison of level sets for the stored energy functions of GSVK and EGSVK hyperelastic models ($E_1 = E$, $E_2 = 10E$, $G = 0.8E$, $\nu_{12} = 0.2$, $a_5 = E$, $a = 2$). The curves correspond to two-dimensional tests, after [281].

Similarly to Fung's model [176], one can propose the following generalisation of (8.58) (EGSVK):

$$\bar{W}(J_i) = \frac{1}{a}\left(e^{\Psi(J_i)} - 1\right), \tag{8.59}$$

where the function $\Psi(J_i)$ coincides with $\tilde{W}(J_i)$ defined by (8.58), and a is a positive constant. The level sets of functions (8.59) and comparison with (8.58) is depicted in Fig. 86

Substituting (8.59) into the relevant relations derived in Section 8.3.1 and taking into account Remark 3 we get constitutive relationships of the pseudo-hyperelastic model. Those relations are indispensable, among others, to the interpretation of basic tests. In Fig. 87 we show typical curves characterizing the nominal stress-stretch relation, obtained for loading and unloading with controlled displacements. The data are the same as in Fig. 86, which determine function (8.59). The additional parameters appearing in the formula for η (8.11) are taken from paper [278].
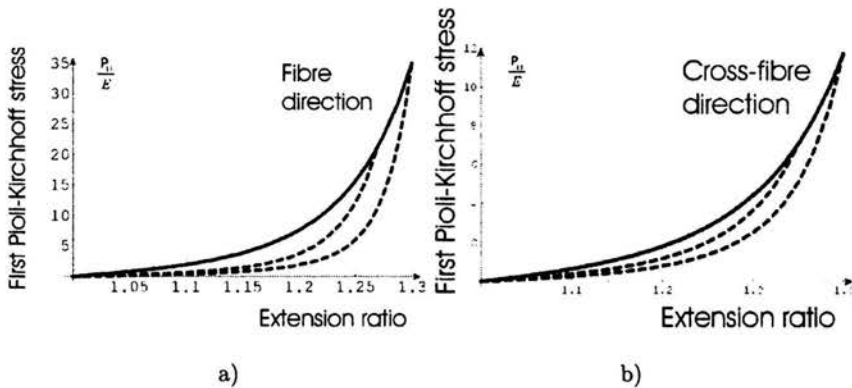
FIGURE 87. EGSVK pseudo-hyperelastic model. Loading and unloading diagrams: a) uniaxial tension tests in fibre direction; (continuous curves) – the loading line; (dotted curves) – the unloading line, b) uniaxial tension test in cross-fibre direction, after [281].

Remark 18. It seems that the assumption of natural state can be weakened and one can take into account residual stresses $\mathbf{T}^r(\mathbf{X})$. It suffices to replace the pseudo-potential $\breve{\mathcal{P}}(\mathbf{C}, \mathbf{M}, \eta)$ by $\hat{\mathcal{P}}(\mathbf{C}, \mathbf{M}, \mathbf{T}^r, \eta)$. Now we have

$$\hat{\mathcal{P}}(\mathbf{C}, \mathbf{M}, \mathbf{T}^r, \eta) = \eta\bar{W}(\mathbf{C}, \mathbf{M}, \mathbf{T}^r) + \Phi(\eta),$$

and

$$\bar{W}(\mathbf{C}, \mathbf{M}, \mathbf{T}^r) \neq 0.$$

For more details on residual stresses the reader is referred to the comprehensive paper [570].

Remark 19. Humphrey [253] compared three anisotropic constitutive relations used in the literature to describe pseudoelastic response of common carotid arteries. Two of these relations are of exponential type, and one is logarithmic. In our opinion the comparisons performed by Humphrey are not conclusive since no criterion of switching from loading to unloading curves has been proposed.

Remark 20. Recently, Chagnon et al. [68] demonstrated that Continuum Damage Mechanics can be used as an efficient tool to model the Mullins effect in rubbers. It seems possible to extend this model to the description of pseudoelastic behaviour of soft tissues.

9. Thermal modelling of soft tissues

In this section most important issues of modelling of heat transfer in tissues are reviewed. In Section 9.1 most important heat loads, that a tissue can be subjected to, are briefly described. In Section 9.2 the mechanisms of thermal damage at elevated temperatures are discussed along with the modelling techniques available in the literature. Section 9.3 contains the information concerning the vascular system, that is pertinent to heat transfer modelling. The available models of heat transfer in soft tissues are described in Section 9.4. The Section 9.5 follows with the discussion of the phenomena of metabolic heating. In Section 9.6 we briefly consider the question whether the hyperbolic bioheat transfer equation is more suitable for the description of experimental results than, the usually assumed, parabolic one. Finally, the Section 9.7 is concerned with a mixture model (within the geometrically nonlinear theory) of heat-induced changes in hydration and mechanical properties of soft tissues.

9.1. Heat loads

During the lifetime the human body is exposed to wide array of heat loads. These can be roughly classified in two groups: these occurring in everyday life (e.g. exposure to sunlight, cold wind, immersion in water etc.) and these, which are the result of medical treatments. Regardless of the source, the heat is transferred via one or more of the basic mechanisms: conduction, convection (natural or forced) and radiation. The mathematical description of possible surface and volumetric heat loads, along with appropriate formulation is given in Table 10.

TABLE 10. Mathematical description of heat loads

name	formulation
boundary convection	$\frac{\partial T}{\partial n}\big|_{\partial\Omega} = \frac{\alpha}{\lambda}(T_\infty - T)$
perfect thermal contact	$T\big|_{\partial\Omega} = T_c$
imperfect thermal contact	$\frac{\partial T}{\partial n}\big|_{\partial\Omega} = \frac{\beta}{\lambda}(T_c - T)$
boundary radiation	$\frac{\partial T}{\partial n}\big|_{\partial\Omega} = \gamma(T_s^4 - T^4)$
volumetric heating	$q_v = q_v(\mathbf{x}, t)$

Here we used the following notation: T – temperature [K], α – convection coefficient $[\mathrm{W/(m^2K)}]$, λ – thermal conductivity [W/(mK)], T_∞ – ambient (environmental) temperature [K], T_c – temperature of contacting body [K], β – thermal contact conductivity $[\mathrm{W/(m^2K)}]$, γ – coefficient taking into account the geometry of radiating surfaces $[1/(\mathrm{mK^3})]$ and q_v – volumetric heat generation rate $[\mathrm{W/m^3}]$.

The response of the material (i.e. tissue) determines various factors such as thermal comfort, cold-water survival, effectiveness of the cryotherapeutic or hyperthermal treatment etc. In Table 11 the basic kinds of heat loads to soft tissues are summarized.

TABLE 11. Examples of heat loads applied to soft tissues and areas of their importance.

name	type	importance
cold water immersion	boundary convection	survival during accidents at sea, heat loss rate
metabolism	volumetric heating	thermoregulation
cryosurgery	thermal contact (probe)	estimation of the frozen region
cryotherapy	boundary convection (cold gases), thermal contact (ice packs)	therapeutic procedure design
hyperthermic treatment	thermal contact (probe), boundary radiation (laser), volumetric heating (microwave)	calculation of the irreversibly damaged region, procedure design

9.2. Thermal damage

When the temperature of living tissue becomes lower or higher than normal thermal damage may occur. The lowering or elevation of temperature may occur as a result of application of the heat loads, cf. Table 11. The situation, where the temperature is significantly below normal value but still well above freezing, is described as 'hypothermia'; if the temperature rises above normal — one says that the hyperthermic event occurs. The situation, where normal temperature is maintained is sometimes denoted 'normothermic'.

The lowering of the temperature usually has no local negative effect as long as it is well above freezing point. It can be however important in the scale of the entire organism. In the case of cold water immersion, no local tissue damage may occur (no frostbite) and still, subject may die because of excessive energy loss, cf. [145]. The heat–conduction properties of tissues become more important than their tolerance to low temperatures.

Here the emphasis will be put on the thermal damage in hyperthermic regime since it applies to most of the practical problems encountered in the field of soft tissue heat transfer, such as cancer therapy (application of lasers, microwaves, hot saline baloons etc.), burn injury, electrical trauma etc.

One of the first investigations into nature of the thermal injury during hyperthermia were provided by Henriquez [227, 613], after the second world war.

The thermal treatment of cells leads to numerous degenerative events; the sequence of events leading to the cellular death is still not well established. Various internal structures of the cell were implicated to be targets of the thermal treatment but none have been proven conclusively to be responsible for cellular death.

The widely-accepted model of thermal damage in soft tissues is the first-order rate process (Arrhenius model), cf. [6, 38, 226, 228, 447].

The measure of injury Ω is introduced and its rate is postulated to satisfy the equation:

$$\frac{d\Omega}{dt} = A \exp\left(-\frac{E_a}{BT}\right), \tag{9.1}$$

where B is the universal gas constant and A, E_a are the frequency constant and activation energy respectively; t denotes time. The constants A, E_a are model parameters usually obtained experimentally. One can assume that $\Omega = 1$ marks the threshold of irreversible thermal injury that can be detected experimentally. Once this threshold is attained in a given mode of heating after the time t_A the measured thermal history of the system is used to derive

the values of model parameters in accordance with the equation:

$$1 = A \int\limits_{0}^{t_A} \exp\left(-\frac{E_a}{BT(t)}\right) dt.$$

For an isothermal regime the time t_A is simply the reciprocal of the damage rate defined in Eq.(9.1).

Another way of normalization is to define Ω in terms of concentrations of the original (native) tissue $C_0(t)$ and the damaged tissue $C_d(t)$, cf. [76]

$$\Omega(t) = \ln\left(\frac{C_0(0)}{1 - C_d(t)}\right), \qquad (9.2)$$

where $C_0(t) + C_d(t) = 1$ holds for every t.

There is a wide variety of experimental methods used to identify the time t_A at which irreversible cellular damage occurs. They rely on different physiological effects and therefore the damage mechanisms to which they respond are different. Some methods involve using fluorescent dye markers like propidium iodide, trypan blue or neutral red, which diffuse through heat-damaged cellular membranes. These methods measure essentially cellular membrane damage level which not necessarily are equal to the overall damage measure Ω. Another approach consists of assessing the colony-forming ability (clonogenics) of the heat-damaged cells after treatment, cf. [38] for details. While this seems to give a good indication of cell viability, the method needs considerable time for post treatment incubation. In investigations of the viability of the collagenous tissues the heat-induced shrinkage is usually regarded to be a good, measurable indicator of collagen denaturation, cf. [76, 77, 78, 632].

TABLE 12. First-order rate process model of thermal injury parameters (see Eq.(9.1)), after [38, 228, 447].

tissue	$E_a \left[\frac{kJ}{mol}\right]$	$A \left[\frac{1}{s}\right]$
skin	$628,5$	$3,1 \times 10^{98}$
prostate tumor (clonogenics measurements)	$526,4$	$1,04 \times 10^{84}$
prostate tumor (propidium iodide uptake measurements)	$244,8$	$2,99 \times 10^{37}$
prostate tumor (calcein leakage measurements)	$81,33$	$5,069 \times 10^{10}$
arterial tissue	430	$5,6 \times 10^{63}$
erythrocyte membrane	212	10^{31}
hemoglobin	455	$7,6 \times 10^{66}$
whole blood	448	$7,6 \times 10^{66}$

As can be inferred from Table 12 the values of model parameters obtained by using different methods vary in a wide range, cf. also [38] or [447] for comparison. This can give a clue as to what damage mechanisms are responsible

for the detected effects. This insight can be gained from the consideration of the activation energy E_a.

In general, the activation energy of any physical/chemical process is the critical minimum energy that must be possessed by the constituents involved for the process to take place. Therefore the rate of the process will be proportional to the fraction of these constituents which do possess the energy at least equal to the value of the activation energy. This fraction f is deduced from the Maxwell–Boltzman energy distribution law [228]

$$f = \exp\left(-\frac{E_a}{BT}\right). \tag{9.3}$$

Since the constant E_a as used in Eq.(9.1) can be viewed as the mean activation energy of the physical and chemical processes leading to heat-induced cellular damage (according to certain experimental criterion) the measured value of this constant, in comparison with the values of activation energy of various well-known processes provides foundation for speculations about the mechanisms of cellular injury [38, 228]. Henriquez [228] divided the potential damage mechanisms into three categories:

1. *Thermal alterations in proteins.* Proteins contribute to the maintenance of cell life in various ways and undoubtedly even minor heat-induced alterations to these molecules can lead to irreversible damage. Studies on the subject indicate that alterations to proteins occurring in the temperature range 0–100°C at measurable rates are not unusual. The activation energy of these processes are often well in excess of 200 kJ/mole and can be strongly dependent on pH (heat denaturation of egg albumin: $E_a = 553$ kJ/mole at pH=5; heat inactivation of invertase $E_a = 461$ kJ/mole at pH=4 and $E_a = 218$ kJ/mole at pH=5,7; of haemoglobin $E_a = 318$ kJ/mole at pH=5), see [38, 228].

2. *Other possible alterations in metabolic processes.* This class of effects includes the temperature influence on kinetics of metabolic processes that don't involve proteins. These are changes in the rates of diffusion, formation and degradation of chemical reactants, etc. The activation energy of these processes is usually on the order of $40 - 80$ kJ/mole. These effects are usually regarded of minor importance to cellular thermal injury as compared to previous group.

3. *Nonprotein induced alterations in the physical characteristics of cells.* The physical phenomena characteristic of protoplasm but not primarily affected by the thermal alterations of proteins, e.g. diffusion of metabolites through an unaltered cell wall.

The model presented by Eq.(9.1) gives a definite connection between time–temperature history and damage accumulation. It can facilitate design of the hyperthermic treatment procedures allowing, in principle, accurate damage prediction provided the temperature field is known, the model constants are chosen appropriately and the temperature range is suitable. However, it has several shortcomings. For instance, it does not take into account the history of thermal insult — larger and smaller thermal loads produce the same result, irrespective of their relative order, cf. [226] .

Another issue brought up by experimental investigations is that pH variations may play a similar sensitizing role for some kind of cells, cf. [226] and references therein. It is probable that preheating as well as acid pH may cripple the cell's capacity to accumulate and/or repair sublethal heat damage which is in turn different for different kinds of cells and may depend on mechanical loading cf. [76, 78]. Surprisingly, the influence of the latter is usually neglected. While *in vitro* tests in thermal baths and on isolated cells yield data usually specific to unloaded specimens, in the clinical *in vivo* experiments the tissue is often loaded in unknown and uncontrollable manner. The investigations of heat–induced shrinkage of collagenous tissue indicate that the increase in the mechanical loading during heating delays the denaturation, cf. [78, 117]. Introducing the characteristic time of damage process t_2 one may write

$$t_2 = \exp\left(\alpha + \beta P + \frac{m}{T}\right),$$

where α, β and m are experimental constants. Scaling the time variable of experimental results obtained in different temperature-load regimes with t_2 proved to be an effective way to reduce them to a single master-curve, cf. [76, 78, 117, 632].

Another possible disadvantage of Ω as a measure of thermal damage, as defined by Eq.(9.1) is that most experimental data suggests that thermal damage tends toward an asymptotic value at large t (under isothermal conditions) or constant T (constant heating rates). The model presented, however, does not display such a behaviour. The following model can be suggested to overcome this difficulty, cf. [76] and references therein,

$$\omega = w_0(1 - f) + \omega_d f,$$

where $f = 1 - e^{-\Omega}$ and ω_0, ω_d denote the considered physical property at the original and damaged state respectively. However, some physical properties (e.g. shrinkage) do not follow this law and display piecewise linear behaviour, cf. [76].

For practical applications it is convenient to compare thermal treatment to tissue against the normalized treatment. Sapareto and Dewey [500] pro-

posed such a 'common denominator' — a thermal dose generated at 43°C. They introduced *equivalent time of the treatment at* 43°C equal to

$$t_{43} = tR^{43-T}, \tag{9.4}$$

where T is the temperature, measured here in °C and R – the constant identified to be 0.5 for $T > 43$°C and 0.25 for $T \leq 43$°C.

The measure (9.4) applies to isothermal treatments but can be without difficulty extended to non–isothermal ones.

In Fig. 88 the percentage of surviving cells of various kinds is given as a function of equivalent minutes at 43°C. It is noticeable that, when the temperature is lower, the experimental curves are deviating from the general pattern. It can be attributed to the development of the thermotolerance.
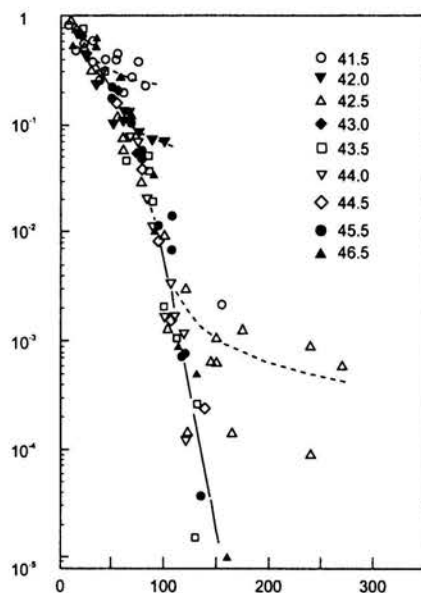
FIGURE 88. Surviving fraction of Chinese hamster ovary cells at various temperatures plotted as a function of equivalent minutes at 43°C. The data for lowest temperatures deviate from a single line, as shown by the dashed lines, due to development of thermotolerance, after [500].

9.3. Vasculature

Once the thermal loads applied to the tissue system are known, one can obtain the temperature field. To do this an appropriate thermal model needs to be devised for this system. From the point of view of heat transfer soft tissue is a complex physical entity because it is inhomogeneous, anisotropic, multiphasic and — above all — incorporates a massively sophisticated

vascular tree. Blood flowing through this tree has temperature that is often different from the temperature of surrounding tissue and carries thermal energy which is then transferred to the tissue, blood vessels and interstitial fluids.

So, theoretically, to correctly calculate the temperature distribution in the soft tissue one has to obtain information on the detailed structure of the vascular tree and mass and energy flows in each blood vessel. This seems to be an impossible task since the vessels diameters range from over a centimeter (vena cava) down to several microns (capillaries) and the individual description of heat transfer with each vessel is not possible, even with the use of contemporary computers, cf. [58].

Fortunately, the importance of all the vessels in the process of heat transfer is not equal. Chen and Holmes in [74] introduced *the thermal equilibration length* of the vessel, namely the length over which the temperature difference between blood and surrounding tissue is reduced by the factor e. In Table 13 the basic data pertaining to various types of vessels are presented.

TABLE 13. Properties of different kinds of blood vessels; V_v – vascular volume, r_{avg} – average radius, l_{avg} – average length, x_{eq} - thermal equilibration length, after [74].

vessel	% V_v	r_{avg} [μm]	l_{avg} [mm]	x_{eq} [mm]
aorta	3,30	5000	380	190000
large artery	6,59	1500	200	4000
arterial branch	5,49	500	90	300
terminal art. branch	0,55	300	8	80
arteriole	2,75	10	2	0,005
capillary	6,59	4	1,2	0,0002
venula	12,09	15	1,6	0,002
terminal vein	3,30	750	10	100
venous branch	29,67	1200	90	300
large vein	24,18	3000	200	5000
vena cava	5,49	6250	380	190000

As can be inferred from the Table 13 the temperature of blood in larger vessels is virtually independent of the tissue temperature (very large equilibration lengths) while the smallest vessels are practically at the local tissue temperature (their thermal equilibration lengths are much smaller than their actual lengths). This means that, while the larger vessels provide a kind of 'linear heat sources' embedded within the tissue, the smallest ones give rise to the blood convection through tissue.

In Fig. 89 the blood temperature, as it circulates through various scales of vessels is presented, after [74].
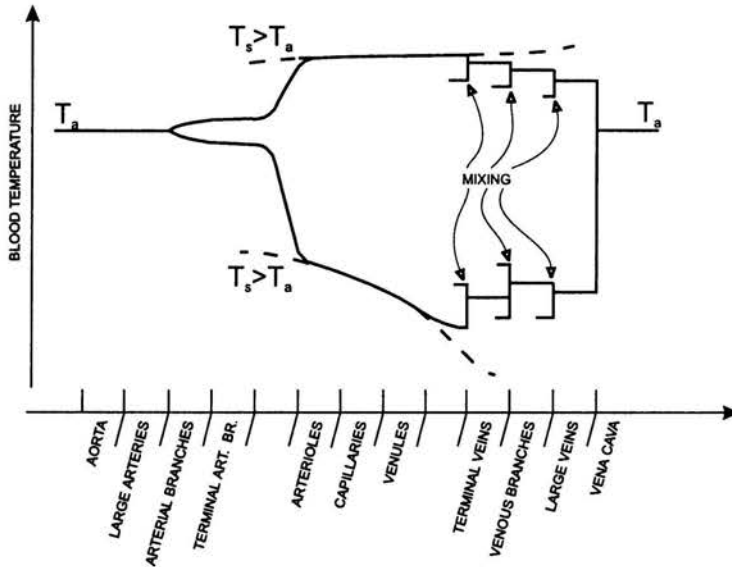
FIGURE 89. Temperature of the blood as it circulates through the vascular system, after [74].

Important property of human vascular system is that almost all blood vessels, except capillaries, exist in artery-vein pairs. Vessels in the pair lie close to each other and can thus exchange heat in counter-current regime. This effect allows for better energy conservation in cold environments because not all energy carried by the artery reaches superficial layers of skin since part of it is returned to the countercurrent vein.

The vascularization of each internal organ has specific structure. The spatial location and orientation of the largest vessels is known and such information is available in textbooks on human anatomy, e.g. [47]. The internal organs are most often maintained at the body core temperature so perhaps the most interesting, from the point of view of heat exchange, is the architecture of the subcutaneous circulation. The investigations of the subcutaneous vascularization of the rabbit thigh tissue were performed by Weinbaum et al. [614]. These authors concluded that the major arteries and veins supplying the animal's limb are 500–1000 μm in diameter and lie deeper than at 6 mm. The primary vessels supplying the peripherial tissue are at first 200–300 μm in diameter. Next, as one proceeds in the direction of the skin, the vessels undergo five or more branching generations terminating in transverse vessels 30–50 μm in diameter, that supply the capillaries. These vessels, termed by Weinbaum et al. [614] the 'terminal vessels' form a roughly periodic array of arterioles and venules, roughly perpendicular to the skin surface.

They supply the capillary beds that feed the muscle fibres and are situated along them, i.e. roughly parallel to the skin. The spacing of the terminal vessels in the rabbit thigh was found to be about 0.5–1 mm. The density of the capillaries varies with the type of muscle 'served'.

As the vascular castings of the Weinbaum and his coworkers showed, from the point of view of the vascularization, the cutaneous layer (the skin) is essentially independent of the immediately underlying layer. The deeper part of the skin, called the cutaneous plexus contains large, countercurrent vessel pairs lying parallel to the skin surface. They are supplied by the few large 'riser' vessels that originate from the deeper portions of the limb, traverse the skeletal muscle layers and connect to the skin circulation. This feature of the subcutaneous circulation is important because it implies that the entire circulation in the outermost regions is controlled by the vasoconstriction and vasodilation of the riser vessels, cf. [614]. In Fig. 90 this architecture is schematically depicted.
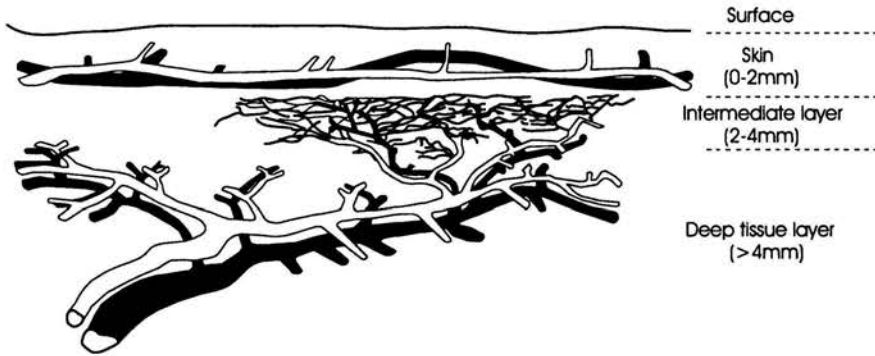
FIGURE 90. Architecture of the subcutaneous circulation; The information was obtained experimentally by means of vascular castings of the vessels in rabbit thigh, after [74].

9.4. Bio-heat transfer models

The first model that will be presented here is the Pennes equation, cf. [444]. It was proposed by Pennes in 1948 and has enjoyed long-lasting popularity. Basically the ground for proposing this model were measurements of the blood temperature in resting human forearm in normothermic conditions. These led Pennes to hypothesize that the soft tissue temperature obeys the equation (called now the *Pennes equation*):

$$\rho_t c_t \frac{\partial T_t}{\partial t} = \lambda_t \nabla^2 T_t + w_{bl} c_{bl} (T_t - T_a) + q_v, \qquad (9.5)$$

where ρ and c are the mass density [kg/m^3] and specific heat [J/(kgK)], respectively; w_{bl} is blood perfusion rate [m^3 blood/(s kg tissue)]. The subscript 'bl' labels the blood and T_a denotes arterial supply blood temperature that is assumed to be constant. The subscript t denotes tissue. The heat generation term q_v encompasses the thermal effects of metabolism and, if necessary, other volumetric heat loads (e.g., microwave irradiation). The tissue temperature T_t in Pennes's model is typically defined by, cf. [25, 74],

$$T_t(\mathbf{x}) = \frac{1}{\mathcal{V}} \int\limits_{\mathcal{V}} T(\mathbf{x})dV, \tag{9.6}$$

where the scale of the averaging volume $\mathcal{V}$ is assumed to be much larger than the size of thermally significant vessels and much smaller than the size of the tissue region itself. Baish [25] suggests that such a scale does not exist.

Pennes model is widely used for prediction of thermal response of soft tissues during hyperthermia, cf. [102, 269, 368, 369, 486, 488]. Copious references on the analytical solutions and sensitivity analysis of Pennes equation, can be found in [116, 126, 148, 151, 247, 356].

Thermal parameters occurring in the Pennes equation, such as thermal conductivity, blood perfusion, metabolic rate, specific heat, etc. reported in the literature are characterized by a considerable scatter, cf. the references in [356]. Therefore Liu [356] performed 1-D uncertainty analysis treating the temperature as a function of five parameters: the thermal conductivity of tissue, blood perfusion rate, volumetric metabolic heating, scattering coefficient and the heating power flux at the skin surface. Implications for clinical hyperthermia were also suggested. It seems that in assessing the role of those parameters the sensitivity analysis would be more appropriate, see e.g. [116, 367, 368].

The Pennes equation belongs to the class of the so-called continuum models. These describe the average tissue temperature distribution using the global parameters such as the perfusion rate. Therefore, by their very nature, they cannot predict the local variation of the temperature due to large (thermally-significant), blood vessels traversing the tissue.

Equation (9.5) is basically the usual Fourier-Kirchhoff equation of heat conduction for the isotropic material (λ is a scalar, in most formulations independent of temperature) equipped with the linear *heat-sink term* $w_{bl}c_{bl} \times (T_t - T_a)$ describing the fact that the energy input to tissue from the blood flow is proportional to the difference between the arterial supply temperature T_a and local tissue temperature T_t.

The originally proposed form of the heat-sink term was $w_{bl}c_{bl}(T_v - T_a)$ where T_v is venous return temperature. The equation thus represents a sim-

plified case where the blood arrives in the tissue at the arterial temperature, despite the obvious heat–exchange on the way, perfuses it and departs at the venous return temperature. Pennes then hypothesized further that $T_v \approx T_t$, which yields Eq.(9.5).

While the glance at the Fig. 89 convinces that the latter assumption is indeed plausible, the statement that the blood retains its arterial supply temperature until it reaches the capillaries is questionable. It basically means that there is no heat exchange with blood in the larger vessels and the thermal equilibration occurs in the capillaries only and is complete $(T_v = T_t)$.

Wulff [635] pointed out that these requirements are physically impossible. He raised four important points:

1. The Pennes model assumes that no heat exchange with blood takes place until the level of capillaries. There is no transport mechanism that could accomplish this. In reality, the local arterial temperature depends on the temperature gradient in tissue resulting from environmental conditions as shown in [58].

2. The blood perfusion term is isotropic and thus fails to account for the possible directed character of the blood flow.

3. The blood perfusion term has been obtained via the *global* energy balance for the blood and is applied to describe the *local* energy balance for tissue.

4. The first-order differentiability condition of numerous physical entities in the equation (e.g. heat flux, physical properties and heat generation), is not necessarily met in heterogeneous tissue structure.

While the last two have a rather formal character and are inherent to continuum models (the last objection not applying to variational formulations), the first and the second highlight possibly vitally important features of the real tissue that were neglected in the Pennes model.

Wulff proposed the solution to the second problem proposing a different model [635]. He treated the tissue as a porous medium, perfused with the blood. The blood remains thermally equilibrated with the tissue and its movement is described by means of the Darcy velocity **U**. The heat flux can be now decomposed into conductive and convective terms:

$$\mathbf{q} = -\lambda_t \nabla T_t + \rho_{bl} h_{bl} \mathbf{U}, \qquad (9.7)$$

where h_{bl} is the specific blood enthalpy. The first term on the r.h.s. of Eq.(9.7) is the usual Fourier conductive flux. The second accounts for the directed convection of blood. When one assumes that blood is always at the local tissue temperature one gets $h_{bl} = c_{bl} T_t$. This yields the equation:

$$\rho_t c_t \frac{\partial T_t}{\partial t} = \lambda_t \nabla^2 T_t - \rho_{bl} c_{bl} \mathbf{U} \cdot \nabla T_t + q_v. \qquad (9.8)$$

The assumptions made by Wulff are effectively the other extreme view on the problem of effectiveness of blood–tissue heat exchange mechanisms. Namely, Eq. (9.8) implies that these mechanisms are *perfect* everywhere throughout the vascular tree while the Pennes model assumes they are 100% ineffective until the level of capillaries where they suddenly become perfect. Given the data in Fig. 89 one may speculate that the intermediate case actually occurs.

Creeze and Lagendijk [103] also pointed out that the blood flow is not always unidirectional, vessels are often combined to form counter-current pairs and their orientation is frequently isotropic.

Another class of models are the so-called 'effective conductivity models' which are based on the assumption that the influence of the blood flow on the heat transport mechanisms in the tissue can be contained in the effective conductivity of the latter. In other words, one considers a temperature field in a replacement solid material, where only conduction (and no blood flow) is present. The conductivity of this replacement material is carefully selected so the temperature fields in the original and replacement material are approximately identical. The conductivity of the replacement material is termed the 'effective conductivity'. Such an approach resembles the micro-macro modelling, cf. Section 7 of our paper. In [103, 104] the authors compared the effective conductivity model against the Pennes equation experimentally.

In 1985 Weinbaum and Jiji provided theoretical arguments for the effective conductivity models [612]. Their approach resulted from extensive studies on the anatomy of the vascularization and from earlier, somewhat more complicated models [74, 286, 614]. Introduction of this model inspired many work in the field and triggered the publication of many papers [24, 70, 489, 535, 536, 589, 615, 653, 654, 655, 656]. We pass to the presentation of the model.

The fundamental assumptions of the Weinbaum–Jiji effective conductivity model are as follows [612]:

- local average blood temperature can be approximated by local tissue temperature,
- the primary heat transfer mechanism is the incomplete countercurrent exchange in thermally significant vessels (greater than 40μm in diameter), which means that the heat loss from the artery is *nearly but not quite* equal to the heat gained by the vein,
- the blood flows in vessels of the artery–vein pair are identical,

- axial conduction is negligible,
- the vessels in the pair have identical diameters.
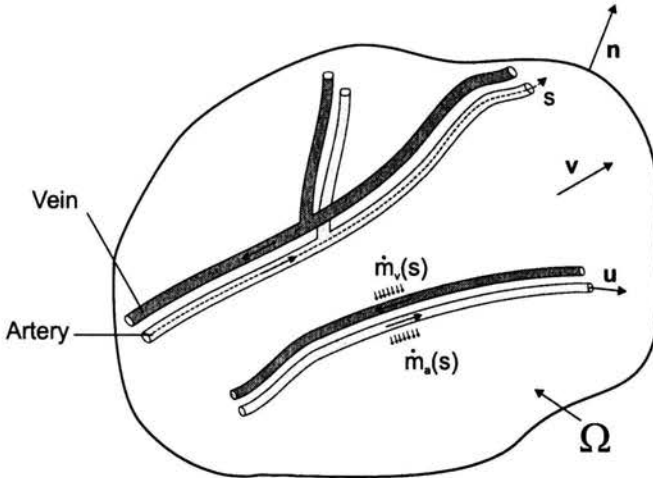
FIGURE 91. The control volume. By s we denote the direction tangent to the vessel, v is the local perfusion velocity and u is the average blood velocity in the vessel.

In Fig. 91 the control volume Ω is depicted. Its boundary Γ consists of two subsets: Γ_n — the part intersected by the vessels and the rest Γ_t. The energy conservation equation takes the form:

$$\int_\Omega \left((1 - \phi)\, \rho_t c_t \frac{\partial T_t}{\partial t} + \phi \rho_{bl} c_{bl} \frac{\partial T_{bl}}{\partial t} \right) d\Omega - \int_\Gamma \lambda_t \nabla T_t \cdot \mathbf{n} d\Gamma$$

$$= \int_\Omega q_v dV - \int_{\Gamma_t} \rho_{bl} c_{bl} T_{bl} \mathbf{v} \cdot \mathbf{n} d\Gamma_t - \int_{\Gamma_n} \rho_{bl} c_{bl} T_{bl} \mathbf{u} \cdot \mathbf{n} d\Gamma_n, \quad (9.9)$$

where ϕ is the volumetric fraction of the vessels in the volume of interest.

In the next step, Weinbaum and Jiji assumed that the blood uniform perfusion through the tissue gives no net effect:

$$\int_{\Gamma_t} \rho_{bl} c_{bl} T_{bl} \mathbf{v} \cdot \mathbf{n} dA = 0$$

and that the blood temperature T_{bl} in the term $\phi \rho_{bl} c_{bl} \frac{\partial T_{bl}}{\partial t}$ can be replaced by the tissue temperature T_t when the effective thermal capacity is introduced by $\bar{\rho} c = \phi \rho_{bl} c_{bl} + (1 - \phi) \rho_t c_t$.

The net heat exchange by the countercurrent vessels can be presented in the form:

$$\int_{\Gamma_n} \rho_{bl} c_{bl} T_{bl} \mathbf{u} \cdot \mathbf{n} dA = \int_{\Omega} (Q_v - Q_a) \, d\Omega,$$

where

$$Q_v - Q_a = \pi \rho_{bl} c_{bl} \left(\frac{d}{ds}(na^2 u T_v) - \frac{d}{ds}(na^2 u T_a) \right)$$

and n is the number density of the vessel pairs, T_a and T_v is the arterial and venous temperature respectively. All the integrals in Eq.(9.9) are therefore reduced to volume integrals and since the volume Ω is arbitrary, the energy balance (9.9) yields:

$$\bar{\rho} c \frac{\partial T_t}{\partial t} = \nabla \cdot \lambda_t \nabla T_t + \pi \rho_{bl} c_{bl} \left(\frac{d}{ds}(na^2 u T_v) - \frac{d}{ds}(na^2 u T_a) \right) + q_v, \quad (9.10)$$

where a is the diameter of the single vessel, u is the blood velocity in the vessel and s is the local coordinate of the vessel pair.

The equation for the axial variation of the temperature in the vessels is assumed in the form:

$$\pi \rho_{bl} c_{bl} \frac{d}{ds} \left(na^2 u T_a \right) = -n(q_a + 2\pi a \rho_{bl} c_{bl} g T_a),$$

$$\pi \rho_{bl} c_{bl} \frac{d}{ds} \left(na^2 u T_v \right) = -n(q_v + 2\pi a \rho_{bl} c_{bl} g T_v),$$

where g denotes bleed–off rate i.e. the rate of mass flow of the blood from the unit length of vessel into the surrounding tissue and q_a, q_v denote the heat loss by conduction from the unit length of artery and vein respectively. Equation (9.10) can be thus rewritten and we get:

$$\bar{\rho} c \frac{\partial T_t}{\partial t} = \nabla \cdot \lambda_t \nabla T_t + q_v + n \left[(q_a - q_v) + 2\pi a \rho_{bl} c_{bl} g (T_a - T_v) \right]. \quad (9.11)$$

Since

$$(q_a - q_v) = -\pi a^2 u \rho_{bl} c_{bl} \left(\frac{dT_a}{ds} - \frac{dT_v}{ds} \right),$$

the energy balance yields

$$\bar{\rho} c \frac{\partial T_t}{\partial t} = \nabla \cdot \lambda_t \nabla T_t + q_v - n \rho_{bl} c_{bl} \left[\pi a^2 u \frac{d}{ds} (T_a - T_v) - 2\pi a \, g(T_a - T_v) \right].$$

Next, Weinbaum and Jiji, [612] introduced the assumption that $T_t \simeq \frac{1}{2}(T_a + T_v)$ and $q_a + q_v \simeq 2q_a$. These assumptions were in fact the most often criticized ones. We can also write

$$-(q_a + q_v) = 2\pi\rho_b c_b a^2 u \frac{dT_t}{ds} \simeq -2q_a$$

and

$$q_v \simeq q_a \simeq \sigma k(T_a - T_v),$$

where σ is a shape coefficient defined by

$$\sigma = \frac{\pi}{\cosh^{-1}\frac{l(s)}{2r(s)}}.$$

Here l is the distance between the axes of the countercurrent vessels at the point determined by the coordinate s along the axis of the vessels.

We also have

$$(T_a - T_v) = -\frac{1}{\sigma\lambda_t}\left(\pi\rho_{bl}c_{bl}a^2 u \frac{dT_t}{ds}\right).$$

Consequently the energy equation takes on the form:

$$\bar{\rho}c\frac{\partial T_t}{\partial t} = \nabla \cdot \lambda_t \nabla T_t + q_v + \frac{n\pi^2 a \,\lambda_{bl}^2 \mathrm{Pe}}{4\lambda}\left(\frac{d}{ds}\left(\frac{a\mathrm{Pe}}{\sigma}\frac{dT_t}{ds}\right) - \frac{2g\mathrm{Pe}}{\sigma u}\frac{dT_t}{ds}\right),$$

where Pe is the Péclet number:

$$\mathrm{Pe} = 2a\rho_{bl}c_{bl}u/\lambda_{bl}.$$

If we denote the local direction cosines of the vessel pair by l_j we have

$$\frac{\partial\theta}{\partial s} = l_j \frac{\partial\theta}{\partial x_j}.$$

Thus we finally get the Weinbaum–Jiji bioheat equation:

$$\bar{\rho}c\frac{\partial T_t}{\partial t} = \nabla \cdot (\lambda_{eff}\nabla T_t) + q_v - $$
$$- \frac{\pi^2 a\lambda_{bl}^2 \mathrm{Pe}}{4\lambda_t \sigma}\left(\frac{\partial}{\partial x_i}(na\mathrm{Pe}l_i) + \frac{2ng\mathrm{Pe}}{u}\right)l_j\frac{\partial T_t}{\partial x_j}, \tag{9.12}$$

where the effective conductivity is given by:

$$(\lambda_{eff})_{ij} = \lambda_t\left(\delta_{ij} + \frac{\pi^2}{4\sigma\lambda_t^2}na^2\lambda_{bl}^2\mathrm{Pe}^2 l_i l_j\right). \tag{9.13}$$

As usual, (δ_{ij}) denotes the Kronecker delta.

According to Weinbaum and Jiji, application of the mass conservation equation:

$$\frac{d}{ds}(na^2 u) = -2nag$$

leads to the final, compact form of the Eq.(9.12)

$$\bar{\rho}c\frac{\partial T}{\partial \tau} = \frac{\partial}{\partial x_i}\left(\lambda_{ij}^{eff}\frac{\partial T}{\partial x_j}\right) + q_v - \frac{\pi^2 n r^2 \lambda_{bl}^2}{4\sigma \lambda_t}\text{Pe}^2 l_j \frac{\partial l_i}{\partial x_i}\frac{\partial T}{\partial x_j}. \qquad (9.14)$$

This equation is the ordinary Fourier-Kirchhoff equation for heat conduction in anisotropic media with the effective conductivity and an additional term on the r.h.s. This term accounts for the possible variation of vessel radius along its length and for the directed capillary perfusion between artery and vein. It is small and vanishes entirely when the vessels are straight (i.e., l_i does not change in space).

From Eq.(9.13) the formula for the effective scalar conductivity in one-dimensional case can be obtained.

$$\lambda_{\text{eff}} = \lambda_t \left(1 + \frac{n\pi^2 a^2}{4\sigma}\left(\frac{\lambda_{bl}}{\lambda_t}\right)^2 \text{Pe}^2\right). \qquad (9.15)$$

As estimations by Weinbaum and Jiji [612] indicate, for tissue with vessels that have radius of more than $100\,\mu$m, the enhancement in conductivity is noticeable and for larger vessels the effective conductivity is several times larger than the tissue intrinsic property.

Assumptions, specified earlier, leading to the development of the Weinbaum-Jiji bioheat equation, mainly that average arterio-venous temperature is equal to the tissue temperature, have been criticized in [58] and [628]. Results of computations on elaborate vascular model by Brinck and Werner contradict this assumption, cf. [58].

The existence and importance of countercurrent heat exchange at the certain vessel scale range has been confirmed by numerous experiments both in normothermic and hyperthermic (vasodilated state), cf. [535, 536, 653, 654].

The effective conductivity models do not depend explicitly on arterial temperature. Increase of the blood flow rate results therefore in enhancement in effective conductivity of the tissue, regardless of whether warm blood perfuses cold tissue or cold blood perfuses warm tissue. The consequence is that perfusing cooler tissue with warm blood will result in decrease in temperature owing to enhanced conduction to the surface — the effect opposite to the one predicted by Pennes equation (9.5). Wissler [628] argues that this

discrepancy is in favour of the latter and proposes supplementing the Pennes equation with additional 'efficiency factor' to account for the incomplete countercurrent heat exchange in a simple way. Similar concept was proposed by Brinck and Werner [57] who validated such model against the predictions of a complex vascular model of human extremity.

Weinbaum and Jiji [615] suggested that a hybrid model should be used, consisting of Pennes model and the effective conductivity approach. They propose that thermal equilibration parameter (thermal equilibration distance normalized by the length of the representative vessel):

$$e = \frac{\pi r \mathrm{Pe}}{2\sigma L} \qquad (9.16)$$

should be used to distinguish whether the Pennes model ($e > 0,3$) or the Weinbaum-Jiji bioheat equation ($e \leq 0,3$) applies. Similar suggestions were made by Charny et al. [70], who compared the normothermic and hyperthermic response of the Weinbaum-Jiji λ_{eff} model, the Pennes model and more sophisticated three-equation model. The main conclusion of their study was that the Pennes model provides a relatively good prediction capabilities and should be therefore incorporated in the proposed hybrid model by means of the criterion (9.16). This means that under normothermic conditions the Eq.(9.5) should be used in regions of tissue containing first generations of supply vessels (larger than $500\,\mu$m in diameter). As the study by Charny et al. [70] have shown, neglecting the countercurrent heat exchange in these regions does not lead to any serious discrepancies. The Weinbaum-Jiji model is more suitable in regions of tissue containing smaller vessels. A hybrid axisymmetric model of human limb, containing layers governed by Pennes equation (9.5) and layers governed by Weinbaum–Jiji simplified bioheat equation (9.14) was investigated in [541].

Limitations of applicability of Weinbaum-Jiji bioheat equation were also shown by Valvano et al. [589] by means of analysis and thermistor measurement of temperature field in canine cortex.

The validity of effective conductivity approach was tested by Baish who viewed the tissue with embedded countercurrent vessels as a composite material consisting of low-conductivity tissue matrix and high conductivity fibers representing paired countercurrent vessels [24]. He obtained the formula for the fiber conductivity:

$$\lambda_f = \frac{(\dot{m}c_{bl})^2}{2lr\pi^2\lambda}\cosh^{-1}\left(\frac{l}{r}\right), \qquad (9.17)$$

where $2l$ is the distance between axes of the countercurrent vessels.

Because of the quadratic dependence on the blood flow rate, the conductivity computed using Eq.(9.17) varies in the very wide range. For example, for vessels with the radius of $300\,\mu$m the respective fiber conductivity exceeds $3000\,\mathrm{W/mK}$ and for vessel radius of $500\,\mu$m this conductivity is $320\,000\,\mathrm{W/(mK)}$. No real material has such a high conductivity. This result is explained by the fact that convection really taking place within the veins is much more efficient heat transfer mechanism than the conduction. The tissue has an intrinsic conductivity on the order of 0.2–$0.6\,\mathrm{W/(mK)}$. If we consider the array of parallel countercurrent vessel pairs embedded in tissue, lying along the z-axis and impose an external temperature gradient parallel to the axes of vessels, the total heat flux can be expressed as, cf. [24],

$$q = -\lambda_t \frac{dT_t}{dz} + n(Q_a + Q_v),$$

where $(Q_a + Q_v)$ is the heat exchange with the tissue by a single vessel pair. So the effective conductivity approach is admissible only if $(Q_a + Q_v)$ is proportional to the tissue temperature gradient dT_t/dz. Heat exchange by blood vessel pair is, however, proportional to the gradient of mean blood temperature T_m. Therefore, assumption by Weinbaum and Jiji $dT/dz = dT_m/dz$ is necessary in the derivation of effective conductivity model, cf. [24].

The Pennes, Wulff and Weinbaum-Jiji models can be combined to obtain a hybrid model. Chen and Holmes [74], for the bio-heat equation propose the following formulation:

$$\rho_t c_t \frac{\partial T_t}{\partial \tau} = \nabla \cdot (\lambda_{eff} \nabla T_t) + w_{bl}^* c_{bl}(T_a^* - T_t) - \rho_{bl} c_{bl} \mathbf{U} \cdot \nabla T_t + q_v, \qquad (9.18)$$

where w_{bl}^* and T_a^* are the perfusion rate and arterial temperature respectively, modified to avoid double-counting of the contribution of large vessels (these contributions are separately calculated).

Crezee et al. [104] considered a mixed heat sink-effective conductivity approach, formulated in the following way:

$$\rho_t c_t \frac{\partial T_t}{\partial \tau} = \lambda_{eff} \nabla^2 T_t + f w_{bl} c_{bl}(T_a - T_t) + q_v, \qquad (9.19)$$

where f is a model parameter depending on the local vascularity structure. It can be shown that for closed vessel network $0 \leq f \leq 1$, cf. [104]. The role of f is similar to the 'efficiency function' as introduced in [57, 628].

Roemer and Dutton [489] argued that the Pennes perfusion term and the effective conductivity are nonphysiological values that are related to true capillary perfusion in a problem-dependent manner. These authors provided detailed derivation of the universal tissue convective energy balance equation.

Many times, in the present notes, the term 'vascular model' has been used. It therefore needs some clarification. Unlike the continuum models, which describe the thermal response of the tissue with the use of the continuous effective properties (the perfusion rate, thermal conductivity, Darcy velocity etc.) the vascular models describe the energy exchange on a vessel–by–vessel basis. During the calculations one keeps track of the flow and temperature in each blood vessel (or vessel pair) as well as of the tissue temperature. It is the complexity of the vascular tree that makes the task so formidable. The limitations of the contemporary computers enable one to calculate the transient temperature fields only in small samples of tissue [58]. Apart from that, to perform useful calculations, one needs enormous quantity of data regarding the actual placement of blood vessels throughout the vascular tree, their sizes and the flow. In return, the vascular models can attain the goal which no continuum model can reach — they can predict the local effects of large, thermally–significant blood vessels [79].

9.5. Metabolic heating

All the formulations of the heat transfer in the living tissue (with the possible exception of those related to bone tissue) have to take into account the heat generated within the volume of the material. They manifest themselves through the source term q_v present in the energy balance equation, see Eq. (9.5), (9.8), and (9.14). The heat generation within the living tissue results from the metabolic activity and depends on the type of tissue as well as on the conditions. In his investigation of tumor tissue Jain suggests that metabolic heat generation rate is a function of oxygen supply, which is in turn dependent on the local blood perfusion rate, [269]. He proposes the quantitative relation, which unfortunately contains an error (it yields values of order of $1\,\mathrm{GW/m^3}$ which are too high). In Table 14 the typical values of the metabolic heat generation rate are provided, after [518].

TABLE 14. Heat generation rates in different kinds of tissues, after [518]

type of tissue	q_v [W/m^3]
Muscle	631.9
Fat	5.0
Skin	247.4

The sensitivity analysis of the Pennes equation performed by Liu reveals that the temperature field is quite insensitive to the variations of the metabolic heat generation term, [356]. The metabolic heat generation is

therefore frequently omitted in the analysis of the local temperature field. It can be of importance when dealing with the problems of whole-body energy balance and thermal comfort or in the extreme cases such as cold-water survival cf. [145].

The problem of metabolic energy generation in muscle was recently studied by Bhargava et al., [37]. These authors developed a simple phenomenological model for predicting muscle heat generation which will be now briefly described.

The heat generation rate in muscle q is divided in the following manner:

$$q = q_a + q_m + q_s + q_b, \tag{9.20}$$

where q_a is the activation heat rate, q_m is maintenance rate, q_s is shortening heat rate and q_b is the basal metabolic heat rate. The activation heat rate corresponds to tension-independent heat, liberated upon the stimulation of the muscle and is thought to be due to the movement of the Ca^{++} ions. It is further split into two terms related to the fast and slow muscle fibers respectively:

$$q_a = m\phi(t) \sum_{i=\text{slow, fast}} f_i A_i u_i(t), \tag{9.21}$$

where $\phi(t)$ is the prescribed decay function, m is the total mass of the muscle, f_i is the mass fraction of muscle fibers of type i, A_i are prescribed constants and $u_i(t)$ are the excitation levels of the respective muscle fibers.

The maintenance heat rate q_m is the stationary heat rate produced during isometric tetanus due to cycling of actin-myosin bridges. Analogously to the activation rate, q_m is also split in two components:

$$q_m = mL(l_m) \sum_{i=\text{slow, fast}} f_i M_i u_i(t), \tag{9.22}$$

where $L(l_m)$ is the prescribed function of muscle length and M_i are prescribed constants.

The shortening heat rate q_s corresponds to the heat generated during contraction beyond that which occurs during isometric contraction at the same force. It is proportional to the velocity of shortening.

$$q_s = -\alpha v_{\text{CE}}, \tag{9.23}$$

where v_{CE} is the velocity of the contraction of the muscle contractile element (positive velocity for lengthening or eccentric contraction). The coefficient α is dependent on the isometric force of the muscle as well as on the current muscle force.

The basal metabolic rate is assumed to be proportional to muscle mass.

For more details on the assumed form of the model functions and parameters the reader is referred to [37]. The calculations performed therein allow one to estimate the distribution of the heat into the various mechanisms of heating and predict the heat generation in particular muscles during various activities. The largest shortcoming, as the authors of the paper [37] seem to admit, is the fact that the decomposition (9.20) is somewhat arbitrary and it is not known what processes are responsible for heat production and if these processes are independent. Moreover the model requires a number of parameters to be known and their estimation seems to be a rather difficult task.

9.6. Comment on hyperbolic conduction in tissues

In all presented considerations of thermal modelling of soft tissue the classical Fourier-Kirchhoff heat conduction equation was used. The Pennes (9.5) or Weinbaum-Jiji model (9.14) are extensions of this equation. All these equations share the assumption that the Fourier law holds, namely that the instantaneous heat flux vector is proportional to the instantaneous negative gradient of temperature:

$$\mathbf{q}(\mathbf{x}, t) = -\lambda \nabla T(\mathbf{x}, t). \qquad (9.24)$$

The consequence of this assumption is the fact that the thermal disturbances travel at infinite speed through the medium, i.e. perturbation of the temperature in one point of the solid body causes instantaneous change in temperature at arbitrarily distant points of the body. This is obviously non-physical prediction.

Another approach is to assume that finite time τ elapses between establishment of the heat flux and the appearance of the corresponding temperature gradient.

$$\mathbf{q}(\mathbf{x}, t + \tau) = -\lambda \nabla T(\mathbf{x}, t). \qquad (9.25)$$

The l.h.s. of Eq. (9.25) can be expanded in the Taylor series with respect to t and, for small τ, omission of all terms but the first two yields the Cattaneo-Vernotte equation:

$$\mathbf{q}(\mathbf{x}, t) + \tau = -\lambda \nabla T(\mathbf{x}, t). \qquad (9.26)$$

Substitution of this constitutive equation for heat flux into the energy balance equation yields the hyperbolic equation of conduction:

$$\rho c \left(\frac{\partial T}{\partial t} + \tau \frac{\partial^2 T}{\partial t^2} \right) = \nabla \cdot (\lambda \nabla T). \qquad (9.27)$$

In case of Eq. (9.27) the speed of propagation of thermal wave is not infinite but is (in the case of isotropic body where $\boldsymbol{\lambda} = \lambda\mathbf{I}$) $v = \sqrt{\lambda/(\rho c \tau)}$. In the material described by Eq. (9.26) the heat flux depends not only on the present value of temperature gradient but also on its past history, see [294].

Theory of hyperbolic heat conduction is not widely used in technical applications, because the relaxation time τ for most materials is very small (of the order of 10^{-12}–10^{-8}) and the corresponding speed of thermal wave (second sound) is very high so the non-Fourier effects are negligible. They need to be taken account of only in cases of violent heat treatment processes when the rate of heat flux is very high. There is evidence, however, that these effect may be present in highly heterogeneous materials due to very high (of the order of several seconds) effective relaxation time, [294].

Mitta et al. [400] conducted a series of experiments to compare the applicability of the parabolic and hyperbolic heat transfer models for meat. These experiments sought to determine the finite thermal wave propagation speed and demonstrate thermal wave superposition. They consisted of instantaneous (step) thermal loading scenarios. Thermal wave propagation speed was assessed on the basis of time elapsed between thermal loading and the registration of the significant (i.e. larger than the measurement uncertainty) temperature deviation within the material. The corresponding relaxation times were found to be 15–17 sec. with uncertainty of 13.6%. For short times, the measured time histories of the sample temperature were in good agreement with the prediction of the hyperbolic model. For long times, the predictions of both models coincided and were in good agreement with the experiment.

Liu [355] attempted to justify theoretically the hyperbolic heat conduction model. The thermal wave model for bioheat transfer (termed TWMBT by Liu [355]) was developed, and then compared with the known Pennes model in a variety of scenarios. Similarly as in [400], the hyperbolic model agrees with a parabolic one for long times during step loading. This is not the case, however, for periodic thermal loading (e.g. boundary temperature varying sinusoidally with time). The predictions of the hyperbolic model exhibit a noticeable phase shift when compared to temperatures calculated in accordance with parabolic one, [355].

The hyperbolic model of heat conduction in tissue was also adopted by Deng and Liu for considerations of freezing of skin tissue [127]. Among the conclusions presented in [127] perhaps the most important is that the thermal stresses developed during freezing can be significantly larger in the case of the hyperbolic model of heat conduction.

Finally it should be noted that hyperbolic model of heat transfer in biomechanics is by no means a widely accepted one, cf. [256].

9.7. Mixture theory applicable to modelling of heat–induced changes in hydration and mechanical properties of soft tissues

In the previous section various heat transport problems in soft tissues have been presented. The aim of this Section is to investigate the diffusion problem, specifically the diffusion of water through a thermally damaged biological soft tissue that undergoes *finite deformations*. To this end we follow the paper by Tao et al. [563], based on the mixture theory. The model proposed aims at the description of heat-induced alterations in soft tissue. For instance the effect on collagen can be 'reversible' or 'irreversible'. It is known that moderate heating can result in a local unfolding within the protein that is reversed upon the restoration of normal temperatures. More intensive heating results in a time-dependent irreversible transformation of the native triple helical structure into a more random (coiled) structure, cf. the relevant references in Tao et al. [563]. It is believed that the latter transformation occurs primarily via the breaking of long sequences of hydrogen bonds that stabilise the triple helix. Heat-induced breakage of reducible cross-links may also play a role. Regardless of the precise mechanisms, on a gross scale denaturation results in an irreversible shrinkage of the tissue, which Tao et al. [563] assume as a conventional measure of thermal damage. According to these authors this shrinkage may result due to exposure of hydrophobic regions of the molecule that are initially within the centre of the helical structure. Denaturation also results in a gross change in the hydration of the collagen, which is thought to be due first to the liberation of water and then a subsequent increased absorption of water via water bridges.

9.7.1. Basic equations. The body considered consists of mobile water, loosely bonded with the tissue, and a porous solid having tightly bonded water molecules. The tissue may be further partitioned into two sub-components: one associated with that part wherein the hydrogen bonds are broken due to thermal damage and another that is the intact native part. It is expected that the damaged and the native components intermingle (over the representative volume elements), with inter-conversion occurring from damaging and healing. It is assumed that the solid components undergo at a point the same motion in an average sense.

Before passing to the presentation of the model developed by Tao et al. [563] on a classical example of periodic homogenization of transport equation (diffusion equation) we will show that the mixture theory approach is only an approximate one from the point of view of homogenisation, cf. Cioranescu and Donato [84].

Example 8. *(relation between homogenization and mixture theory)*

Let $\Omega \subset \mathbb{R}^N$ be a bounded domain with sufficiently smooth boundary. Let $\varepsilon > 0$ be a small parameter characterizing the microstructure of material body $\bar{\Omega}$ is made of. Here $\bar{\Omega}$ denotes the closure of Ω.

Consider the problem, see Cioranescu and Donato [84],

$$
\begin{cases}
-\operatorname{div}(\mathbf{a}(\mathbf{x})\nabla^\varepsilon) = g & \text{in } \Omega, \\
\\
\phantom{-\operatorname{div}(\mathbf{a}(\mathbf{x})\nabla^\varepsilon) = } u^\varepsilon = 0 & \text{on } \partial\Omega.
\end{cases}
$$

Here g is a given function and the matrix $\mathbf{a}^\varepsilon$ is the εY-periodic matrix defined by

$$
\mathbf{a}^\varepsilon_{ij}(\mathbf{x}) = a_{ij}(\mathbf{x}/\varepsilon), \quad i, j = 1, \dots, N.
$$

We assume that $a^\varepsilon_{ij} = a^\varepsilon_{ji}$ and

$$
c_1|\mathbf{b}|^2 \leq a_{ij}(\mathbf{y})b_i b_j \leq c_1|\mathbf{b}|^2, \quad \forall \mathbf{b} \in \mathbb{R}^N, \quad \mathbf{y} = \mathbf{x}/\varepsilon,
$$

for almost every $\mathbf{y} \in Y$.

The small parameter $\varepsilon > 0$ is a ratio of characteristic *microscopic* dimension and a characteristic *macroscopic* one. By Y we denote the so-called basic or reference cells defined by

$$
Y = (0, l_1) \times \cdots \times (0, l_N),
$$

where $l_1, \dots, l_n$ are given positive numbers. The functions $a_{ij}(\mathbf{y})$ are not necessarily continuous, thus layered materials are not precluded. We observe that $\mathbf{y} = \mathbf{x}/\varepsilon$ and $N = 3$ for three-dimensional problems.

Homogenization means passing with ε, in appropriate sense, to 0 (smearing out heterogeneities). It can be shown that the homogenized coefficients a^h_{ij} (constants) are given by, cf. Cioranescu and Donato [84],

$$
a^h_{ij} = \langle a_{ij} \rangle + \langle a_{jk} \frac{\partial \chi_i}{\partial y_k} \rangle, \tag{9.28}
$$

where

$$
\langle g \rangle = \frac{1}{|Y|} \int_Y g(\mathbf{y}) d\mathbf{y}.
$$

The so-called local functions $\chi_i(\mathbf{y})$, $\mathbf{y} \in Y$ are solutions to the following problem:

$$
\begin{cases}
\chi_i \in H^1_{per}(Y), \quad \langle \chi_i \rangle = 0, \\
\\
\int_Y a_{jk} \frac{\partial \chi_i}{\partial y_j} \frac{\partial v}{\partial y_k} d\mathbf{y} = \int_Y a_{ki} \frac{\partial v}{\partial y_k} d\mathbf{y},
\end{cases} \tag{9.29}
$$

for each $v \in H^1_{per}(Y)$ such that $\langle v \rangle = 0$. The space $H^1_{per}(Y)$ is defined by

$$H^1_{per}(Y) = \{v \in H^1(Y)|\ v \text{ takes equal values on the opposite faces of } Y\},$$

whilst $H^1(Y)$ is the classical Sobolev space:

$$H^1(Y) = \{v \in L^2(Y)|\ \frac{\partial v}{\partial u_i} \in L^2(Y),\ i = 1, \ldots N\}.$$

We recall that $L^2(Y)$ denotes the space of square integrable functions.

From Eq. (9.28) we conclude that in order to find the homogenized (macroscopic) ceofficients a^h_{ij}, we have to solve the local problem (9.29), by no means an easy one. Similar situation, yet still more complex, arises in the case of homogenisation of nonlinear problems. The local functions χ_i, and consequently fluctuations, play thus an important role. Deleting the term with χ_i in Eq. (9.29) we get the so-called 'mixture law' and effective coefficients in the form, cf. Cioranescu and Donato [84],

$$a^*_{ij} = \langle a_{ij} \rangle. \tag{9.30}$$

Obviously, $a^*_{ij} \neq a^h_{ij}$ and the difference may be significant. In fact, a^*_{ij} present the so-called Voigt bounds.

To find a^h_{ij} by using the theory of volume averaging one would have to solve the so-called *closure problem*, involving fluctuations, cf. Whittaker [622]. As far as we know, the closure problem has been solved only for a class of transport problems, see the book by Whittaker, just cited. It is thus not surprising that within the mixture theory, where the closure problem (a counterpart of local problem) is rarely discussed, the macroscopic constitutive relationships are postulated, and not derived by a micro-macro approach. Consequently, the problem of, say, temperature of mixture is still disputable. For instance, in the literature one finds models with different constituent temperatures (Klisch, [304] and the references therein), and models with the same temperatures of constituents, cf. Tao et al. [563], and the references therein.

We pass to the presentation of the approach used by Tao et al. [563]. The model we intend to present is rather complex. As a first step the reader is advised to study a simpler paper by Hron et al. (2002), where a mixture model for nonlinearly elastic solids that is infused with a fluid was proposed. Then the Helmholtz potential can be expressed as a function of $\mathbf{C} = \mathbf{F}^T\mathbf{F}$ and the fluid volume fraction. Within the framework of mixture theory, a set of thermodynamic quantities can be assigned to each component: quantities associated with the mobile water and tissue will be denoted by superscripts

f and t, respectively, and quantities associated with the damaged and native constituents will be denoted, respectively, by the superscripts d and n. The equations describing the balance of mass, linear momentum, and energy for each component α are given by:

$$\frac{\partial \rho^\alpha}{\partial t} + \operatorname{div}(\rho^\alpha \mathbf{v}^\alpha) = m^\alpha, \quad \alpha = f, n, d, \tag{9.31}$$

$$\sum_{n,d} m^\alpha = 0, \quad m^f = 0, \tag{9.32}$$

$$\frac{\partial}{\partial t}(\rho^\alpha \mathbf{v}^\alpha) + \operatorname{div}(\rho^\alpha \mathbf{v}^\alpha \otimes \mathbf{v}^\alpha) = \operatorname{div}\boldsymbol{\sigma}^\alpha + \mathbf{p}^\alpha, \quad \alpha = f, t, \tag{9.33}$$

$$\rho^t = \rho^n + \rho^\alpha, \tag{9.34}$$

$$\sum_{t,f} \mathbf{p}^\alpha = \mathbf{0}, \tag{9.35}$$

$$\frac{\partial}{\partial t}[\rho^\alpha(\epsilon^\alpha + \frac{1}{2}|\mathbf{v}^\alpha|^2)] + \operatorname{div}[\rho^\alpha(\epsilon^\alpha + \frac{1}{2}|\mathbf{v}^\alpha|^2)\mathbf{v}^\alpha]$$
$$= \operatorname{div}(\boldsymbol{\sigma}^\alpha \mathbf{v}^\alpha - \mathbf{q}^\alpha) + \mathbf{p}^\alpha \cdot \mathbf{v}^\alpha + s^\alpha, \quad \alpha = t, f \tag{9.36}$$

$$\sum_{t,f}(\mathbf{p}^\alpha \cdot \mathbf{v}^\alpha + s^\alpha) = 0. \tag{9.37}$$

Here ρ^α, $\mathbf{v}^\alpha$, $\boldsymbol{\sigma}^\alpha$, ϵ^α and $\mathbf{q}^\alpha$ denote, respectively, the mass density, velocity, Cauchy stress tensor, internal energy density, and heat flux associated with the αth component; $m^\alpha, \mathbf{p}^\alpha$ and s^α are, respectively, the mass density conversion rate, the internal momentum supply, and the energy supply to the αth constituent resulting from the interactions between the components.

To the above framework we append a thermodynamic notion that is widely used in non-equilibrium thermodynamics. The entropy η^α for constituent α can be introduced, for instance, under the hypothesis of local equilibrium, and then a balance equation can be proposed that has an analogous structure to Eqs. (9.31), (9.32), and (9.36), cf. Groot and Mazur [202],

$$\frac{\partial}{\partial t}(\rho^\alpha \eta^\alpha) + \operatorname{div}(\rho^\alpha \eta^\alpha \mathbf{v}^\alpha) = \operatorname{div}\mathbf{J}^\alpha + \sigma^\alpha, \quad \alpha = f, t. \tag{9.38}$$

Here $\mathbf{J}^\alpha$ and σ^α denote, respectively the entropy flux and the internal entropy production rate per unit volume. The separation of the r.h.s. of (9.38) into two parts leads to a natural representation due to the restrictions imposed by the second law of thermodynamics for isolated systems.

We observe that introduction of sufficiently regular fields ρ^α, $\mathbf{v}^\alpha$, $\mathbf{J}^\alpha$, η^α, σ^α, etc. is based on the assumption that each constituent can be modelled

as a continuum and on the hypothesis of local equilibrium. In other words, these fields are averaged over some characteristic volume $\mathcal{V}$ or area, large compared with the characteristic dimension l.

Tao et al. [563] derived a restriction on σ^α by applying (9.38) to an isolated mixture $\mathcal{U}$ with isolated $\mathcal{V} \subseteq \mathcal{U}$

$$\int_\mathcal{U} \sigma dv = \frac{\partial}{\partial t} \int_\mathcal{U} \sum_{f,t} \rho^\alpha \eta^\alpha \, dv \geq 0, \quad \sigma = \sum_{f,t} \sigma^\alpha. \tag{9.39}$$

Due to smallness of l and assuming that the form of σ is independent of whether the mixture in motion is isolated or not, we get

$$\sigma = \sum_{f,t} \sigma^\alpha \geq 0, \tag{9.40}$$

for the motion of the mixture in general.

Consider now some issues related to the solid constituent. According to our assumptions the two subcomponents of the tissue have individual mass densities but undergo the same motions, i.e.,

$$\rho^t = \rho^n + \rho^\alpha, \quad \mathbf{v}^n = \mathbf{v}^d = \mathbf{v}^t. \tag{9.41}$$

Then Eqs. (9.31) and $(9.32)_1$ imply

$$\frac{\partial \rho^t}{\partial t} + \operatorname{div}(\rho^t \mathbf{v} t) = 0. \tag{9.42}$$

We recall that

$$J\rho^t = \rho_0^t, \quad J = \det \mathbf{F}, \tag{9.43}$$

where ρ_0^t denotes the effective mass density of the tissue component in the original reference configuration κ_0 of the tissue, and $\mathbf{F}$ is the deformation gradient of the solid with respect to κ_0. This κ_0 might be identified with the state of the tissue in which $\rho^d = 0$ or ρ^d is negligible compared with ρ^n and it is almost stress free. As the thermal damage takes place, ρ^d increases, and the response of the material is no longer purely elastic. The subcomponent of damaged constituent will have a different reference configuration κ_d from which its response is elastic. Tao et al. [563] introduced a reference configuration κ that is intermediate between κ_0 and κ_d and may evolve due to thermal damage. The deformation gradient $\mathbf{F}$ can be decomposed into a part $\mathbf{F}_\kappa$ that is associated with an elastic response and another that is associated with the evolution of natural configurations. If the configuration κ is determined by $\mathbf{G}$ then we have

$$\mathbf{F}_\kappa = \mathbf{F}\mathbf{G}^{-1}. \tag{9.44}$$

9.7.2. Specific case. To apply the above framework to study the diffusion of water through thermally damaged tissue, we set

$$
\rho = \sum_{f,t} \rho^\alpha, \qquad \mathbf{v} = \frac{1}{\rho} \sum_{f,t} \rho^\alpha \mathbf{v}^\alpha, \qquad \eta = \frac{1}{\rho} \sum_{f,t} \rho^\alpha \eta^\alpha,
$$

$$
\epsilon = \frac{1}{\rho} \sum_{f,t} \rho^\alpha \epsilon^\alpha, \qquad \mathbf{q} = \sum_{f,t} \mathbf{q}^\alpha, \qquad \mathbf{u}^\alpha = \mathbf{v}^\alpha - \mathbf{v}, \tag{9.45}
$$

$$
\varphi = \frac{\rho^\alpha}{\rho^t}, \qquad \mathbf{L}^\alpha = \mathrm{grad}\,\mathbf{v}^\alpha.
$$

Equation $(9.45)_7$ defines the mass fraction of the damaged solid. Assume that both components — mobile water and tissue — have the same absolute temperature T whilst the entropy and the internal energy of the mixture are completely determined by the primary fields ρ^f, φ, T, $\mathbf{F}_\kappa$, $\mathbf{G}$ and the reference configuration κ:

$$
\eta = \hat{\eta}(\rho^f, \varphi, T, \mathbf{F}_\kappa, \mathbf{G}; \kappa), \quad \epsilon = \hat{\epsilon}(\rho^f, \varphi, T, \mathbf{F}_\kappa, \mathbf{G}; \kappa). \tag{9.46}
$$

Hence we infer that the entropy η and the internal energy ϵ are modelled similar to an elastic process with deformation $\mathbf{F}_\kappa$ with respect to κ for fixed ρ^f and φ. The dissipative response due to the viscosity of water is accounted for through the internal momentum supply $\mathbf{p}^f$.

Classically, we introduce the Helmholz potentials:

$$
\psi^\alpha = \epsilon^\alpha - T\eta^\alpha, \quad \psi = \frac{1}{\rho} \sum_{f,t} \rho^\alpha \psi^\alpha. \tag{9.47}
$$

Then we have

$$
\psi = \epsilon - T\eta = \hat{\psi}(\rho^f, \varphi, T, \mathbf{F}_\kappa, \mathbf{G}; \kappa). \tag{9.48}
$$

Choosing classical relations:

$$
\mathbf{J}^\alpha = -\frac{1}{T}(\mathbf{q}^\alpha + \rho^\alpha \psi^\alpha \mathbf{u}^\alpha) \tag{9.49}
$$

and

$$
\eta = -\frac{\partial \hat{\psi}}{\partial T} \tag{9.50}
$$

and introducing a Lagrange multipler p associated with the volume additivity constraint, i.e.,

$$
\frac{\rho^f}{\rho^{fR}} + \frac{\rho^t}{\rho^{tR}} = 1, \tag{9.51}
$$

after some calulations we get

$$T\sigma = \mathrm{tr}\left\{\left[\mathbf{T}^t + \left(p - \rho^{fR}\rho\frac{\partial\hat{\psi}}{\partial\rho^f}\right)\frac{\rho^f}{\rho^{fR}}\mathbf{I} - \rho\mathbf{F}_\kappa\frac{\partial\hat{\psi}}{\partial\mathbf{F}_\kappa^T}\right]\mathbf{L}^t + \left(\mathbf{T}^f + p\frac{\rho^f}{\rho^{fR}}\mathbf{I}\right)\mathbf{L}^f\right\}$$

$$+ \left[\mathbf{p}^f - p\,\mathrm{grad}\left(\frac{\rho^f}{\rho^{fR}}\right) + \rho^f\,\mathrm{grad}\hat{\psi} - \rho^f\frac{\partial\hat{\psi}}{\partial T}\mathrm{grad}\mathbf{T}\right]\cdot(\mathbf{v}^t - \mathbf{v}^f)$$

$$+ T\sum_{f,t}(\mathbf{q} + \rho^\alpha\epsilon^\alpha\mathbf{u}^\alpha)\cdot\mathrm{grad}\left(\frac{1}{T}\right) - \rho\frac{\partial\hat{\psi}}{\partial\varphi}\frac{m^d}{\rho^t}$$

$$+ \mathrm{tr}\left[\rho\left(\mathbf{F}_\kappa^T\frac{\partial\hat{\psi}}{\partial\mathbf{F}_\kappa}\mathbf{G}^{-T} - \frac{\partial\hat{\Psi}}{\partial\mathbf{G}}\right)\left(\frac{\partial}{\partial t} + \mathbf{v}^t\cdot\mathrm{grad}\right)\mathbf{G}^T\right] \geq 0. \quad (9.52)$$

Here ρ^{fR} and $\rho^{tR}(= \rho_0^t/(1-\varphi_0^f))$ are the physical mass densities of the water and tissue in κ_0, respectively, and φ_0^f is the volume fraction of mobile water in κ_0. It was also assumed that the tissue and the mobile water are intrinsically mechanically incompressible (though thermally compressible). Inequality (9.52) was derived under an additional assumption that ρ^{fR} and ρ^{tR} can be treated as constant. We observe that the range of temperature changes over the processes modelled justifies such an assumption. Then Eqs. (9.41), (9.43) and (9.51) yield

$$\mathrm{grad}\left(\frac{\rho^t}{\rho^{tR}}\right)\cdot(\mathbf{v}^t - \mathbf{v}^f) + \mathrm{tr}\left(\frac{\rho^t}{\rho^{tR}}\mathbf{L}^t + \frac{\rho^f}{\rho^{fR}}\mathbf{L}^f\right) = 0.$$

Tao et al. [563] proposed the following set of constitutive relationships:

$$\mathbf{T}^t = -\left(p - \rho^{fR}\rho\frac{\partial\hat{\psi}}{\partial\rho^f}\right)\frac{\rho^t}{\rho^{tR}}\mathbf{I} + \rho\mathbf{F}_\kappa\frac{\partial\hat{\psi}}{\partial\mathbf{F}_\kappa^T}, \quad (9.53)$$

$$\mathbf{T}^f = -p\frac{\rho^f}{\rho^{fR}}\mathbf{I}, \quad (9.54)$$

$$\mathbf{p}^f = p\,\mathrm{grad}\left(\frac{\rho^f}{\rho^{fR}}\right) - \rho^f\,\mathrm{grad}\hat{\psi} + \rho^f\frac{\partial\hat{\psi}}{\partial T}\mathrm{grad}T + \mathbf{b}(\mathbf{v}^t - \mathbf{v}^f), \quad (9.55)$$

$$T\sum_{f,t}(\mathbf{q} + \rho^\alpha\epsilon^\alpha\mathbf{u}) = \mathbf{A}\,\mathrm{grad}\left(\frac{1}{T}\right), \quad (9.56)$$

$$m^\alpha = -\gamma\rho^t\frac{\partial\hat{\psi}}{\partial\varphi},$$

$$\left(\frac{\partial}{\partial t} + \mathbf{v}^t \cdot \mathrm{grad}\right) \mathbf{G}^T = \beta(\mathbf{F}_\kappa^T \frac{\partial \hat{\psi}}{\partial \mathbf{F}_\kappa^T} \mathbf{G}^{-T} - \frac{\partial \hat{\psi}}{\partial \mathbf{G}}). \tag{9.57}$$

Here $\gamma \geq 0$, $\beta \geq 0$, while $\mathbf{b}$ and $\mathbf{A}$ denote, respectively, the drag tensor and heat conductivity tensor, both (symmetric) positive definite second-order tensors. These tensors are, in general, anisotropic. From the physical point of view, $\mathbf{b}$ characterizes the momentum exchange (due to viscosity), between the viscous water, which moves relative to the solid phases, and the tissue. We note, that it is important to retain this term even though the diffusion is slow since the 'channels' for the diffusion are very small and the contact area per unit volume between the water and tissue is very large. Equation (9.55) may be viewed as a nonlinear combined version of Darcy's and Fick's laws. Indeed, for isothermal slow diffusion, which occurs during the 'recovery' process post-heating [71], from Eqs. (9.33), (9.51), and (9.55) with $\alpha = f$, we easily obtain:

$$\mathbf{v}^f - \mathbf{v}^t = -\frac{\rho^f}{\rho^{fR}} \mathbf{b}^{-1} \mathrm{grad}(p + \rho^{fR} \hat{\Psi}). \tag{9.58}$$

The last relation shows that there are two parts affecting the isothermal slow diffusion of water; the first part is associated with the gradient of the pressure p, similar to the commonly used Darcy's Law, whilst the second part (similar to Fick's law) is associated the gradient of Ψ, which accounts for variations in the effective mass density ρ^f (concentration) and the deformation $\mathbf{F}$.

Under the assumptions on β, γ, $\mathbf{b}$ and $\mathbf{A}$, and taking into account the constitutive relationships (9.50)–(9.57) we conclude that the entropy inequality (9.52) is satisfied.

The form of $\hat{\Psi}$ has further to be restricted by the *principle of material frame indifference* (objectivity), cf. Section 5.1.4. Then we get

$$\hat{\psi}(\rho^f, \varphi, T, \mathbf{F}_\kappa, \mathbf{G}; \kappa) = \hat{\psi}(\rho^f, \varphi, T, \mathbf{U}_\kappa, \mathbf{G}; \kappa), \tag{9.59}$$

where $\mathbf{C}_\kappa = \mathbf{U}_\kappa^2 = \mathbf{F}_\kappa^T \mathbf{F}_\kappa$. Since $\mathbf{C}_\kappa = \mathbf{U}_\kappa^2$, the Helmholtz potential can also be treated as a function of $(\rho^f, \varphi, T, \mathbf{C}_\kappa, \mathbf{G}; \kappa)$.

We observe that Tao et al. [563] do not exploit the principle of frame indifference but less restrictive Galilean invariance. This invariance requires that the form of $\hat{\Psi}$ be invariant under the coordinate transformation:

$$\mathbf{x}^* = \mathbf{Q}\mathbf{x} + \mathbf{c}t + \mathbf{a},$$

where $\mathbf{Q}$ and $\mathbf{c}$ are constant with $\mathbf{Q}^T\mathbf{Q} = \mathbf{Q}\mathbf{Q}^T = \mathbf{I}$. Recently, (Synka and Kainz [554]), the concept of objectivity was extended to the intermediary Eulerian-Lagrangian reference frame (E-L). The (E-L) concept is sometimes useful in the numerical procedures. Though the authors do not mention it, it seems that this notion is worth of being exploited in the study of solid-fluid

interactions, say of blood with arteries. Additional restrictions on $\hat{\psi}$ can be obtained if the symmetry of κ is taken into account (e.g. transverse isotropy, orthotropy, etc.).

9.7.3. Interfacial conditions. Consider an interface S in a mixture. On each side of S, denoted by the superscripts $+$ and $-$ respectively, there may be mobile water (denoted by the superscript f). The two tissue components may differ from each other or one component may be absent. It is assumed that there are no physical properties attached to the interface except those derivable from the components on both sides of S.

Tao et al. [563] studied three classes of interface conditions:

Class 1. An interface with tissues on both sides.

Class 2. The interface, where on the side $(-)$ the mixture is present and the side $(+)$ is occupied by the water.

Class 3. On the side $(-)$ of the interface the mixture is present and on the side $(+)$ there is water and the static rigid porous solid through which the water follows.

For details on interface conditions and two illustrative examples pertaining to:

(i) slow isothermal diffusion of water through a thin orthotropic membrane without thermal damage,

(ii) radial diffusion in a membrane-covered cylindrical tissue,

the reader is referred to Tao et al. [563].

Remark 21. The general setting for the description of heat-induced alterations in hydration and mechanical properties in soft tissues was certainly inspired by the previous one-dimension case, cf. Chen and Humphrey [75], Chen et al. [71]. Its usefulness has yet been exploited. Even in specific cases a combined theoretical, experimental and numerical analysis is needed.

Remark 22. As is well-known, rubber-like materials and many soft tissues exhibit a significant stiffening or hardening in their stress-strain curves at large strains. To describe this phenomenon, *limiting chain extensibility* models have been proposed. These are models with a maximum achievable length of the polymeric molecular chains composing the material and are described, for instance by strain energies of the form

$$W(I_1, I_1^\star),$$

where $I_1 = \text{tr}\mathbf{C} = \lambda_1^2 + \lambda_2^2 + \lambda_3^2$, and the constant $I_1^\star$ is the limiting value of I_1, reflecting limiting chain extensibility. The function W is such that the

stress components are unbounded as $I_1 \to I_1^\star$ and so one must impose the restriction

$$I_1 < I_1^\star.$$

We observe that such a material is a *material with locking*, cf. Ciarlet [83]. For applications of limiting chain extensibility models to the description of soft tissue the reader is referred to Horgan and Saccomandi [241, 242].

Horgan and Saccomandi [242] elaborated a general approach that allows an extension of the limiting chain extensibility model concept to nonlinear thermoelasticity.

10. Final Comments and Remarks

Hyperelastic behaviour of soft tissues undergoing finite deformations is described by stored energy functions falling, grosso modo, within one of the following classes:

(i) polynomial-type functions,

(ii) exponential functions,

(iii) logarithmic functions.

Combinations thereof and other functional forms are also used. The logarithmic strain energy function was proposed by Takamizawa and Hayashi in 1986, cf. the relevant references in Jemioło and Telega [277] and Humphrey [253]. The logarithmic strain energy function proposed by Takamizawa and Hayashi for modelling arterial wall has the following form:

$$W = -c\ln(1 - \Psi), \tag{10.1}$$

where

$$\Psi = \frac{1}{2}(a_1 E_{\theta\theta}^2 + a_2 E_{zz}^2) + a_3 E_{\theta\theta} E_{zz}. \tag{10.2}$$

Here $E_{\theta\theta}$ and E_{zz} are the normal components of the Green strain tensor in the circumferential and axial directions, respectively. The constants c, a_1, a_2 and a_3 characterize the mechanical properties of the material of arterial wall.

Pseudoelastic behaviour still requires a reliable modelling accounting for switching from loading to unloading and vice-versa. The exponential model due to Fung [175] is generally believed to describe pseudoelastic behaviour of soft tissue but is by no means capable of modelling such a behaviour. In fact, the situation resembles modelling elasto-plastic behaviour of materials under cyclic loadings.

In the sequel we shall review mainly recent developments pertaining to soft tissues, including also cell biomechanics and cellular engineering. The

review is by no means comprehensive, yet covers a broad spectrum of issues on modelling and experimental investigations.

10.1. Biomembranes, Cell Biomechanics

As a good introduction to biomechanical issues of biological membranes, the book by Evans and Skalak [160] is advised. These authors, treat biomembranes as thin membranes undergoing finite deformations. The molecular structure of biomembranes is essentially anisotropic. Therefore, membrane is treated as a two-dimensional continuum, comprised of several layers. Consequently, the properties of the membrane are defined similarly to a 2D composite material. Constitutive equations were obtained within the framework of thermodynamics. These include elastic behaviour of biomembranes accounting also for surface elasticity (surface compressibility and surface shear), and chemically induced changes of curvature. Irreversible processes in biomembranes were also investigated (viscoelasticity, creep, viscoplasticity).

According to Humphrey [251], membranes are defined differently in medicine, biophysics and biomechanics. In medicine, a membrane is defined as a thin layer of tissue that covers a surface, lines a cavity, or divides a space. The lectures by Hendrich and Mozrzymas in this volume deal with membranes in the sense of biophysics (a thin barrier involved in diffusive transport), cf. also the papers included in the book edited by Layton and Weinstein [335], Hernández [231].

Passive transport of nonelectrolytic solutions in biological and artificial solutions in biological and artificial membranes includes several phenomena, most notably osmosis, filtration, diffusion and convection. Kargol [295] proposed a somewhat restricted definition of osmosis: the solvent diffusion through a semi-permeable membrane, i.e. one that forms an ideal barrier to the solute molecules. The model proposed was criticized by Monticelli [403], since it wrongly contains only two phenomenological parameters (the filtration coefficient L_p and the reflection coefficient σ), as opposed to the three parameter description (L_p, σ and the solute permeability ω) in the standard Kedem-Katchalsky transport equation derived by means of thermodynamics of irreversible processes, cf. Layton and Weinstein [335] and the relevant papers in Kargol [295].

Understanding of heart diseases, especially ventricular fibrillation, requires understanding the electrical behaviour of cardiac membrane, cf. the references in Mitchell and Schaeffer [398]. The last authors presented a simplified model with only two currents that, at least qualitatively should reproduce restitution behaviour.

As we already know, the human body contains many different membranes like aneurysms which form in the vasculature, cell membranes, the mesen-

tery, the meninges which develop the brain and spinal cord, the pericardia which surround the heart, the pleura which cover the lungs, skin, the urinary bladder etc. Humphrey [251] reviewed general concepts and methods from nonlinear mechanics that are applicable to these membranes. Some of these ideas are illustrated via specific results. The presentation covers constitutive modelling, experimental methods and methods for solving initial and boundary value problems.

10.1.1. Cell mechanics. Cell mechanics (and cellular engineering) may be defined as the application of principles and methods of engineering and life sciences toward fundamental understanding of structure-function relationships in normal and pathological cells and the development of biological substitutes to restore cellular functions, cf. Mow et al. [408]. To study cellular deformations and the material properties, investigators have used micropipet manipulation, laser tweezers, flow chambers, and rheometers.

The volume edited by Mow et al. [408] compiles a representative set of studies in seven different areas of cell mechanics and cellular engineering. Part I deals with the constitutive modelling and mechanical properties of circulating cells, Part II presents papers on flow-induced effects on cell morphology and function, with special emphasis on endothelial cell response. Part III examines the mechanics and biology of cell-substrate interactions, which addresses specific questions on the process of cell adhesion. Part IV describes cell-matrix interaction and adhesion molecules. Part V focuses on the molecular and biophysical mechanisms of mechanical signal transduction in cells. Part VI utilizes articular cartilage as a paradigm for the physical regulation of tissue metabolic activity and examines how various mechanical factors may affect cellular response. Finally, the papers in Part VII encompass the mechanics of cell motility and morphogenesis, and examine the mechanisms of force generation and mechanochemical coupling in cells. For recent results on cell biomechanics the reader is referred to Bao [27], Chiu et al. [81], Craelius [101], Dao et al. [112], Flieger and Grebe [167], Hansen et al. [215], Humphrey [254], Lehoux and Tedgui [341], Lacolley [321], Lim et al. [350], Mathur et al. [372], Mestel et al. [383], Motlagh et al. [411], Ohta et al. [435], Ramtami [475], Shyy et al. [519], Stéphanou et al. [545], Sugihara-Seki and Skalak [548], Sun et al. [552], and Zhu et al. [651].

Seshaiyer and Humphrey [512] discussed the shortcomings of the inverse finite element method used in many areas of experimental mechanics. In particular, the shortcomings become visible in cases wherein the material is heterogeneous. Therefore, the authors suggest to apply the inverse finite element method over separate subdomains. To illustrate the subdomain ap-

proach, Seshaiyer and Humphrey [513] presented numerical simulation for pressurized hyperelastic membranes, including biological soft tissues.

David and Humphrey [115] performed a theoretical study of the stress and strain fields in anisotropic biomembranes due to the surgical or traumatic introduction of a circular hole. Earlier investigations were confined to isotropic membranes, cf. the relevant references in David and Humphrey [115]. Such results may provide insight into the analysis of early mechanotransduction mechanisms related to needle sticks, skin biopsies, percutaneous catheterization, laparoscopic surgery, cataract surgery, and similar surgical procedures.

Vaughn et al. [596] designed and evaluated a new theoretically motivated device for measuring finite strain-dependent diffusion in biomembranes and illustrated the utility of the device via pilot measurements (excised sheets of visceral pericardium – i.e. epicardium – from the antero-lateral surface of the left ventricle of 6 fresh bovine hearts). Specimens were trimmed to about $20 \times 20\,\mathrm{mm}^2$ in planar area, and were $\sim 100 - 150\,\mu$m in thickness.

An alternative approach to constitutive modelling of biomembranes was proposed by Criscione et al. [107]. These authors treat a membrane as a laminar material, but with only one laminar. The stress tensor is decomposed into a hyperelastic part plus a hypoelastic-stress-residual. In the second part of their paper Criscione et al. [108] illustrated experimental advantages of this novel constitutive model via analysis of biaxial test data obtained from chemically treated bovine pericardium.

10.2. Viscoelasticity of soft tissues

Woo et al. [630] reviewed structure and modelling of tissues such as ligaments and tendons, including viscoelastic (nonlinear) response to loading. Puso and Weiss [462] developed a theoretical and computational framework for modelling viscoelastic soft tissues that accomodated transverse anisotropy, cf. also Weiss et al. [617], Provenzano et al. [461]. This aim was achieved using FEM and discrete spectrum approximation to the theory of quasi-linear viscoelasticity. Assuming that the motion starts at $t = 0$ and the stress and strain are zero prior to this time, the second Piola-Kirchhoff stress $\mathbf{T}(t)$ is written in the form

$$\mathbf{T}(t) = \int_0^t G(t - s)\frac{d\mathbf{T}^e}{ds}ds. \qquad (10.3)$$

Here $G(t)$ is a relaxation function (in general, the scalar-valued relaxation can be replaced by a fourth order tensor to produce direction-dependent relaxation phenomena). Discretization in time of (10.3) can be performed using a specific form of $G(t)$ and an iterative (Newton) method. Moreover,

the stress $\mathbf{T}^e$ has a familiar form:

$$\mathbf{T}^e = \frac{1}{2}\left(\frac{\partial W}{\partial \mathbf{C}} + \frac{\partial W}{\partial \mathbf{C}^T}\right),\tag{10.4}$$

where, as usual, $\mathbf{C} = \mathbf{F}^T\mathbf{F}$, and

$$W = W_1(I_1, I_2) + W_2(\lambda) + W_3(I_1, I_2, \lambda).\tag{10.5}$$

Here $I_1 = \mathrm{tr}\mathbf{C}$, $I_2 = 1/2((\mathrm{tr}\mathbf{C})^2 - \mathrm{tr}\mathbf{C}^2)$ and

$$\lambda\tilde{\mathbf{m}} = \mathbf{Fm},\tag{10.6}$$

where λ denotes the fibre stretch and $\mathbf{m}$ is a unit vector field in the undeformed configuration used to describe the local fibre direction. Obviously $\mathbf{a}$ is the fiber direction (a unit vector field) after deformation.

We observe that three hyperelastic strain energy functions of type (10.5) were also used by Quapp and Weiss [464] in their study of behaviour of MCL (medial collateral ligament). These authors performed also uniaxial tests allowing to determine the longitudinal and transverse tensile properties of the human MCL (ten human cadaveric MCL; age= 62 ± 18 years, 9 male, 1 female).

Sarver et al. [501] proposed an incremental procedure to the quasi-linear viscoelastic model due to [175]. Only one-dimensional case was considered.

An alternative approach was proposed by Holzapfel and Gasser [238]. These authors developed a viscoelastic model for anisotropic materials conceived as fibre-reinforced composites subjected to finite strains. A constitutive modelling exploiting internal variables describing the thermodynamical state of the material and a time integration scheme adequate for computer implementation into finite element model were developed.

For quite recent results, the reader is referred to Quaglini et al. [463], who exploit the discrete time framework from the very beginning, and to Haslach [219], who proposed thermodynamically consistent model of nonlinear viscoelastic soft tissues. According to the author, the models can be extended to the temperature-dependent behaviour of biological tissue, such as the change in temperature during uniaxial loading.

Funk et al. [178] produced data for modelling the behaviour of eight major ankle ligaments at a wide variety of strains and strain rates. The ligaments included in their study included the anterior talofibular (ATaF), anterior tibiofibular (ATiF), anterior tibiotalar (ATT), calcaneofibular (CF), posterior talofibular (PTaF), posterior tibiofibular (PTiF), posterior tibiotalar (PTT), and tibiocalcaneal (TiC) ligaments, cf. Fig. 92

MEDIAL VIEW   **LATERAL VIEW**
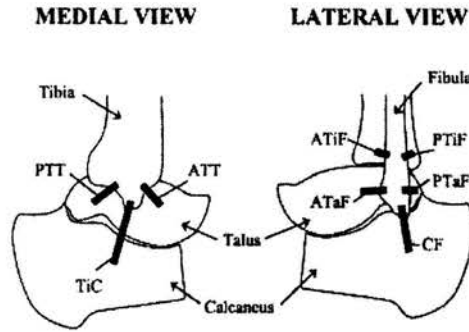
FIGURE 92. Locations of the eight major ankle ligaments examined by Funk et al. [178].

Failure data was also reported, as well as a method to model ligaments in an unpreconditioned state. All ankle ligaments were found to be nonlinear viscoelastic. Nonlinear constitutive relationships are recommended for every application, and viscoelastic constitutive models are recommended for applications involving strain rates between 1/s and 0.0001/s. The quasi-linear model was found to be valid to up to 15 percent strain.

Carew et al. [66] applied Fung's (1991) quasi-linear viscoelastic model to the study of internal shear in porcine aortic heart valve leaflets.

Pioletti and Rakotomanana [449] proposed the following constitutive equation modelling nonlinear viscoelastic behaviour of soft tissues:

$$\mathbf{T} = \mathbf{T}^e(\mathbf{C}(t)) + \mathbf{T}^v(\dot{\mathbf{C}}(t); \mathbf{C}(t)) + \mathcal{J}^{\infty}_{s=\delta}\{\mathbf{G}(t-s); \mathbf{C}(t)\}. \qquad (10.7)$$

Here $\mathbf{T}^e$ is derivable from a hyperelastic strain energy function, $\mathbf{G}(t-s) = \mathbf{C}(t-s) - \mathbf{C}(t)$, $\mathbf{T}^v$ denotes the second Piola-Kirchhoff viscous stress tensor and $\dot{\mathbf{C}}$ is the strain rate tensor. The second term on the r.h.s. of (10.7) represents the short time memory while the third term represents the delayed contribution, i.e. the long time memory. Under additional, commonly used, mathematical assumptions, the third term of (10.7) takes the form

$$\mathcal{J}^{\infty}_{s=\delta}\{\mathbf{G}(t-s); \mathbf{C}(t)\} = \int_{\delta}^{\infty} \mathbf{\Sigma}(\mathbf{G}(t-s), s; \mathbf{C}(t))ds.$$

The constitutive equation proposed was used for the description proposed was used for the description of response of tendons. Experimental tests were performed on specimens from fresh frozen Caucasian knees (4 males, mean age ±SE: 73.4±2.2 years). The fibres were aligned along the loading direction. The elastic potential was assumed to be isotropic, of exponential type.

unfortunately, such a law does not describe properly the fibrous structure of tendons (and ligaments). Also, preconditioning which plays an essential role in the modelling of behaviour of tendons was not discussed, cf. Section 6.2.3 of these Notes.

Fu et al. [173] investigated changes of soft tissue under expansion. These authors expanded skin, muscles, nerves and blood vessels and determined the biorheological and biomechanical features of nerves and blood vessels under expansion (thirteen adult dogs were used). The stress relaxation features, the continuous spectrum of relaxation time, and the stress-strain relationship of expanded and control specimens were measured. Huang et al. [248] performed a similar study on the effects of limb lengthening on the biorheological features of nerves and blood vessels to understand the mechanism involved in callus elongation.

Del Prete et al. [124] investigated both transient (creep response) and dynamic (complex compliance) measures of viscoelasticity of skin of transgenic and mutant mice. Similarities and differences between the three groups studied were established. For instance, the loss of compliance of each group differed significantly from the others.

Koop and Lewis [308] investigated the accuracy of two recently proposed methods of fracture testing of viscoelastic tissues such as ligaments and tendons.

10.3. Cardiovascular system, arteries angioplasty

The literature on biomechanical aspects of cardiovascular system and its various elements is copious. By now classical textbooks by Fung [175, 176] have become standard and cover both experimental data and elements of mathematical modelling. Recently published impressive volume by Humphrey [255] covers a comprehensive introduction to continuum mechanics with finite elements and systematic presentation of vascular and cardiac biomechanics. The book edited by Glass et al. [191] is still a rich source on the mechanics of the heart wall, electrical activities of the cardiac cells, wave propagation in myocardium, ventricular fibrillation and defibrillation, arrythmia and related problems. The books edited by Hayashi and Ishikawa [221], and Yamaguch [637] cover various computational aspects of biomechanics, cf. also Maurel et al. [374]. For recent development in cardiac biomechanics the reader is referred to Lee et al. [339], Stevens et al. [546], Luo et al. [360], Remme et al. [480], Weind et al. [616], Choy et al. [82], Waters [605], Conway et al. [92], Gaudette et al. [185], Kirn and Starc [303], Jørgensen et al. [290], Niederer et al. [420], Marchon et al. [371], Mouret et al. [407], Nash and Hunter [416], Usyk et al. [588], Taber and Perucchio [556], Casey and Bao

[67], and references therein. Of particular interest is a special issue of the Journal of Cardiovascular Research (Dhein and Jongsma, 2004). The articles contained in this issue provide evidence for a central role of gap junctions in the functioning of the cardiovascular system, forming a complex and highly dynamic network of cells. We recall that intercellular communication is maintained by gap junctional channels that connect neighbouring cells and allow electrical and metabolic communication, thus forming a functional syncytium instead of a simple agglomeration of cells.

For various aspects of biomechanical investigations of arteries the reader is referred to recent investigations by Holzapfel et al. [239, 240], Coulson et al. [95], Ponomarev et al. [451], Stephanis et al. [544], O'Rourke [439], Spofford and Chilian [539], Williamson et al. [626], Mchedlishvili et al. [377], Shabrykina et al. [514], Prosi et al. [460], Schulze-Bauer and Holzapfel [510], Weydahl and James [621], Johnston et al. [288], Dixon et al. [137], Monson et al. [402], Zulliger et al. [658], Li et al. [348].

Chordae tendinae are fibrous strings that connect anterior and posterior mitral valve leaflets to the papillary muscles on the inner wall of the left ventricle. They are stretched and relaxed cyclically during each heartbeat, cf. the relevant references in Chen et al. [73]. The anatomy of the chordae tendinae and their attachment to other structures have been concisely described by these authors. The valve and chordae tendinae are composed primarily of elastin, collagen and glycosaminglycans (GAGs). Chordae exhibit a significantly higher collagen content and lower elastin content than the mitral leaflets, cf. the references in Chen et al. [73]. The leaflets have a higher water content and more GAGs than the chordae. The structure of the chordae is layered concentrically, with a collagenous core surrounded by an elastin/GAG sheath. The composition of the tissue varies from leaflet to chordae. Previous measurements of collagen fibre angles in the mitral valve using Small Angle Light Scattering (SALS) have demonstrated that collagen fibres in the central region of the anterior leaflet are oriented parallel to the annulus, with a gradual transition to an orthogonal orientation of the commisures. These previous findings of variations in both composition and collagen fibre orientation provide the foundation for assumption by Chen et al. [73] that regional mechanical properties reflect the tissue microstructure in the leaflet-chordae transition zone (LCT). Chen et al. [73] quantified the structure-property relations in the strut LCT using a combination of experimental testing, histological analysis and theoretical constitutive modelling. Experiments on porcine valve leaflet were performed using a biaxial testing apparatus. The basis of mathematical description for valve tissue is transverse isotropy, for which the preferred direction is that of the collagen fibres

(as usual). The strain energy function is exponential:

$$W = C(e^Q - 1), \tag{10.8}$$

where

$$Q = C_1(I_1 - 3)^2 + C_2(\alpha - 1)^4. \tag{10.9}$$

Here $I_1 = \mathrm{tr}\mathbf{C} = \mathrm{tr}\mathbf{F}^T\mathbf{F}$, $\alpha^2 = \mathbf{m} \cdot \mathbf{F}^T\mathbf{F} \cdot \mathbf{m}$ with $\mathbf{m}$ being the unit vector denoting the mean collagen fibre orientation. The directionality averaged formula for the Cauchy stress tensor $\boldsymbol{\sigma}$ is given by formula (8) in Chen et al. [73]. A fibre orientation probability distribution incorporates the degree of fibre alignment:

$$f(\theta) = \frac{1}{\sigma\sqrt{2\pi}} \exp\left(-\frac{1}{2}\frac{(\theta_f - \Delta)}{\sigma^2}\right), \tag{10.10}$$

where θ_f is the local fibre orientation, Δ is the mean fibre orientation, and σ is the degree of fibre alignment (standard deviation). The results obtained showed that collagen fibre angle and degree of alignment play a critical role in determining the regional mechanical properties of the mitral valve.

It seems that in the coming years the nonlinear models of soft tissue behaviour, which have been proposed until now will be verified from the point of view of fundamental mathematical concepts of solid mechanics. For instance, Holzapfel et al. [240] discussed a fully 3D material description of healthy arteries in the passive state of the smooth muscles, proposed earlier by Holzapfel et al. cf. the relevant references in that paper. Only elastic behaviour of arteries was considered, without taking into account residual stresses. The strain energy function has a familiar form, cf. Section 5 of our paper,

$$W = W_1(\mathbf{C}, \mathbf{M}_\alpha) - p^{J-1}, \quad \alpha = 1, 2. \tag{10.11}$$

As usual $\mathbf{M}_\alpha = \mathbf{m}_\alpha \otimes \mathbf{m}_\alpha$, where $\mathbf{m}_\alpha$ are directional vectors of two families of fibres arranged in symmetrical layers. These vectors differ in each layer (intima, media, and adventitia). Only one-layer and two-layer materials were investigated, and simplified form of the strain energy function was employed

$$\tilde{W} = \hat{W}_1(I_1, I_4, I_6) - p(J - 1), \tag{10.12}$$

where $I_1 = \mathrm{tr}\mathbf{C}$, $I_4 = \mathrm{tr}\mathbf{M}_1^T\mathbf{C}\mathbf{M}_1$, $I_6 = \mathrm{tr}\mathbf{M}_2^T\mathbf{C}\mathbf{M}_2$. Obviously, incompressibility condition is incorporated in (10.12). One can easily find the constitutive equation for $\mathbf{T}$, the second Piola-Kirchhoff stress tensor as well as for $\boldsymbol{\sigma}$, the Cauchy stress tensor. Holzapfel et al. [240] investigated only the following particular form of $\tilde{W}$:

$$\tilde{W} = \mu(I_1 - 3) + \frac{k_1}{2k_2} \sum_{a=4,6} \left\{\exp[k_2(I_a - 1)^2] - 1\right\}, \tag{10.13}$$

where μ and k_1 are material parameters with dimension of stress, and k_2 is a dimensionless material parameter. For physical reasons these parameters have to be positive.

The Fung-type model is described by

$$W_2 = \frac{1}{2}c[\exp(\Psi) - 1] - p(J - 1), \qquad (10.14)$$

where $c > 0$ is a stress-like material parameter and Ψ is a quadratic form of strains $E_{\theta\theta}$, E_{zz}, E_{RR}, $E_{\theta Z}$, E_{RZ} and $E_{R\theta}$.

Essential novelty of the paper by Holzapfel et al. [240] lies in studying material stability and strong ellipticity condition, cf. also Lanir [329], Wilber and Walton [625].

The relevant papers contained in Holzapfel and Ogden [237] present a good introduction to modelling angioplasty.

10.4. Atherosclerosis, stenosis, thrombosis, aneurysms

Intracranial aneurysms are focal dilatation of the arterial wall that usually occur in or near the circle of Willis, the primary network of vessels that supplies blood to the brain. In general, these aneurysms occur in one of two forms: *fusiform lesions*, which are elongated dilatations of an artery, and *saccular lesions*, which are local sack-like out-pouchings, cf. Fig. 93
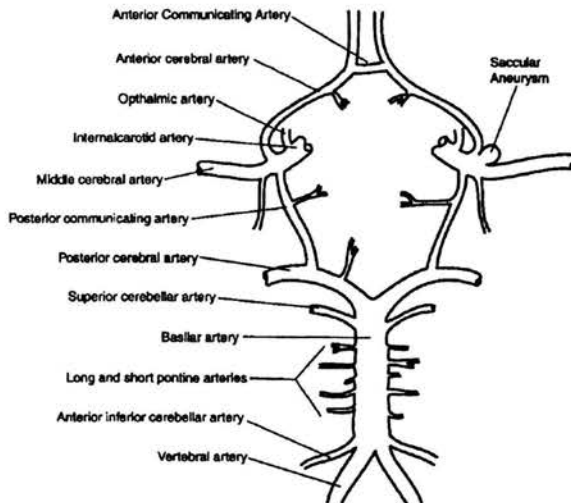

FIGURE 93. Schema of the cerebral vasculature illustrating circle of Willis and surrounding arteries; shown, too, is a typical aneurysm at a bifurcation (where the fundus-pole) after Humphrey and Canham [258].

Humphrey and Canham [258] reviewed findings up to year 2000 that discount limit instabilities in pressure and resonance under dynamic loading as possible mechanisms of enlargement of saccular aneurysms. The latter is treated as a nonlinear membrane obeying the following constitutive equation; cf. also the book by Humphrey [255] which includes a section on vascular disorders

$$\sigma_{\alpha\beta} = \frac{1}{\det \mathbf{F}} F_{\alpha\gamma} F_{\beta\kappa} \frac{\partial W}{\partial E_{\gamma\kappa}}, \quad \alpha, \beta, \gamma, \kappa = 1, 2,$$

where W is a standard exponential hyperelastic potential. For further development pertaining to saccular aneurysms the reader is referred to Haslach and Humphrey [220], Seshaiyer and Humphrey [513], and Shah and Humphrey [515].

Abdominal aortic aneurysms were investigated by Vorp and Wang (a paper in Casey and Bao [67]), Wang et al. [608] cf. also the references therein.

Various aspects of atherosclerosis and atherogenesis were discussed in Cobbold et al. [89], Younis et al. [641], cf. also the relevant references therein and papers in Casey and Bao [67].

The role of biomaterials in the treatment of vascular diseases, including arterial aneurysms, was examined in Metcalfe et al. [384], cf. also references therein. Biomaterial-associated thrombosis was investigated in Gorbet and Setton [194].

For the studies of flows through stenotic arteries (in fact, fluid-solid interactions), the reader is referred to Bathe and Kamim [32], Claessens et al. [86], Ghalichi et al. [189], Kostin et al. [311], Meier et al. [380], Moayeri and Zendehbudi [401], Tang et al. [561, 562].

10.5. Fluid-structure interactions of flowing blood with arteries, stenosis and stents

Zamir [645] showed significant difference in blood flow in rigid and deformable arteries. Pulsatile blood flow leads to wave propagation; this phenomenon can only be described in the case of deformable arteries. The lectures by Hill in this volume treat the problem of deformability in a simplified manner, without taking into account complex structure of arteries, cf. also the review paper by Heil and Jensen [223] and the paper by Heil [222].

In our future, comprehensive paper [571] we shall synthesize various aspects of flowing (pulsating) blood with nonlinearly deforming arteries. To cite but a few papers the reader is referred to Bathe and Kamm [32], De Hart et al. [121], Gleason et al. [192], Damiano [111], Lakin et al. [325], Lemmon and Yoganathan [343], Tang et al. [561], Weston and Tarball [620]. Mathematical aspects of fluid-structure interaction were studied by Beirão da Veiga [34] and Grandmont [197].

For recent results on interaction between stents and vascular walls (including bioprosthetic heart valves) the reader is referred to Akutsu and Masuda [7], Etave et al. [159], Migliavacca et al. [389, 390], Prendergast et al. [457], Sun et al. [552], Zhu et al. [652], see also the references therein.

10.6. Ligaments and tendons

Comprehensive article by Woo et al. [630] synthesizes basic results on structure and biomechanical properties of ligaments and tendons, including influence of biological factors (aging, immobilization, etc.), nonlinear viscoelastic properties and modelling, and healing. In these Notes, at many instances we have already discussed various aspects of ligaments and tendons and their properties. For recent developments, covering experimental investigations and mathematical modelling the reader is referred to Abramovitch and Woo [2], Funk et al. [177], Lavagnino et al. [332], Lin et al. [352], Kuhl and Steinmann [315], Gupte et al. [211], Maganaris and Paul [363], Derwin and Soslowsky [131], Lakes and Vanderby [324], Maurel et al. [374], Thomopoulos et al. [580], Silver et al. [522], Pini et al. [448], Yamamoto et al. [639], Lynch et al. [361], Komatsu et al. [306], Schechtman and Bader [506], Robinson et al. [487], Moore et al. [404], Yin and Elliott [643], and references therein.

10.7. Soft tissues remodelling, growth and residual stresses

As we have already mentioned various aspects of growth and remodelling as well as residual stresses and strains are discussed in the volume containing a set of lectures (Telega ed., [570]). Here we only refer the reader to the book edited by Singal et al. [526] on biological and clinical aspects of heart failure and therapy, remodelling and heart failure, and the papers by Driessen et al. [146], Rachev [467], Humphrey and Rajgopal [259], Lappa [330], Schellings et al. [509], Kasikcioglu et al. [296], Matsumoto et al. [373], Wakisaka et al. [602], Khan et al. [301], Garikipati et al. [184], Rachev et al. [470], Rachev and Greenwald [468], Fridez et al. [171], Wentzel et al. [619], Gleason et al. [192], Humphrey [253], Yamamoto et al. [638, 639], Lu and Gregersen [359], Summerour et al. [550], Omens et al. [437], Taber and Chabert [555], Gregersen et al. [200], Dou et al. [141], Zamir and Taber [646], Zulliger et al. [657], and the relevant references therein. We observe that though the papers by Gregersen et al. [200] and Lu and Gregersen [359] dealt with residual stresses in oesophagus, yet Vanags et al. [590] completely ignored this aspect in their study of biomechanical properties and structure of the wall of the oesophagus in cases of both norm and pathology.

10.8. Cartilage and meniscus

In Section 6.3 we have provided some comments on investigations of cartilage treated as a multiphase medium. In reality, the body of publications on biology and biomechanics of cartilage and meniscus, including cellular aspects, is enormous. The reader interested in acquiring deeper insight into those various aspects of cartilage and meniscus structure and behaviour is referred to comprehensive and excellent review papers (Guilak et al. [208], Mow and Ratcliffe, [410]) and to Ateshian et al. [19], LeRoux and Setton [344], DiSilvestro and Suh [136], Federico et al. [162], Ehrlich et al. [154], Fortin et al. [169], Gu and Justiz [205], Garcia et al. [182], Garon et al. [183], Heiner and Martin [224], Han et al. [214], Korhonen et al. [310], Li and Herzog [346], Nalim et al. [415], Nieminen et al. [421], Quinn et al. [465], Töyräs et al. [584], Wang et al. [606], and the references therein.

The articular disc of the temporomandibular joint (TMJ) provides a mechanism by which frictional forces are reduced during the initial mandibular movement. Understanding the biomechanical nature of the degeneration of the TMJ requires a coupling between experimental measurements and numerical simulation. Donzelli et al. [143] measured geometry using MRI while motion was obtained from a specially designed optoelectronic system. Those data were fed into a 3D biphasic finite element analysis to generate the spatial and temporal response of the disc.

10.9. Intervertebral disc, TMJ disc, annulus fibrosus

The book by Adams et al. [4], with over 800 bibliographical items, constitutes a good introduction to the structure and properties of these tissues. Let us proceed to a brief presentation of recent results.

Ferguson et al. [163] developed computer models to calculate the fluid flow patterns within the intervertebral disc resulting from the average diurnal spinal loading and to determine the relative contribution of diffusion and convection to solute transport in the intervertebral disc. Moreover, the influence of obstruction of the endplate or annulus flow paths on the timing and fluid exchange were evaluated. Walsh and Lotz [604] tested experimentally the hypothesis that dynamical mechanical forces are important regulators in vivo of disc cellularity and matrix synthesis.

Elliott and Setton [157] determined the tensile moduli and Poisson's ratios of human annulus fibrosus (AF) along circumferential, axial and radial orientation. Test samples were prepared from 10 fresh-frozen intervertebral discs from the lumbar spine levels L1–L2 and L2–L3 from 7 human tissue donors. The average tissue donor age was 53 years old (range 27–72 years).

Anisotropy was evident at both outer and inner sites in the AF. For specific values, the reader is referred to the results obtained by Elliott and Setton [157].

In situ intercellular strains in the outer annulus fibrosus under an applied biaxial tissue strain were measured by Bruehlmann et al. [59]. Specimens were obtained from eighteen upper (CC1-CC2) bovine caudal discs from 12 to 24 month old steers. The specimen was placed in a custom-built load apparatus mounted on the stage of an inverted laser scanning confocal microscope, see Bruehlmann et al. [59] for details. The in situ mechanical environment of the AF was shown to be complex and nonuniform. Intercellular Lagrangian strains did not correspond with the Lagrangian strains applied to the tissue and varied substantially in both magnitude and directions.

Elliott and Setton [156] modelled the AF as a continuum containing two families of fibres assumed to be of equal density and uniform distribution with and isotropic matrix. Only linear behaviour was considered; consequently usefulness of the model is very limited since the response of the AF is nonlinear.

A nonlinear model for human AF was developed by Klisch and Lotz [305]. These authors introduced a special theory of an intrinsically incompressible mixture of an elastic solid and an inviscid fluid and quantified the mechanical properties of the AF using experimental data from a confined compression protocol. Thirty two specimens of the AF were harvested from the middle-lateral portion of intact intervertebral disc from the L23, L34, L45 motion segments of seven intact human spines. Though the authors considered only isotropic free energy for the solid part of the mixture, yet, as we know, it is not difficult to include anisotropy of the AF, cf. Section 9.5.

Intradiscal electrothermal therapy has been recently introduced as a minimally invasive, nonoperative, therapy, in which a temperature elevation is applied in order to treat discogenic low-back pain. This procedure is thought to produce temperatures sufficient to shrink annular collagen and ablate annular nociceptors, cf. the relevant references in Bass et al. [30]. The aim of the experimental investigations performed by Bass et al. [30] was to examine the acute biomechanical effects of heat on annulus fibrosus of porcine lumbar spines.

10.10. Very soft tissues (abdomen, brain, kidney, liver, nerves)

This particular class of soft tissues was mostly studied from the point of view of trauma caused by impact loading (traffic accidents, sport accidents or falls) cf. Farshad et al. [161], Melvin et al. [381], Brands [54], Viano et al. [598], Waxweiler et al. [610], Schmidlin et al. [507], Bschleipfer et al. [62], Lau and Viaro [331], Rouhana [491], Rouhana et al. [492], Snedeker et al. [531].

We observe that the experimental results on brain, kidney and liver deal mainly with compression, indentation, impact and torsional tests, cf. Miller [392, 393] and the relevant references therein. The last author [392] performed a theoretical analysis of uniaxial tension of brain sample, employing isotropic constitutive models used for the description of rubber. In our opinion such an assumption is not very convincing, cf. our previous discussions on soft tissues. Typically, in experiments on brain tissue cylindrical samples of diameter ~ 30 mm and height ~ 10 mm are used, cf. Miller [392].

We proceed now to a concise description of modelling of brain and kidney tissues.

According to Peters et al. [446] injuries of the human head can be divided in two groups. First, the head and brain can be injured by impacts, deforming the skull and also the brain. The second group are injuries caused by fast and large rotations or translations of the human head. These movements are regarded as responsible for injuries like diffuse axonal injury and acute subdural hematoma.

Peters et al. [446] investigated cylindrical samples with a height of 1–2 mm and a diameter of 10–12 mm. The samples were prepared from white brain matter of a six month old calf and placed between the flat parallel disks in the rheometer; the upper plate, on which the torque was measured, was kept stationary while the lower one was forced to rotate. The temperature was kept constant and a moist chamber was used to prevent dehydration of the sample. Oscillatory dynamic experiments were performed with frequencies between 0.16–16 Hz. The maximum frequency was limited by inertial effects of the RFS II (Rheometric Fluids Spectrometer II). The relaxation experiments were done with strain steps of 50% (maximum strain at the outer radius of the plate), and lasted for about 300 s while the sampling rate for these experiments was 1 Hz. We observe that the typical duration of the loads in traffic accidents is 1–50 ms. Roughly, this range corresponds to a frequency range in dynamic measurements of 20–1000 Hz.

The aim of investigations was threefold. First, the assumption that brain tissue shows linear viscoelastic material behaviour for sufficiently small strains was investigated. Secondly, the reproducibility of the measurements was discussed, and finally, the results from oscillatory and relaxation experiments were presented. An example of results achieved is presented in Fig. 94

For dynamic measurements a sinusoidal strain $\gamma(t)$ was imposed on the sample: $\gamma(t) = \gamma_0 \cos \omega t$.

Bilston et al. [42] performed shear relaxation tests and strain sweep experiments on fresh bovine brains. Brain was sliced into a 30 mm diameter disk, 1.5 mm thick, using a custom jig. The results indicate that the brain exhibits nonlinear viscoelastic behaviour from very low strains (0.1%). Bil-
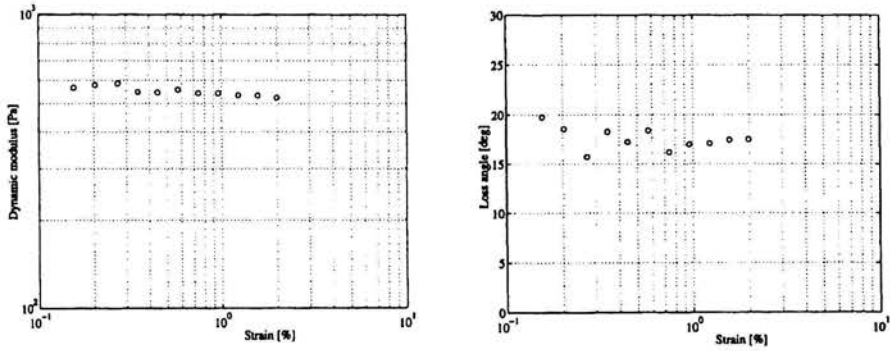
FIGURE 94. Dynamic modulus (a) and loss angle (b) as a function of the strain $\gamma_0 = 0.2 - 2\%$ (angular frequency is 16.0 Hz, after Peters et al. (1997).

ston et al. [42] also discussed earlier investigation on cadaveric brain tissue, and human and monkey brain tissues.

Mendes et al. [382] carried out a finite element analysis of cylindrical brain tissue sample under transient dynamic conditions. It was assumed that the brain tissue material is isotropic, what is not quite true, cf. Prange et al. [456, 455]. These authors underline that a confined specimen test protocol would reveal the volumetric stress-strain response which would completely overshadow shear deformation effects due to approximately 10^5 ratio of bulk to shear moduli of brain tissue. Consequently, the authors employed the Mooney-Rivlin strain energy density function for the description of incompressible hyperelastic behaviour, being a specific isotropic case of Eq. (5.100). A simple form is that proposed in 1940 by Mooney:

$$W = A_{10}(I_1 - 3) + A_{01}(I_2 - 3), \tag{10.15}$$

where $I_1 = \lambda_1^2 + \lambda_2^2 + \lambda_3^2$, $I_2 = \lambda_1^2\lambda_2^2 + \lambda_2^2\lambda_3^2 + \lambda_3^2\lambda_1^2$.

To include energy dissipated by viscous means, it is assumed that the coefficients A_{ij} in the Mooney-Rivlin stored energy function depend on time (Prony series):

$$A_{ij}(t) = \left[A_{ij}^\infty + \sum_{k=1}^{M} \left(A_{ij}^k - A_{ij}^\infty \right) e^{-t/\tau_k} \right] H(t).$$

Here A_{ij}^∞ is the steady-state value of the coefficient (determined from the quasi-static test) and $H(t)$ is the Heaviside step function. Then a simple strain energy function, corresponding to Mooney function (10.15), due to

time varying strain invariants is expressed in terms of a convolution integral:

$$W(t) = \int\limits_0^t \left[A_{10}(t-s)\frac{d}{ds}I_1(s) + A_{01}(t-s)\frac{d}{ds}I_2(s) \right] ds.$$

Similar constitutive modelling was also used by Miller and Chinzei [394]. These authors carried out unconfined compression experiments of porcine brain tissue and compared experimental results with the experimental data, cf. also Miller [393]. An alternative hyperelastic-linear viscoelastic model was employed by Miller [391]. The author claims that his model requires fewer material coefficients than the model used in Miller and Chinzei [394]. However, there are no convincing results that simpler models are more advantageous. On the contrary, as we know from the papers by Jemioło and Telega [279, 278] apparently simpler nonlinear models can lead to physically unacceptable results, cf. Section 5 of our paper.

Kyriacou et al. [319] discussed the following issues pertaining to quasistatic behaviour of brain tissues: poroelastic vs. viscoelastic and compressible vs. incompressible material behaviour, a fluid vs. solid approach, differentiating between gray and white matter properties, the effect of tissue weight, fluid filled cavities (ventricles, subarachnoid space) and falx/tentorium. Also different constitutive models are compared under various simple 1D simulations.

Miga et al. [388] claim that at loading rates consistent with brain surgery, purely viscoelastic description can be limited, given the hydrated nature of the brain and inherent coupling between deformation and hydrodynamic behaviour cf. the relevant references in that paper. These authors had developed an in vivo experimental porcine protocol that was intended to be representative of clinical conditions during surgery. The constitutive model used is an adaptation of (linear) Biot's description of consolidation theory (a solid isotropic, linear elastic matrix and an interstitial fluid). The fluid flow is governed by the Darcy filtration law.

Surgery for craniosynostis aims to decompress the brain, and to remodel the deformed skull into a normal shape. Vander Sloten et al. [529] introduced a simulation system developed in a computer aided design environment where a 3D mathematical model of the skull is entered.

Taylor and Miller [566] performed a finite element study of the biomechanics of hydrocephalus, with special emphasis on a reassesment of the parenchyma elastic modulus. Unfortunately, the constitutive modelling is not quite lucid.

Brands et al. [53], to model the nearly incompressible brain tissue, decompose the Cauchy stress tensor as the sum of a volumetric part, $\boldsymbol{\sigma}^v$, which

depends on the volumetric changes only (an acceptable limitation), and a deviatoric part $\boldsymbol{\sigma}^d$, which depends on change of shape only:

$$\boldsymbol{\sigma} = \boldsymbol{\sigma}^v + \boldsymbol{\sigma}^d.$$

Here

$$\boldsymbol{\sigma}^v = K(\sqrt{I_3^B} - 1)\mathbf{I},$$

where K denotes the bulk modulus. I_3^B denotes the third invariant of the elastic tensor $\mathbf{B}^e = \mathbf{F}^e(\mathbf{F}^e)^T$, and the deformation gradient tensor $\mathbf{F}$ is split multiplicatively as follows $\mathbf{F} = \mathbf{F}^e\mathbf{F}^p$. Obviously $\mathbf{F}^p$ denotes an inelastic part.

The deviatoric part of the stress is modelled as a nonlinear and viscoelastic. It is decomposed in a number of viscoelastic modes, $\boldsymbol{\sigma}_i^d$:

$$\boldsymbol{\sigma}^d = \sum_{i=1}^{N} \boldsymbol{\sigma}_i^d.$$

The model is written in a differential formulation as opposed to the quasilinear viscoelastic formulations in explicit FE packages. For details of the constitutive modelling and numerical implementation the reader is referred to the thesis by Brands [54]. Other related issues on brain investigations and modelling are discussed in Zhang et al. [648], Donnely and Medige [144], Guillame et al. [210], Bilston et al. [43], Pamidi and Advani [442], Walsh and Settini [603], Darvish and Crandall [114], Galbraith et al. [179], Sahay et al. [498], Kumaresan et al. [317].

Meaney [379] developed a structurally based material models of the *optic nerve*. The models relate tissue strain to the deformation and stress of subcellular elements that occur during simple elongation of the optic nerve; see also Ommaya [438], Gennarelli et al. [188].

A series of three papers (Farshad et al., [161]; Snedeker et al., [532, 533]), is concerned with experimental investigations and simple constitutive modelling (much similar to that used for brain tissue) of *kidney*, cf. also Herbert et al. [230]. It seems that these are the first studies related to kidney deformability modelled by using isotropic models. Experimental results revealed that mechanical behaviour of the kidney tissue is anisotropic. It seems that anisotropy can be incorporated into the models of very soft tissues available in the literature. For instance, one can use models of type (5.100) and generalizations including viscous effects (by applying time convolution).

Finite element model of the *human abdomen* was developed by Lee and Yang [340].

10.11. Tumours

According to Araujo and McElwain [13], cancer is now poised to over-take heart disease as the major cause of premature death in the Western World. In our opinion, not only in that part of the world. Obviously, the study of tumour growth, and the development of anti-cancer therapies are of primal importance. One of such therapies, hyperthermia, has been discussed in the previous section. An excellent review paper by Araujo and McEl-wain [13] pursues the important mathematical contributions to the study of solid tumour growth with historical comments. The paper includes also seminal experimental publications (see also Thoumine and Ott, [581]; Thapa et al. [579]; Ambrosi and Mollica, [12]; Ambrosi and Preziosi, [10]; Basse et al. [31]; Cristini et al. [109]; Villasana and Radunskaga, [600]) and some sig-nificant papers which employ stochastic approaches. The paper covers the following topics: earliest mathematical contributions to the study of solid tumours, beginning with Hill's study of diffusion in tissues (Hill, 1928), and leading to Burton's often-cited paper on tumour growth dynamics as a diffu-sion problem (Burton, 1966); some early theoretical approaches to the study of avascular tumours and multicell spheroids in the wake of Folkman's im-portant discoveries relating to angiogenesis and prevascular stage of tumour development (see also Ambrosi and Mollica, [12]); seminal contributions to this theoretical study of tumour invasion and metastasis in the 1970s; the development of mathematical approaches in the 1980s; an overview of ma-thematical papers on solid tumour growth published in the 1990's , including those relating to cell migration in multicell spheroids and tumour rods, mul-tiphase models, mechanical models and models of residual stress formation, models of invasion and metastasis and models of avascular and vascular tu-mour growth, cf. also Whyne et al. [624] and the releveant references therein.

Diaz and Tello [134] studied the controllability of the growth of the tu-mours by the internal localized action of inhibitors in a simplified mathe-matical model. The tumour, formed by live cells is assumed to have the density proportional to the concentrations of a nutrient $\hat{\sigma}(X_i, t)$, $i = 1, 2, 3$, mainly oxygen and glucose. These authors studied the behaviour after an-giogenesis, the formation of capillary sprouts from blood vessels, in response to externally applied chemical stimuli. Once the angiogenesis occurs, the tu-mour receives nutrients from the vessels. To simplify the analysis Diaz and Tello [134] assumed that the tumour is a radially symmetric ball of $\mathbb{R}^3$ of radius $R(t)$, which is unknown. Hence the problem belongs to a class of free boundary problems. Denoting by σ_B the constant nutrient concentration in the vasculature, $\hat{r}_1$ the rate, per unit length, of nutrient transferred to the tissue, $\hat{\sigma}$ satisfies the equation, cf. also Diaz and Tallo [133]

$$\frac{\partial \hat{\sigma}}{\partial t} - d_1 \Delta \hat{\sigma} - \hat{r}_1(\sigma_B - \hat{\sigma}) + \alpha_1 \hat{\sigma} + \alpha \hat{\beta} = 0, \quad |\mathbf{X}| < R(t), \quad t \in (0, T).$$

Here, d_1 is the diffusion coefficient of the nutrient concentration, and $\alpha \hat{\sigma}$, $\alpha \hat{\beta}$ represent the consumption rate of nutrient and inhibition respectively.

The density of the inhibitor $\hat{\beta}(\mathbf{X}, t)$ is assumed to satisfy a similar reaction-diffusion equation:

$$\frac{\partial \hat{\beta}}{\partial t} - d_2 \Delta \hat{\beta} - \hat{r}_2(\beta_B - \hat{\beta}) + \alpha_2 \hat{\beta} = f \chi_{\omega_0}, \quad |\mathbf{X}| < R(t), \quad t \in (0, T)$$

with d_2 the diffusion coefficient, β_B the critical value of the inhibitor concentration for vasculature, $\hat{r}_2$ the rate, per unit length, of inhibitor transferred to the tissue, and $\alpha_2 \beta$ is the inhibitor consumption rate. The permanent supply of inhibitors is assumed to be localized on a small domain ω_0 with a rate given by f (the control function of the problem).

According to the mass conservation principle, assuming the cell mass density constant, the tumour mass is proportional to the volume $4\pi R(t)^3/3$. The balance between birth and death of cells is determined by the concentration of nutrient and inhibitor. Denoting the above balance by Z, after normalizing we obtain the law:

$$\frac{d}{dt}\left(\frac{4}{3}\pi R^3(t)\right) = \int\limits_{\{|\mathbf{X}| < R(t)\}} Z(\hat{\sigma}(\mathbf{X}, t), \hat{\beta}(\mathbf{X}, t)) d\mathbf{X}, \quad \mathbf{X} \in \mathbb{R}^3.$$

The main result due to to Diaz and Tello concerns the *approximate controllability* of the internal distribution of density of cells, that is proportional to the concentration of nutrients, injecting the inhibitor in ω_0. More precisely, the inhibitor allows to approximately control (in the usual weak or variational, sense typical for parabolic problems) the tumour density. Approximate, and not exact controllability is typical for parabolic equations, cf. Telega and Zuazua [578]. In the last book the reader will find a good introduction to various mathematical aspects of controllability, including historical comments, deterministic and stochastic controllability of finite dimensional systems as well as parameter distributed systems. Many applications to control of solid bodies and structures like beams, membranes, plates and shells are also provided.

10.12. Biomaterial-tissue interactions

The biocompatibility of biomaterial is an important issue in interaction with bones (e.g. orthopaedics) and soft tissue (e.g. grafts). Available results are mostly restricted to experimental data, cf. Silver and Christiansen [521].

In our opinion the issue is worth of mathematical modelling. Of particular interest is the interface tissue-biomaterial.

Let us provide a recent example of a new thin film material, tetrahedral amorphous carbon (ta-C), that combines some of the more desirable properties of carbon and diamond films. This material has strength, hardness, and modulus close to that of crystalline diamond, yet can be produced as a smooth and stress free (or controlled stress) film that can be micromachined to produce microelectromechanical systems (MEMS) and large unsupported membranes. For earlier experimental findings on tissue (including cells)-thin film interactions the reader is referred to the relevant papers in LaVan [334]. We also observe that in the literature on mathematical modelling of heterogeneous materials, one finds many contributions concerned with thin films, cf. the paper by Bhattacharya in Ponte Castañeda et al. [453].

LaVan et al. [334] focused on the in vivo tissue response of ta-C. The ta-C films were produced by pulsed laser deposition to be rich in either 3- or 4-fold content. The bonding character was analysed using Raman spectroscopy. Tissue reaction to the materials over a period of 6 months was assessed following subcutaneous implantation of ta-C coated silicon die. Moreover, the authors studied the reaction to ta-C particles injected near the sciatic nerve. These particles were used as a simple analogue to small free floating ta-C devices that might be used in vivo, and as a well-characterized system to study tissue reaction to possible μm scale debris from a ta-C-coated device. The vicinity of the sciatic nerve was selected because it contains a variety of tissues (nerve, blood vessel, muscle, loose connective tissue), and the local reaction to injected microparticles in this area has been well characterized, cf. the relevant references in LaVan et al. [334].

10.13. Properties of cadaveric tissues

Van Ee et al. [153] characterized the time-dependent properties of skeletal muscle through the perimortem and postmortem periods using an animal model (twelve New Zealand white rabbits). The immediate postmortem properties were not significantly different from the live passive properties (for instance, the stress-strain response of muscle and tendon). In contrast to the immediate postmortem response, the mechanical properties of the muscle varied significantly over the postmortem period. For results on postmortem properties of bone, ligament, tendon, skin, articular cartilage, and spinal segments the reader is referred to the relevant references in Van Ee et al. [153].

10.14. Tissue engineering

The field of tissue engineering has developed to meet the tremendous needs for organs and tissues. In the most general sense, tissue engineering seeks to fabricate living replacement parts of the body. The special issue of the well-known journal "Biomaterials" (Jansen, [271]) presents an overview of animal models currently available for tissue engineering research. The included papers cover models that can be used to test tissue engineered constructs designed, to replace the most relevant tissue structures and organs. One paper included discusses the ethical implications of animal research for tissue engineered applications.

The paper by Drury and Mooney [149] reviews the use of hydrogels as scaffolds for tissue engineering. Adequate scaffold design and material selection for each specific application depend on several variables, including physical properties (e.g. mechanical, degradation, gel formation), mass transport properties (e.g. diffusion), and biological properties (e.g. cell adhesion and signalling). All these properties were briefly discussed.

Motlagh et al. [411] critically assessed the shortcomings of conventional cardiac systems and proposed a new cell culture system that provides a three-dimensional environment enabling the maintenance of the in vivo cardiac myocyte phenotype. Myocytes were plated on nontextured, micropegged ($5\,\mu$m high), microgrooved (parallel groves with a depth of $5\,\mu$m) or combination (micropegged and grooved) substrata.

In contrast to research on blood vessels and heart valves, research on cardiac muscle tissue engineering has been delayed because of the difficulty of establishing myocardial cell sources, cf. Ramamurthi and Vesely [474] and Ogle and Mooradian [433]. However, recent progress in stem biology has shown the possibility of implantable human myocardial cell sources and has accelerated myocardial tissue engineering, cf. Shimizu et al. [517] and the relevant references therein. At present, researchers attempt to repair not all of the myocardial tissue, but part of it. Shimizu et al. [517] presented the progress achieved in myocardial tissue engineering and discussed future perspectives. Figure 95 presents tissue engineering methodologies, used also for the construction of 3D myocardial tissue.

Mahoney et al. [366] produced microchannels using litographic technique to pattern polyimide walls ($11\,\mu$m in height and 20–$60\,\mu$m in width) onto a planar glass substrate. These authors characterized the properties of neurite growth in such channels.
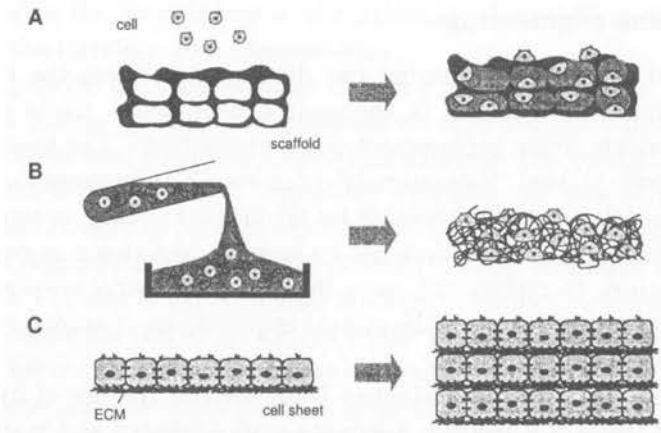
Figure 95. Tissue engineering methodologies. A. Isolated cells are poured onto prefabricated, highly porous scaffolds. The scaffolds are biodegraded, and extra-cellular matrix (ECM) occupies the space within the cells, leading to 3-D tissues. B. A mixture of isolated cells and biodegradable molecules is poured into an appropriate mold, and then the molecules are polymerized. The construct is re-generated into tissues. C. Intact cell sheets released from temperature-responsive culture surfaces are layered. Cell sheets adhere to each other via biological ECM, resulting in 3-D tissues containing no biodegradable scaffolds, after Shimizu et al. [517].

Acknowledgement

References

1. *ABAQUS Theory manual, Version 5.7; ABAQUS/Standard Example prob-lems manual, Version 5.7; ABAQUS/Standard User's manual, Version 5.7; ABAQUS/Standard Verification manual, Version 5.7.* Hibbitt, Karlsson and Sørensen Inc., Pawtucket 1997.

2. S.D. Abramowitch and S.L-Y. Woo, An improved method to analyze the stress relaxation of ligaments following a finite ramp time based on the quasi-linear vis-coelastic theory, *J. Biomech. Eng.*, Vol. 126, pp.92–97, 2004.

3. T. Adachi, M. Tanaka, and Y. Tomita, Uniform stress state in bone structure with residual stress, *J. Biomech. Eng.*, Vol. 120 pp.342–347, 1998.

4. M. Adams, N. Bogduk, K. Burton, and P. Dolan, *The biomechanics of back pain*, Churchill Livingstone, Edinburgh 2002.

5. N. Akkas, Continuum modeling of head injury, In: N. Akkas [ed.], *Progress in Biomechanics*, pages 297–331, 1979.

6. A. Aksan and J. McGrath, Thermomechanical analysis of soft-tissue thermother-apy, *J. Biomech. Eng.*, Vol. 125, pp.700–708, 2003.

7. T. Akutsu and T. Masuda, Three-dimensional flow analysis of a mechanical bileaflet mitral prosthesis, *J. Artif. Organs*, Vol. 6, pp.112–123, 2003.

8. B.D. Alberts, D. Bray, J. Lewis, M. Raff, K. Roberts, and J.D. Watson, *Molecular biology of the cell*, Garland, New York 1994.

9. G. Allaire, *Shape Optimization by the Homogenization Method*, Springer, New York 2002.

10. D. Ambrosi and L. Preziosi, On the closure of mass balance models for tumour growth, *Math. Mod. Appl. Sciences*, Vol. 12, pp.737–754, 2002.

11. D. Ambrosi and F. Mollica, The role of stress growth of a multicell spheroid, *J. Math. Biol.*, Vol. 48, pp.477–499, 2004.

12. D. Ambrosi and F. Mollica, On the mechanics of a growing tumor, *Int. J. Eng. Sci.*, Vol. 40, pp.1297–1316, 2002.

13. R.P. Araujo and D.L.S. McElwain, A history of the study of solid tumour growth: the contribution of mathematical modelling, *Bull. Math. Biol.*, Vol. 66, pp.1039–1091, 2004.

14. I.P. Arlart, G.M. Bongartz, and G. Marchal, *Magnetic Resonance Angiog-raphy*, Springer-Verlag, Berlin 2002.

15. W.K. Arnold, S. Hirsekorn [Eds.], Acoustical Imaging, Kluwer, Dordrecht, 2004.

16. J.E. Arruda, E.M. Arruda, and K. Grosh, Orthotropic hyperelasticity in terms of an arbitrary molecular chain model, *J. Appl. Mech.*, Vol. 69, pp.198–201, 2002.

17. T. Arts, P. Bovendeerd, T. Delhaas, and F. Prinzen, Modeling the rela-tion between cardiac pump function and myofiber mechanics, *J. Biomech.*, Vol. 36, pp.731–736, 2003.

18. G.A. Ateshian, M.A. Soltz, R.L. Mauck, I.M. Basalo, C.T. Hung, and W.M. Lai, The role of osmotic pressure and tension-compression nonlinearity in the frictional response of articular cartilage, *Transport in Porous Media*, Vol. 50, pp.5–33, 2003.

19. G.A. Ateshian, N.O. Chahinke, I.M. Basalo, and C.T. Hung, The correspon-dendce between equilibrium biphasic and triphasic material properties in mixture model models of articular cartilage, *J. Biomech.*, Vol. 37, pp.391–400, 2004.

20. A.D. Augst, D.C. Barratt, A.D. Hughes, F.P. Glor, S.A.M.G. Thom, and X.Y. Xu, Accuracy and reproducibility of CFD predicted wall shear stress using 3D ultrasound images, *J. Biomech. Eng.*, Vol. 125, pp.218–222, 2003.

21. H.K. Ault, A.H. Hoffman, A composite micromechanical model for connective tissues: Part I – Theory, *J. Biomech. Eng.*, Vol. 114, pp.137–141, 1992.

22. H.K. Ault, A.H. Hoffman, A composite micromechanical model for connective tissues: Part I – Application to rat tail tendon and joint capsule, *J. Biomech. Eng.*, Vol. 114, pp.142–146, 1992.

23. J.-L. Auriault, C. Geindreau, P. Royer, J.-F. Bloch, C. Boutin, and J. Lewandowska [Eds.], Poromechanics II, Balkema Publ., Lisse, The Netherlands 2002.

24. J.W. BAISH, Heat transport by countercurrent blood vessels in the presence of an arbitrary temperature gradient, *J. Biomech. Eng.*, Vol. 112, pp.207–211, 1990.

25. J.W. BAISH, Formulation of a statistical model of heat transfer in perfused tissue, *J. Biomech. Eng.*, Vol. 116, pp.521–527, 1994.

26. J.M. BALL, Convexity condition and existence theorems in nonlinear elasticity, *Arch. Rat. Mech. Anal.*, Vol. 63, pp.337–406, 1997.

27. G. BAO, Mechanics of biomolecules, *J. Mech. Physics Solids*, Vol. 50, pp.2237–2274, 2002.

28. V.H. BAROCAS and R.T. TRANQUILLO, An anisotropic biphasic theory of tissue-equivalent mechanics: the interplay among cell traction, fibril network deformation, and contact guidance, *J. Biomech. Eng.*, Vol. 119, pp.135–145, 1997.

29. V.H. BAROCAS and R.T. TRANQUILLO, A finite element solution for the anisotropic biphasic theory of tissue-equivalent mechanics: the effect of contact guidance on isometric call traction measurement, *J. Biomech. Eng.*, Vol. 119, pp.261–268, 1997.

30. E.C. BASS, E.V. WISTROM, C.J. DIEDERICH, W.H. NAU, R. PELLEGRINO, J. RUBERTI, and J.C. LOTZ, Heat-induced changes in porcine annulus fibrosus biomechanics, *J. Biomech.*, Vol. 34, pp.233–240, 2004.

31. B. BASSE, B.C. BAGULEY, E.S. MARSHALL, W.R. JOSEPH, B. VAN BRUNT, G. WAKE, and D.J.N. WALL, A mathematical model for analysis of the cell cycle in cell lines derived from human tumours, *J. Math. Biology*, Vol. 47, pp.295–312, 2003.

32. M. BATHE and R.D. KAMM, A fluid-structure interaction finite element analysis of pulsatile blood flow through a compliant stenotic artery, *J. Biomech. Eng.*, Vol. 121, pp.361–369, 1999.

33. M.F. BEATTY, Introduction to nonlinear elasticity, In: M.M. Carroll and M. Hayes [eds.], *Nonlinear Effects in Fluids and Solids*, Plenum Press, New York 1996.

34. H. BEIRÃO DA VEIGA, On the existence of strong solution to a coupled fluid-structure evolution problem, *J. Math. Fluid. Mech.*, Vol. 6, pp.21–52, 2004.

35. D.M. BERS, Excitation–Contraction Coupling and Cardiac Contractile Force, Kluwer, Dordrecht 1991.

36. L.J. BHARGAVA, M.G. PANDY, and F.C. ANDERSON, A phenomenological model for estimating metabolic energy consumption in muscle contraction, *J. Biomech.*, Vol. 37, pp.81–88, 2004.

37. L.J. BHARGAVA, M.G. PANDY, and F.C. ANDERSON, A phenomenological model for estimating metabolic energy consumption in muscle contraction, *J. Biomech.*, Vol. 37, pp.81–88, 2004.

38. S. BHOWMICK, D.J. SWANLUND, and J.C. BISCHOF, Supraphysiological thermal injury in Dunning AT-1 prostrate tumor cells, *J. Biomech. Eng.*, Vol. 122, pp.51–59, 2000.

39. W. BIELSKI and J.J. TELEGA, Effective properties of geomaterials: rocks and porous media, Publications of the Institute of Geophysics, Polish Academy of Sciences, A-26(285), p.120, Warszawa 1997.

40. W. BIELSKI and J.J. TELEGA, Transversely isotropic hyperelasticity with stored energy function exhibiting nonpolynomial growth, In: W. Szcześniak [ed.], *Theoretical Foundations of Civil Engineering* pages 853–862, OW PW, Warsaw 2004.

41. K.L. BILLIAR and M.S. SACKS, Biaxial mechanical properties of the natural and glutaraldehyde treated aortic valve cusp – Part I. Experimental results, *J. Biomech. Eng.*, Vol. 122, pp.23–30, 2000.

42. L.E. BILSTON, Z. LIU, N. PHAN-THIEN, Linear viscoelastic properties of bovine brain tissue in shear, *Biorheology*, Vol. 34, pp.377–385, 1997.

43. L.E. BILSTON, Z. LIU, N. PHAN-THIEN, Large strain behaviour of brain tissue in shear: some experimantal data and differential constitutive model, *Biorheology*, Vol. 38, pp.335–345, 2001.

44. J.E. BISCHOFF, E.M. ARRUDA, and K. GROSH, A microstructurally based orthotropic hyperelastic constitutive law, *J. Appl. Mech.*, Vol. 69, pp.570–579, 2002.

45. J.E. BISCHOFF, E.M. ARRUDA, and K. GROSH, A rheological network model for the continuum anisotropic and viscoleastic behavor of soft tissue, *Biomech. Model. Mechanobiol.*, Vol. 3, pp.56–65, 2004.

46. A. BOCHENEK and M. REICHER, *Human Anatomy, Vol. 1: General Anatomy, Bones, Joints and Ligaments, Muscles* Państwowy Zakład Wydawnictw Lekarskich, Warszawa 1978, *in Polish.*

47. A. BOCHENEK and M. REICHER, *Human Anatomy, Vol. 3: Vascular System* Państwowy Zakład Wydawnictw Lekarskich, Warszawa 1978, *in Polish.*

48. A. BOCHENEK and M. REICHER, *Human anatomy, Vol. 4: Central nervous system* (in Polish) Państwowy Zakład Wydawnictw Lekarskich, Warszawa 2000.

49. J.P. BOEHLER, Application of Tensor Functions in SOlid Mechanics, CISM Courses and Lectures, No.292, Springer-Verlag, Wien-New York 1987.

50. J. BONET and R. D. WOOD, *Nonlinear continuum mechanics for finite element analysis*, Cambridge University Press, Cambridge 1997.

51. E.M.H. BOSBOOM, M.K.C. HESSELINK, C.W.J. OOMENS, C.V.C. BOUTEN, M.R. DROST, and F.P.T. BAAIJENS, Passive transverse mechanical properties of skeletal muscle under in vivo compression, *J. Biomech.*, Vol. 34, pp.1365–1368, 2002.

52. A. BRAIDES and A. DEFRANCESCHI, Homogenization of Multiple Integrals, Clarendon Press, Oxford 1998.

53. D.W.A. BRANDS, P.H.M. BOVENDEERD, and J.S.H.M. WISMANS, On the potential importanceof non-linear viscoelastic material modelling for numerical prediction of brain tissue response: test and application, *Stapp Car Crash J.*, Vol. 46, pp.103–121, 2002.

54. D.W.A. BRANDS, Predicting brain mechanics during closed head impact: numerical and constitutive aspects, Ph.D. Thesis, Eindoven University of Technology, Eindhoven, The Netherlands; available on the internet: http://alexandria.tue.nl/extra2/200210809.pdf, 2002.

55. N.D. BROOM, Connective tissue function and multifunction: a biomechanical perspective, The Third George Swanson Christie Memorial Lecture, *Pathology*, Vol. 20, pp.93–104, 1988.

56. R.G. BREULS, C.V.C. BOUTEN, C.W. OOMENS, D.L. BADER, and F.P.T. BAAI-
    JENS, A theoretical analysis of damage evolution in skeletal muscle tissue with ref-
    erence to pressure ulcer development, *J. Biomech. Eng.*, Vol. 125, pp.902–909, 2003.

57. H. BRINCK and J. WERNER, Efficiency function: improvement of classical bioheat
    equation, *J. Appl. Physiology*, Vol. 77(4), pp.1617–1622, 1994.

58. H. BRINCK and J. WERNER, Estimation of the thermal effect of blood flow in
    a branching countercurrent network using a three-dimensional vascular model,
    J. Biomech. Eng., Vol. 116, pp.324–330, 1994.

59. S.B. BRUEHLMANN, P.A. HULME, and N.A. DUNCAN, In situ intercellular mechan-
    ics of the bovine outer annulus fibrosus subjected to biaxial strains, *J. Biomech.*,
    Vol. 37, pp.223–231, 2004.

60. M.R. BRYANT and P.J. MCDONNELL, Constitutive laws for biomechanical model-
    ing of refractive surgery, *J. Biomech. Eng.*, Vol. 118, pp.473–481, 1996.

61. M.R. BRYANT and P.J. MCDONNELL, A triphasic analysis of corneal swelling and
    hydration control, *J. Biomech. Eng.*, Vol. 120, pp.370–381, 1998.

62. T. BSCHLEIPFER, D. KALLIERIS, E.W. HAUCK, W. WIDNER, R.A. PUST, Blunt
    renal trauma: biomechanics and origination of renal lesions, *European Urology*,
    Vol. 42, pp.614–621, 2002.

63. P. DE BUHAN, X. CHATEAU, and L. DORMIEUX, The constitutive equations of
    finite strain poroelasticity in the light of micro-macro approach, *Eur. J. Mech.
    A/Solids*, Vol. 17, pp.909–921, 1998.

64. G. BURNSTOCK, Structure of smooth muscle and its innervation, In G. Bülbring
    et al. [ed.], *Smooth Muscle* pages 1–69, Arnold, London 1970.

65. P. BURSAĆ, C.V. MCGRATH, S.R. EISENBERG, and D. STAMENOVIĆ, A mi-
    crostructural model of elastostatic properties of articular cartilage in confined com-
    pression, *J. Biomech. Eng.*, Vol. 122, pp.347–353, 2000.

66. E.D. CAREW, E.A. TALMAN, D.R. BOUGHNER, and I. VESELY, Quasi-linear vis-
    coelastic theory applied to internal shearing of porcine aortic valve leaflets, *J. Bio-
    mech. Eng.*, Vol. 121, pp.386–392, 1999.

67. J. CASEY and G. BAO [Eds.], Mechanics in Biology, AMD-Vol. 242, BED-Vol. 46,
    The American Society of Mechanical Engineers, New York 2000.

68. G. CHAGNON, E. VERRON, L. GORNET, G. MARCKMANN, and P. CHARRIER, On
    the relevance of Continuum Damage Mechanics to the Mullins effect in elastomers,
    J. Mech. Phys. Solids, Vol. 52, pp.1627–1650, 2004.

69. M. CHARLEBOIS, M.D. MCKEE, and M.D. BUSCHMANN, Nonlinear tensile prop-
    erties of bovine cartilage and their variation with age and depth, *J. Biomech. Eng.*,
    Vol. 126, pp.129–137, 2004.

70. C.K. CHARNY, S. WEINBAUM, and R.L. LEVIN, An evaluation of the Weinbaum-
    Jiji bioheat equation for normal and hyperthermic conditions, *J. Biomech. Eng.*,
    Vol. 112, pp.80–87, 1990.

71. C.-T CHEN, D.S. MALKUS, and R. VANDERBY JR., A fiber matrix model for
    interstitial fluid flow and permeability in ligaments and tendons, *Biorheology*, Vol. 35,
    pp.103–118, 1998.

72. A.C. CHEN, W.C. BAE, R.M. SCHINAGL, and R.L. SAH, Depth and strain-dependent mechanical and electromechanical properties of full-thickness bovine articular cartilage in confined compression, *J. Biomech.*, Vol. 34, pp.1–12, 2001.

73. L. CHEN, F.C-P. YIN, and K. MAY-NEWMAN, The structure and mechanical properties of the mitral valve leaflet-strut chordae transition zone, *J. Biomech. Eng*, Vol. 126, pp.244–251, 2004.

74. M.M. CHEN and K.R. HOLMES, Microvascular contributions in tissue heat transfer, *Annals New York Acad. Sci.*, Vol. 335, pp.137–154, 1980.

75. M.M. CHEN and K.R. HOLMES, Heat-induced changes in the mechanics of a collagenous tissue: pseudoelastic behavior at 37°C, *J. Biomech.*, Vol. 31, pp.211–216, 1998.

76. S.S. CHEN, N.T. WRIGHT, and J.D. HUMPHREY, Phenomenological evolution equations for heat-induced shrinkage of a collagenous tissue, *IEEE Trans. BME*, Vol. 45(10), pp.1234–1240, 1998.

77. S.S. CHEN, N.T. WRIGHT, and J.D. HUMPHREY, Heat-induced changes in the mechanics of a collagenous tissue: Isothermal, free shrinkage, *J. Biomech. Eng.*, Vol. 119, pp.372–378, 1997.

78. S.S. CHEN, N.T. WRIGHT, and J.D. HUMPHREY, Heat-induced changes in the mechanics of a collagenous tissue: Isothermal, isotonic shrinkage, *J. Biomech. Eng.*, Vol. 120, pp.382–388, 1998.

79. Z.-P. CHEN and R.B. ROEMER, The effects of large blood vessels on temperature distributions during simulated hyperthermia, *J. Biomech. Eng.*, Vol. 114, pp.473–481, 1992.

80. R. CHERKAEV and R. KOHN [Eds.], Topics in the Mathematical Modelling of Composite Materials, Birkhäuser, Boston 1997.

81. J.-J. CHIU, L.-J. CHEN, C.-N CHEN, P.-L. LEE, and C.-I. LEE, A model for studying the effect of shear stress on interactions between vascular endothelial cells and smooth muscle cells, *J. Biomech.*, Vol. 37, pp.531–539, 2004.

82. Y.B. CHOY, H. CAO, S. TUNGJITKUSOLMUN, J.-Z. TSAI, D. HAEMMERICH, V.R. VORPERIAN, and J.G. WEBSTER, Mechanical compliance of the endocardium, *J. Biomech.*, Vol. 35, pp.1671–1676, 2002.

83. P.G. CIARLET, *Mathematical elasticity*, North Holland, Amsterdam 1988.

84. D. CIORANESCU and P. DONATO, *Introduction to Homogenization*, Oxford University Press, Oxford 1999.

85. D. CIORANESCU and J. SAINT JEAN PAULIN, *Homogenization of Reticular Structures*, Springer, New York 1999.

86. T.E. CLAESSENS, P.L. VAN HERCK, K.S. MATTHYS, P. SEGERS, C.J. VRINTS, and P.R. VERDONCK, Influence of zero flow pressure on fractional flow reserve, *Biomech. Model. Mechanobiol.*, Vol. 3, pp.48–55, 2004.

87. J.M. CLARK and S. GLAGOV, Structural integration of the arterial wall, *Lab. Invest*, Vol. 40, pp.587–602, 1979.

88. J.M. CLARK and S. GLAGOV, Transmural organization of the arterial media, *Arteriosclerosis*, Vol. 5, pp.19–34, 1985.

89. C.A. Cobbold, J.A. Sherratt, and S.R.J. Maxwell, Lipoprotein oxidation and its significance for atherosclerosis: a mathematical approach, *Bull. Math. Biol*, Vol. 64, pp.65–95, 2002.

90. B. Cohen, W.M. Lai, and V.C. Mow, A transversely isotropic biphasic model for unconfined compression of growth plate and chondroepiphysis, *J. Biomech. Eng.*, Vol. 120, pp.491–496, 1998.

91. J.H. Comroe, R.E. Forster, A.B. Dubuis, W.A. Briscoe, and E. Carlsen, The lung clinical physiology and pulmonary functions tests, Yaer Book Medical Publisher, Chicago 1962.

92. T.A. Convay, N. Mazilu, and J. Vossoughi, On the uniqueness of a constitutive law for soft tsissue and its implications on the phenomenological thermodynamics of solids, *Russian Journal of Biomechanics*, Vol. 8, pp.27–36, 2004.

93. K.D. Costa and F.C.P. Yin, Analysis of indentation: implications for measuring mechanical properties with atomic force microscopy, *J. Biomech. Eng.*, Vol. 121, pp.462–471, 1999.

94. M.L. Costantino, P. Bagnoli, G. Dini, G.B Fiore, M. Soncini, C. Corno, F. Acocella, and R. Colombi, A numerical and experimental study of compliance and collapsibility of preetrm lamb tracheae, *J. Biomech.*, Vol. 37, pp.1837–1847, 2004.

95. R.J. Coulson, M.J. Cipolla, L. Vitullo, and N.C. Chesler, Mechanical properties of rat middle cerebral arteries with and without myogenic tone, *J. Biomech. Eng*, Vol. 126, pp.76–81, 2004.

96. O. Coussy, Mécanique des Milieux Poreux, *Editions Techniq*, Paris 1991 (English translation: Mechanics of Porous Continua, John Wiley & Sons, New York 1995).

97. S.C. Cowin, The relationship between the elasticity tensor and the fabric tensor, *Mech. Mater.*, Vol. 4, pp.137–147, 1985.

98. S.C. Cowin, How is tissue built?, *J. Biomech. Eng*, Vol. 122, pp.553–569, 2000.

99. S.C. Cowin and J.D. Humphrey [Eds.], Cardiovascular Soft Tissue Mechanics, Kluwer, New York 2003.

100. S.C. Cowin and J.M. Huyghe [Eds.], The Mechanics of Physicochemical and Electromechanical Interactions in Porous Media, Kluwer Academic Publishers, 2004, in press.

101. W. Craelius, C.-J. Huang, H. Guber, and C.A. Palant, Rheological behavior of rat mesangial cells during swelling in vitro, *Biorheology*, Vol. 34, pp.387–403, 1997.

102. E.G. Cravalho, L.R. Fox, and J.C. Kan, The application of the bioheat equation to the design of thermal protocols for local hyperthermia, *Annals New York Acad. Sci.*, Vol. 335, pp.86–97, 1980.

103. J. Crezee and J. J. W. Lagendijk, Experimental verification of bioheat transfer theories: Measurement of temperature profiles around large artificial vessels in perfused tissue, *Phys. Med. Biol.*, Vol. 35(7), pp.905–923, 1990.

104. J. Crezee, J. Mooibroek, J. J. W. Lagendijk, and G. M. J. Van Leneuven, The theoretical and experimental evaluation of the heat balance in perfused tissue, *Phys. Med. Biol.*, Vol. 39, pp.813–832, 1994.

105. J.C. CRISCIONE, A.S. DOUGLAS, and W.C. HUNTER, Physically based strain invariant set for materials exhibiting transversely isotropic behavior, *J. Mech. Phys. Solids*, Vol. 49, pp.871–897, 2001.

106. J.C. CRISCIONE, A.D. McCULLOCH, and W.C. HUNTER, Constitutive framework optimized for myocardium and other high-strain, laminar materials with one fiber family, *J. Mech. Phys. Solids*, Vol. 50, pp.1681–1702, 2002.

107. J.C. CRISCIONE, M.S. SACKS, and W.C. HUNTER, Experimentally tractable, pseudoelastic constitutive law for biomembranes: I. Theory, *J. Biomech. Eng.*, Vol. 125, pp.94–99, 2003.

108. J.C. CRISCIONE, M.S. SACKS, and W.C. HUNTER, Experimentally tractable, pseudoelastic constitutive law for biomembranes: II. Application, *J. Biomech. Eng.*, Vol. 125, pp.100–105, 2003.

109. V. CRISTINI, J. LOWENGRUB, and Q. NIE, Nonlinear simulation of tumor growth, *J. Math. Biology*, Vol. 46, pp.191–224, 2003.

110. B. DACOROGNA, Direct Methods in the Calculus of Variations, Springer-Verlag, Berlin 1989.

111. E.R. DAMIANO, A poroelastic continuum model of the cupula partition and the response dynamics of the vestibular semicircular canal, *J. Biomech. Eng.*, Vol. 121, pp.449–461, 1999.

112. M. DAO, C.T. LIM, and S. SURESH, Mechanics of the human red blood cell deformed by optical tweezers, *J. Mech. Physics Solids*, Vol. 51, pp.2259–2280, 2003.

113. M. DAROWSKI, Sterowanie Sztuczną Wentylacją Płuc, *Control of Artificial Ventillation of the Lungs*, Wydawnictwo Komunikacji i Łączności, Warszawa 1994, in Polish.

114. K.K. DARVISH and J.R. CRANDALL, Nonlinear viscoelastic effects in oscillatory shear deformation of brain tissue, *Medical Eng. Physics*, Vol. 23, pp.633–645, 2001. in Polish.

115. G. DAVID and J.D. HUMPHREY, Redistribution of stress due to a circular hole in a nonlinear anisotropic membrane, *J. Biomech.*, Vol. 37, pp.1197–1203, 2004.

116. C.R. DAVIES, G.M. SAIDEL, and H.HARASAKI, Sensitivity analysis of one-dimensional heat transfer in tissue with temperature-dependent perfusion, *J. Biomech. Eng.*, Vol. 119(1), pp.77–80, 1997.

117. E.D. DAVIS, D.J. DOSS, J.D. HUMPHREY, and N.T. WRIGHT, Effects of heat-induced damage on the radial component of thermal diffusivity of bovine aorta, *J. Biomech. Eng.*, Vol. 122(3), pp.283–286, 2000.

118. S.P. DAVIS, B.J. LANDIS, Z.H. ADAMS, M.G. ALLEN, and M.R. PRAUSNITZ, Insertion of microneedles into skin: measurement and prediction of insertion force and needle fracture force, *J. Biomech*, Vol. 37, pp.1155–1163, 2004.

119. R. DE BOER, *Theory of Porous Media: Highlights in Historical Development and Current State*, Springer-Verlag, Berlin 2000.

120. J. DE HART, F.P.T. BAAIJENS, G.W.M. PETERS, and P.J.G. SCHREURS, A computational fluid-structure interaction analysis of a fiber-reinforced stentles aortic valve, *J. Biomech.*, Vol. 36, pp.699–712, 2003.

121. J. de Hart, G.W.M. Peters, P.J.G. Schreurs, and F.P.T. Baaijens, A three-dimensional computational analysis of fluid-structure interaction in the aortic valve, *J. Biomech.*, Vol. 36, pp.103–112, 2003.

122. P.P. de Tombe, Cardiac myofilaments: mechanics and regulation, *J. Biomech.*, Vol. 36, pp.721–730, 2003.

123. A. Delfino, N. Stergiopulos, J.E. Moore, and J.-J. Meister, Residual strain effects on the stress field in a thick wall finite element model of the human carotid bifurcation, *J. Biomech.*, Vol. 30, pp.777–786, 1997.

124. Z. Del Prete, S. Antoniucci, A.H. Hoffman, and P. Grigg, Viscoelastic properties of skin in Mov-13 and Tsk mice, *J. Biomech.*, Vol. 37, pp.1491–1497, 2004.

125. S.L. Delp, S. Suryanarayanan, V.M. Murray, J. Uhlir, and R.J. Triolo, Architecture of the rectus abdminis, quadratus lumborum, and erector spinae, *J. Biomech.*, Vol. 34, pp.371–375, 2001.

126. Z.-S. Deng and J. Liu, Analytical study on bioheat transfer problems with spatial or transient heating on skin surface or inside biological bodies, *J. Biomech. Eng.*, Vol. 124, pp.638–649, 2002.

127. Z.-S. Deng and J. Liu, Non-Fourier heat conduction effect on prediction of temperature transients and thermal stress in skin cryopreservation, *J. Thermal Stress*, Vol. 26, pp.779–798, 2003.

128. E. Denny and R.C. Shroter, The micro-mechanical behaviour of a mammalian lung alveolar duct model, *J. Biomech. Eng.*, Vol. 117, pp.254–261, 1995.

129. E. Denny and R.C. Schroter, Viscoelastic behavior of a lung alveolar duct model, *J. Biomech. Eng.*, Vol. 122, pp.143–151, 2000.

130. E. Denny and R.C. Shroter, Relationship between arveolar size and fibre distribution in a mammalian lung alreolar duct model, *J. Biomech. Eng.*, Vol. 119, pp.289–297, 1997.

131. K.A. Derwin and L.J. Soslowsky, A quantitative investigation of structure-function relationships in a tendon fascicle model, *J. Biomech. Eng.*, Vol. 121, pp.598–604, 1999.

132. M.S. Detamore and K.A. Athanasiou, Tensile properties of the porcine temporomandibular joint disc, *J. Biomech. Eng.*, Vol. 125, pp.558–565, 2003.

133. J.I. Diaz and J.I. Tello, Mathematical analysis of a simple model for the growth of necrotic tumors in the presence of inhibitors, *Int. J. Pure Appl. Math.*, Vol. 9, pp.359–381, 2003.

134. J.I. Diaz and J.I. Tello, On the mathematical controllability in a simple growth tumors model by the internal localized action of inhibitors, *Nonlinear Analysis: Real World Applications*, Vol. 4, pp.109–125, 2003.

135. M.A. Dimicco and R.L. Sah, Dependence of cartilage matrix composition on biosynthesis, diffusion, and reaction, *Transport in Porous Media*, Vol. 50, pp.57–73, 2003.

136. M.R. DiSilvestro and J.-K.F. Suh, A cross-validation of the biphasic poroviscoelastic model of articular cartilage in unconfined compression, indentation, and confined compression, *J. Biomech.*, Vol. 34, pp.519–529, 2001.

137. S.A. Dixon, R.G. Heikes, and R.P. Vito, Constitutive modeling of porcine coronary arteries using designed experiments, *J. Biomech. Eng.*, Vol. 125, pp.274–279, 2003.

138. P. Dłużewski, Anisotropic hyperelasticity based upon general strain measures, *J. Elasticity*, Vol. 60, pp.119–129, 2000.

139. P. Dłużewski, G. Jurczak, and H. Antúnez, Logarithmic strain measure in finite element modelling of anisotropic hyperelastic materials, *Comp. Assisted Mech. Eng. Sci.*, Vol. 10, pp.69–79, 2003.

140. S. Dokos, I. J. LeGrice, B. H. Small, J. Kar, and A. A. Young, A triaxial-measurement shear–test device for soft biological tissues, *J. Biomech. Eng.*, Vol. 122, pp.471–478, 2000.

141. Y. Dou, J. Zhao, and H. Gregersen, Morphology and stress-strain properties along the small intestine in the rat, *J. Biomech. Eng.*, Vol. 125, pp.267–273, 2003.

142. J.C. Downs, J.-K.F. Suh, K.A. Thomas, A.J. Bellezza, C.F. Burgoyne, and R.T. Hart, Viscoelastic characterization of peripapillary sclera: Material properties by quadrant in rabbit and monkey eyes, *J. Biomech. Eng.*, Vol. 125, pp.124–131, 2003.

143. P.S. Donzelli, L.M. Gallo, R.L. Spilker, and S. Palla, Biphasic finite element simulationof the TMJ disc from in vivo kinematic and geometric measurements, *J. Biomech.*, Vol. 37, pp.1787–1791, 2004.

144. B.R. Donnelly and L. Medige, Shear properties of human brain tissue, *J. Biomech. Eng.*, Vol. 119, pp.423–432, 1997.

145. W. G. van Dorn, Thermodynamic model for cold water survival, *J. Biomech. Eng.*, Vol. 122(5), pp.541–544, 2000.

146. N.J.B. Driessen, R.A. Boerboom, J.M. Huyghe, C.V.C. Bouten, and F.T.P. Baaijens, Computational analyses of mechanically induced fiber remodelling in the aortic heart valve, *J. Biomech. Eng.*, Vol. 125, pp.549–557, 2003.

147. M.R. Drost, M. Maenhout, P.J.B. Willems, C.W.J. Oomens, F.P.T Baaijens, and M.K.C. Hesselink, Spatial and temporal heterogeneity of superficial muscle strain during in situ fixed-end contractions, *J. Biomech.*, Vol. 36, pp.1055–1063, 2003.

148. J.W. Durkee Jr, P.P. Antich, and C.E. Lee, Exact solutions to the multiregion time-dependent bioheat equation. I: Solution development, *Phys. Med. Biol.*, Vol. 35(7), pp.847–867, 1990.

149. J.L. Drury and D.J. Mooney, Hydrogels for tissue enginering: scaffold design variables and applications, *Biomaterials*, Vol. 24, pp.4337–4351, 2003.

150. Dumitru and Garrett, *Arch. Biochem. Biophys*, Vol. 66, pp.245, 1947.

151. J.W. Durkee Jr, P.P. Antich, and C.E. Lee, Exact solutions to the multiregion time-dependent bioheat equation. II: Numerical evaluation of the solutions, *Phys. Med. Biol.*, Vol. 35(7), pp.869–889, 1990.

152. M. Edlich, C.E. Yellowley, C.R. Jacobs, and H.J. Donahke, Oscillating fluid flow regulates cytosolic calcium concentration in bovine articular chondrocytes, *J. Biomech.*, Vol. 34, pp.59–65, 2001.

153. C.A. VAN EE, A.L. CHASSE, and B.S. MYERS, Quantifying skeletal muscle prop-
erties in cadaveric test specimens: effects in mechanical loading, postmortem time,
and freezer storage, *J. Biomech. Eng.*, Vol. 122, pp.9–14, 2000.

154. S. EHRLICH, N. WOLFF, R. SCHNEIDERMAN, A. MAROUDAS, K.H. PARKER, and
C.P. WINLOVE, The osmotic pressure of chondroitin sulphate solutions: Experimen-
tal measurements and theoretical analysis, *Biorheology*, Vol. 35, pp.383–397, 1998.

155. I. EKELAND and R. TEMAM, Convex Analysis and Variational Problems, North-
Holland, 1976.

156. D.M. ELLIOTT and L.A. SETTON, A linear material model for fiber-induced
anisotropy of the anulus fibrosus, *J. Biomech. Eng.*, Vol. 122, pp.173–179, 2000.

157. D.M. ELLIOTT and L.A. SETTON, Anisotropic and inhomogeneous tensile beha-
vior of the human anulus fibrosus: Experimental measurement and material model
predictions, *J. Biomech. Eng.*, Vol. 123, pp.256–263, 2001.

158. P. ELSNER, E. BERARDESA, K. P. WILHELM, and H. I. MAIBACH [eds.], *Bioengi-
neering of the skin: Skin biomechanics*, CRC Press, Boca Raton 2002.

159. F. ETAVE, G. FINET, M. BOIVIN, J.-C. BOYER, G. RIOUFOL, and G. THOLLET,
Mechanical properties of coronary stents determined by using finite element analysis,
J. Biomech., Vol. 34, pp.1067–1075, 2001.

160. E.A. EVANS and R. SKALAK, *Mechanics and Thermodynamics of Biomemembranes*,
CRC Press, Boca Raton, Florida 1980.

161. M. FARSHAD, M. BARBEZAT, P. FLÜELER, F. SCHMIDLIN, P. GRABER, and P.
NIEDERER, Material characterization of the pig kidney in relation with teh biome-
chanical analysis of the renal trauma, *J. Biomech.*, Vol. 32, pp.417–425, 1999.

162. S. FEDERICO, W. HERZOG, J.Z. WU, G.L. ROSA, A method to estimate the elastic
properties of the extracellular matrix of articular cartilage, *J. Biomech.*, Vol. 37,
pp.401–404, 2004.

163. S.J. FERGUSON, K. ITO, and L.-P. NOLTE, Fluid flow and convective transport of
solutes within the intervertebral disc, *J. Biomech.*, Vol. 37, pp.213–221, 2004.

164. B. FENG and R.Z. GAN, Lumped parametric model of the human ear for sound
transmission, *Biomech. Model. Mechanobiol.*, Vol. 3, pp.33–47, 2004.

165. J.W. FERNANDEZ, P. MITHRARATNE, S.F. THRUPP, M.H. TAWHAI, and
P.J. HUNTER, Anatomically based geometric modelling of the musculo-skeletal
system and other organs, *Biomech. Model. Mechanobiol.*, Vol. 2, pp.139–155, 2004.

166. M. FIGURSKA and J.J. TELEGA, Cytoskeletal organization of tissue and tensegrities,
in preparation.

167. R. FLIEGER and R. GREBE, Cell-elastometry: a new method to measure erythrocyte
membrane elasticity, *Biorheology*, Vol. 34, pp.223–234, 1997.

168. M. FORTIN, M.D. BUSCHMANN, M.J. BERTRAND, F.S. FOSTER, and J. OPHIR,
Dynamic measurement of internal solid displacement in articular cartilage using
ultrasound backscatter, *J. Biomech.*, Vol. 36, pp.443–447, 2003.

169. M. FORTIN, J. SOULHAT, A. SHIRAZI-ADL, E.B. HUNZIKER, and M.D.
BUSCHMANN, Unconfined compression of articular cartilage: nonlinear behavior

and comparison with a fibril-reinforced biphasic model, *J. Biomech. Eng.*, Vol. 122, pp.189–195, 2000.

170. A.J.H. FRIJNS, J.M. HUYGHE, and J.D. JANSSEN, A validation of the quadriphasic mixture theory for intervertebral disc tissue, *Int. J. Eng. Sci.*, Vol. 35, pp.1419–1429, 1997.

171. P. FRIDEZ, M. ZULLIGER, F. BOBARD, G. MONTORZI, H. MIYAZAKI, K. HAYASHI, and N. STERGIOPULOS, Geometrical, functional, and histomorphometric adaptation of rat carotid artery in induced hypertension, *J. Biomech.*, Vol. 36, pp.661–670, 2003.

172. M.A.R. FREEMAN [Ed.], Adult Articular Cartilage, Pitman Medical, Tunbridge Wells, England 1979.

173. G. FU, Y. ZENG, Z. XIA, J. LEE, Rheological features of some soft tissues under a surgical tissue expansion procedure, *Biorheology*, Vol. 34, pp.281–293, 1997.

174. Y.C. FUNG, *Biomechanics: mechanical properties of living tissues*, Springer-Verlag, New York 1981.

175. Y.C. FUNG, *Biomechanics, mechanical properties of living tissues*, second, enlarged and revised edition, Springer-Verlag, Berlin–New York 1993.

176. Y.C. FUNG, *Biomechanics: Circulation*, Springer-Verlag, New York 1997.

177. J.R. FUNK, J.R. CRANDALL, L.J. TOURRET, C.B. MACMAHON, C.R. BASSAND J.T. PATRIE, N. KHAEWPONG, and R.H. EPPINGER, The axial injury tolerance of the human foot/ankle complex and the effect of the achilles tendon, *J. Biomech. Eng.*, Vol. 124, pp.750–757, 2002.

178. J.R. FUNK, G.W. HALL, J.R. CRANDALL, and W.D. PILKEY, Linear and quasi-linear viscoelastic characterization of ankle ligaments, *J. Biomech. Eng.*, Vol. 122, pp.15–22, 2000.

179. J.A. BALBRAITH, L.E. THIBAULT, and D.R. MATTESON, Mechanical and electrical responses of the squit giant axon to simple elongation, *J. Biomech. Eng.*, Vol. 115, pp.13–22, 1993.

180. J.E. GALFORD and J.H. MCELHANEY, A viscoelastic study of scalp, brain and dura, *J. Biomech.*, Vol. 3, pp.211–221, 1970.

181. A. GAŁKA, J.J. TELEGA, and R. WOJNAR, Macroscopic elastic properties of cartilage, *Acta Bioeng. Biomech.*, Vol. 2, Supplement 1, pp.187–192, 2000.

182. J.J. GARCIA, N.J. ALTIERO, and R.C. HAUT, Estimation of in situ elastic properties of biphasic cartilage based on a transversely isotropic hypo-elastic model, *J. Biomech. Eng.*, Vol. 122, pp.1–8, 2000.

183. M. GARON, A. LÉGARÉ, R. GUARDO, P. SAVARD, and M.D. BUSCHMANN, Streaming potentials map are spatially resolved indicators of amplitude, frequency and ionic strength dependent responses of articular cartilage to load, *J. Biomech.*, Vol. 35, pp.207–216, 2002.

184. K. GARIKIPATI, E.M. ARRUDA, K. GROSH, H. NRAYAN, and S. CALVE, A continuum treatment of growth in biological tissue: the coupling of mass transport and mechanics, *J. Mech. Phys. Sol.*, Vol. 52, pp.1595–1625, 2004.

185. G.R. Gaudette, I.B. Krukenkamp, E.U. Azeloglu, A.E. Saltman, M. Lense, J. Todaro, and F.-P. Chiang, Effects of ischemia on epicardial deformation in the passive rabbit heart, *J. Biomech. Eng*, Vol. 126, pp.70–75, 2004.

186. A. Gefen and S.S. Margulies, Are in vivo and in situ brain tissues mechanically similar?, *J. Biomech.*, Vol. 37, pp.1339–1352, 2004.

187. J.P.V. Geest, E.S. Di Martino, and D.A. Vorp, An analysis of the complete strain field within Flexercell™ membranes, *J. Biomech.*, Vol. 37, pp.1923–1928, 2004.

188. T.A. Gennarelli, L.E. Thibault, G. Tomei, D. Graham, and J. Adams, Directional dependence of axonal brain injury due to centroidal and non-centroidal acceleration, SAE paper 872197, [in:] Proc. 31th Stapp Car Crash Conf., Society of Automotive Engineers, pp.49–53, 1987.

189. F. Ghalichi, X. Deng, A. De Champlain, Y. Douville, M. King, and R. Guidoin, Low Reynolds number turbulence modeling of blood flow in arterial stenoses, *Biorheology.*, Vol. 35, pp.281–294, 1998.

190. R. Glaser, *Biophysics*, Springer, Berlin 2001.

191. L. Glass, P. Hunter, and A. McCulloch [eds.] *Theory of heart*, Springer-Verlag, New York 1991.

192. R.L. Gleason, L.A. Taber, and J.D. Humphrey, A 2-D model of flow-induced alterations in the geometry, structure, and properties of carotid arteries, *J. Biomech. Eng.*, Vol. 126, pp.371–381, 2004.

193. T.A. Godwin, Structure and function of the lung, http://edcenter.med.cornell.edu/CUMC_PathNotes/Respiratory/Respiratory.html

194. M.B. Gorbet, M.V. Sefton, Biomaterial-associated thrombosis: roles of coagulation factors, complement platelets and leukocytes, *Biomaterials*, Vol. 25, pp.5681–5703, 2004.

195. C.W. Gottschalk, Osmotic concentration and dilution of the urine, *Am. J. Med.*, Vol. 36, pp.670–685, 1964.

196. R.M. Gowda, I.A. Khan, B.C. Vasavada, T.J. Sacchi, and R. Patel, History of the evolution of echocardiography, *Int. J. Cardiology*, Vol. 97, pp.1–6, 2004.

197. C. Grandmont, Existence for a three-dimensional steady state fluid-structure interaction problem, *J. Math. Fluid. Mech.*, Vol. 4, pp.76–94, 2002.

198. A.S. Green, Modelling of peak-flow wall shear stress in major airways of the lung, *J. Biomech.*, Vol. 37, pp.661–667, 2004.

199. A.E. Green and J.E. Adkins, *Large Elastic Deformations*, Clarendon Press, Oxford 1970.

200. H. Gregersen, T.C. Lee, S. Chien, R. Skalak, and Y.C. Fung, Strain distribution in the layered wall of the esophagus, *J. Biomech. Eng.*, Vol. 121, pp.442–448, 1999.

201. Q. Grimal, A. Watzky, and S. Naili, A one-dimensional model for the propagation of transient pressure waves through the lung, *J. Biomech.*, Vol. 35, pp.1081–1089, 2002.

202. S.R. DE GROOT and P. MAZUR, *Non-equilibrium Thermodynamics*, Dover, New York, 1984.

203. W.Y. GU, W.M. LAI, and V.C. MOW, A mixture theory for charged-hydrated soft tissues containing multi-electrolytes: passive transport and swelling behaviours, *J. Biomech. Eng.*, Vol. 120, pp.169–180, 1998.

204. W.Y. GU, X.G. MAO, B.A. RAWLINS, J.C. IATRIDIS, R.J. FOSTER, D.N. SUN, M. WEIDENBAUM, and V.C. MOW, Streaming potential of human lumbar anulus fibrosus is anisotropic and affected by disc degeneration, *J. Biomech.*, Vol. 32, pp.1177–1182, 1999.

205. W.Y. GU and M.A. JUSTIZ, Apparatus for measuring the swelling dependent electrical conductivity of charged hydrated soft tissues, *J. Biomech. Eng.*, Vol. 124, pp.790–79, 2002.

206. J.M. GUCCIONE, L.K. WALDMAN, AND A.D. MCCULLOCH, Mechanics of the active cotnraction in cardiac muscle: Part II. Cylindrical models of the systolic left ventricle, *J. Biomech. Eng.*, Vol. 115, pp.82–89, 1993.

207. F. GUILAK, The deformation behavior and viscoelastic properties of chondrocytes in articular cartilage, *Biorheology*, Vol. 37, pp.27–44, 2000.

208. F. GUILAK, R. SAH, and L.A. SETTON, Physical regulation of cartilage metabolism, [in:] *Basic Orthopeadic Biomechanics*, V.C. Mow and W.C. Hayes [eds.], pp.179–207, Lippincott-Raven Publishers, Philadelphia 1997.

209. F. GUILAK, M. SATO, C.M. STANFORD, and R.A. BRANDT [Eds.], Cell Mechanics, *J. Biomechanics*, Special Issue, vol. 33, No.1, pp.1–135, 2000.

210. A. GUILLAUME, D. OSMONT, D. GAFFIE, J.C. SARRON, and P. QUANDIEU, Effect of perfusion on the mechanical gehavior of the brain exposed to hypergravity, *J. Biomech.*, vol. 30, pp.383–389, 1997.

211. C.M. GUPTE, A. SMITH, N. JAMIESON, A.M.J. BULL, R. DEW. THOMAS, and A.A. AMIS, Meniscofemoral ligaments – structural and material properties, *J. Biomech.*, Vol. 35, pp.1623–1629, 2002.

212. A.C. GUYTON, *Anatomy and physiology*, Saunders College Publishing, New York 1985.

213. K.M. HABERSTROH, M. KAEFER, N. DePAOLA, S.A. FROMMER, and R. BIZIOS, A novel in-vitro system for the simultaneous exposure of bladder smooth muscle cells to mechanical strain and sustained hydrostatic pressure, *J. Biomech. Eng.*, Vol. 124, pp.208–213, 2002.

214. S.-K. HAN, S. FEDERICO, M. EPSTEIN, and W. HERZOG, An articular cartilage contact model based on real surface geometry, *J. Biomech.*, Vol. 38, pp.179–184, 2005.

215. J.C. HANSEN, R. SKALAK, S. CHIEN, and A. HOGER, Spectrin properties and the elasticity of the red blood cell membrane skeleton, *Biorheology*, Vol. 34, pp.327–348, 1997.

216. K.A. HANSON, J.A. WEISS, and J.K. BARTON, Recruitment of tendon crimp with applied tensile strain, *J. Biomech. Eng.*, Vol. 124, pp.72–77, 2002.

217. B. D. HAMES, N. M. HOOPER, and J. D. HOUGHTON, *Instant notes in biochemistry*, BIOS Scientific Publishers, Polish edition: Wydawnictwo Naukowe PWN, Warszawa 1999.

218. J.L. HARRIS, P.B. WELLS, and J.D. HUMPHREY, Altered mechanical behavior of epicardium due to isothermal heating under biaxial isotonic loads, *J. Biomech. Eng.*, Vol. 125, pp.381–388, 2003.

219. H.W. HASLACH JR., Nonlinear viscoelastic, thermodynamically consistent models for biological soft tissues, *Biomech. Modelling Mechanobiology*, Vol. 3, 2004.

220. H.W. HASLACH and J.D. HUMPHREY, Dynamics of biological soft tissues and rubber: internally pressurized spherical membranes surrounded by a fluid, *Int. J. Non-Linear Mech.*, Vol. 39, pp.339–420, 2004.

221. K. HAYASHI and H. ISHIKAWA, [Eds.], Computational Biomechanics, Springer-Verlag, Tokyo 1996.

222. M. HEIL, Airway closure: occluding liquid bridges in strongly buckled elastic tubes, *J. Biomech. Eng.*, Vol. 121, pp.487–493, 1999.

223. M. HEIL and O.E. JENSEN, Flows in deformable tubes and channels, [in:] *Flow in Collapsible Tubes and Past Other Highly Compliant Boundaries* [ed.] T.J. Pedley and P.W. Carpenter, pp.15–50, Kluwer, Dordrecht 2003.

224. A.D. HEINER and J.A. MARTIN, Cartilage responses to a novel triaxial mechanosimulatory culture system, *J. Biomech.*, Vol. 37, pp.689–695, 2004.

225. J. HENLE, *Handbuch der systematische Anatomie des Menschen*, Friedrich Vieweg und Sohn Braunschweig.

226. K.J. HENLE and L.A. DETHLEFSEN, Time-temperature relationships for heat-induced killing of mammalian cells, *Annals New York Acad. Sci.*, Vol. 335, pp.234–253, 1980.

227. F.C. HENRIQUEZ and A.R. MORITZ, Studies of thermal injury, I. The conduction of heat to and through skin and the temperature attained therein: A theoretical and experimental investigation, *Am. J. Pathology*, Vol. 23, pp.531–549, 1947.

228. F.C. HENRIQUEZ JR, Studies of thermal injury: V. The predictability and the significance of thermally induced rate processes leading to irreversible epidermal injury, *Arch. Pathology*, Vol. 43, pp.489–502, 1947.

229. D.G. HEPWORTH, A. STEVEN-FOUNTAIN, D.M. BRUCE, and J.F.V. VINCENT, Affine versus non-affine deformation in soft biological tissues, measured by the reorientation and stretching of collagen fibres through the thickness of compressed porcine skin, *J. Biomech.*, Vol. 34, pp.341–346, 2001.

230. L.A. HERBERT, W.C. CHEN, A. HARTMANN, J.C. GARANCIS, Mechanical properties of the dog renal capsule, *J. Appl. Physiology*, Vol. 40, pp.164–170, 1976.

231. J.A. HERNÁNDEZ, Stability properties of elementary dynamic models of membrane transport, *Bull. Math. Biol.*, Vol. 65, pp.175–197, 2003.

232. W. HERZOG [ed.] *Skeletal muscle mechanics: from mechanisms to function*, John Wiley&Sons, Chichester 2000.

233. R. HILFER, Review on scale dependent characterization of the microstructure of porous media, *Transport in Porous Media*, Vol. 46, pp.373–390, 2002.

234. R. Hill, On constitutive macro-variables for heterogeneous solids at finite strains, *Proc. R. Soc. A*, Vol. 326, pp.131–147, 1971.

235. A. Hoger, On the residual stress possible in an elastic body with material symmetry, *Arch. Rat. Mech. Anal.*, Vol. 88, pp.271–289, 1985.

236. A. Hoger, T.J. van Dyke, and V.A. Lubarda, Symmetrization of the growth deformation and velocity gradients in residually stressed biomaterials, *Z. Angew. Math. Physik*, Vol. 55, pp.848–860, 2004.

237. G.A. Holzapfel and R.W. Ogden [eds.], *Biomechanics of Soft Tissue*, CISM Courses and Lectures, Springer-Verlag, Wien-New York 2003.

238. G.A. Holzapfel and T.C. Gasser, A viscoelastic model for fiber-reinforced composites at finite strains: continuum basis, computational aspects and applications, *Comp. Meth. Appl. Mech. Eng.*, Vol. 190, pp.4379–4403, 2001.

239. G.A. Holzapfel, T.C. Gasser, and R.W. Ogden, A new constitutive framework for arterial wall mechanics and a comparative study of material models, *J. Elasticity*, Vol. 61, pp.1–48, 2000.

240. G.A. Holzapfel, T.C. Gasser, and R.W. Ogden, Comparison of a multi-layer structural model for arterial walls with a fung-type model, and issues of material stability, *J. Biomech. Eng*, Vol. 126, pp.264–274, 2004.

241. C.O. Horgan and G. Saccomandi, Constitutive modelling of rubber-like and biological materials with limiting chain extensibility, *Math. Mech. Solids*, Vol. 7, pp.353–371, 2002.

242. C.O. Horgan and G. Saccomandi, Finite thermoelasticity with limiting chain extensibility, *J. Mech. Phys. Solids*, Vol. 51, pp.1127–1146, 2003.

243. W.H. Horl, K.M. Koch, R.M. Lindsay, C. Ronco, and J.F. Winchester [Eds.], Replacement of Renal Function by Dialysis, Kluwer, Dordrecht 2004.

244. J.A. Howell, V. Sanchez and R.W. Field [Eds.], Membranes in Bioprocessinf: Theory and Applications, Blackie Academic & Professional, London 1993.

245. C.C.W. Hsia, C.J.C. Chuong, R.L. Johnson Jr., Critique of conceptual basis of diffusing capacity estimates: a finite element analysis, *J. Appl. Physiol.*, Vol. 79, pp.1039–1047, 1995.

246. L. Hu, A. Gupta, J.P. Gore, and L.X. Xu, Effect of forced convection on the skin thermal expression of breast cancer, *J. Biomech. Eng.*, Vol. 126, pp.204–211, 2004.

247. H.W. Huang, C.L. Chan, and R.B. Roemer, Analytical solution of Pennes bioheat transfer equation with a blood vessel, *J. Biomech. Eng.*, Vol. 116, pp.208–212, 1994.

248. K. Huang, Y. Zeng, H. Xia, and C. Liu, Alterations in the biorheological features of some soft tissues after limb lenghtening, *Biorheology*, Vol. 35, pp.355–363, 1998.

249. D.J.S. Hulmes and A. Miller, Quasi-hexagonal molecular packing in collagen fibrils, *Nature*, Vol. 282, pp.878–880, 1979.

250. J.D. Humphrey, Arterial wall mechanics: review and directions, *Crit. Rev. Biomed. Eng.*, Vol. 23), pp.1–162, 1995.

251. J.D. HUMPHREY, Computer methods in membrane biomechanics, *Computer Meth. Biomech. Biomed. Eng.*, Vol. 1, pp.171–210, 1998.

252. J.D. HUMPHREY, An evaluation of pseudoelastic descriptors used in arterial mechanics, *J. Biomech. Eng.*, Vol. 121, pp.259–262, 1999.

253. J.D. HUMPHREY, Remodelling of a collagenous tissue at fixed lengths, *J. Biomech. Eng.*, Vol. 121, pp.591–597, 1999.

254. J.D. HUMPHREY, On mechanical modeling of dynamic changes in the structure and properties of adherent cells, *Math. Mech. Solids*, Vol. 7, pp.521–539, 2002.

255. J.D. HUMPHREY, *Cardiovascular Solid Mechanics: Cells, Tissues and Organs*, Springer Verlag, New–York 2002.

256. J.D. HUMPHREY, Continuum thermomechanics and the clinical treatment of disease and injury, *Appl. Mech. Rev.*, Vol. 56(2), pp.231–260, 2003.

257. J.D. HUMPHREY, Continuum biomechanics of soft biological tissues, *Proc. R. Soc. London. A*, Vol. 459, pp.3–46, 2003.

258. J.D. HUMPHREY and P. B. CANHAM, Structure, mechanical properties and mechanics of intracranial saccular aneurysmus, *J. Elasticity*, Vol. 61, pp.49–81, 2000.

259. J.D. HUMPHREY AND K.R. RAJAGOPAL, A constrained mixture model for arterial adaptations to a sustained step change in blood flow, *Biomech. Model. Mechanobiol.*, Vol. 2, pp.109–126, 2003.

260. J.D. HUMPHREY and E. WILSON, A potential role of smooth muscle tone in early hypertension: a theoretical study, *J. Biomech.*, Vol. 36, pp.1593–1601, 2003.

261. P.J. HUNTER, M.P. NASH, and G.B. SANDS, Computational electromechanics of the heart, [in:] *Computational Biology of the Heart*, A.V. Panfilor and A.V. Holden [eds.], pp.345–407, John Wiley, London 1997.

262. C. HURSCHLER, B. LOITZ-RAMAGE, and R. VANDERBY, A structurally based stress-stretch relationship for tendon and ligament, *J. Biomech. Eng.*, Vol. 119, pp.392–399, 1997.

263. C. HURSCHLER, P.P. PROVENZANO, and R. VANDERBY, Application of a probabilistic model to determine reference length and toe-to-linear region transition in fibrous connective tissue, *J. Biomech. Eng.*, Vol. 125, pp.415–422, 2003.

264. A.F. HUXLEY, Cross-bridge action: present views, prospects, and unknowns, In: W. Herzog [ed.], *Skeletal Muscle Mechanics* pages 7–31, John Wiley&Sons, Chichester 2000

265. J.M. HUYGHE, Intra-extrafibrillar mixture formulation of soft charged hydrated tissues, *J. Theor. Appl. Mech.* pp.519–536, 1999.

266. J.M. HUYGHE and P.H.M. BOVENDEERD, Biological mixtures, [in:] Modelling Coupled Phenomena in Saturated Porous Media, ed. by J. Kubik, M. Kaczmarek, I. Murdoch, AMAS Lecture Notes, Vol. 20, Bydgoszcz 2003, pp.227–276.

267. J.M. HUYGHE and J.D. JANSSEN, Quadriphasic mechanics of swelling incompressible porous media, *Int. J. Eng. Sci.* Vol. 35, pp.793–802, 1997.

268. J.C. IATRIDIS and I. AP GWYNN, Mechanisms for mechanical damage in the intervertebral disc annulus fibrosus, *J. Biomech.*, Vol. 37, pp.1165–1175, 2004.

269. RAKESH K. JAIN, Temperature distributions in normal and neoplastic tissues during normothermia and hyperthermia, *Annals New York Acad. Sci.*, Vol. 335, pp.98–106, 1980.

270. R.L. JAMISON, Urinary concentration mechanism, In H.E. Layton and A.M. Weinstein [eds.], *Membrane transport and Renal Physiology*, pages 177–192, Springer, New York 2002.

271. J.A. JANSEN [Ed.], Special Issue: Animal Models for Tissue Engineering Applications, *Biomaterials*, Vol. 25(9), pp.1461–1734, 2004.

272. S. JEMIOŁO and A. SZWED, Implementation of subroutine UHYPER of ABAQUS finite element program for hyperelastic Blatz-Ko material, In: W. Szcześniak [ed.], *Theoretical Foundations of Civil Engineering* pages 251–262, ZG OW PW, Warsaw 1999.

273. S. JEMIOŁO and J.J. TELEGA, Representations of tensor functions and applications in continuum mechanics, *IFTR Reports*, Vol. 3 1997.

274. S. JEMIOŁO and J.J. TELEGA, Fabric tensor and constitutive equations for a class of plastic and locking orthotropic materials, *Arch. Mech.*, Vol. 49, pp.1041–1067, 1997.

275. S. JEMIOŁO and J.J. TELEGA, Fabric tensor in bone mechanics, *Eng. Trans.*, Vol. 46, pp.3–26, 1998.

276. S. JEMIOŁO and J.J. TELEGA, Modelling elastic behaviour of soft tissues. Part I. Isotropy, *Eng. Trans.*, Vol. 49(2–3), pp.213–240, 2001.

277. S. JEMIOŁO and J.J. TELEGA, Modelling elastic behaviour of soft tissues. Part II. Transverse isotropy, *Eng. Trans.*, Vol. 49(2–3), pp.241–281, 2001.

278. S. JEMIOŁO and J.J. TELEGA, A pseudo-hyperelastic model of soft tissues, *Acta Bioeng. Biomech.*, Vol. 3(Supp. 1), pp.208–216, 2001.

279. S. JEMIOŁO and J.J. TELEGA, Transversely isotropic materials undergoing large deformations and applications to modelling of soft tissues, *Mech. Res. Commun.*, Vol. 29, pp.397–404, 2001.

280. S. JEMIOŁO and J.J. TELEGA, Fabric tensors in bone mechanics: elastic constitutive relationships and strength criteria, [in:] *Orthopaedic Biomechanics*, AMAS Workshop OBM'02, J.J. Telega [ed.], Institute of Fundamental Technological Research, Warsaw 2003.

281. S. JEMIOŁO and J.J. TELEGA, Pseudo-hyperelastic response of orthotropic soft tissues, *Acta Bioeng. Biomech.*, Vol. 5(Supp. 1), pp.206–213, 2003.

282. S. JEMIOŁO, J.J. TELEGA, and C. MICHALAK, Pseudo-hyperelastic model of soft tissues: two-dimensional case, *Acta Bioeng. Biomech.*, Vol. 4, Supplement, pp.270–271, 2002.

283. S. JEMIOŁO, J.J. TELEGA, and C. MICHALAK, Pseudo-hyperelastic anisotropic model of soft tissues: two-dimensional case, *Acta Bioeng. Biomech.*, Vol. 4, Supplement 1, pp.470–471, 2002.

284. T.R. JENKYN, R.L. LEHMAN, and K.-N. AN, Noninvasive muscle tension measurement using the novel technique of magnetic resonance elastography (MRE), *J. Biomech.*, Vol. 36, pp.1917–1921, 2003.

285. J.A. Jensen, *Estimation of blood velocities using ultrasound: a signal processing approach*, Cambridge University Press, Cambridge 1996.

286. L.M. Jiji, S. Weinbaum, and D.E. Lemons, Theory and experiment for the effect of vascular microstructure on surface tissue heat transfer - Part II : Model formulation and solution, *J. Biomech. Eng.*, Vol. 106, pp.331–341, 1984.

287. V.V. Jikov, S.M. Kozlov, and O.A. Oleinik, Homogenization of Differential Operators and Integral Functionals, Springer-Verlag, Berlin 1994.

288. B.M. Johnston, P.R. Johnston, S. Corney, and D. Kilpatrick, Non-Newtonian blood flow in human right coronary arteries: ateady state simulations, *J. Biomech.*, Vol. 37, pp.709–720, 2004.

289. D. S. Jones and B. D. Sleeman [eds.], *Differential equations and mathematical biology*, Chapman & Hall/CRC, Boca Raton-London-Washington 2003.

290. P. Jørgensen, C. Schäfer, P.G. Guerra, M. Talajic, S. Nattel, and L. Glass, A mathematical model of human atrioventricular nodal function incorporating concealed conduction, *Bull. Math. Biol.*, Vol. 64, pp.1083–1099, 2002.

291. F. Jouve, Modélisation de lœil en élasticité non linéaire, *Recherche en Mathématiques Appliquées*, 26, Masson, Paris 1993.

292. J.-H. Jun, J.L. Harris, J.D. Humphrey, and S. Rastegar, Effect of thermal damage and biaxial loading on the optical properties of a collageneous tisue, *J. Biomech. Eng.*, Vol. 125, pp.540–548, 2003.

293. Y. Kagawa, Y. Tsuchiya, Stochasticity of the step sizein the force generating process due to a single myosin molecule, *Bull. Math. Biol.*, Vol. 64, pp.407–419, 2002.

294. W. Kaminski, Hyperbolic heat conduction equation for materials with a nonhomogeneous inner structure, *J. Heat Transfer*, Vol. 112, pp.555–560, 1990.

295. A. Kargol, A mechanical model of transport processes in porous membranes generaetd by osmotic and hydrostatic pressure, *J. Membrane Sci.*, Vol. 191, pp.61–69, 2001.

296. E. Kasikcioglu, H. Oflaz, H. Akhan, A. Kayserilioglu, F. Mercanoglu, B. Umman, and Z. Bugra, Left ventricular remodelling and aortic distensibility in elite power athletes, *Heart Vessels*, Vol. 19, pp.183–188, 2004.

297. S. Katzir, The discovery of the piezoelectric effect, *Arch. History Exact Sci.*, Vol. 57, pp.61–91, 2003.

298. M. Kaya, W. Carvalho, T. Leonard, and W. Herzog, Estimation of cat medial gastrocnemius fascicle lengths during dynamic contractions, *J. Biomech.*, Vol. 35, pp.893–902, 2002.

299. O. Kedem and A. Katchalsky, Thermodynamic analysis of the permeability of biological membranes to non-electrocytes, *Biochem. Biophys. Acta*, Vol. 27, pp.229–246, 1958.

300. B.-S. Kim and D.J. Mooney, Scaffolds for engineering smooth muscle under cyclic mechanical strain conditions, *J. Biomech. Eng.*, Vol. 122, pp.210–215, 2000.

301. I.A. Khan, C.K. Nair, N. Singh, R.M. Gowda, and R.C Nair, Acute ventricular rate control in atrial fibrillation and atrial flutter, *Int. J. Cardiology*, Vol. 97, pp.7–13, 2004.

302. A. Kirpalani, H. Park, J. Butany, K.W. Johnston, and M. Ojha, Velocity and wall shear stress pattern in human right coronary artery, *J. Biomech. Eng.*, Vol. 121, pp.370–375, 1999.

303. B. Kirn and V. Starc, The vide technique developed for measuring epicardial strains on guinea pig's left ventricle, *J. Biomech.*, Vol. 38, pp.169–173, 2005.

304. S.M. Klisch, A mixture of elastic materials with different constituent temperatures and internal constraints compression, *Int. J. Eng. Sci.*, Vol. 40, pp.805–828, 2002.

305. S.M. Klisch and J.C. Lotz, A special theory of biphasic mixtures and experimantal results for human annulus fibrosus tested in confined compression, *J. Biomech. Eng.*, Vol. 122, pp.180–188, 2000.

306. K. Komatsu, T. Shibata, A. Shimada, A. Viidik, and M. Chiba, Age-related and regional differences in the stress-strain and stress-relaxation behaviours of the rat incisor periodontal ligament, *J. Biomech.*, Vol. 37, pp.1097–1106, 2004.

307. S. Konturek, *Human Physiology, Vol.II: Cardiovascular System*, Wydawnictwo Uniwersytetu Jagiellońskiego, Kraków 2000, in Polish.

308. B.E. Koop and J.L. Lewis, A model of fracture testing of soft viscoelastic tissues, *J. Biomech.*, Vol. 35, pp.605–608, 2003.

309. R.K. Korhonen, M.S. Laasanen, J. Töyräs, R. Lappalainen, H.J. Helminen, and J.S. Jurvelin, Fibril reinforced poroelastic model predicts specifically mechanical behavior of normal, proteoglycan depleted and collagen degraded articular cartilage, *J. Biomech.*, Vol. 36, pp.1373–1379, 2003.

310. R.K. Korhonen, M.S. Laasanen, J. Töyräs, J. Rieppo, J. Hirvonen, H.J. Helminen, and J.S. Jurvelin, Comparison of the equilibrium response of articular cartilage in unconfined compression, confined compression and indentation, *J. Biomech.*, Vol. 35, pp.903–909, 2002.

311. S. Kostin, S. Dammer, S. Hein, W.P. Klovekorn, E.P. Bauer, and J. Schapper, Connexin 43 expression and dsitribution in compensated and decompensated hypertrophy in patients with aortic stenosis, *Cardiovascular Res.*, Vol. 62, pp.426–436, 2004.

312. V. Koulich, J.L. Lage, C.C.W. Hsia, and R.L. Johnson Jr., A porous medium model of alveolar gas diffusion, *J. Porous Media*, Vol. 2, pp.263–275, 1999.

313. P. Kowalczyk and M. Kleiber, Modelling and numerical analysis of stresses and strains in the human lung including tissue-gas interaction, *Eur. J. Mech., A/Solids*, Vol.13, pp.367–393, 1994.

314. E.J. Kucharz, *The Collagens: Biochemistry and Pathophysiology*, Springer-Verlag, Berlin 1993.

315. E. Kuhl and P. Steinmann, Computational modelling of healing: an application of the material force method, *Biomech. Model. Mechanobiology*, Vol. 2, pp.187–203, 2004.

316. V. Kulish, J.L. Lage, C.C.W. Hsia, and R.L. Johnson Jr., Three dimentsional, unsteady simulation of alveolar respiration, *J. Biomech. Eng.*, Vol. 124, pp.609–616, 1999.

317. S. Kumaresan and S. Radhakrishnan, Importance of the partitioning membranes of the brain and the influence of the neck in head injury modeling, *Medical Biolog. Eng. Comput.*, Vol. 34, pp.27–32, 1996.

318. M.K. Kwan, and S.L.-Y. Woo, A structural model to describe the nonlinear stress-strani behavior for parallel-fibered collageneous tissues, *J. Biomech. Eng.*, Vol. 111, pp.361–363, 1989.

319. S.K. Kyriacou, A. Mohamed, K. Miller, and S. Neff, Brain mechanics for neurosurgery: modelling issues, *Biomechan. Model. Mechanobiol.*, Vol. 1, pp.151–164, 2002.

320. C.A. Lachenbruch and K.R. Diller, A network thermodynamic model of kidney perfusion with a cryoprotective agent, *J. Biomech. Eng.*, Vol. 121, pp.574–583, 1999.

321. P. Lacolley, Mechanical influence of cyclic stretch on vascular endothelial cells, *Cardiovascular Res.*, Vol. 63, pp.577–579, 2004.

322. A. Lagzdiņš, V. Tamužs, G. Teters, and V. Krēgers, Orientational Averaging in Mechanics of Solids, *Pitman Research Notes in Mathematics Series*, Vol. 265, Longman Scientific & Technical Longman House, Burnt Mill, Harlow Essex; John Wiley&Sons, New York 1992.

323. W.M. Lai, V.C. Mow, D.D. Sun, and G.A. Ateshian, On the electric potentials inside a charged soft hydrated biological tissue: streaming potential versus diffusion potential, *J. Biomech. Eng.*, Vol. 122, pp.336–346, 2000.

324. R.S. Lakes and R. Vanderby, Interrelation of creep and relaxation: a modeling approach for ligaments, *J. Biomech. Eng.*, Vol. 121, pp.612–615, 1999.

325. W.D. Lakin, S.A. Stevens, B.C. Trammer, and P.L. Penar, A whole-body mathematical model for intracranial pressure dynamics, *J. Math. Biology*, Vol. 46, pp.347–383, 2003.

326. Y. Lanir, Constitutive equations for the lung tissue, *J. Biomech. Eng.*, Vol. 105, pp.374–380, 1983.

327. Y. Lanir, Constitutive equations for fibrous connective tissue, *J. Biomech.*, Vol. 16, pp.1–12, 1983.

328. Y. Lanir, Plausibility of structural constitutive equations for isotropic soft tissues in finite static deformations, *J. Appl. Mech.*, Vol. 61, pp.695–702, 1994.

329. Y. Lanir, Plausibility of structural constitutive equations for swelling tissues – implications of the C-N and S-E conditions, *J. Biomech. Eng.*, Vol. 118, pp.10–16, 1996.

330. M. Lappa, A CFD level-set method for soft tissue growth: theory and fundamental equations, *J. Biomech.*, Vol. 38, pp.185–190, 2005.

331. V.K. Lau and D.C. Viano, Influence of impact velocity on the severity of nonpenetrating hepatic injury, *J. Trauma*, Vol. 21, pp.115–123, 1981.

332. M. Lavagnino, S.P. Arnoczky, K. Frank, T. Tian, Collagen fibril diamtere distribution does not reflect changes in the mechanical properties of in vitro stress-deprived tendons, *J. Biomech.*, Vol. 38, pp.69–75, 2005.

333. M.M. Lavail, J.G. Hollyfield, R.E. Anderson [eds.], *Retinal Degenerations*, Kluwer, New York 2003.

334. D.A. Lavan, R.F. Padera, T.A. Friedman, J.P. Sullivan, R. Langer, and D.S. Kohane, In vivo evaluation of tetrahedral amorphous carbon, *Biomaterials*, Vol. 26, pp.465–473, 2005.

335. H.E. Layton and A. M. Weinstein [eds.], *Membrane transport and renal physiology*, Springer-Verlag, New York 2002.

336. B.E. Layton, A.M. Sastry, H. Wang, K.A. Sullivan, E.L. Feldman, T.E. Komorowski, and M.A. Philbert, Differences between collagen morphologies, properties and distribution in diabetic and normal biobreeding and Sprague-Dewley rat sciatic nerves, *J. Biomech*, Vol. 37, pp.879–888, 2004.

337. A.A. Lee, D.A. Graham, S.D. Cruz, A. Ratcliffe, and W.J. Karlon, Fluid shear stress-induced alignment of cultured vascular smooth muscle cells, *J. Biomech. Eng.*, Vol. 124, pp.37–43, 2002.

338. H.-D. Lee, W. Herzog, and T. Leonard, Effects of cyclic changes in muscle length on force production in in-situ cat solens, *J. Biomech.*, Vol. 34, pp.979–987, 2001.

339. T.C. Lee, R.J. Midura, V.C. Hascall, and I. Vesely, The effect of elastin damage on the mechanics of the aortic valve, *J. Biomech.*, Vol. 34, pp.203–210, 2001.

340. J.B. Lee and K.H. Yang, Development of finite element model of the human abdomen, *Stapp Car Crash J.*, Vol. 45, pp.79–100, 2001.

341. S. Lehoux and A. Tedgui, Cellular mechanics and gene expression in blood vessels, *J. Biomech.*, Vol. 36, pp.631–643, 2003.

342. N.D. Leipzig and K.A. Athanasiou, Unconfined creep compression of chondrocytes, *J. Biomech.*, Vol. 38, pp.77–85, 2005.

343. J. D. Lemmon and A. P. Joganathan, Three–dimensional computational model of left heart diastolic function with fluid–structure interaction, *J. Biomech. Eng.*, Vol. 122, pp.109–117, 2000.

344. M.A. Leroux and L.A. Setton, Experimental and biphasic fem determinations of the material properties and hydraulic permeability of the meniscus in tension, *J. Biomech. Eng.*, Vol. 124, pp.315–332, 2002.

345. T. Lewiński and J.J. Telega, Plates, Laminates and Shells: Asymptotic Analysis and Homogenization, *Series on Advances in Mathematics for Applied Sciences*, vol.52, World Scientific, Singapore 2000.

346. L.P. Li and W. Herzog, Strain-rate dependence of cartilage stiffness in unconfined compression: the role of fibril reinforcement versus tissue volume change in fluid pressurization, *J. Biomech.*, Vol. 37, pp.375–382, 2004.

347. L.Y. Li, B.J. Tighe, and J.W. Ruberti, Mathematical modelling of corneal swelling, *Biomech. Model. Mechanobiol.*, Vol. 3, pp.114–123, 2004.

348. J. Li, X.Y. Luo, and Z.B. Kuang, A nonlinear anisotropic model for porcine aortic heart valves, *J. Biomech.*, Vol. 34, pp.1279–1289, 2001.

349. Z. Liao, C.K. Poh, P.A. Hardy, W.R. Clark, and D. Gao, A numerical and experimental study of mass transfer in the artificial kidney, *J. Biomech. Eng.*, Vol. 125, pp.472–480, 2003.

350. B. Lim, P.J. Bascom, and R.S.C. Cobbold, Simulation of red blood cell aggregation in shear flow, *Biorheology*, Vol. 34, pp.423–441, 1997.

351. D.C. Lin and T.R. Nichols, Parameter estimation in a crossbridge muscle model, *J. Biomech. Eng.*, Vol. 125, pp.132–140, 2003.

352. T.W. Lin, L. Cardenas, and L.J. Soslovsky, Biomechanics of tendon injury and repair, *J. Biomech.*, Vol. 37, pp.865–877, 2004.

353. R. Lipton and B. Vernescu, Composites with imperfect interface, *Proc. Royal Soc. London*, Vol. A452, pp.329–358, 1996.

354. I.-S. Liu, On Euclidean objectivity and the principle of material frame-indifference, *Continuum Mech. Thermodyn.*, Vol. 16, pp.177–183, 2004.

355. J. Liu, Preliminary survey on the mechanisms of the wave-like behaviors of heat transfer in living tissues, *Forch. Ing.*, Vol. 66, pp.1–10, 2000.

356. J. Liu, Uncertainty analysis for temperature prediction of biological bodies subject to randomly spatial heating, *J. Biomech.*, Vol. 34, pp.1637–1642, 2001.

357. S.Q. Liu, Influence of tensile strain on smooth muscle cell orientationin rat blood vessels, *J. Biomech. Eng.* Vol. 128, pp.313–320, 1998.

358. E.G. Loboa, T.A.L. Wren, G.S. Beaupré, and D.R. Carter, Mechanobiology of soft skeletal tissue differentiation – a computational approach of a fiber reinforced poroelastic model based on homogeneous and isotropic simplifications, *Biomech. Model. Mechanobiol.*, Vol. 2, pp.83–96, 2003.

359. X. Lu and H. Gregersen, Regional distribution of axial strain and circumferential residual strain in the layered rabbit oesophagus, *J. Biomech.*, Vol. 34, pp.225–233, 2001.

360. X.Y. Luo, W.G. Li, and J. Li, Geometrical stress-reducing factors in the anisotropic porcine heart valves, *J. Biomech. Eng.*, Vol. 125, pp.735–744, 2003.

361. H.A. Lynch, W. Johannessen, J.P. Wu, A. Jawa, and D.M. Elliott, Effect of fiber orientation and strain rate on the nonlinear uniaxial tensile material properties of tendon, *J. Biomech. Eng.*, Vol. 125, pp.726–731, 2003.

362. H. Maas, P.A. Huijing, C.A. Yucesoy, B.H.F.J.M. Koopman, and H.J. Grootenboer, The relative position of EDL muscle affects the length of sarcomeres within muscle fibers: experimental results and finite-element modeling, *J. Biomech. Eng.*, Vol. 125, pp.745–753, 2003.

363. C.N. Maganaris, Tensile property of in vivo human tendinous tissue, *J. Biomech.*, Vol. 35, pp.1019–1027, 2002.

364. C.N. Maganaris and J.P. Paul, Tensile properties of the in vivo human gastrocnemius tendon, *J. Biomech.*, Vol. 35, pp.1639–1646, 2002.

365. C.N. Maganaris, Validity of procedures involved in ultrasound-based measurement of human plantarflexor tendon elongation on contraction, *J. Biomech.*, Vol. 38, pp.9–13, 2005.

366. M.J. Mahoney, R.R. Chen, J. Tan, and W.M. Saltzman, The influence of microchannels on neurite growth and architecture, *Biomaterials*, Vol. 26, pp.771–778, 2005.

367. E. Majchrzak and M. Jasiński, Sensitivity study of burn predictions to variations in thermophysical parameters of skin, pp.273–280, [in:] *Advances in Boundary Element Techniques II*, M. Denda, M.H. Aliabadi and A. Charafi [eds.], Hoggar, Geneve 2001.

368. E. Majchrzak and M. Jasiński, Sensitivity analysis of bioheat transfer in 2D tissue domain subjected to an external heat source, *Acta Bioengng. Biomech.*, Vol. 3, pp.329–336, 2001.

369. E. Majchrzak and B. Mochnacki, The analysis of thermal processes proceeding in the tissue with a tumor region using the BEM, *J. Theor. Appl. Mech.*, Vol. 40, pp.101–112, 2002.

370. J.E. Maloney and B.L. Castle, Pressure-diameter relations of capillaries and small blood vessels in frog lung, *Respir. Physiol.*, Vol. 7, pp.150–162, 1969.

371. D.C. Marchon, J.C. Pfau, P.A. Weber, A.C. Grobe, C.M.G. Duran, D.T. Cheung, An in vitro model of pericardial tissue healing, *Biomaterials*, Vol. 24, pp.89–95, 2003.

372. A.B. Mathur, A.M. Collinsworth, W.M. Reichert, W.E. Kraus, and G.A. Truskey, Endothelial, cardiac muscle and skeletal muscle exhibit different viscous and elastic properties as determined by atomic force microscopy, *J. Biomech.*, Vol. 34, pp.1545–1553, 2001.

373. T. Matsumoto, T. Goto, T. Furukawa, and M. Sato, Residual stress and strain in the lamellar unit of the porcine aorta: experiment and analysis, *J. Biomech.*, Vol. 37, pp.807–815, 2004.

374. W. Maurel, Y. Wu, N.M. Thalmann, and D. Thalmann, Biomechanical Models for Soft Tissues Simulation, Esprit Basic Research Series, Springer, Berlin 1998.

375. K. May-Newman and F.C.P. Yin, A constitutive law for mitral valve tissue, *J. Biomech. Eng.*, Vol. 120, pp.38–47, 1998.

376. A.D. McCulloch, Cardiac biomechanics, [in:] The Biomechanical Engineering Handbook, J.D. Bronzino [ed.], pp.418–439, CRC Press, Boca Raton 1995.

377. G. Mchedlishvili, M. Mantskava, and T. Urdulashvili, Appraisal of functional state of the human resistance arteries, *Russian Journal Biomech.*, Vol. 8, pp.55–59, 2004.

378. R.M.H. McMinn, R.T. Hutchings, J. Pegington, and P. Abrahams, *A Colour Atlas of Human Anatomy*, Mosby-Year Book Europe Limited, Polish edition: Wydawnictwo Slovart, Bratislava and SOLIS, Warszawa 1993.

379. D.F. Meaney, Relationship between structural modeling and hyperelastic material behavior: application to CNS white matter, *Biomech. Model. Mechanobiol.*, Vol. 1, pp.279–293, 2003.

380. J. MEIER, M. KLEEN, and K. MESSMER, A computer of fractal myocardial perfu-
sion heterogeneity to elucidate mechanisms of changes in critical coronary stenosis
and hypotension, *Bull. Math. Biol.*, Vol. 66, pp.1155–1171, 2004.

381. J.W. MELVIN, R.L. STALNAKER, V.L. ROBERTS, and M.L. TROLLOPE, Impact
injury mechanisms in abdominal organs, SAE paper 730968 [in:] Proc. 17th Stapp
Car Crash Conf., pp.115–126, 1973.

382. K.K. MENDES, R.L. STALNAKER, and S.H. ADVANI, A constitutive relationship
for large deformation finite element modeling of brain tissue, *J. Biomech. Eng.*,
Vol. 117, pp.279–285, 1995.

383. A.J. MESTEL, A.J. MOKADY, K.H. PARKER, and C.P. WINLOVE, Effects of the
glycocalyx on the electrophoretic mobility of red cells and on streaming potentials
in blood vessels: predictions of a structurally-based models, *Biorheology*, Vol. 35,
pp.365–381, 1998.

384. A. METCALFE, A.-C. DESFAITS, I. SALAZKIN, L'H. YAHIA, W.M. SOKOLOWSKI,
and J. RAYMOND, Cold hibernated elastic memory foams for endovascular interven-
tions, *Biomaterials*, Vol. 24, pp.491–497, 2003.

385. B.S. MEYERS, C.T. WOOLEY, T.L. SLOTTER, W.E. GARRETT, and T.M. BEST,
The influence of strain rate on the passive and stimulated engineering stess-large
strain behavior of the rabbit tibialis anterior muscle, *J. Biomech. Eng.*, Vol. 120,
pp.126–132, 1998.

386. M.Z. MICHELE, R.J. LUTZ, and W.E. COLLINS, Simulated lipoprotein transport
in the wall of branched arteries, ASAIO J., Vol. 46, pp.669–678, 2000.

387. C. MIEHE, S. GÖKTEPE, and F. LULEI, A micro-macro approach to rubber-like
materials – Part I: the non-affine micro-sphere model of rubber elasticity, *J. Mech.
Phys. Solids*, Vol. 52, pp.2617–2660, 2004.

388. M.I. MIGA, K.D. PAULSEN, P.J. HOOPES, F.E. KENNEDY, A. HARTOV, and
D.W. ROBERTS, In vivo modelling of interstitial pressure in the brain under surgical
load using finite elements, *J. Biomech. Eng.*, Vol. 122, pp.354–363, 2000.

389. F. MIGLIAVACCA, L. PETRINI, M. COLOMBO, F. AURICCHIO, and R. PIETRA-
BISSA, Mechanical behavior of coronary stents investigated through the finite ele-
ment method, *J. Biomech.*, Vol. 35, pp.803–811, 2002.

390. F. MIGLIAVACCA, L. PETRINI, P. MASSAROTTI, S. SCHIEVANO, F. AURICCHIO,
and G. DUBINI, Stainless and shape memory alloy coronary stents: a computational
study on the interaction with the vascular wall, *Biomech. Model. Mechanobiol.*,
Vol. 2, pp.205–217, 2004.

391. K. MILLER, Constitutive model of brain tissue suitable for finite element analysis
of surgical procedures, *J. Biomech.*, Vol. 32, pp.531–537, 1999.

392. K. MILLER, How to test very soft tissues in extension?, *J. Biomech.*, Vol. 34, pp.651–
657, 2001.

393. K. MILLER, Methods of testing very soft biological tissues in compression, *J. Bio-
mech.*, Vol. 38, pp.153–158, 2005.

394. K. MILLER and K. CHINZEI, Constitutive modelling of brain tissue: experiment and
theory, *J. Biomech.*, Vol. 30, pp.1115–1121, 1997.

395. W.R. MILNER, *Cardiovascular physiology*, Oxford University Press, Oxford 1990.

396. G.W. MILTON, *The Theory of Composites*, Cambridge University Press, Cambridge 2001.

397. A. MIRANVILLE and R. TEMAM, *Mathematical modelling in continuum mechanics*, Cambridge University Press, Cambridge 2002.

398. C.C. MITCHELL, D.G. SCHAEFFER, A two-current model for the dynamics of cardiac membrane, *Bull. Math. Biol.*, Vol. 65, pp.767–793, 2003.

399. J. MIZRAHI, Muscle/Bone Interactions in the Musculo-Skeletal System, ABIOMED Lecture Notes, Vol. 1, Institute of Fundamental Technological Research, Warsaw, 2004.

400. K. MITRA, S. KUMAR, A. VEDAVARZ, and M. K. MOALLEMI, Experimental evidence of hyperbolic heat conduction in processed meat, *J. Heat Transfer*, Vol. 117, pp.568–573, 1995.

401. M.S. MOAYERI and G.R. ZENDEHBUDI, Effects of elastic property of the wall on flow characteristics through arterial stenoses, *J. Biomech.*, Vol. 36, pp.525–535, 2003.

402. K.L. MONSON, W. GOLDSMITH, N.M. BARBARO, and G.T. MANLEY, Axial mechanical properties of fresh human cerebral blood vessels, *J. Biomech. Eng.*, Vol. 125, pp.288–294, 2003.

403. G. MONTICELLI, Some remarks about a mechanistic model of transport processes in porous membranes, *J. Membrane. Sci.*, Vol. 214, pp.331–333, 2003.

404. S.M. MOORE, P.J. MCMAHON, and R.E. DĘBSKI, Bi-directional mechanical properties of the auxillary puch of the glenohumeral capsule: Implications for modeling and surgical repair, *J. Biomech. Eng*, Vol. 126, pp.284–288, 2004.

405. M.R. MORENO, J.E. MOORE, and R. MEULI, Cross-sectional deformation of the aorta as measured with magnetic resonance imaging, *J. Biomech. Eng.*, Vol. 120, pp.18–21, 1998.

406. T.F. MORIARTY, The law of Laplace: Its limitations as a relation for diastolic pressure, volume, or wall stress of the left ventricle, *Circ. Res.*, Vol. 46, pp.321–331, 1980.

407. F. MOURET, V. GARITEY, E. BERTRAND, F. DERIVAUX, J. FUSERI, and R. RIEU, In vitro atrial flow dynamics: normal conditions versus atrial fibrillation, *J. Biomech.*, Vol. 37, pp.1749–1755, 2004.

408. V.C. MOW, F. GUILAK, R. TRAN-SON-TAY, R.M. HOCHMUTH [Eds.], *Cell mechanics and Cellular Engineering*, Springer-Verlag, New York, 1994.

409. V.C. MOW, S.C. KUEI, W.M. LAI, and C.G. ARMSTRONG, Biphasic creep and stress relaxation of articular cartilage in compression: theory and experiments, *J. Biomech. Eng.*, Vol. 102, pp.73–84, 1980.

410. V.C. MOW and A. RATCLIFFE, Structure and function of articular cartilage and meniscus, In: V.C. Mow and W.C. Hayes [eds.], *Basic orthopaedic biomechanics*, pages 113–178, Lippincott-Raven Publishers, Philadelphia 1997.

411. D. MOTLAGH, S.E. SENYO, T.A. DESAI, and B. RUSSELL, Microtextured substrata alter gene expression, protein localization and the shape of cardiac myocytes, *Biomaterials*, Vol. 24, pp.2463–2476, 2003.

412. T. Muramatsu, T. Muraoka, Y. Kawakami, and T. Fukunaga, Superficial aponeurosis of human gastrocnemius is elongated during contraction: implications for modelling muscle-tendon unit, *J. Biomech.*, Vol. 35, pp.217–223, 2002.

413. J.D. Murray, *Mathematical Biology*, Springer, Berlin 1993.

414. S. Na, Z. Sun, G.A. Meiniger and J.D. Humphrey, On atomic force microscopy and the constitutive behavior of living cells, *Biomechan. Modelling Mechanobiol.*, Vol. 3, pp.75–84, 2004.

415. R. Nalim, K. Pekkan, H.B. Sun, and H. Yokota, Oscillating Couette flow for in vitro cell loading, *J. Biomech*, Vol. 37, pp.939–942, 1999.

416. M.P. Nash and P.J. Hunter, Computational mechanics of the heart, From tissue structure to ventricular function, *J. Elasticity*, Vol. 61, pp.113–141, 2000.

417. D.A. Noarmoneva, J.Y. Wang, and L.A. Setton, Nonuniform swelling-induced residual strains in articular cartilage, *J. Biomech.*, Vol. 32, pp.401–408, 1999.

418. S. Nemat-Nasser and M. Hori, Micromechanics: Overall Properties of Heterogeneous Materials, North-Holland, Amsterdam 1993.

419. S. Neukirch, G.H.M. van der Heijden, Geometry and mechanics of uniform n-plies: from engineering ropes to biological filaments, *J. Elasticity*, Vol. 69, pp.41–72, 2002.

420. P.F. Niederer, P.P. Lunkenheimer, and C.W. Cryer, On the significance of fiber branching in the human myocardium, *Biomech. Model. Mechanobiol.*, Vol. 3, pp.1–5, 2004.

421. M.T. Nieminen, J. Töyras, M.S. Laasanen, J. Silvennoinen, H.J. Helminen, and J.S. Jurvelin, Prediction of biomechanical properties of articular cartilage with quantitative magnetic resonance imaging, *J. Biomech.*, Vol. 37, pp.321–328, 2004.

422. A. Nowicki, *Fundamentals of Doppler ultrasonography (in Polish)*, Wydawnictwo Naukowe PWN, Warszawa 1995.

423. A. Nowicki and P. Karłowicz [eds.], *Doppler angiography: Selected topics (in Polish)*, Domino, Warszawa 2001.

424. A. Nowicki and J.J. Telega [eds.], *Ultrasound in Biomeasurements, Diagnostics and Therapy*, ABIOMED Lecture Notes 2, Warsaw 2004.

425. R.W. Ogden, On the overall moduli of non-linear elastic composite materials, *J. Mech. Phys. Solids*, Vol. 22, pp.541–553, 1974.

426. R.W. Ogden, *Non-linear Elastic Deformations*, Ellis Horwood, Chichester 1984 (second edition: 1997).

427. R.W. Ogden, Nonlinear elasticity, anisotropy, material stability and residual stresses in soft tissue, In: G. A. Holzapfel and R. W. Ogden [eds.], *Biomechanics of Soft Tissue, CISM Courses and Lectures*, Springer-Verlag, Wien-New York 2002.

428. R.W. Ogden, *Nonlinear Elasticity with Applications to Material Modelling*, Centre of Excellence AMAS, Institute of Fundamental Technological Research, Warsaw 2003.

429. R.W. OGDEN and D.G. ROXBURGH, An energy-based model of the Mullins effect, In: A. Dorfman and A. Muhr [eds.], *Constitutive models for rubber, Proc. The First European Conference on Constitutive Models for Rubber, held in Viena 9-10 September 1999*, pages 23–28, Rotterdam-Brookfield, Balkema 1999.

430. R.W. OGDEN and D.G. ROXBURGH, A pseudo-elastic model for the Mullins effect in filled rubber, *Proc. R. Soc. Lond. A.*, Vol. 455A, pp.2861–2877, 1999.

431. R.W. OGDEN, *Non-linear Elastic Deformations* Dover Publications, New York 1997.

432. R.W. OGDEN, *Nonlinear Elasticity with Application to Material Modelling, Lecture Notes 6*, Centre of Excellence for Advanced Materials and Structures, AMAS, IFTR PAS Warsaw, Poland 2003.

433. B.M. OGLE and D.L. MOORADIAN, Manipulation of remodelling to enhance the mechanical properties of a tissue engineered blood vessel, *J. Biomech. Eng.*, Vol. 124, pp.724–733, 2002.

434. S. OHEIN, H.J. JONGSMA [Eds.], Spot-light Issue: Gap Junctions and Cell-cell Communication the Cardiovascular System, *Cardiovascular Research*, Vol. 62, Issue 2, pp.225–436, 2004.

435. Y. OHTA, D. ENG, C. OTSUKA, and H. OKAMATA, Changes in surface roughness of erytrocytes due to shear stress: atomic force microscopic visualisation of the surface microstructure, *J. Artif. Organs.*, Vol. 6, pp.101–105, 2003.

436. J.B. OLANSEN, J.W. CLARK, D. KHOURY, F. GHORBEL, and A. BIDANI, A closed-loop model of the canine cardiovascular system that includes ventricular interaction, *Comp. Biomed. Res.*, Vol. 33, pp.260–295, 2000.

437. J.H. OMENS, S.M. VAPLON, B. FAZELI, and A.D. McCULLOCH, Left ventricular geometric remodeling and residual stress in the rat heart, *J. Biomech. Eng.*, Vol. 120, pp.715–719, 1998.

438. A.K. OMMAYA, Mechanical properties of tissues of the nervous system, *J. Biomech.*, Vol. 1, pp.127–138, 1968.

439. M.F. O'ROURKE, Vascular mechanics in the clinic, *J. Biomech.*, Vol. 36, pp.623–630, 2003.

440. E.M. ORTT, D.J. DOSS, E. LEGALL, N.T. WRIGHT, and J.D. HUMPHREY, A device for evaluating the multiaxial finite strain thermomechanical behavior of elastomers and soft tissues, *J. Appl. Mech.*, Vol. 67, pp.465–471, 2000.

441. PACKARD, *J. Chem. Phys.*, Vol. 21 pp.303–307, 1953.

442. M.R. PAMIDI and S.H. ADVANI, Nonlinear constitutive relations for human brain tissue, *J. Biomech. Eng.*, Vol. 100, pp.44–48, 1978.

443. S. PARK, K.D. COSTA, and G.A. ATESHIAN, Microscale frictional response of bovine articular cartilage from atomic force microscopy, *J. Biomech.*, Vol. 37, pp.1679–1687, 2004.

444. H.H. PENNES, Analysis of tissue and arterial blood temperatures in the resting human forearm, *J. Appl. Physiology*, Vol. 1, pp.93–122, 1948.

445. E.J. PERREAULT, C.J. HECKMAN, and T.G. SANDERCOCK, Hill muscle model errors during movement are greatest within the physiologically relevant range of motor unit firing rates, *J. Biomech.*, Vol. 36, pp.211–218, 2003.

446. G.W.M. PETERS, J.H. MEULMAN, A.A.H.J. SAUERN, The applicability of the time temperature superposition principle to brain tissue, *Biorheology*, Vol. 34, pp.127–138, 1997.

447. T.J. PFEFER, B. CHOI, G. VARGAS, K.M. MCNALLY, and A. J. WELCH, Pulsed laser-induced thermal damage in whole blood, *J. Biomech. Eng.*, Vol. 122, pp.196–202, 2000.

448. M. PINI, PH. ZYSSET, J. BOTSIS, and R. CONTRO, Tensile and compressive behaviour of the bovine periodontal ligament, *J. Biomech.*, Vol. 37, pp.111–119, 2004.

449. D.P. PIOLETTI, L.R. RAKOTOMANANA, Non-linear viscoelastic laws for soft biological tissues, *Eur. J. Mech. A/Solids*, Vol. 19, pp.749–759, 2000.

450. C.K. POH, P.A. HARDY, Z. LIAO, Z. HUANG, W.R. CLARK, and D. GAO, Effect of flow baffles on the dialysate flow distribution of hollow-fiber hemodialysers: a nonintrusive experimental study using mri, *J. Biomech. Eng.*, Vol. 125, pp.481–489, 2003.

451. S.B. PONOMAREV, I.G. RUSYAK, S.P. KRIVILEVA, A.G. PETROV, and A.S. DYUNDLIK, Development of mathematical models defining the affectio of coronary vessels according to the myocardium movement at realization of the stress-echocardiography, *Russian J. Biomech.*, Vol. 8, pp.59–70, 2004.

452. P. PONTE CASTAÑEDA, P. SUQUET, Nonlinear composites, *Adv. Appl. Mech.*, Vol. 34, pp.171–303, 1998.

453. P. PONTE CASTAÑEDA, J.J. TELEGA, and B. GAMBIN [eds.], *Nonlinear homogenization and its Application to Composites, Polycrystals and Smart Materials* Kluwer Academic Publishers, in press.

454. A.R. POOLE, T. KOJIMA, T. YASUDA, F. MWALE, M. KOBAYASHI, and S. LAVERTY, Composition and structure of articular cartilage, *Clin. Orthopaedics Rel. Res.*, Vol. 391S, pp. S26–S33, 2001.

455. M.T. PRANGE, D.F.M. MEANEY, and S.S. MARGULIES, Regional, directional and age-dependant properties of the brain undergoing large deformations, *J. Biomech. Eng.*, Vol. 124, pp.198–207, 2002.

456. M.T. PRANGE, D.F. MEANEY, and S.S. MARGULIES, Defining brain mechanical properties: effect of region, direction and species, *Stapp Car Crash J.*, Vol. 44, pp.205–214, 2000.

457. P.J. PRENDERGAST, C. LALLY, S. DALLY, A.J. REID, T.C. LEE, D. QUINN, and F. DOLAN, Analysis of prolapse in cardiovascular stents: A constitutive equation for vascular tissue and finite element modelling, *J. Biomech. Eng.*, Vol. 125, pp.692–699, 2003.

458. J.M. PRICE, Biomechanics of smooth muscle, In: G.W. Schmid-Schönbein, S.L.-Y. Woo, and B.W. Zweifach [eds.], *Frontiers in biomechanics*, pages 51–61, Springer-Verlag, New York 1986.

459. PRIDE, *Phys. Rev. B*, Vol. 50, pp.15678–15696, 1994.

460. M. PROSI, K. PERKTOLD, Z. DING, M.H. FRIEDMAN, Influence of curvature dynamics on pulsatile coronary artery flow in a realistic bifurcation model, *J. Biomech.*, Vol. 37, pp.1767–1775, 2004.

461. P.P. PROVENZANO, R. S. LAKES, D. T. CORR, and R. VANDERBY JR., Application of nonlinear viscoelastic models to describe ligament behavior, *Biomech. Model. Mechanobiology*, Vol. 1, pp.45–57, 2002.

462. M.A. PUSO and J.A. WEISS, Finite element implementation of anisotropic quasilinear viscoelasticity using a discrete spectrum approximation, *J. Biomech. Eng.*, Vol. 120, pp.62–70, 1998.

463. V. KUAGLINI, P. VENA, and R. CONTRO, A discrete-time approach to the formulation of constitutive models for viscoelastic soft tissues, *Biomech. Model. Mechanobiology*, Vol. 3, pp.85–97, 2004.

464. K.M. QUAPP and J.A. WEISS, Material characterization of human medial collateral ligament, *J. Biomech. Eng.*, Vol. 120, pp.757–763, 1998.

465. T.M. QUINN, P. DIERICKY, and A.J. GRODZINSKY, Glycosaminoglycan network geometry may contribute to anisotropic hydrauli permeability in cartilage under compression, *J. Biomech.*, Vol. 34, pp.1483–1490, 2001.

466. T.M. QUINN, V. MOREL, and J.J. MEISTER, Static compression of articular cartilage can reduce solute diffusivity and partitioning: implications for the chondrocytes biological response, *J. Biomech.*, Vol. 34, pp.1463–1469, 2001.

467. A. RACHEV, A model of arterial adaptation to alterations in blood flow, *J. Elasticity*, Vol. 61, pp.83–111, 2000.

468. A. RACHEV and S.E. GREENWALD, Residual strains in conduit arteries, *J. Biomech.*, Vol. 36, pp.661–670, 2003.

469. A. RACHEV and K. HAYASHI, Theoretical study of the effects of vascular smooth muscle contraction on strain and stress distributions in arteries, *Ann. Biomed. Eng.*, Vol. 27, pp.459–468, 1999.

470. A. RACHEV, N. STERGIOPULOS, and J.-J. MEISTER, A model for geometric and mechanical adaptation of arteries to sustained hypertension, *J. Biomech. Eng.*, Vol. 120, pp.9–17, 1998.

471. M. RAFF, M. WELSH, H. GÖHL, H. HILDWEIN, M. STORR, AND B. WITTNER, Advanced modeling of highflux hemodialysis, *J. Membrane Sci.*, Vol. 216, pp.1–11, 2003.

472. K.R. RAJAGOPAL, Multiple configurations in continuum mechanics, *Reports of the Institute for Computational and Applied Mechanics*, University of Pittsburgh, p.6, 1995.

473. K.R. RAJAGOPAL and L. TAO, *Mechanics of Mixtures*, World Scientific, River Edge, NJ., 1995.

474. A. RAMAMURTHI and I. VESELY, Evaluation of the matrix-synthesis potential of crosslinked hyaluronan gels for tissue engineering of aortic heart valves, *Biomaterials*, Vol. 26, pp.999–1010, 2005.

475. S. RAMTANI, Mechanical modelling of cell/ECM and cell/cell interactions during the contraction of a fibroblast-populated collagen macrosphere: theory and model simulation, *J. Biomech.*, Vol. 37, pp.1709–1718, 2004.

476. D.E. RASSIER and W. HERZOG, Effects of shortening on stretch-induced force enhancement in single skeletal muscle fibers, *J. Biomech.*, Vol. 37, pp.1305–1312, 2004.

477. A. REDAELLI, M. SONCINI, and F.M. MONTEVECCHI, Myosin cross-bridge mechanics: geometrical determinants for continuous sliding, *J. Biomech.*, Vol. 34, pp.1607–1617, 2001.

478. A. REDAELLI, S. VESENTINI, M. SONCINI, P. VENA, S. MANTERO, and F.M. MONTEVECCHI, Possible role of decorin glycosaminoglycans in fibril to fibril force in relative nature tendons – a computational study from molecular to microstructural level, *J. Biomech.*, Vol. 36, pp.1555–1569, 2003.

479. M.C. REED, Why is mathematical biology so hard?, *Notices Amer. Math. Soc.*, pp.338–342, 2004.

480. E.W. REMME, P.J. HUNTER, O. SMISETH, C. STEVENS, S.I. RABBEN, H. SKULSTAD, and B. ANGELSEN, Development of an in vivo method for determining material properties of passive myocardium, *J. Biomech.*, Vol. 37, pp.669–678, 2004.

481. P.M. REPPERT and F.D. MORGAN, Streaming potential collection and data processing techniques, *J. Colloid Interface Sci.*, Vol. 233, pp.348–355, 2001.

482. P.M. REPPERT, F.D. MORGAN, D.P. LESMES, and L. JOUNIAUX, Frequency-dependent streaming potentials, *J. Colloid Interface Sci.*, Vol. 234, pp.194–203, 2001.

483. F.J. ROMERO, A. PASTOR, J. LOPEZ, and P.V. ROMERO, A recruitment-based rheological model for mechanical behaviour of soft tissues, *Biorheology*, Vol. 35, pp.17–35, 1998.

484. M.E. LEVENSTON, E.H. FRANK, A.J. GRODZINSKY, Electrokinetic and poroelastic coupling during finite deformations of charged porous materials, *J. Appl. Mech.*, Vol. 66, pp.323–333, 1999.

485. J.A.G. RHODIN, Architecture of the vessel wall, In: R.M. Berne [ed.], *Handbook of Physiology, section 2.* American Physiological Society 1979.

486. B. RIVOLTA, F. INZOLI, S. MANTERO, and A. SEVERINI, Evaluation of temperature distribution during hyperthermic treatment in biliary tumors: A computational approach, *J. Biomech. Eng.*, Vol. 121, pp.141–147, 1999.

487. P.S. ROBINSON, T.W. LIU, P.R. REYNOLDS, K.A. DERWIN, R.V. IOZZO, and L.J. SOSLOWSKY, Strain-rate sensitive mechanical properties of tendon fascicles from mice with genetically engineered alterations in collagen and decorin, *J. Biomech. Eng*, Vol. 126, pp.252–257, 2004.

488. R.B. ROEMER and T.C. CETAS, Application of bioheat transfer simulations to hyperthermia, *Cancer Res.*, Vol. 44, pp.4788s–4798s, 1984.

489. R.B. ROEMER and A.W. DUTTON, A generic tissue convective energy balance equation: Part I — theory and derivation, *J. Biomech. Eng.*, Vol. 120, pp.395–404, 1998.

490. T.H. ROSENQUIST, S. BERNACK, S.S. COBIN, and Y.C. FUNG, The structure of the pulmonary interalveolar microvascular sheet, *Microvasc. Res.*, Vol. 5, pp.199–212, 1973.

491. S.W. ROUHANA, Biomechanics of abdominal trauma, [in:] *Accidental Injury: Biomechanics and Prevention*, J.W. Melvin [ed.], Springer-Verlag, New York 2002.

492. S.W. ROUHANA, I.V. LAU, and S.A. RIDELLA, Influence of velocity and forced compression on the severity of abdominal injury in blunt, nonpenetrating lateral impact, *J. Trauma*, Vol. 25, pp.490–500, 1985.

493. J.C. RÜEGG, Calcium and Muscle Activation, Springer-Verlag, New York 1988.

494. M. SACKS, A method for planar biaxial mechanical testing that includes in-plane shear, *J. Biomech. Eng.*, Vol. 121, pp.551–555, 2001.

495. M. SACKS and C.J. CHUONG, Orthotropic mechanical properties of chemically treated bovine pericardium, *Ann. Biomed. Eng.*, Vol. 26, pp.892–902, 1998.

496. M.S. SACKS, Biaxial mechanical evaluation of planar biological materials, *J. Elasticity*, Vol. 61, pp.199–246, 2000.

497. M.S. SACKS, Incorporation of experimentally-derived fiber orientation into a structural constitutive model for planar collageneous tissues, *J. Biomech. Eng.*, Vol. 125, pp.280–287, 2003.

498. K.B. SAHAY, R. MEHROTRA, U. SACHDEVA, and K. BANERJI, Elastomechanical characterization of brain tissues, *J. Biomech.*, Vol. 25, pp.319–326, 1992.

499. J.E. SANDERS and B.S GOLDSTEIN, Collagen fibril diameters increase and fibril densities decrease in skin subjected to repetitive compressive and shear stresses, *J. Biomech.*, Vol. 34, pp.1581–1587, 2001.

500. S.A. SAPARETO and W.C. DEWEY, Thermal dose determination in cancer therapy, *Int. J. Radiation Oncology Biol. Physiol.*, Vol. 10, pp.787–800, 1984.

501. J.J. SARVER, P.S. ROBINSON, and D.M. ELLIOTT, Methods for quasi-linear viscoelastic modeling of soft tissue: application to incremental stress-relaxation experiments, *J. Biomech. Eng.*, Vol. 125, pp.754–758, 2003.

502. N. SASAKI and S. ODAJIMA, Elongation mechanism of collagen fibrils and force-strain relations of tendon at each level of structural hierarchy, *J. Biomechanics*, Vol. 29, pp.1131–1136, 1996.

503. N. SASAKI and S. ODAJIMA, Stress–strain curve and Young's modulus of a collagen molecule as determined by the X ray diffraction technique, *J. Biomechanics*, Vol. 29, pp.655–658, 1996.

504. N. SASAKI, N. SHIWA, S. YAGIHARA, and H. HIKICHI, X-ray diffraction studies on the structure of the hydrated collagen, *Biopolymers*, Vol. 22, pp.2539–2547, 1983.

505. R. SCHACHAR, W. HERZOG, and T.R. LEONARD, The effects of muscle stretching and shortening on isometric forces on the descending limb of the force-length relationship, *J. Biomech.*, Vol. 37, pp.917–926, 2004.

506. H. SCHECHTMAN and D.L. BADER, Fatigue damage of human tendons, *J. Biomech.*, Vol. 35, pp.347–353, 2002.

507. F.R. SCHMIDLIN, C.E. ISELIN, A. NAIMI, S. ROHNER, F. BORST, M. FARSHAD, P. NIEDERER, and P. GRABER, The higer injury risk of abnormal kidneys in blunt renal trauma, *Scand. J. Urology Nephrology*, Vol. 32, pp.388–392, 1998.

508. D.C. SCHNEIDER, T.M. DAVIDSON, and A.M. NAHUM, *In vitro* biaxial stress-strain response of human skin, *Arch. Otolaringol.*, Vol. 110 1984.

509. M.W.H. SCHELLINGS, Y.M. PINTO, and S. HEYMANS, Matricellular proteins in the heart: possible role during stress and remodelling, *Cardiovascular Res.*, Vol. 64, pp.24–31 2004.

510. C.A.J. SCHULZE-BAUER and G.A. HOLZAPFEL, Determination of constitutive equations for human arteries from clinical data, *J. Biomech.*, Vol. 36, pp.165–169, 2003.

511. C.A.J. SCHULZE-BAUER, C. MÖRTH, and G.A. HOLZAPFEL, Passive biaxial mechanical response of aged human iliac arteries, *J. Biomech. Eng.*, Vol. 125, pp.395–406, 2003.

512. P. SESHAIYER and J.D. HUMPHREY, A sub-domain inverse finite element characterization of hyperelastic membranes including soft tissues, *J. Biomech. Eng.*, Vol. 125, pp.363–371, 2003.

513. P. SESHAIYER and J.D. HUMPHREY, On the potentially protective role of contact constraints on saccular aneurysms, *J. Biomech.*, Vol. 34, pp.607–612, 2001.

514. N.S. SHABRYKINA, N.N. VISTALIN, and A.G. GLACHAEV, Influence of blood capillary formation form on filtration-reabsorption process, *Russian J. Biomech*, Vol. 8, pp.60–67, 2004.

515. A.D. SHAH and J.D. HUMPHREY, Finite strain elastodynamics of intracranial saccular aneurysms, *J. Biomech*, Vol. 32, pp.593–599, 1999.

516. M. SHILLOR, M. SOFONEA, and J.J. TELEGA, *Contact Problems for Solids and Structures*, in preparation.

517. T. SHIMIZU, M. YAMATO, A. KIKUCHI, and T. OKANO, Tissue engineering for myocardial regeneration, *J. Artif. Organs*, Vol. 5, pp.216–222, 2002.

518. A. SHITZER, S. BELLOMO, L. A. STROSCHEIN, R. R. GONZALEZ, and K. B. PANDOLF, Simulation of a cold-stressed finger including the effects of wind, gloves and cold-induced vasodilatation, *J. Biomech. Eng.*, Vol. 120, pp.389–394, 1998.

519. W. SHYY, M. FRANCOIS, H.S. UDAYKUMAR, N. N'DRI R. TRAN-SON-TAY, Moving boundaries in microscale biofluid dynamics, *Appl. Mech. Rev.*, Vol. 54, pp.405–4, 2001.

520. S. SIDEMAN, *The State of the Heart*, Lectures delivered at the Centre of Excellence ABIOMED, August 2004, Institute of Fundamental Technological Research, Polish Academy of Sciences, Warsaw.

521. F.H. SILVER and D.L. CHRISTIANSEN, Materials Science and Biocompatibility, Springer-Verlag, New York 1999.

522. F.H. SILVER, J.W. FREEMAN, and G.P. SEEHRA, Collagen self-assembly and the development of tendon mechanical properties, *J. Biomech.*, Vol. 36, pp.1529–1553, 2003.

523. B.R. SIMON, Multiphase poroelastic finite element models for soft tissue structures, *Appl. Mech. Rev.*, Vol. 45, pp.191–218, 1992.

524. B.R. Simon, M.V. Kaufman, M.A. McAfee, and A.L. Baldwin, Porohyper-elastic finite element analysis of large arteries using ABAQUS, *J. Biomech. Eng.*, Vol. 120, pp.296–298, 1998.

525. B.R. Simon, M.V. Kaufman, M.A. McAfee, A.L. Baldwin, and L.M. Wilson, Identification and determination of material properties for porohyperelastic analysis of large arteries, *J. Biomech. Eng.*, Vol. 120, pp.188–194, 1998.

526. P.K Singal, I. M. C. Dixon, L. A. Kirshanbaum, and N. S. Dhalla [eds.], *Cardiac remodelling and failure*, Kluwer Academic Publishers, Boston 2003.

527. P. Sipkema, P.J.W. van der Linden, N. Westerhof, and F.C.P. Yin, Effect of cyclic axial stretch af rat arteries on endothelial cytoskeletal morphology and vascular reactivity, *J. Biomech.*, Vol. 36, pp.653–659, 2003.

528. L. Skubiszak, *New insight into the structural aspect of muscle contraction*, Habilitation Thesis, Prace Instytutu Biocybernetyki i Inżynierii Biomedycznej, No. 58, Polish Academy od Sciences, Warszawa 2004.

529. J. Vander Sloten, K. Degryse, R. Gobin, G. Van der Perre, and M.Y. Mommaerts, Interactive simulation of cranial surgery in a computer aided design environment, *J. Cranio-Maxillofacial Surgery*, Vol. 24, pp.122–129, 1996.

530. B. H. Smaill and P. J. Hunter, Structure and function of the diastolic heart, In L. Glass, P. Hunter, and A. McCulloch [eds.], *Theory of heart*, pages 1–29, Springer Verlag, New York 1991.

531. J.G. Snedeker, M. Bajka, J.M. Hug, G. Székely, and P. Niederer, The creation of high-fidelity finite element model of the kidney for use in trauma research, *J. Visualisation Computer Animation*, Vol. 13, pp.53–64, 2002.

532. J.G. Snedeker, P. Niederer, F.R. Schmidlin, M. Farshad, C.K. Demetropoulos, J.B. Lee, and K.H. Yang, Strain-rate dependent material properties of the porcine and human kidney capsule, *J. Biomech.*, Vol. 38, in press, 2005.

533. J.G. Snedeker, M. Barbezat, P. Niederer, F.R. Schmidlin, and M. Farshad, Strain energy density as a rupture criterion for the kidney: impact tests on porcine organs, finite element simulation, and a baseline comparison between human and porcine tissues, *J. Biomech.*, Vol. 38, in press, 2005.

534. M. Soncini, A. Redaelli, and F.M. Montevecchi, Myosin head mechanical performance under different conformational changes mechanisms, *J. Biomech.*, Vol. 37, pp.1031–1041, 2004.

535. J. Song, L. X. Xu, D.E. Lemons, and S. Weinbaum, Enhancements in the effective thermal conductivity in rat spinotrapezius due to vasoregulation, *J. Biomech. Eng.*, Vol. 119, pp.461–468, 1997.

536. J. Song, L.X. Xu, D.E. Lemons, and S. Weinbaum, Microvascular thermal equilibration in rat spinotrapezius muscle, *Annals Biomed. Eng.*, Vol. 27, pp.56–66, 1999.

537. J. Soulhat, M.D. Buschmann, and A. Shirazi-Adl, A fibril-network-reinforced biphasic model of cartilage in unconfined compression, *J. Biomech. Eng.*, Vol. 121, pp.340–347, 1999.

538. E.A. De Souza Neto, D. Perić, and D.R.J. Owen, A phenomenological three-dimensional rate-independent continuum damage model for highly filled polymers: Formulation and computational aspects, *J. Mech. Phys. Solids*, Vol. 42, pp.1533–1550, 1994.

539. C.M. Spofford and W.M. Chilian, Mechanotransduction via elastin-lamini receptor (elr) in resistance arteries, *J. Biomech.*, Vol. 36, pp.645–652, 2003.

540. R. Stagni, A. Leardini, and A. Ensini, Ligament fibre recruitment of the human ankle joint complex in passive flexion, *J. Biomech.*, Vol. 37, pp.1823–1829, 2004.

541. M. Stańczyk and J.J. Telega, Modelling of heat transfer phenomena during cementation of femoral prosthesis, In *Proceedings of the 13th Conference of European Society of Biomechanics* volume 4 of *Acta Bioengng. Biomech.*, pages 247–248, Wrocław, September 1–4 2002.

542. M. Stańczyk and J.J. Telega, Heat Transfer in Biological Tissues – from Modelling to Applications, book, in preparation.

543. M. Stańczyk and B. van Rietbergen, Thermal analysis of bone cement polymerisation at the bone-cement interface, *J. Biomech*, Vol. 37, pp.1803–1810, 2004.

544. C.G. Stephanis, D.E. Mourmouras, and D.G. Tsagadopoulos, On the elastic properties of arteries, *J. Biomech.*, Vol. 36, pp.1727–1731, 2003.

545. A. Stéphanou, M.A.J. Chaplain, and P. Tracqui, A mathematical model for the dynamics of large membrane deformationof isolated fibroblasts, *Bull. Math. Biol.*, Vol. 66, pp.1119–1154, 2004.

546. C. Stevens, E. Remme, I. LeGrice, and P. Hunter, Ventricular mechanics in diastole: material parameter sensitivity, *J. Biomech.*, Vol. 36, pp.737–748, 2003.

547. J.-F. Stoltz [Ed.], Mechanobiology: Cartilage and Chondrocytes, IOS Press, Amsterdam 2000.

548. M. Sugihara-Seki, R. Skalak, Force acting on spheres adhered to a vessel wall, *Biorheology*, Vol. 34, pp.249–260, 1997.

549. J.-K. Suh, I. Youn, and F.H. Fu, An in-situ calibration of an ultrasound transducer: a potential application for an ultrasonic indentation test of articular cartilage, *J. Biomech.*, Vol. 34, pp.1347–1353, 2001.

550. S.R. Summerour, J.L. Emery, B. Fazeli, J.H. Omens, and A.D. McCulloch, Residual strain in ischemic ventricular myocardium, *J. Biomech. Eng.*, Vol. 120, pp.710–714, 1998.

551. Y.-L. Sun, Z.-P. Luo, A. Fertala, and K.-N. An, Stretching type II collagen with optical tweezers, *J. Biomech.*, Vol. 37, pp.1665–1669, 2004.

552. W. Sun, M.S. Sacks, T.L. Sellaro, W.S. Slaughter, and M.J. Scott, Biaxial mechanical response of biprosthetic heart valve biomaterials to high in-plane shear, *J. Biomech. Eng.*, Vol. 125, pp.372–380, 2003.

553. A. Sverdlik and Y. Lanir, Time-dependent mechanical behavior of sheep digital tendons including the effects of preconditioning, *J. Biomech. Eng.*, Vol. 124, pp.78–84, 2002.

554. J. Synka and A. Kainz, Extension of the concept of material objectivity to mixed Eulerian-Lagrangian reference systems, *Acta Mech.*, Vol. 166, pp.13–25, 2003.

555. L.A. TABER and S. CHABERT, Theoretical and experimental study of growth and remodelling in the developing heart, *Biomech. Model. Mechanobiology*, Vol. 1, pp.29–43, 2002.

556. L.A. TABER and R. PERUCCHIO, Modelling heart development, *J. Elasticity*, Vol. 61, pp.165–197, 2000.

557. A. TAJADDININ, D.L. KILPATRICK, and D.G. VINCE, A novel experimental method to estimate stress-strain behavior of intact coronary arteries using intravascular ultrasound (IVUS), *J. Biomech. Eng.*, Vol. 125, pp.120–123, 2003.

558. H. TAKAMATSU, R. TAKEYA, S. NAITO, and H. SUMIMOTO, On the mechanism of cell lysis by deformation, *J. Biomech.*, Vol. 38, pp.127–124, 2005.

559. P. LE TALLEC, Numerical methods for nonlinear three-dimensional elasticity, In P.G. Ciarlet and J.L. Lions [eds.], *Handbook of numerical analysis*, vol. III, pp.465–622, Elsevier Science, Amsterdam 1994.

560. E. TANAKA, H. YAMADA, and S. MURAKAMI, Inelastic constitutive modeling of arterial and ventricular walls, In: K. Hayashi and H. Ishikawa [eds.], *Computational Biomechanics*, pages 137–163, Springer,Tokyo 1996.

561. D. TANG, J. YANG, S. KOBAYASHI, and D.N. KU, Effect of a lipid pool on stress/strain distribution in stenotic arteries: 3-D fluid-structure interactions (FSI) models, *J. Biomech. Eng.*, Vol. 126, pp.363–370, 2004.

562. D. TANG, J. YANG, C. YANG, and D.N. KU, A nonlinear axisymmetric model with fluid-wall interactions for steady viscous flow in stenotic elastic tubes, *J. Biomech. Eng.*, Vol. 121, pp.494–501, 1999.

563. L. TAO, J.D. HUMPHREY, and K.R. RAJAGOPAL, A mixture theory for heat-induced alterations in hydration and mechanical properties in soft tissues, *Int. J. Eng. Sci.*, Vol. 39, pp.1535–1556, 2001.

564. I. TASAKI and G. MATSUMOTO, On the cable theory of nerve conduction, *Bull. Math. Biol.*, Vol. 64, pp.1069–1082, 2002.

565. T. TATEISHI, G. CHEN, and T. USHIDA, Biodegradable porous scaffolds for tissue engineering, *J. Artif. Organs*, Vol. 5, pp.77–83, 2002.

566. Z. TAYLOR and K. MILLER, Reassessment of brain elasticity for analysis of biomechanics of hydrocephalus, *J. Biomech.*, Vol. 37, pp.1263–1269, 2004.

567. J.J. TELEGA, Stochastic homogenization: Convexity and nonconvexity, [in:] Nonlinear Homogenization and Its Applications to Composites, Polycrystals and Smart Materials, P. Ponte-Castañeda, J.J. Telega, and B. Gambin [eds.], NATO Science Series, Kluwer Academic Publishers, pp.305-347, Dordrecht-Boston-London 2004. Vol. 28, pp.327–377, 2002.

568. J.J. TELEGA and W. BIELSKI, Stochastic homogenization and macroscopic modelling of composites and flow through porous media, *Theoret. Appl. Mech.*, Vol. 28, pp.327–377, 2002.

569. J.J. TELEGA and W. BIELSKI, Flow in random porous media, *Comp. Geotech.*, Vol. 30, pp.271–288, 2003.

570. J.J. TELEGA and M. STAŃCZYK, Residual stresses and remodelling, [in:] *Tissue Remodelling*, J.J. Telega [ed.], ABIOMED Lecture Notes, in preparation.

571. J.J. TELEGA and M. STAŃCZYK, Fluid-structure interactions of flowing blood with arteries, in preparation.

572. J.J. TELEGA [ed.], *Modelling in Biomechanics*, Centres of Excellence AMAS and ABIOMED, Institute of Fundamental Technological Research, Polish Academy of Sciences, Warsaw 2004

573. J.J. TELEGA, A. GAŁKA, B. GAMBIN, and S. TOKARZEWSKI, Homogenization methods in bone mechanics, [in:] Orthopaedic Biomechanics, J.J. Telega [ed.], *AMAS Conference Proceedings*, Vol.5, Institute of Fundamental Technological Research, pp.333–382, Warsaw 2003.

574. J.J. TELEGA and S. JEMIOŁO, Polyconvexity for anisotropic materials undergoing finite deformations. Part I General setting and existence theorems, In: W. Szcześniak [ed.], *Polish-Ukrainian Transactions, Theoretical Foundations of Civil Engineering* pp.431–438, OW PW, Warsaw 2002, Part II. Incompressibility, injectivity, interval and boundary unilateral constraints, idib., pp.439–450.

575. J.J. TELEGA and R. WOJNAR, Flow of electrolyte through porous, piezoelectric medium: macroscopic equations, *C.R. Acad. Sci. Paris, Série IIb*, Vol.328, pp.225–330, 2000.

576. J.J. TELEGA and R. WOJNAR, Streaming potentials in biological tissue, [in:] Orthopaedic Biomechanics, J.J. Telega [ed.], *AMAS Conference Proceedings*, Vol.5, Institute of Fundamental Technological Research, pp.387–454, Warsaw 2003.

577. J.J. TELEGA and R. WOJNAR, Electrokinetics in random deformable media, [in:] IUTAM Symp. on the Mechanics of Physicochemical and Electrochemical Interactions in Porous Media, 18–23 May, 2003, Rolduc, Kerkrude, The Netherlands; S.C. Cowin and J.M. Huyghe [Eds.], Kluwer, in press.

578. J.J. TELEGA and E. ZUAZUA [Eds.], Control of Solids and Structures: Mathematical Modelling and Engineering Applications, *CISM Courses and Lectures*, Springer-Verlag, Wien-New York, in press.

579. A. THAPA, D.C. MILLER, T.J. WEBSTER, and K.M. HABERSTROH, Nano-structured polymers enhance bladder smooth muscle cell function, *Biomaterials*, Vol. 24, pp.2915–2926, 2003.

580. S. THOMOPOLUOS, G.R. WILLIAMS, and L.J. SOSLOWSKY, Tendon to bone healing: differences in biomechanical, structural, and compositional properties due to a range of activity levels, *J. Biomech. Eng.*, Vol. 125, pp.106–113, 2003.

581. O. THOUMINE and A. OTT, Comparison of the mechanical properties of normal and transformed fibroblasts, *Biorheology*, Vol. 54, pp.509–526, 1997.

582. S. TOKARZEWSKI and J.J. TELEGA, Two-point Padé approximants and their application to composite materials, Appl. Math. Comp. Sci., Vol. 8, pp.417–434, 1998.

583. S. TORQUATO, Random Heterogeneous Materials: Microstructure and Macroscopic Properties, Springer, New-York 2002.

584. J. TÖYRÄS, T. LYYRA-LAITINEN, M. NIINIMÄKI, R. LINDGREN, M.T. NIEMINEN, L. KIRIVANTA, and J.S. JURVELIN, Estimation of the young's modulus of articular cartilage using an arthoscopic indentation instrument and ultrasonic measurement of tissue thickness, *J. Biomech.*, Vol. 34, pp.251–256, 2001.

585. A. TÖZEREN, Continuum rheology of muscle contraction and its application to cardiac contractility, *J. Biophys.*, Vol. 47, pp.303–312, 1985.

586. P.C. TURNER, A.G. MCLENNAN, A.D. BATES, and M.R.H. WHITE, *Instant notes in molecular biology*, BIOS Scientific Publishers Limited, Polish ed.: PWN, Warszawa, 1997, 1999.

587. J.P.G. URBAN, A. MAROUDAS, M.T. BAYLISS, and J. DILLON, Swelling pressures of proteoglycans at the concentrations found in cartilaginous tissues, *Biorheology*, Vol. 16, pp.447–464, 1979.

588. T. P. USYK, R. MAZHARI, and A. D. MCCULLOCK, Effect of laminar orthotropic myofiber architecture on regional stress and strain in the canine left ventricle, *J. Elasticity*, Vol. 61, pp.143–164, 2000.

589. J. W. VALVANO, S. NHO, and G. T. ANDERSON, Analysis of the Weinbaum-Jiji model of blood flow in the canine kidney cortex for self-heated thermistors, *J. Biomech. Eng.*, Vol. 116, pp.201–207, 1994.

590. I. VANAGS, A. PETERSONS, V. OSE, I. OZOLANTA, V. KASYANOV, J. LAIZANS, E. VJATERS, J. GARDOVSKIS, and A. VANAGS, Biomechanical properties of oesophagus wall under loading, *J. Biomech.*, Vol. 36, pp.1387–1390, 2003.

591. R. VANDERBY and P.P. PROVENZANO, Collagen in connective tissue: from tendon to bone, *J. Biomech.*, Vol. 36, pp.1523–1527, 2003.

592. E.J.VANDERPLOEG, S.M. IMLER, K.R. BRODKIN, A.J. GARCIA, and M.E. LEVENSTON, Oscillatory tension modulates matrix metabolism and cytoskeletal organization in chondrocytes and fibrochondrocytes, *J. Biomech.*, Vol. 37, pp.1941–1952, 2004.

593. P. VAN KEMENADE, Water and ion transport through intact and damaged skin, *Ph.D. thesis, Technische Universteit Eindhoven* 1998.

594. P. VAN KEMENADE, J.M. HUYGHE, and L.F.A. DOUVEN, Triphasic FE modeling of the skin water barrier, *Transport in Porous Media*, Vol 50, pp.93–109, 2003.

595. J. VAN MEERVELD, M.M. MOLENAAR, J.M. HUYGHE, and F.P.T. BAAIJENS, Analytical solution of compression, free swelling and electrical loading of saturated charged porous media, *Transport in Porous Media*, Vol 50, pp.111–126, 2003.

596. J. VAUGHN, A. CZIPURA, and J.D. HUMPHREY, Measurement of finite-strain dependent permeability of biomembranes, *J. Biomech.*, Vol. 35, pp.287–291, 2002.

597. A.I. VERESS, J.A. WEISS, G.T. GULLBERG, D.G. VINCE, and R.D. RABBITT, Strain measurement in coronary arteries using intravascular ultrasound and deformable images, *J. Biomech. Eng.*, Vol. 124, pp.735–741, 2002.

598. D. VIANO, H. VON HOLST, and E. GORDON, Serious brain injury from traffic related causes: priorities for primary prevention, *Accident Analysis & Prevention*, Vol. 29, pp.811–816, 1997.

599. A. VIIDIK, Simultaneous mechanical and light microscopic studies of collagen fibres, *Z. Anat. Entwicklungsgesch*, Vol. 136, pp.204–212, 1972.

600. M. VILLASANA and A. RADUNSKAYA, A delay differential equation for tumor growth, *J. Math. Biol.*, Vol. 47(5), pp.270–294, 2003.

601. J. Vossoughi and A. Tözeren, Determination of an effective shear modulus of aorta, *Russian J. Biomech.* (1–2), pp.20–35, 1998.

602. Y. Wakisaka, S. Niwano, H. Niwano, J. Saito, T. Yoshida, S. Hirasawa, H. Kawada, and T. Izumi, Structural and electrical remodelling in rat acute myocarditis and subsequent heart failure, *Cardiovascular Res.*, Vol. 63, pp.689–699, 2004.

603. E.K. Walsh and A. Schettini, Calculation of brain elastic properties in vivo, *Amer. J. Physiology*, Vol. 247, pp.R637–R700, 1984.

604. A.J.L. Walsh, J.C. Lotz, Biological response of the intervertebral disc to dynamic loading, *J. Biomech.*, Vol. 37, pp.329–337, 2004.

605. S.L. Waters, A mathematical model for the laser treatment of heart disease, *J. Biomech.*, Vol. 37, pp.281–288, 2004.

606. C.C.-B. Wang, N.O. Cahine, C.T. Hung, and G.A. Athesian, Optical determination of anisotropic material properties of bovine articular cartilage in compression, *J. Biomech.*, Vol. 36, pp.339–353, 2003.

607. C.C.-B. Wang, C.T. Huang, and V.C. Mow, An analysis of the effects of depth-dependent aggregate modulus on articular cartilage stress-relaxation behavior in compression, *J. Biomech.*, Vol. 34, pp.75–84, 2001.

608. D.H.J. Wang, M. Makaroun, M.W. Webster, and D.A. Vorp, Mechanical properties and microstructure of intraluminal thrombus from abdominal aortic aneurysm, *J. Biomech. Eng.*, Vol. 123, pp.536–539, 2001.

609. P.N. Watson, N.A. Hill, and M. Heil, A mathematical model for the growth of the abdominal aortic aneurysm, *Biomech. Mode. Mechanobiol.*, Vol. 3, pp.98–113, 2003.

610. R.J. Waxweiler, D. Thurman, J. Sniezek, S.O. Sosin, and J.O. Niell, Monitoring the impact of traumatic brain injury and injury: a review and update, *J. Neurotrauma*, Vol. 12, pp.509–516, 1995.

611. W. Weibull, A statistical distribution function of wide applicability, *J. Appl. Mech.*, Vol. 18, pp.293–297, 1951.

612. S. Weinbaum and L.M. Jiji, A new simplified bioheat equation for the effect of blood flow on local average tissue temperature, *J. Biomech. Eng.*, Vol. 107, pp.131–139, 1985.

613. S. Weinbaum and L.M. Jiji, The matching of thermal fields surrounding countercurrent microvessels and the closure approximation in the Weinbaum-Jiji equation, *J. Biomech. Eng.*, Vol. 111, pp.271–275, 1989.

614. S. Weinbaum, L.M. Jiji, and D.E. Lemons, Theory and experiment for the effect of vascular microstructure on surface tissue heat transfer - Part I: Anatomical foundation and model conceptualization, *J. Biomech. Eng.*, Vol. 106, pp.321–330, 1984.

615. S. Weinbaum, L.M. Jiji, and D.E. Lemons, The bleed-off perfusion term in the Weinbaum-Jiji bioheat equation, *J. Biomech. Eng.*, Vol. 114, pp.539–544, 1992.

616. K.L. Weind, M.M. Thornton, C.G. Ellis, and D.R. Boughner, A precise radiographic technique for the measurement of dimensional changes in heart valve biomaterials following fixation, *J. Biomech.*, Vol. 35, pp.983–987, 2002.

617. J.A. WEISS, J.C. GARDINER, and C. BONIFASI-LISTA, Ligament material behavior nonlinear, viscoelastic and rate-independent under shear loading, *J. Biomech.*, Vol. 35, pp.943–950, 2002.

618. J.A. WEISS, B.N. MAKER, and S. GOVINDJEE, Finite element implementation of incompressible, transversely isotropic hyperelasticity, *Comp. Meth. Appl. Mech. Eng.*, Vol. 135, pp.107–128, 1996.

619. J.J. WENTZEL, F.J.H. GIJSEN, N. STERGIOPULOS, P.W. SERRUYS, C.J. SLAGER, and R. KRAMS, Shear stress, vascular remodeling and neointimal formation, *J. Biomech.*, Vol. 37, pp.681–688, 2003.

620. M.W. WESTON and J.M. TARBELL, Wall shear rate measurements in an elastic curved artery model, *Biorheology*, Vol. 34, pp.1–17, 1997.

621. E.S. WEYDAHL and J.E. MOORE, Dynamic curvature strongly affects shear rates in coronary artery bifurcation model, *J. Biomech.*, Vol. 34, pp.1189–1196, 2001.

622. S. WHITTAKER, The Method of Volume Averaging, Kluwer Academic Publishers, Dordrecht 1999.

623. J.P. WHITELEY, D.J. GAVAGHAN, and C.E.W. HAHN, Mathematical modelling of pulmonary gas transport, *J. Math. Biol.*, Vol. 47, pp.79–99, 2003.

624. C.M. WHYNE, S.S. HU, and J.C. LOTZ, Parametric finite element analysis of vertebral bodies affected by tumors, *J. Biomech.*, Vol. 34, pp.1317–1324, 2001.

625. J.P. WILBER and J.R. WALTON, Teh convexity properties of a class of constitutive models for biological soft tissues, *Math. Mech. Solids*, Vol. 7, pp.217–235, 2002.

626. S.D. WILLIAMSON, Y. LAM, H.F. YOUNIS, H. HUANG, S. PATEL, M.R. KAAZEMPUR-MORFAD, and R.D. KAMM, On the sensitivity of wall stresses in diseased arteries to variable material properties, *J. Biomech. Eng.*, Vol. 125, pp.147–155, 2003.

627. W. WILSON, C.C. VAN DONKELAAR, B. VAN RIETBERGEN, K. ITO, R. HUISKES, Stresses in the local collagen network of articular cartilage: a poroviscoelastic fibril-reinforced finite element study, *J. Biomech.*, Vol. 37, pp.357–366, 2004.

628. E.H. WISSLER, Comments on the new bioheat equation proposed by Weinbaum and Jiji, *J. Biomech. Eng.*, Vol. 109, pp.226–233, 1987.

629. H. WOLINSKY and S. GLAGOV, A lamellar unit of aortic medial structure and function in mammals, *Circ. Res.*, Vol. 20, pp.99–111, 1967.

630. S. L. Y. WOO, G. A. LIVESAY, T. J. RUNCO, and E. P. YOUNG, Structure and function of tendons and ligaments, In: V. C. Mow and W. C. Hayes [eds.], *Basic orthopaedic biomechanics*, pages 209–251, Lippincott–Raven, Philadelphia 1997.

631. T.A.L. WREN and D.R. CARTER, A microstructural model for the tensile constitutive and failure behavior of soft skeletal connective tissues, *J. Biomech. Eng.*, Vol. 120, pp.55–61, 1998.

632. N.T. WRIGHT, S. S. CHEN, and J.D. HUMPHREY, Time-temperature equivalence of heat-induced changes in cells and proteins, *J. Biomech. Eng.*, Vol. 120(1), pp.22–26, 1998.

633. J.Z. WU, W. HERZOG, and M. EPSTEIN, Modelling of location – and time – dependent deformation of chondrocyte during cartilage loading, *J. Biomech.*, Vol. 32, pp.563–572, 1999.

634. J. WU and W. HERZOG, Elastic anisotropy of articular cartilage is associated with the microstructures of collagen fibers and chondrocytes, *J. Biomech.*, Vol. 35, pp.931–942, 2002.

635. W. WULFF, The energy conservation equation for living tissue, *IEEE Trans. BME*, Vol. 21(6), pp.494–495, 1974.

636. H. YAMADA, Strength of Biological Materials, F.G. Evans [ed.], The Williams & Wilkins Company, Baltimore 1970.

637. T. YAMAGUCHI, [Ed.], Clinical Application of Computational Mechanics to the Cardiovascular System, Springer-Verlag, Tokyo 2000.

638. E. YAMAMOTO, W. IWANAGA, H. MIYAZAKI, and K. HAYASHI, Effects of static stress on the mechanical properties of cultured collagen fascicles from the rabbit patellar tendon, *J. Biomech. Eng.*, Vol. 124, pp.85–93, 2002.

639. E. YAMAMOTO, S. TOKURA, and K. HAYASHI, Effects of cyclic stress on the mechanical properties of cultured collagen fascicles from the rabbit patellar tendon, *J. Biomech. Eng.*, Vol. 125, pp.893–901, 2003.

640. Y. YOSHIMOTO, T. SHIBAMOTO, N. SANO, M. KUWAHARA, T. AKIBA, and F. MARUMO, Kinetics of anticoagulant to continouos hemofilter membranes, *J. Artif. Organs*, Vol. 5, pp.136–140.

641. H.F. YOUNIS, M.R. KAAZEMPUR-MOFRAD, R.C. CHAN, A.G. ISASI, D.P. HINTON, A.H. CHAU, L.A. KIM, R.D. KAMM, Hemodynamics and wall mechanics in human carotid bifurcation and its consequences for atherogenesis: investigation of inter-individual variation, *Biomech. Model. Mechanobiol.*, Vol. 3, pp.17–32, 2000.

642. M.T. YOUNG, S.M. BLANCHARD, M.W. WHITE, E.E. JOHNSON, W.M. SMITH, and R.E. IDEKER, Using an artificial neural network to detect activation during ventricular fibrillation, *Comp. Biomed. Res.*, Vol. 33, pp.43–58, 2000.

643. L. YIN and D.M. ELLIOTT, A biphasic and transversely isotropic mechanical model for tendon: application to mouse tail fascicles in uniaxial tension, *J. Biomech.*, Vol. 37, pp.907–916, 2004.

644. G.I. ZAHALAK, V. DE LABORDERIE, and J.M. GUCCIONE, The effects of cross-fiber deformation on axial fiber stress in myocardium, *J. Biomech. Eng.*, Vol. 121, pp.376–385, 1999.

645. M. ZAMIR, *The Physics of Pulsatile Flow*, Springer-Verlag, New York 2000.

646. E.A. ZAMIR and L.A. TABER, On the effects of residual stress in microindentation tests of soft tissue structures, *J. Biomech. Eng*, Vol. 126, pp.276–283, 2004.

647. Y. ZENG, J. YANG, K. HUANG, Z. LEE, and X. LEE, A comparison of biomechanical properties between human and porcine cornea, *J. Biomech.*, Vol. 34, pp.533–537, 2001.

648. L. ZHANG, K.H. YANG, and A.I. KING, Comparison of brain responses between frontal and lateral impacts by finite element modeling, *J. Neurotrauma*, Vol. 18, pp.21–30, 2001.

649. S.Z. Zhao, X.Y. Xu, and M.W. Collins, The numerical analysis of fluid-solid interactions for blood flow in arterial structures. Part 1: a review model for arterial wall behaviour, *Proc. Inst. Mech. Eng.*, Vol. 212, Part H, pp.229–240, 1989; Part 2: Development of coupled fluid-solid algorithms, ibid. pp.241-252.

650. Q.-S. Zheng, Theory of representations for tensor functions – a unified invariant approach to constitutive equations, *Appl. Mech. Rev.*, Vol. 47, pp.545–587, 1994.

651. C. Zhu, G. Bao, and N. Wang, Cell mechanics: mechanical response, cell adhesion, and molecular deformation, *Annu. Rev. Biomed. Eng.*, Vol. 2, pp.189–226, 2000.

652. H. Zhu, J.J. Warner, T.R. Gehrig, and M.H. Friedman, Comparison of coronary artery dynamics pre- and post- stenting, *J. Biomech.*, Vol. 35, pp.689–697, 2003.

653. L. Zhu, D.E. Lemons, and S. Weinbaum, A new approach for predicting the enhancements in the effective conductivity of perfused muscle due to hyperthermia, *Annals Biomed. Eng.*, Vol. 22, pp.1–12, 1995.

654. L. Zhu, D.E. Lemons, and S. Weinbaum, Microvascular thermal equilibration in rat cremaster muscle, *Annals Biomed. Eng.*, Vol. 24, pp.109–123, 1996.

655. M. Zhu, S. Weinbaum, and L.M. Jiji, Heat exchange between unequal countercurrent vessels asymetrically embedded in a cylinder with surface convection, *J. Heat Mass Transfer*, Vol. 33(10), pp.2275–2284, 1990.

656. M. Zhu, S. Weinbaum, and D.E. Lemons, A three-dimensional variable geometry countercurrent model for whole limb heat transfer, *J. Biomech. Eng.*, Vol. 114(3), pp.366–376, 1992.

657. M.A. Zulliger, G. Montorzi, and N. Stergiopulos, Biomechanical adaptation of porcine carotid vascular smooth muscle to hypo and hypertension in vitro, *J. Biomech.*, Vol. 35, pp.757–765, 2002.

658. M.A. Zullinger, P. Fridez, K. Hayashi, and N. Stergiopulos, A strain energy function for arteries accounting for wall composition and structure, *J. Biomech.*, Vol. 37, pp.989–1000, 2004.

———◇———